Stability of Swirl Tube Flow

A thesis accepted to the Faculty of Aerospace Engineering and Geodesy of the University of Stuttgart in partial fulfillment of the requirements for the degree of
Doctor of Engineering Sciences (Dr.-Ing.)

by

Ing. Pavel Novotný

born in Vimperk, Czech Republic

Main referee:	Prof. Dr.-Ing. habil. Bernhard Weigand
Co-referee:	Prof. Ing. František Maršík, DrSc.
Date of defence:	5 March 2019

Institute of Aerospace Thermodynamics
University of Stuttgart
2019

Preface

This thesis was written within a cooperation of the Institute of Aerospace Thermodynamic (ITLR), University of Stuttgart, Stuttgart, Germany with the Institute of Thermomechanics, The Czech Academy of Sciences, Prague, Czech Republic, and New Technologies-Research Centre, University of West Bohemia, Plzeň, Czech Republic, where I worked as research assistant.

Firstly, I want to express my deep gratitude to Prof. Dr.-Ing. habil. Bernhard Weigand, Director of the ITLR, for his sincere support and patience during this work. I have really enjoyed his guidance, discussions relating to thermodynamics and its application and also the scientific freedom that was given to me.

I would also like to express my deep regard to Prof. Ing. František Maršík, DrSc. for opening my mind to thermodynamics, his guidance during my work as research assistant in Prague and in Plzeň, and inspiriting discussions about the application of thermodynamics to engineering and living systems.

For the financial support, I would like to acknowledge that this work was developed within the CENTEM project, reg. no. CZ.1.05/2.1.00/03.0088, co-funded by the ERDF as part of the Ministry of Education, Youth and Sports OP RDI programme, and, in the follow-up sustainability stage, supported through the CENTEM PLUS (LO1402) by financial means from the Ministry of Education, Youth and Sports under the National Sustainability Programme I.

Moreover, I want to thank all my colleagues in the Czech Republic. My special thanks go to Ing. Hynek Chlup, Ph.D., who revealed to me the beauty of the applied mechanics. I would like to express my deep regard to PhDr. Martin Tomáš, Ph.D. for his comments to my work, support and for being my closest colleague in Plzeň.
For introduction to swirl flows and measurement via PIV technique, and for inspiriting discussions related to numerical methods, turbulence modeling and data postprocessing, I would like to express my thanks to Dr.-Ing. Bernhard Kobiela, who, moreover, together with Dr.-Ing. Joachim Karnahl, provided me a friendly workspace in their office during my first stay at the ITLR.
I want to give my deep gratitude to Dr.-Ing. Christoph Biegger, who, at the beginning, helped me to start studying at the ITLR and who became to be one of my friends. I want to thank him for deep discussions about thermodynamics, swirl flows, vortex breakdown, stability and his inspiring positive mind attitude. In addition, I am very grateful to every single colleague at the ITLR for the open, friendly and positive atmosphere. My special thanks belong to Dipl.-Ing. Julia Wienand, Dr.-Ing. Alexandros Terzis and Patrick Foltyn, M.Sc. for the asylum in their office, their support and patience with me during my stays at the ITLR. I would also like to give my special thanks to Dr.-Ing. Anuradha Bhatia for her support and inspiriting discussions in the field of flow in porous media.
Furthermore, the next special thanks belong to Florian Seibold, M.Sc., Andreas Schwab, M.Sc., and Dipl.-Ing. Philipp Wellinger, who discuss with me particular parts of my work and who helped me with organisational procedures at the ITLR.
Finally, my greatest gratitude belongs to my family, especially to my parents, for their everlasting support and their positive influence on me throughout my life and education.

Stuttgart, 2019

Contents

List of Figures ix

List of Tables xvii

List of Symbols xix

Abstract xxvii

Kurzfassung xxix

1 Introduction 1
- 1.1 Motivation . . . 1
- 1.2 Objectives . . . 2
- 1.3 Procedure . . . 3
- 1.4 Characteristic/Dimensionless Numbers . . . 4

2 Swirl Flows 9
- 2.1 Swirling Kind of Flow . . . 9
- 2.2 Stability of Fluid Flows . . . 24
- 2.3 Vortex Breakdown . . . 29

3 Stability Condition **37**
3.1 General Balance Law 37
3.2 Definition of Entropy 39
3.3 Thermodynamic Stability Condition (TSC) 43
3.4 Application of the Thermodynamic Stability Condition . . . 47
3.4.1 Steady Axial Flow 47
3.4.1.1 Laminar Flow 48
3.4.1.2 Turbulent Flow 49
3.4.2 Steady Flow in an Annulus 51
3.4.2.1 Couette Flow between Two Rotating Cylinders 52
3.4.2.2 Axial Flow in an Annulus between Rotating Tubes 56

4 Experimental Methods **63**
4.1 Experimental Apparatus 63
4.2 Mass Flow Measurement 64
4.3 Particle Image Velocimetry 65
4.4 Measurement Uncertainty 66

5 Numerical Methods **69**
5.1 Governing Equations 70
5.1.1 Balance of Mass 70
5.1.2 Balance of Momentum 71
5.2 Turbulence Modeling 72
5.2.1 Baseline Explicit Algebraic Reynolds Stress Model . 72
5.2.2 Gamma Transition Model 78
5.3 Numerical Setup 80
5.3.1 Numerical Solution 80
5.3.2 Numerical Errors 83

6 Results **85**
6.1 Experimental Details 86
6.2 Numerical Details 87
6.3 Approximation of the Results 88
6.4 Velocity Field 90
6.4.1 Axial Velocity Distribution 90
6.4.2 Tangential Velocity Distribution 92
6.5 Vortex Structure 94

6.6 Flow Analysis . . . 96
6.6.1 Swirl Number . . . 96
6.6.2 Vortex Breakdown . . . 98
6.7 Stability . . . 104
6.7.1 Local Values of the Thermodynamic Stability Condition . . . 104
6.7.1.1 Axial Velocity . . . 105
6.7.1.2 Tangential Velocity . . . 107
6.7.1.3 Axial and Tangential Velocities . . . 109
6.7.2 Global Values of the Thermodynamic Stability Condition . . . 112
6.7.2.1 Axial Velocity . . . 112
6.7.2.2 Tangential Velocity . . . 114
6.7.2.3 Axial and Tangential Velocities . . . 116
6.7.3 Stability and Vortex Breakdown . . . 119

7 Conclusions and Outlook **123**

Bibliography **127**

Appendix

A Thermodynamic Stability Condition in Cylindrical Coordinates **141**
A.1 Covariant and Contravariant Basis . . . 142
A.2 Relations between Coordinates . . . 144
A.3 Covariant Derivative . . . 145
A.4 Christoffel Symbols . . . 146
A.4.1 Christoffel Symbol of the First Kind . . . 146
A.4.2 Christoffel Symbol of the Second Kind . . . 146
A.5 Covariant and Contravariant Components of the Velocity Vector . . . 147
A.6 Divergence of the Second Order Tensor . . . 150
A.7 Covariant Derivative of a Constant . . . 155
A.8 Thermodynamic Stability Condition in the Cylindrical Coordinates . . . 157

B Thermodynamic Stability Condition for Laminar Flow **159**

C Thermodynamic Stability Condition for Turbulent Flow **163**

D Thermodynamic Stability Condition for Couette Flow between Rotating Cylinders **165**

E Supplementary Results **169**
E.1 Contour Plots of the Velocity Field 170
E.2 Local Values of the Thermodynamic Stability Condition . . 176
E.2.1 Axial Velocity 176
E.2.2 Tangential Velocity 177
E.2.3 Axial and Tangential Velocities 179
E.3 Global Values of the Thermodynamic Stability Condition . 180
E.3.1 Axial Velocity 180
E.3.2 Tangential Velocity 182
E.3.3 Axial and Tangential Velocities 183

List of Figures

1.1 Geometry of swirl tube with used coordinate system 2

2.1 Formation of a tornado [83] 11
2.2 2D maps showing swirling patterns, which can be developed after 8.5 h from initially passive tracers at time 0.0 h [67] . . . 12
2.3 Different forms of tornadoes appearance [60]; the left side shows the case when the critical cross-section close to the ground is followed by a supercritical A-type vortex up to the top; the right side shows the case of a B-type vortex flow, which is characterised by a tornado funnel 13
2.4 Schematics of Taylor-Couette flow with indicated flow structures [94]; in the scheme, h represents the period (size) of the Taylor cells in the axial flow direction 14
2.5 Regimes of Taylor-Couette flow [5] 15
2.6 Schematics of rotating flow in a cylinder a) no axial flow, b) with axial flow (helical structure) [2] 17

2.7 Radial and axial velocity vectors with azimuthal velocity contours for vortical flow [130]; the upper line in each frame is the rotating inner cylinder; the lower line is the stationary outer cylinder; a) velocity field including the axial velocity profile, b) velocity field with the subtracted axial velocity profile 17
2.8 Regimes of flow according to axial Reynolds number over Taylor number [31, 59] 19
2.9 Swirl cooling configuration proposed by Glezer et al. [37] . . . 21
2.10 Schematics of a vortex tube [27] 23
2.11 Spiral form of instability observed by Taylor [119] 25
2.12 Types of vortex breakdown [2, 30]; a) type 0, b) type 1, c) type 2, d) type 3, e1) type 4 - side view, e2) type 4 - top view, f1) type 5 - at $t = 0$ min, f2) type 5 - at $t = 5$ min, f3) type 5 - at $t = 10$ min, f4) type 5 - at $t = 15$ min, g) type 6 31
2.13 Conical vortex breakdown [97]; a) vortex breakdown at low Reynolds number, b) vortex breakdown at high Reynolds number 32
2.14 Rossby number dependency of wing-tip vortices [117]; variable W represents the characteristic axial velocity (in the text denoted by u^{z*}) 34

3.1 Schematics of 1D flow in the rigid tube 47
3.2 Velocity profile of a laminar flow in a tube and corresponding shape of the local TSC function 49
3.3 Velocity profile of a turbulent flow given by the power law in a tube and corresponding shape of the local TSC function 50
3.4 Flow between two rotating cylinders 53
3.5 Onset of coherent structures, i.e. instability, for flow between two rotating cylinders 55
3.6 Axial and tangential velocities by Pfitzer [99]; $Re = 10{,}000$, $\eta_C = 0.8575$, outer rotating cylinder 57
3.7 Local TSC function determined from data by Pfitzer [99]; $Re = 10{,}000$, $\eta_C = 0.8575$, $\hat{\pi} = \pi D_h^2/(\overline{U^z}^2 \mu)$, outer rotating cylinder 57
3.8 Axial and tangential velocities by Pfitzer [99]; $Re = 10{,}000$, $\eta_C = 0.8575$, inner rotating cylinder 58
3.9 Local TSC function determined from data by Pfitzer [99]; $Re = 10{,}000$, $\eta_C = 0.8575$, $\hat{\pi} = \pi D_h^2/(\overline{U^z}^2 \mu)$, inner rotating cylinder 58
3.10 Axial and tangential velocities by Rothe [109]; $Re = 10{,}000$, $\eta_C = 0.8575$, outer rotating cylinder 59

3.11 Local TSC function determined from data by Rothe [109]; Re = 10,000, $\eta_C = 0.8575$, $\hat{\pi} = \pi D_h^2/(\overline{U^z}^2\mu)$, outer rotating cylinder 60
3.12 Axial and tangential velocities by Rothe [109]; Re = 10,000, $\eta_C = 0.8575$, inner rotating cylinder 60
3.13 Local TSC function determined from data by Rothe [109]; Re = 10,000, $\eta_C = 0.8575$, $\hat{\pi} = \pi D_h^2/(\overline{U^z}^2\mu)$, inner rotating cylinder 61

4.1 Experimental apparatus (CAD) [16]; 1 - laminar flow element, 2 - inlet plenum, 3 - seeding chamber, 4 - swirl generator, 5 - swirl tube, 6 - outlet tube (changeable section), 7 - outlet plenum 64
4.2 Schematics of PIV principle [70] 65

6.1 Schematics of the swirl tube geometry 86
6.2 Hexahedral mesh of the tube with a detail view of the wall resolution 88
6.3 Comparison of experimental (experiment) and numerical (numerics) dimensionless axial velocity profiles; Re = 1,000, S_{IG} = 5.3 91
6.4 Comparison of experimental (experiment) and numerical (numerics) dimensionless axial velocity profiles; Re = 2,000, S_{IG} = 5.3 91
6.5 Comparison of experimental (experiment) and numerical (numerics) dimensionless axial velocity profiles; Re = 5,000, S_{IG} = 5.3 92
6.6 Comparison of experimental (experiment) and numerical (numerics) dimensionless tangential velocity profiles; Re = 1,000, $S_{IG} = 5.3$ 93
6.7 Comparison of experimental (experiment) and numerical (numerics) dimensionless tangential velocity profiles; Re = 2,000, $S_{IG} = 5.3$ 93
6.8 Comparison of experimental (experiment) and numerical (numerics) dimensionless tangential velocity profiles; Re = 5,000, $S_{IG} = 5.3$ 94
6.9 Vortex structures in the swirl tube; a) Re = 1,000, b) Re = 2,000, and c) Re = 5,000; S_{IG} = 5.3; red and blue colours represent positive and negative radial velocities 95
6.10 Local swirl numbers determined from the experimental results; $S_{IG} = 5.3$ 97

6.11 Local swirl numbers determined from the numerical results; $S_{IG} = 5.3$ 97
6.12 Local Rossby numbers over modified axial Reynolds number determined from experimental results; $S_{IG} = 5.3$ 99
6.13 Local Rossby numbers over modified axial Reynolds number determined from numerical results; $S_{IG} = 5.3$ 99
6.14 Local axial Reynolds number and local tangential Reynolds number determined from experimental results; Re = 1,000, $S_{IG} = 5.3$ 101
6.15 Local axial Reynolds number and local tangential Reynolds number determined from numerical results; Re = 1,000, $S_{IG} = 5.3$ 101
6.16 Local axial Reynolds number and local tangential Reynolds number determined from experimental results; Re = 2,000, $S_{IG} = 5.3$ 102
6.17 Local axial Reynolds number and local tangential Reynolds number determined from numerical results; Re = 2,000, $S_{IG} = 5.3$ 102
6.18 Local axial Reynolds number and local tangential Reynolds number determined from experimental results; Re = 5,000, $S_{IG} = 5.3$ 103
6.19 Local axial Reynolds number and local tangential Reynolds number determined from numerical results; Re = 5,000, $S_{IG} = 5.3$ 103
6.20 Comparison of experimental (experiment) and numerical (numerics) dimensionless values of the local TSC function with omitted influence of the wall for the axial velocity; Re = 1,000, $S_{IG} = 5.3$ 105
6.21 Comparison of experimental (experiment) and numerical (numerics) dimensionless values of the local TSC function with omitted influence of the wall for the axial velocity; Re = 2,000, $S_{IG} = 5.3$ 106
6.22 Comparison of experimental (experiment) and numerical (numerics) dimensionless values of the local TSC function with omitted influence of the wall for the axial velocity; Re = 5,000, $S_{IG} = 5.3$ 107
6.23 Comparison of experimental (experiment) and numerical (numerics) dimensionless values of the local TSC function with omitted influence of the wall for the tangential velocity; Re = 1,000, $S_{IG} = 5.3$ 108

6.24 Comparison of experimental (experiment) and numerical (numerics) dimensionless values of the local TSC function with omitted influence of the wall for the tangential velocity; Re = 2,000, $S_{IG} = 5.3$ 109
6.25 Comparison of experimental (experiment) and numerical (numerics) dimensionless values of the local TSC function with omitted influence of the wall for the tangential velocity; Re = 5,000, $S_{IG} = 5.3$ 109
6.26 Comparison of experimental (experiment) and numerical (numerics) dimensionless values of the local TSC function with omitted influence of the wall for the axial and tangential velocities; $Re = 1{,}000$, $S_{IG} = 5.3$ 110
6.27 Comparison of experimental (experiment) and numerical (numerics) dimensionless values of the local TSC function with omitted influence of the wall for the axial and tangential velocities; $Re = 2{,}000$, $S_{IG} = 5.3$ 111
6.28 Comparison of experimental (experiment) and numerical (numerics) dimensionless values of the local TSC function with omitted influence of the wall for the axial and tangential velocities; $Re = 5{,}000$, $S_{IG} = 5.3$ 111
6.29 Comparison of experimental (experiment) and numerical (numerics) dimensionless values of the global TSC function with omitted influence of the wall for the axial velocity; $Re = 1{,}000$, $S_{IG} = 5.3$ 113
6.30 Comparison of experimental (experiment) and numerical (numerics) dimensionless values of the global TSC function with omitted influence of the wall for the axial velocity; $Re = 2{,}000$, $S_{IG} = 5.3$ 114
6.31 Comparison of experimental (experiment) and numerical (numerics) dimensionless values of the global TSC function with omitted influence of the wall for the axial velocity; $Re = 5{,}000$, $S_{IG} = 5.3$ 114
6.32 Comparison of experimental (experiment) and numerical (numerics) dimensionless values of the global TSC function with omitted influence of the wall for the tangential velocity; Re = 1,000, $S_{IG} = 5.3$ 115
6.33 Comparison of experimental (experiment) and numerical (numerics) dimensionless values of the global TSC function with omitted influence of the wall for the tangential velocity; Re = 2,000, $S_{IG} = 5.3$ 116

6.34 Comparison of experimental (experiment) and numerical (numerics) dimensionless values of the global TSC function with omitted influence of the wall for the tangential velocity; $Re = 5{,}000$, $S_{IG} = 5.3$ 116
6.35 Comparison of experimental (experiment) and numerical (numerics) dimensionless values of the global TSC function with omitted influence of the wall for the axial and tangential velocities; $Re = 1{,}000$, $S_{IG} = 5.3$ 117
6.36 Comparison of experimental (experiment) and numerical (numerics) dimensionless values of the global TSC function with omitted influence of the wall for the axial and tangential velocities; $Re = 2{,}000$, $S_{IG} = 5.3$ 118
6.37 Comparison of experimental (experiment) and numerical (numerics) dimensionless values of the global TSC function with omitted influence of the wall for the axial and tangential velocities; $Re = 5{,}000$, $S_{IG} = 5.3$ 118
6.38 Global TSC function with omitted influence of the wall for the axial and tangential velocity component over the local Rossby number determined from experimental results; $S_{IG} = 5.3$ . . . 119
6.39 Global TSC function with omitted influence of the wall for the axial and tangential velocity component over the local Rossby number determined from numerical results; $S_{IG} = 5.3$ 120

A.1 Relations between the Cartesian and cylindrical coordinate system 142

E.1 Axial and tangential velocities at the selected position determined from experimental results; $Re = 1{,}000$, $S_{IG} = 5.3$ 170
E.2 Axial and tangential velocities at the selected position determined from numerical results; $Re = 1{,}000$, $S_{IG} = 5.3$ 171
E.3 Axial and tangential velocities at the selected position determined from experimental results; $Re = 2{,}000$, $S_{IG} = 5.3$ 172
E.4 Axial and tangential velocities at the selected position determined from numerical results; $Re = 2{,}000$, $S_{IG} = 5.3$ 173
E.5 Axial and tangential velocities at the selected position determined from experimental results; $Re = 5{,}000$, $S_{IG} = 5.3$ 174
E.6 Axial and tangential velocities at the selected position determined from numerical results; $Re = 5{,}000$, $S_{IG} = 5.3$ 175

E.7 Comparison of experimental (experiment) and numerical (numerics) dimensionless values of the local TSC function with included influence of the wall for the axial velocity; $Re = 1{,}000$, $S_{IG} = 5.3$ 176
E.8 Comparison of experimental (experiment) and numerical (numerics) dimensionless values of the local TSC function with included influence of the wall for the axial velocity; $Re = 2{,}000$, $S_{IG} = 5.3$ 176
E.9 Comparison of experimental (experiment) and numerical (numerics) dimensionless values of the local TSC function with included influence of the wall for the axial velocity; $Re = 5{,}000$, $S_{IG} = 5.3$ 177
E.10 Comparison of experimental (experiment) and numerical (numerics) dimensionless values of the local TSC function with included influence of the wall for the tangential velocity; $Re = 1{,}000$, $S_{IG} = 5.3$ 177
E.11 Comparison of experimental (experiment) and numerical (numerics) dimensionless values of the local TSC function with included influence of the wall for the tangential velocity; $Re = 2{,}000$, $S_{IG} = 5.3$ 178
E.12 Comparison of experimental (experiment) and numerical (numerics) dimensionless values of the local TSC function with included influence of the wall for the tangential velocity; $Re = 5{,}000$, $S_{IG} = 5.3$ 178
E.13 Comparison of experimental (experiment) and numerical (numerics) dimensionless values of the local TSC function with included influence of the wall for the axial and tangential velocities; $Re = 1{,}000$, $S_{IG} = 5.3$ 179
E.14 Comparison of experimental (experiment) and numerical (numerics) dimensionless values of the local TSC function with included influence of the wall for the axial and tangential velocities; $Re = 2{,}000$, $S_{IG} = 5.3$ 179
E.15 Comparison of experimental (experiment) and numerical (numerics) dimensionless values of the local TSC function with included influence of the wall for the axial and tangential velocities; $Re = 5{,}000$, $S_{IG} = 5.3$ 180
E.16 Comparison of experimental (experiment) and numerical (numerics) dimensionless values of the global TSC function with included influence of the wall for the axial velocity; $Re = 1{,}000$, $S_{IG} = 5.3$ 180

E.17 Comparison of experimental (experiment) and numerical (numerics) dimensionless values of the global TSC function with included influence of the wall for the axial velocity; $Re = 2{,}000$, $S_{IG} = 5.3$ 181
E.18 Comparison of experimental (experiment) and numerical (numerics) dimensionless values of the global TSC function with included influence of the wall for the axial velocity; $Re = 5{,}000$, $S_{IG} = 5.3$ 181
E.19 Comparison of experimental (experiment) and numerical (numerics) dimensionless values of the global TSC function with included influence of the wall for the tangential velocity; $Re = 1{,}000$, $S_{IG} = 5.3$ 182
E.20 Comparison of experimental (experiment) and numerical (numerics) dimensionless values of the global TSC function with included influence of the wall for the tangential velocity; $Re = 2{,}000$, $S_{IG} = 5.3$ 182
E.21 Comparison of experimental (experiment) and numerical (numerics) dimensionless values of the global TSC function with included influence of the wall for the tangential velocity; $Re = 5{,}000$, $S_{IG} = 5.3$ 183
E.22 Comparison of experimental (experiment) and numerical (numerics) dimensionless values of the global TSC function with included influence of the wall for the axial and tangential velocities; $Re = 1{,}000$, $S_{IG} = 5.3$ 183
E.23 Comparison of experimental (experiment) and numerical (numerics) dimensionless values of the global TSC function with included influence of the wall for the axial and tangential velocities; $Re = 2{,}000$, $S_{IG} = 5.3$ 184
E.24 Comparison of experimental (experiment) and numerical (numerics) dimensionless values of the global TSC function with included influence of the wall for the axial and tangential velocities; $Re = 5{,}000$, $S_{IG} = 5.3$ 184

List of Tables

4.1 Values of experimental parameters and the measurement uncertainties 68

6.1 Examined Reynolds numbers and corresponding axial bulk velocity, mass flow rate and angular velocity of solid body rotation 86
6.2 Numerically simulated Reynolds numbers, inlet velocities and outlet boundary condition for $S_{IG} = 5.3$ 87
6.3 R_{fit} values for approximated velocities obtained experimentally 89
6.4 R_{fit} values for approximated velocities obtained numerically . . 90

List of Symbols

Latin Characters

Symbol	Description	Unit
A	constant related to angular velocity	s^{-1}
A	area	m^2
a_{ij}	Reynolds stress anisotropy tensor	Pa
B	constant related to angular velocity	s^{-1}
c	coefficient	
c_p	heat capacity at constant pressure	J kg^{-1} K^{-1}
D	tube diameter	m
D_h	tube hydraulic diameter	m
d	total differential	
đ	inexact (imperfect) differential	
d^{ik}	strain rate tensor	s^{-1}
$\mathrm{d}\overline{A}$	area element	m^2
$\mathrm{d}\overline{V}$	volume element	m^3
$E_{\gamma 1}$	source of transition in the GTM	
$E_{\gamma 2}$	source of destruction (sink) in the GTM, relaminarisation	
F_1	Froude number at state 1	–

Symbol	Description	Unit
F_1	weight function in the BSL turbulence model	
F_2	Froude number at state 2	–
F_c	critical Froude number	–
f_i	external volume forces	–
G_ϕ	angular momentum	kg m^2 s^{-2}
G_z	axial momentum	kg m s^{-2}
$\mathbf{g}_i$	covariant basis vector $i = r, \phi, z$	
$\mathbf{g}^i$	contravariant basis vector $i = r, \phi, z$	
g_{ij}	covariant metric tensor i,$j = r, \phi, z$	
g^{ij}	contravariant metric tensor i,$j = r, \phi, z$	
h	inlet height	m
h_t	specific total enthalpy	J kg^{-1}
$J(\Phi)$	total flux of a balanced quantity Φ	
$J^K(\Phi)$	flux density of a balanced quantity Φ in the material description	
$j^k(\Phi)$	flux density of a balanced quantity Φ in the actual description	
K	constant	
k	turbulent kinetic energy	m^2 s^{-2}
k_w	constant	–
L	length	m
l	pitch of helical symmetry	m
M	number of samples, set of observations	–
$\dot{m}$	mass flow rate	kg s^{-1}
N	rotation number	–
N_K	unit normal vector in the material description	–
n	number of inlets	–
n_k	unit normal vector in the actual description	–
$P(\Phi)$	production of a balanced quantity Φ per unit time	
P_k	production of turbulent kinetic energy	kg m^{-1} s^{-3}
$P_{\gamma 1}$	source of transition in the GTM	
$P_{\gamma 2}$	source of destruction (sink) in the GTM, relaminarisation	
p	pressure	Pa
Q	heat	J
Q	Q - criterion	s^{-2}
Q^K	density of the heat flux in the material description	J m^{-2} s^{-1}

Symbol	Description	Unit
$\tilde{Q}$	density of the absorbed or emitted energy in the material description	J m^{-3} s^{-1}
q^k	density of the heat flux in the actual description	J m^{-2} s^{-1}
$\tilde{q}$	density of the absorbed or emitted energy in the actual description	J m^{-3} s^{-1}
R	tube radius	m
R_{fit}	correlation coefficient	–
$\mathbf{r}$	vector from an upwind node to an integration point	m
r	radial coordinate	m
r_c	vortex core size	m
r^*	characteristic length scale corresponding to position of the maximum tangential velocity	m
$\tilde{r}$	dimensionless radial coordinate	–
Re	Reynolds number	–
Re_ϕ	local tangential Reynolds number	–
Re_z	local axial Reynolds number	–
Re_z^*	modified axial Reynolds number	–
$Re_{\theta c}$	critical Reynolds number in the GTM	–
$Re_{\theta t}$	transition Reynolds number in the GTM	–
Ro	Rossby number	–
S	swirl number	–
S	entropy	J K^{-1}
S_{IG}	geometrical swirl number	–
S_{ij}	strain rate tensor	s^{-1}
S_{ij}^*	dimensionless strain rate tensor	–
s	specific entropy	J kg^{-1} K^{-1}
T	temperature	K
t	time	s
t^{ik}	stress tensor	Pa
t_{dis}^{ik}	dissipative part of the stress tensor	Pa
$\hat{t}$	Student's multiplier	–
Ta	Taylor number	–
$\overline{U^z}$	axial bulk velocity	m s^{-1}
$\mathbf{u}$	velocity vector	m s^{-1}
u^0	velocity at vortex axis	m s^{-1}
u	specific internal energy	J kg^{-1}
u^r	radial velocity	m s^{-1}
u^ϕ	tangential velocity	m s^{-1}

Symbol	Description	Unit
$\overline{u^{\phi}}$	mean tangential velocity	m s^{-1}
$u^{\phi *}$	maximum tangential velocity	m s^{-1}
u^{z}	axial velocity	m s^{-1}
$\overline{u^{z}}$	mean axial velocity	m s^{-1}
u^{z*}	axial velocity at position r^*	m s^{-1}
V	volume	m^3
V^K	propagation velocity of a discontinuity surface in the material description	m s^{-1}
v^k	propagation velocity of a discontinuity surface in the actual description	m s^{-1}
w	inlet width	m
w	specific (mechanical) work	J kg^{-1}
$\mathbf{X}$	position in the material description	m
$\mathbf{x}$	position in the actual description	m
x,y,z	Cartesian coordinates	m
$\hat{y}$	measured value	
y_1^+	dimensionless wall distance	–
z	axial coordinate	m

Greek Characters

Symbol	Description	Unit
α_1	coefficient in the Wilcox $k-\omega$ turbulent model	
α_2	coefficient in the transformed $k-\epsilon$ turbulent model	
β	blend parameter in the numerical scheme	
β_1	coefficient in the Wilcox $k-\omega$ turbulent model	
β_2	coefficient in the transformed $k-\epsilon$ turbulent model	
β'	coefficient in the transformed $k-\epsilon$ and Wilcox $k-\omega$ turbulent model	
Γ	circulation	$m^2 s^{-1}$
Γ_{ij}^k	Christoffel's symbol of the second kind	
γ	intermittency	
Δ	change of a value	
δ	deviation from reference (initial) state, variation	
δ^{ik}	Kronecker delta	
ϵ	turbulent dissipation	m^2 s^{-3}

Symbol	Description	Unit
$\hat{\epsilon}$	measurement uncertainty	%
η_C	ratio of cylinders (pipes) radii	–
$\Theta(r)$	discriminant of stability	s^{-2}
λ	thermal conductivity	W m^{-1} K^{-1}
μ	dynamic viscosity	Pa s
μ_C	ratio of angular velocities	–
ν	kinematic viscosity	m^2 s^{-1}
Π	integral (global) value of the TSC function	J s^{-1}
$\bar{\Pi}$	fundamental thermodynamic inequality, density of energy dissipation in the material description	J m^{-3} s^{-1}
π	fundamental thermodynamic inequality, local value of the TSC function	J m^{-3} s^{-1}
$\bar{\pi}$	fundamental thermodynamic inequality, density of energy dissipation in the actual description	J m^{-3} s^{-1}
$\hat{\pi}$	dimensionless local value of the TSC function	–
ρ	density	kg m^{-3}
$\Sigma(\Phi)$	density production of a quantity Φ in the material description	
σ	corrected sum of relative errors	–
$\sigma(\Phi)$	density production of a quantity Φ in the actual description	
σ_{k1}	coefficient in the Wilcox $k-\omega$ turbulent model	
σ_{k2}	coefficient in the transformed $k-\epsilon$ turbulent model	
σ_γ	coefficient in the GTM	
$\sigma_{\omega 1}$	coefficient in the Wilcox $k-\omega$ turbulent model	
$\sigma_{\omega 2}$	coefficient in the transformed $k-\epsilon$ turbulent model	
τ_{ij}	Reynolds stress tensor	
Υ	surface of a discontinuity in the material description	
υ	surface of a discontinuity in the actual description	
$\Phi(r)$	general balanced quantity	
ϕ	tangential, cylindrical, coordinate	rad
ϕ	potential of external volume forces	J kg^{-1}
$\phi(\mathbf{X},t)$	volumetric density of a balanced quantity in the material description	
$\phi(\mathbf{x},t)$	volumetric density of a balanced quantity in the actual description	
φ	variable in the numerical scheme	

Superscripts

Symbol	Description	Unit
Ω	angular velocity	rad s^{-1}
Ω_{ij}	vorticity tensor	s^{-1}
Ω^*_{ij}	dimensionless vorticity tensor	$-$
ω	turbulent frequency	s^{-1}

Subscripts

Symbol	Description
0	initial state
1	inner cylinder (pipe)
2	outer cylinder (pipe)
a	axial
BSL	baseline
fit	fitted value
i	inner
i,j,k	tensor indices
ip	integration point
o	outer
p	constant pressure
rev	reversible
s	constant entropy
t	turbulent
up	upwind node

Superscripts

Symbol	Description
$\dot{()}$, $\dot{\bar{()}}$	material derivative
$()'$	fluctuation
i,j,k	tensor indices
vc	velocity component

Abbreviations

Abbrevation	Description
1D	One Dimensional
2D	Two Dimensional
3D	Three Dimensional
BSL	Baseline
BSLEARSM	Baseline Explicit Algebraic Reynolds Stress Model
CAD	Computer-Aided Design
CCD	Charge-Coupled Device
CFD	Computational Fluid Dynamics
CFL	Courant-Friedrichs-Lewy
CV	Control Volume
FEM	Finite Element Method
FVM	Finite Volume Method
GTM	Gamma Transition Model
ILU	Incomplete Lower Upper
ITLR	Institut für Thermodynamik der Luft- und Raumfahrt
Nd:YAG	Neodymium-doped Yttrium Aluminum Garnet
PDE	Partial Differential Equations
PIV	Particle Image Velocimetry
RANS	Reynold-Averaged Navier-Stokes
TSC	Thermodynamic Stability Condition

Abstract

Flows in swirl tubes can represent a model of a flow between rotating tubes, a Taylor-Couette flow, a flow in vortex tubes, or a flow in internal cooling channels of turbine blades. Thus, this work focuses on detailed investigation of the flow phenomena and flow stability in swirl tubes. In general, a swirl tube is a tube with one or more tangential inlets generating complex 3D swirling flow. This leads to large tangential velocities near the wall and, moreover, to enhanced turbulent mixing in the tube, which results in a positive influence on the convective heat transfer in the tube.
Firstly, a formulation of a condition to investigate stability of a flow is provided. This formulation reflects the definition of the second law of thermodynamics, i.e. the balance of entropy, and also the balance of the total enthalpy. Due to this general approach based on the second law of thermodynamics, the derived condition may serve as a criterion to investigate processes in general flows, for which an incompressible fluid via the Cauchy stress tensor is approximated. Moreover, the derived criterion can be modified also for a compressible flow or even for flow of a non-Newtonian fluid.
Secondly, a swirl tube with tangential inlets at the upstream end of the tube is investigated. In a detailed study, the flow fields for one swirl number and several mass flow rates, i.e. Reynolds numbers, are obtained experimentally and numerically. The investigated Reynolds numbers cover laminar, intermediate, and also turbulent flow regimes. Hence, the flow fields are measured via Particle Image Velocimetry. The numerical simulations are carried out via the commercial code ANSYS CFX using the Baseline Explicit Algebraic Reynolds Stress Model with the added Gamma Transition Model in case of

the lowest investigated Reynolds number.
The analysis of flow fields shows an axial backflow region in the tube centre determining possible vortex breakdown. For the lowest Reynolds number, an axial backflow region, in contrast to the higher Reynolds numbers, is observable up to the middle of the tube length. So that, there is a region where the flow is dominated by the axial velocity characterised by no vortex breakdown. Moreover, similar behaviour is also observed for the intermediate Reynolds number near the tube outlet. Nevertheless, for swirl dominated flow, a possible vortex breakdown may be expected for a Rossby number lower than 0.65. Here, the Rossby number is defined as the ratio between the axial velocity at the position of the maximum tangential velocity and the maximum tangential velocity. Furthermore, a vortex breakdown can also be represented via a comparison of the local axial Reynolds number with the local tangential Reynolds number, which are based on the mean values of the velocities. It is shown that a vortex breakdown may occur in regions where the ratio between the local tangential Reynolds number and the local axial Reynolds number is greater than 1. So, in these regions, the swirl flow becomes dominated by the tangential velocity.
In addition, a connection between the derived stability criterion and the vortex breakdown is investigated. It is confirmed that the redistribution of flow fields is due to the highest swirl strength dominant at the beginning of the tube. Moreover, it is shown that according to the derived stability criterion, vortex breakdown is accompanied by processes causing flow stabilisation.
In swirl dominated flows, the tangential velocity may be characterised as a Rankine vortex consisting of a solid body vortex in the tube centre and a potential vortex in the outer region. According to the derived stability criterion, the solid body vortex is at the margin of stability meaning that even a small disturbance or fluctuation may cause instability of the flow. On the other hand, the potential vortex is stable according to the derived stability criterion. Due to these two points, the solid body vortex is transformed to a potential vortex downstream towards the tube outlet. It is also shown that an influence of the axial velocity on this transition is insignificant and the derived stability criterion is driven mainly by the tangential velocity. Moreover, the velocity transition is dominant in the first 20 % of the tube length. Due to this, the strong dissipative processes in this region would lead to an enhanced heat transfer. Thus, in application of the swirl flow in cooling devices, usage of multiple tangential inlets along the tube length would lead to a more effective and homogeneous heat transfer over the entire tube length.

Kurzfassung

Eine Wirbelrohrströmung kann als Modell einer Strömung im Rohr mit rotierenden Wellen, einer Taylor-Couette Strömung oder einer Strömung in internen Kühlkanälen von Gasturbinenschaufeln dienen. Die vorliegende Arbeit behandelt daher die auftretenden Strömungsphänomene und die Stabiltätsanalyse im Wirbelrohr. Ein Wirbelrohr ist im Allgemeinen ein Rohr mit einem oder mehreren tangentialen Einlässen, die eine komplexe dreidimensionale Drallströmung erzeugen. Durch diese Drallströmung ergeben sich in Wandnähe hohe tangentiale Geschwindigkeiten und eine ausgeprägte turbulente Mischung im Rohr, welche den konvektiven Wärmeübergang im Rohr erhöhen.
Im ersten Schritt wird die Formulierung eines Kriteriums für die Stabilitätsanalyse der Strömungen entwickelt. Dieses Kriterium basiert auf den zweiten Hauptsatz der Thermodynamik, ausgedrückt durch die Bilanz der Entropie, und die Bilanz der Gesamtenthalpie. Durch diesen allgemeinen Ansatz dient das hergeleitete Kriterium zur Untersuchung der Prozesse in allgemeinen Strömungen, für welche ein inkompressibles Fluid mittels des Cauchy Spannungstensors approximiert wird. Darüber hinaus kann das hergeleitete Kriterium generell auch für kompressible Strömungen, oder sogar für Strömungen eines nichtnewtonschen Fluids, angepasst werden.
Im zweiten Schritt wird ein einfaches Wirbelrohr mit tangentialen Einlässen am Rohranfang untersucht. In detaillierten Untersuchungen werden das Strömungsfeld für eine Drallzahl und verschiedene Massenströme, bzw. Reynoldszahlen, mittels experimenteller und numerischer Methoden bestimmt. Die

untersuchten Reynoldszahlen umfassen laminare, transitionale und auch turbulente Strömungen. Das Geschwindigkeitsfeld wird mittels PIV (Particle Image Velocimetry) gemessen. Die numerischen Simulationen werden mittels des kommerziellen Codes ANSYS CFX unter Verwendung des Baseline expliziten algebraischen Reynoldsspannungsmodells mit hinzugefügtem Gamma Transitionsmodell für die niedrigste untersuchte Reynoldszahl durchgeführt.
Die Strömungsfeldanalyse zeigt ein axiales Rückströmgebiet im Rohrkern, welches einen Wirbelzusammenbruch als Folge haben kann. Für die niedrigste Reynoldszahl tritt dieses axiale Rückströmgebiet, im Gegensatz zu höheren Reynoldszahlen, bis zur axialen Rohrmitte auf. Dieser Sachverhalt zeigt deutlich, dass es eine Region gibt, welche von der Axialgeschwindigkeit dominiert wird und daher kein Wirbelzusammenbruch zu erwarten ist. Darüber hinaus wird ein analoges Verhalten des Rückströmgebietes für die transitionale Reynoldszahl in der Nähe des Rohrauslasses beobachtet. Jedoch wird gezeigt, dass für dralldominierte Strömungen ein möglicher Wirbelzusammenbruch für eine Rossbyzahl niedriger als 0,65 erwartet werden kann. Diese Rossbyzahl ist definiert als ein Verhältnis von Axialgeschwindigkeit an der Position des Maximums der Umfangsgeschwindigkeit zu dem Maximum der Umfangsgeschwindigkeit. Darüber hinaus kann ein Wirbelzusammenbruch mittels eines Vergleichs der lokalen Axial-Reynoldszahl mit der lokalen Umfangs-Reynoldszahl dargestellt werden. Daher kann gezeigt werden, dass es im Strömungsgebiet zu einem Wirbelzusammenbruch kommen kann, wo das Verhältnis der lokalen Umfangs-Reynoldszahl zur lokalen Axial-Reynoldszahl größer als eins ist. In diesen Bereichen ist daher die Gesamtströmung durch die Umfangsgeschwindigkeit dominiert.
Zusätzlich wird ein Zusammenhang zwischen dem hergeleiteten Stabilitätskriterium und einem Wirbelzusammenbruch untersucht. Es kann gezeigt werden, dass am Anfang des Rohres die Umwandlung des Strömungsfeldes aufgrund der höchsten Drallstärke am größten ist. Das hergeleitete Stabilitätskriterium zeigt, dass ein Wirbelzusammenbruch von strömungstabilisierenden Prozessen begleitet wird.
Bei dralldominierter Strömung kann die Umfangsgeschwindigkeit als ein Rankinewirbel, bestehend aus einem Starrkörperwirbel im Rohrkern und einem Potenzialwirbel im Außenbereich, modelliert werden. Nach dem hergeleiteten Stabilitätskriterium ist die Stabilität des Starrkörperwirbels im Randbereich entscheidend, da sogar eine kleine Störung oder Fluktuation zur Instabilität der Gesamtströmung führen kann. Hierbei wird eine Störung oder Fluktuation durch dissipative Prozesse der Strömung nicht abgeschwächt. Im Gegensatz dazu ist ein Potenzialwirbel nach dem hergeleiteten Stabilitäts-

kriterium stabil. Aufgrund dieser beiden Ergebnisse wird der Starrkörperwirbel in einen Potenzialwirbel stromabwärts zum Rohrauslass umgewandelt. Es wird ferner gezeigt, dass ein Einfluss der Axialgeschwindigkeit auf diese Umwandlung vernachlässigbar ist und dass das hergeleitete Stabilitätskriterium von der Umfangsgeschwindigkeit abhängt. Darüber hinaus dominiert die Umwandlung der Geschwindigkeit in den ersten 20 % der Rohrlänge. Deswegen können die starken dissipativen Prozesse in dieser Region zu einer verbesserten Wärmeübertragung führen. Bei einer Verwendung der Wirbelströmung in Kühlapparaten würde somit der Einsatz von mehrfachen tangentialen Einlässe längs der Rohrlänge zu einer effektiveren und homogeneren Wärmeübertragung über die gesamte Rohrlänge beitragen.

CHAPTER 1

Introduction

1.1 Motivation

Due to its complexity, the swirl flow is taken as a vortex flow model in the fundamental research and is utilised and investigated in engineering applications as well, mainly in aircraft engines, gas turbines, and vortex tubes. The complexity of the swirl is characterised by enhanced turbulence and in case of the bounded flow, i.e. bounded by tube walls, by large tangential velocities near the tube wall. Thus, the swirl flow in the tube positively affects the convective heat transfer compared to a non-swirling flow. This positive effect leads to application of the swirl flow in turbomachinery for blade cooling to protect turbine blades from extreme thermal loads. On the other hand, complexity of the unbounded swirl flow serves as a tool to clarify formation and flow description of hurricanes or tornadoes.
The influence of rotation on the flow has been investigated for many years. The investigation has shown that as the fluid rotates, i.e. the swirl flow is generated, different flow phenomena occur, e.g. vortex breakdown, generation and decay of vortices, flow redistribution, flow instabilities. Furthermore, flow phenomena may positively or negatively affect the flow characteristics,

e.g. constant fluid stirring, convective heat transfer. Thus, a great effort is made in the experimental and theoretical investigation of the swirl flow in order to find a suitable tool based on general physical (thermodynamic) relation supported by experimental and numerical techniques.
Unfortunately, there is no generally acceptable tool for capturing all of the flow phenomena occurring in the swirl flow. Hence, this work aims to provide a general overview of commonly used tools to characterise swirl flow. Moreover, the main subject of this work is to extend presented tools by a novel approach utilising consequences of the second law of thermodynamics, which helps to understand the flow phenomena in swirl flow, which can also lead to cooling optimisation of the turbine blades, aircraft engines, and flow in vortex tubes.

1.2 Objectives

In this work, investigation of a swirl tube, representing a simplified model of the vortex tube or swirl tube utilised in turbine blades for internal cooling, is performed. For this, experimental and numerical studies are conducted in order to investigate the complex flow field. Furthermore, theoretical investigation of the second law of thermodynamics and derivation of its alternative form represented by the fundamental thermodynamic inequality being used as a stability criterion are shown. Moreover, an additional approach enabling analysis of the vortex breakdown is presented.
The investigated simplified vortex tube consists of two tangential inlets at the upstream end of the tube, see Fig. 1.1. So, the flow in the tube is induced only tangentially. This simplified geometry enables to gain better information about the flow field of a swirl flow in a tube.
Particle Image Velocimetry (PIV) is used to experimentally obtain the flow

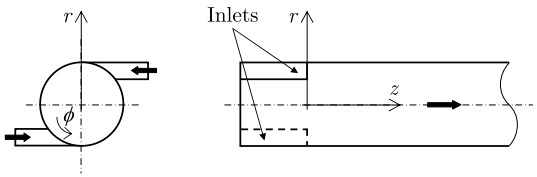

Fig. 1.1: Geometry of swirl tube with used coordinate system

fields. The experimentally obtained data serve also for validation of the conducted numerical simulations allowing detailed analysis of the complex flow fields occurring in the swirl flow. Then, the numerically and experimentally obtained data are utilised for the investigation of the velocity redistribution and the vortex breakdown phenomena. Moreover, these data are used for the stability analysis using the derived fundamental thermodynamic inequality, which provides an additional information about the character of the swirl flow.

1.3 Procedure

The swirl tube is investigated for one swirl number S and different Reynolds numbers Re, whose definitions are given in Section 1.4. Furthermore, the inlet condition may also be characterised by the geometrical swirl number S_{IG} determined for particular inlet dimensions and number of the tangential inlets. Hence, the value of the geometrical swirl number is $S_{IG} = 5.3$. In addition, the experimentally and numerically investigated swirl flow in the tube is characterised by various Reynolds numbers covering laminar, intermediate, and turbulent flow regimes, which are represented by $Re = 1{,}000$, $Re = 2{,}000$, and $Re = 5{,}000$, respectively.
In the experimental work, the velocity field is obtained via the PIV technique with a 2D laser sheet. Thus, the flow needs to be seeded with light scattering particles, also denoted as tracer particles, which are illuminated by two laser pulses in a short time period. The scattered light is then recorded by a CCD camera. The PIV recording is then divided in small interrogation windows, in which the velocity vector is determined from the particles shift and the time period between two pulses.
Moreover, the velocity field and the complex flow structures in swirl tubes are numerically investigated via the commercial code ANSYS CFX by solving the Reynolds-Averaged Navier-Stokes equations (RANS) in order to capture the turbulent behaviour of the swirl flow. Numerical simulation of the laminar-like flow regime is, further, extended by the Gamma Transition Model (GTM) that is used to include the transition to turbulence via an equation for the intermittency.
In the theoretical part, the derivation of the novel stability criterion taking into account the balance of the total enthalpy and the second law of thermodynamics is given. The novel stability criterion utilises the experimentally and numerically obtained data to investigate the redistribution, i.e. dissi-

pative and destabilising processes, of the swirl flow towards the tube outlet. Firstly, the numerical and experimental data are approximated via a model of an axisymmetrical helical vortex, which results in smooth curves evenly distributed over the radial coordinate with no undesirable sharp differences between individual radial positions.
Additionally, the approximated experimental and numerical data are then analysed by means of the flow analysis covering the decrease of the swirl strength, defined by the swirl number, and the vortex breakdown phenomena, characterised by the Rossby number. Vortex breakdown is also analysed via the local axial and tangential Reynolds numbers, which are functions of the mean values of the respective velocities. Definitions of these numbers are given in Section 1.4. Furthermore, it is shown that the flow analysis covering the stability investigation via the novel criterion based on the second law of thermodynamics enables characterisation of the flow redistribution downstream to the tube outlet. Finally, a connection between the vortex breakdown phenomena and the novel stability criterion is presented in order to determine a dominant flow character affecting the performance of the swirl flow.

1.4 Characteristic/Dimensionless Numbers

In general, a flow, e.g. the flow in a swirl tube, can be described via dimensionless numbers. The dimensionless numbers allow a comparison of different experiments and numerical simulations and may be helpful for a transfer of the results from laboratory conditions to the conditions respecting the technical application.

Reynolds Number

The Reynolds number is defined as the ratio of inertial forces to viscous forces. For internal flows, the Reynolds number is a function of the tube diameter D, the axial bulk velocity $\overline{U^z}$ and the fluid kinematic viscosity ν, hence

$$Re = \frac{\overline{U^z} D}{\nu} = \frac{4\dot{m}}{\rho \pi D \nu}, \tag{1.1}$$

where ρ is the fluid density.
So, the Reynolds number allows the comparison of flow conditions, i.e. experimental and/or numerical, at the same mass flow rate $\dot{m}$.

Local Axial Reynolds Number

The local axial Reynolds number takes into account mean values of the axial velocity measured and/or computed at the defined axial position of the tube. It is expressed as

$$Re_z = \frac{\overline{u^z} D}{\nu}. \tag{1.2}$$

Here, $\overline{u^z}$ is the mean value of the axial velocity, D represents the tube diameter and ν is the fluid kinematic viscosity.

Modified Axial Reynolds number

The modified axial Reynolds number is defined for the axial velocity at the radial position corresponding to the maximum value of the tangential velocity at the defined axial position of the tube. Thus, this definition is given by

$$Re_z^* = \frac{u^{z*} r^*}{\nu}. \tag{1.3}$$

Here, r^* is the characteristic length scale corresponding to the position of the maximum value of the tangential velocity, u^{z*} is the axial velocity at the position r^* and ν is the fluid kinematic viscosity.

Local Tangential Reynolds Number

The local tangential Reynolds number takes into account mean values of the tangential velocity at the defined axial position of the tube and has the following form

$$Re_\phi = \frac{\overline{u^\phi} D}{\nu}. \tag{1.4}$$

Here, $\overline{u^\phi}$ is the mean value of the tangential velocity, D represents the tube diameter and ν is the fluid kinematic viscosity.

Swirl Number

The swirl number characterises the swirl strength in a flow and is defined as the ratio of an axial flux of the angular momentum G_ϕ divided by the tube radius R to an axial flux of the axial momentum G_z [41]. Hence, this ratio is written as

$$S = \frac{G_\phi}{RG_z} = \frac{\int\limits_A \rho u^z u^\phi r \mathrm{d}\overline{A}}{R\int\limits_A \rho u^z u^z \mathrm{d}\overline{A}} = \frac{\int\limits_0^R 2\pi\rho u^z u^\phi r^2 \mathrm{d}r}{R\int\limits_0^R 2\pi\rho u^z u^z r \mathrm{d}r}. \tag{1.5}$$

The swirl number decreases downstream as the tangential velocity decays along the tube length. Moreover, the swirl number depends on the local cross-section. So, the local value cannot be calculated in advance since the velocity distribution is unknown.
Based on the inlet conditions and the swirl tube geometry, the geometrical swirl number is introduced in order to show a relation between the different inlet geometries and the swirl tubes [16] and [66]. This quantity reads

$$S_{IG} = \frac{\pi R^2 \left(R - \frac{h}{2}\right)}{Rnwh}, \tag{1.6}$$

where R is the tube radius, w is width of the inlet, h is height of the inlet and n is number of the inlets.

Rossby number

The Rossby number is defined as the ratio of the axial velocity at the radial position corresponding to the maximum value of the tangential velocity at the defined axial position of the tube and the maximum value of the tangential velocity. Thus, this dimensionless number is formulated as

$$Ro = \frac{u^{z*}}{\Omega r^*} = \frac{u^{z*}}{u^{\phi*}}. \tag{1.7}$$

Here, r^* is the characteristic length scale corresponding to the position of the maximum value of the tangential velocity, $u^{\phi*}$ is the maximum value of the tangential velocity determining the value of r^*, u^{z*} is the axial velocity

at the position r^* and Ω characterises the rotation rate of the solid body rotation.

CHAPTER 2

Swirl Flows

This chapter provides a short overview about swirl flows. Elementary examples of the swirl flow and its impact are introduced. Moreover, an introduction to fluid flow phenomena and applications of swirl flows are also mentioned. Attention is also paid to the phenomena called vortex breakdown, which might be observable in swirling flows.

2.1 Swirling Kind of Flow

This section deals with the short overview of spiral flows, also denoted as swirl flows, representing vortex-like flows. This kind of flow is very general and can be met in everyday life. For example mixing coffee, which represents well known "Kaffeelöffel experiment" by Klein in 1910 [65], or by Betz in 1950 [15]. Their work is summarised in the book of Saffman [110], where Saffman stated that if a teaspoon is removed after moving in an ideally incompressible fluid, represented by coffee, a non-zero circulation will be created in the fluid region, where the teaspoon was moved. It must also be noticed that circulation is not generated about closed contours lying entirely in the fluid

[110].

Examples of naturally swirling flows are tornadoes or hurricanes, named also as cyclones or tropical cyclones depending on locality. Generally, a hurricane is a huge vortex reaching even hundreds of kilometres in diameter, which moves as a spiral around the centre. Moreover, the speed of hurricane wind can exceed 33 m s^{-1}, i.e. the so-called conventional magnitude [95]. The most powerful hurricanes can reach a maximum wind velocity up to $90 - 100$ m s^{-1} [95]. The hurricanes are characterised also by an intensive precipitation, downpours and thunderstorms indicating hurricane landfall. The next property is a relatively warm centre comparing to the surrounding atmosphere. The warm core consists of a cylindrical zone with diameter $20 - 50$ km and a height up to 15 km with a temperature difference of $10 - 16$ °C relatively to surroundings [95]. On the other hand, the tornado is supposed to be an atmospheric vortex with similar structure as the hurricane but the scale of the tornado is noticeably less. The diameter of the centre of a tornado is usually tens or hundreds of meters with the higher maximum speeds than in case of hurricanes [95].
Markowski and Richardson [83] discussed phenomena of a tornado with respect to conditions determining if or not a tornado is formed. Moreover, they introduced a term of the atmospheric convection as a relatively small upward and downward movement of air that is given by an imbalance between the gravitational force and a force due to the vertical pressure gradient. These two forces are usually close to balance. Furthermore, vertical accelerations are small compared to horizontal accelerations, so that air moves horizontally [83]. In case of cooler and denser or warmer and less dense pockets of air than surroundings, the forces start to be out of the balance resulting in the buoyancy force. Pockets of air are, in the fact, imaginary fluid elements smaller than characteristics length but sufficiently large to avoid molecular nature of fluids, and are named as air parcels [83]. According to this description, authors introduced processes before a tornado formation as shown in Fig. 2.1. Thus, Fig. 2.1 a) shows highlighted orientation of the vorticity vector (white arrows), sense of spin (yellow curved arrows), downdraft of air parcels (blue line), and updraft of air parcels (red line). Firstly, in step 1, the horizontal vorticity of air (wind) entering the updraft is tilted, which results in a large-scale rotation, the so-called midlevel mesocyclone. Secondly, in step 2, the buoyancy gradient generates horizontal vorticity, given by relatively warm and cold air straddling downdraft air parcels. This generated horizontal vorticity tildes then updraft by surrounding air (wind) as the straddled downdraft air parcels descend. Fig. 2.1 b) shows enlarged white dashed box

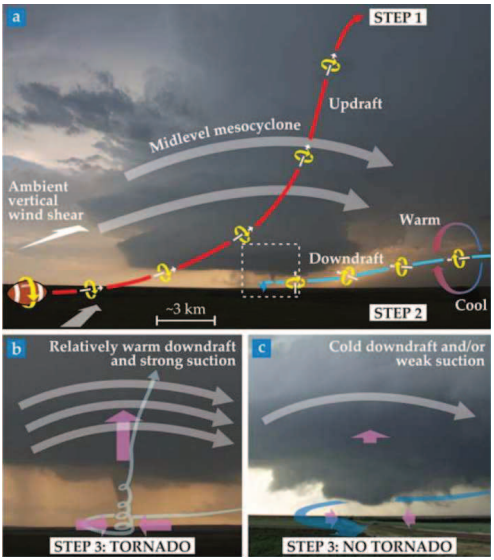

Fig. 2.1: Formation of a tornado [83]

from Fig. 2.1 a). It indicates that due to the balance of angular momentum, vertical vorticity is amplified as air moves towards the axis of rotation being, at the same time, sucked upward by a "mesocyclone". Furthermore, Fig. 2.1 c) represents the case, in which the tornado formation process failed.
Yih [134] described a model comprising exact solutions for horizontal flows with a stagnant core around the axis of symmetry, which represents one of the simplest models of a tornado-like flow. The author stated that this kind of flow satisfies the Navier-Stokes equations and is, for simplification, treated as inviscid, which allows slip at the ground and a vortex sheet at the core surface. The core is supposed to be of a lower density, i.e. concept of the potential density, or of a higher entropy, i.e. compressibility is included. He found out that at any elevation the swirl velocity is highest at the core boundary and that the maximum velocity for the entire flow occurs on the ground near the boundary. The author also confirmed investigations made by Fujita [33], who observed thickening of the core with height and an increase of the swirl velocity downward.

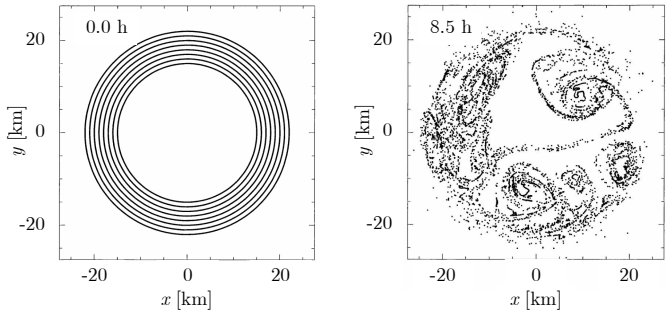

Fig. 2.2: 2D maps showing swirling patterns, which can be developed after 8.5 h from initially passive tracers at time 0.0 h [67]

Kossin et al. [67] introduced a simple 2D barotropic model in order to explain the mechanism for the presence of various swirling patterns within low-level cloud decks in hurricanes. This model supposes the barotropically unstable flow field representing the flow in hurricanes and covers mixing between core, i.e. the eye of the hurricane, and the core boundary, i.e. the eyewall. Hence, the barotropically unstable flow leads to a breakdown of the eyewall and the formation of mesovortices migrating from the eyewall into the eye. Initially passive tracers, representing cloud particles, are convoluted by the mesovortices and form swirling patterns that are very similar to the swirling patterns observed in the eye clouds, as shown in Fig. 2.2.
In a work related to tornado-like flow, Keller [60] introduced a model that also includes effects of the buoyancy and the entrainment on simplified vortex flow. He defined two kind of vortices that can appear in the tornado-like motion, as shown in Fig. 2.3. The A-type vortex, which passes its critical flow state at the maximum cross-section and the B-type vortex, which passes its critical state at the minimum cross-section. The B-type vortex, which is close to its critical state, has a similar behaviour as a gas flow in a Laval nozzle. Thus, supercritical and subcritical flows, which in case of the gas flow are represented by supersonic and subsonic flows, will reach the critical flow state, if the cross-section decreases in the flow direction and will depart from the critical state, if the cross-section increases. The A-type vortex is characterised by the opposite behaviour.
Kieu and Zhang [64] developed a non-linear model in order to capture rapid

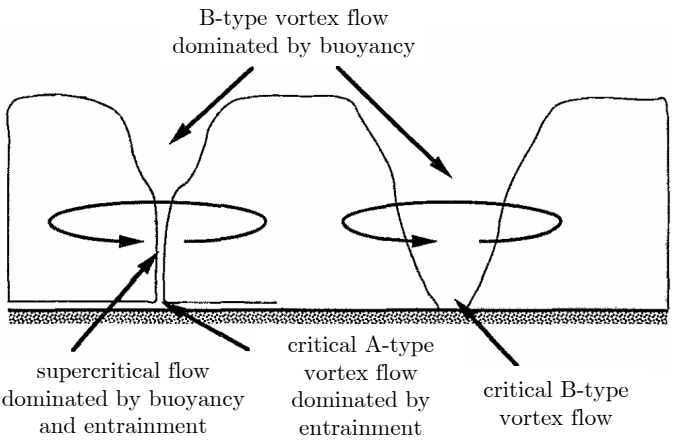

Fig. 2.3: Different forms of tornadoes appearance [60]; the left side shows the case when the critical cross-section close to the ground is followed by a supercritical A-type vortex up to the top; the right side shows the case of a B-type vortex flow, which is characterised by a tornado funnel

growth of tropical cyclones. This model revealed that the rotational flow in the inner region, i.e. the core, grows double-exponentially and the pressure drops in the central region occur at rates much faster than the rotational growth. Moreover, the rotational flow seems to grow from the bottom upwards with the fastest growth occurring at the lowest levels. The main result following from the non-linear model is that growth rates of the tropical cyclones depend on the vertical structure of the tangential flow, where a faster rate belongs to the lower-level rotation.
Refan et al. [105] analysed dataset of the velocity fields of real tornadoes in order to find a relation between laboratory simulations of tornado-like vortices and real tornadoes. They compared full-scale data with experimental results of tornado-like vortices to determine velocity and length scale ratios of numerical simulation. The simulations showed that there are two length scales for a given volume of full-scale data. The first scale is based on the core radius of a tornado and the second scale is based on the height corresponding to the maximum velocity. Generally, the simulations converged to

one value, i.e. a scale, at a certain swirl number. Thus, the results of the simulation serve for determination of the geometrical scaling of experiments that are mandatory for identification of the swirl number of real tornadoes. Refan and Hangan [104] also showed an importance of the suggested swirl number by the convergence point to proper match the flow pattern of real tornadoes. Moreover, they used a similar approach for characterisation of the tornado-like vortex flow in a testing wind chamber, which resulted in qualitatively good agreement of the tornado-like vortices with the real tornadoes.

Another known example of swirl flow represents the Taylor flow, or later noted as the Taylor-Couette flow, between rotating cylinders [20, 119]. Principles of the Taylor-Couette flow were utilised in many practical applications presented over the years including, e.g. liquid-liquid extractors [22], stratorotational instability that is relevant in astrophysical and geophysical applications [35], filtration devices [51], plant cell bioreactors [56], catalytic chemical reactors [93], blood plasmaphoresis devices [93].
Taylor-Couette flow is usually described as stationary circular flow of an incompressible fluid between two concentric rotating cylinders [24], as show in Fig. 2.4. Taylor used this assumption in his work to describe the cellular motion of fluid that develops in rotation [119]. Before the work of Taylor,

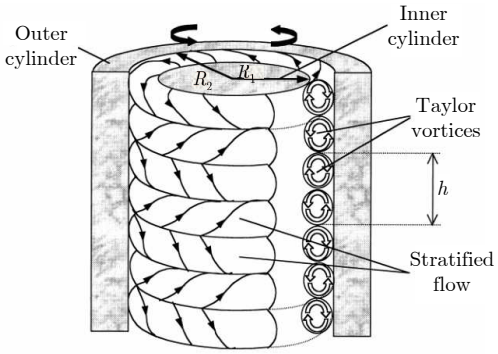

Fig. 2.4: Schematics of Taylor-Couette flow with indicated flow structures [94]; in the scheme, h represents the period (size) of the Taylor cells in the axial flow direction

Couette described a similar apparatus only with a rotating outer cylinder and found out similar structures like Taylor did later, but he did not provide any mathematical description of this problem, as mentioned in [12, 24].
Donelly [24] summarised the history and research of this kind of flow from the time of Isaac Newton, through George Gabriel Stokes, Claude Navier, Max Margules, Reginald Arnulph Mallock, Maurice Marie Alfred Couette, Geoffrey Ingram Taylor, Subrahmanyan Chandrasekhar and Donald Coles. From these listed researchers, Max Margules, Reginald Arnulph Mallock, and Maurice Marie Alfred Couette were focusing on the construction of rotating viscometers, when one cylinder was fixed and the other one was rotating. The other listed researchers investigated fluid motion with respect to visualisation of flow structures (flow patterns), stability and theoretical description [24].
More recent investigations of flow patterns, flow visualisation, and investigation of flow regimes followed work of mentioned scientists. Andereck et al. [5] studied the flow between two concentric independently rotating cylinders. They found out many different flow states, as shown in Fig. 2.5, which are

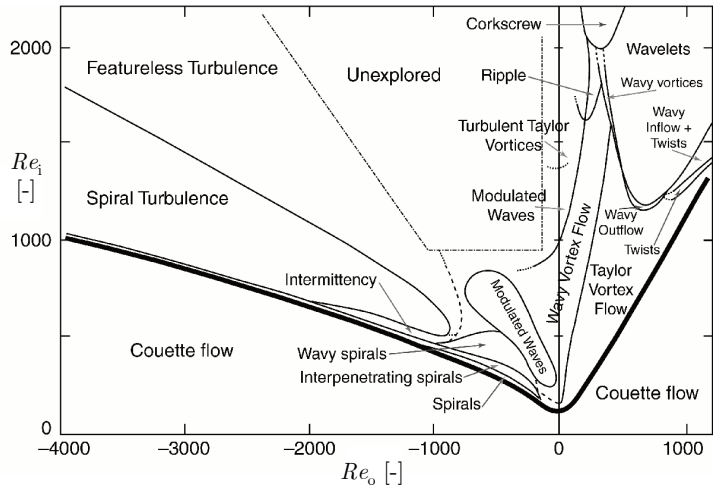

Fig. 2.5: Regimes of Taylor-Couette flow [5]

distinguishable due to symmetry under rotation, azimuthal and axial wavelengths, and rotation frequencies of azimuthal travelling waves. The authors used a statement of Coles [21] that the Taylor-Couette flow can be characterised by the angular velocities of the cylinders or by the Reynolds number of the rotating inner and outer cylinders, i.e. $Re_i = R_i(R_o - R_i)\Omega_i/\nu$ and $Re_o = R_o(R_o - R_i)\Omega_o/\nu$. Also, the radius ratio of the inner cylinder radius to the outer cylinder radius and the aspect ratio of the length of the cylinders to the gap between the cylinders characterises the Taylor-Couette flow [5, 21, 24].

Lim et al. [76] communicated their observation of flow patterns appearing in the Taylor-Couette flow. They fixed the outer cylinder and left only the inner cylinder rotating. They found out that if the acceleration $\mathrm{d}Re/\mathrm{d}t$ is larger than a value of 2.2 s^{-1}, a new flow pattern will occur. This new flow pattern showed a similarity to the Taylor vortex flow with a shorter wavelength, which is represented by the period h, i.e. the size, of the Taylor cells in axial direction, as shown in Fig. 2.4. On the other hand, if the acceleration is smaller than 2.2 s^{-1}, there will be a wavy flow for the same range of the investigated Reynolds numbers.

Akonur and Lueptow [1] conducted measurements of the velocity field of a Couette flow via the PIV method, where the inner cylinder was rotating and the outer cylinder was fixed. This paper followed a previous work of Wereley and Lueptow [129], where the axial and radial velocities were measured. Due to this, the complete velocity field could be evaluated. They found out that motion transports azimuthal (tangential) momentum radially, while the axial exchange of fluids between vortices in wavy flow transports azimuthal (tangential) momentum axially [1]. These effects amplify with increasing Reynolds numbers. Moreover, quite large shear stress near the walls of both cylinders occurs. This shear stress decreases to almost zero in the middle of the gap between the cylinders. Wereley and Lueptow [130] and later Lueptow [82] studied experimentally, via PIV, a flow in the gap between the inner rotating cylinder and the outer stationary cylinder exposed to a pressure driven axial flow; this kind of flow is schematically shown in Fig. 2.6. The measurements showed that the axial flow was winding around vortices, which did not fill the annular gap and appeared displaced toward the inner and outer cylinders. Moreover, after subtraction of the axial flow, the resulting velocity field looked like a velocity field not imposed to the axial flow. An exception was found for the vortices that translate axially and for the distortion of the azimuthal (tangential) velocity that shifts axially by the axial flow, as shown in example Fig. 2.7 taken from [130].

They also concluded that the axial velocity of helical vortices is double of the

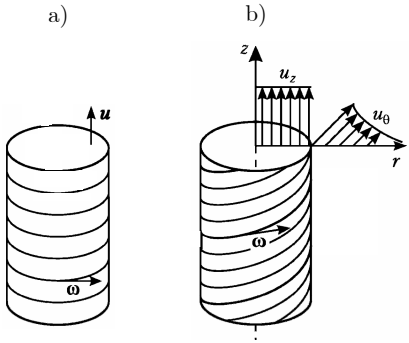

Fig. 2.6: Schematics of rotating flow in a cylinder a) no axial flow, b) with axial flow (helical structure) [2]

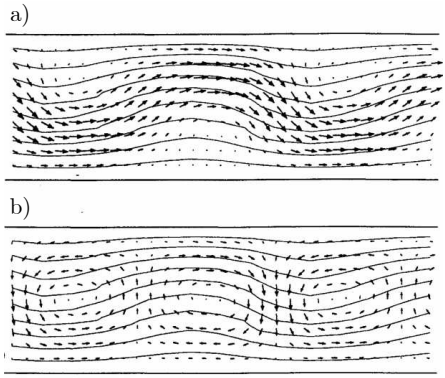

Fig. 2.7: Radial and axial velocity vectors with azimuthal velocity contours for vortical flow [130]; the upper line in each frame is the rotating inner cylinder; the lower line is the stationary outer cylinder; a) velocity field including the axial velocity profile, b) velocity field with the subtracted axial velocity profile

angular frequency of the inner cylinder, which indicates a coupling between the axial translation of the vortices and the cylinder rotation. Due to this coupling, Lueptow stated that the winding flow might be a linear superposition of annular laminar Poiseuille flow and Taylor vortex flow [82].
Guillerm et al. [40] studied numerically and experimentally the Taylor-Couette flow regimes together with an influence of temperature. They concluded that the combination of rotation and radial temperature gradient causes occurrence of helicoidal vortices or modulated waves. Moreover, stationary axisymmetric vortices can be seen only for weak temperature gradients. They also underlined an increase in heat transfer with increasing rotation due to the secondary vortices.

An influence of the swirl flow, i.e. rotating flow, on the axial flow (and vice versa), and on the convective heat transfer were investigated for decades [31]. Fénot et al. [31] also highlighted that for a superimposed flow, i.e. for the rotating or Taylor-Couette flow with the superimposed axial flow, the length of the annulus has to be long enough to permit fully developed flow. Generally, this superimposed flow has four elementary regimes, as described by Kaye and Elgar [59], for the case of axial flow in an annulus with a rotating inner cylinder:

- laminar flow,
- laminar flow with Taylor vortices,
- turbulent flow,
- turbulent flow with Taylor vortices.

These four regimes may be plotted as a function of the axial Reynolds number in dependence on the Taylor number, i.e $Re_a(Ta)$, which is shown in Fig. 2.8. Thus, for this case, the axial Reynolds number is given as $Re_a = u_a D_h/\nu$, the Taylor number can be expressed as $Ta = \Omega_1^2 R_1 (D_h/2)^3/\nu^2$, where the hydraulic diameter D_h is the ratio of the cross-section to wetted perimeter, i.e. $D_h = 4A_p/P_m = 2(R_2^2 - R_1^2)/(R_2 + R_1)$ [31].
Becker and Kaye [11] focused on the fluid flow problem in the narrow gap between rotating devices, where the Taylor-Couette flow with the axial flow seems to be a good approximation. They studied the influence of a heated inner cylinder in three limiting cases, i.e. axial flow with zero rotation, rotation of the inner cylinder with no axial flow, general case combining the axial flow and rotation of the inner cylinder, respectively, in order to determine the influence of the individual kind of flow. They found a good agreement

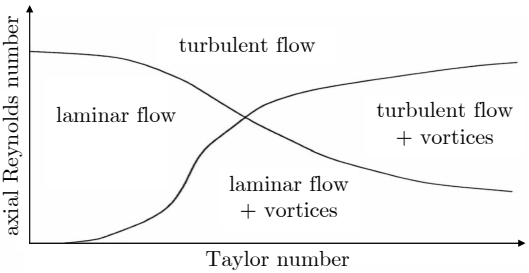

Fig. 2.8: Regimes of flow according to axial Reynolds number over Taylor number [31, 59]

with the theory for the cases of zero rotation and no axial flow. They also concluded that the general case could be capable to capture phenomena appearing in rotating devices. Nevertheless, it should be noted that their study was quite unique and it would not be correct to generalize their results, as also mentioned in [31].

Pfitzer [99] and Pfitzer and Beer [100] focused on the flow in an annulus of rotating tubes. They investigated experimentally and numerically the influence of the rotating inner and outer tube on the axial turbulent flow and on the heat transfer. They determined the velocity field and temperature distribution at the end of the test region assuming a fully developed flow. They found a positive influence on the heat transfer due to the rotation of the inner tube. Counter-rotation of the outer tube had only small positive influence on the heat transfer. On the other hand, co-rotating tubes caused a decrease in heat transfer to its minimum in the case of the outer tube rotating slightly faster than the inner tube. There was observed only negligible influence on the heat transfer in the case of the fixed inner tube and a rotating outer tube for experimentally investigated radius ratio. They also concluded that the numerical analysis revealed a non-negligible influence of the inner rotating tube on the heat transfer for other radius ratios. Rothe [109] followed the work by Pfitzer and studied experimentally and numerically the same problem as Pfitzer. Rothe optimised the measurement of the velocity profiles via hot-wire anemometry already used by Pfitzer. He also modified and extended the model describing the flow phenomena and heat

transfer in the annulus of the rotating tubes with a superimposed axial flow. The results of Rothe confirmed the results and general conclusion given by Pfitzer.
Reich et al. [107] investigated the effect of rotation on laminar flow in a heated tube. They found out that free vortices occur due to the heated tube wall disappearing with increasing rotation rate of the tube. Moreover, a perturbation analysis proved this disappearance. Weigand and Beer [127] analysed the influence of the external insulation and tube rotation on the heat transfer and the fluid flowing inside a tube. They compared their results with experimental data obtained by Reich and Beer [106]. They concluded that laminarisation of the flow due to the tube rotation was responsible for the decrease in heat transfer. Moreover, the thermal entrance length increased with rotation rate of the tube. This phenomenon was analysed to be almost independent of the thermal insulation, i.e. the boundary condition, of the tube wall. Weigand and Beer focused in [128] on changes of the flow patterns of a fluid entered into an axially rotating tube. They stated that as the fluid entered into an axially rotating tube, it received a tangential component of velocity due to the rotating wall. It was also supposed that if the axial flow in the tube was initially turbulent, a flow relaminarisation would appear by increasing rotation rate of the tube. They found an universal velocity profile for turbulent rotating tube taking into account a new rotation parameter as a function of the axial Reynolds number, rotational Reynolds number, and rotation rate instead of only the rotation rate. This new rotation parameter is better for scaling experimental results, as they showed by comparison with experimental data obtained by Reich and Beer [106].

The effect of the rotating flow on the axial flow and on the heat transfer can be directly used in practical applications, where the main interest is taken on research of transport phenomena in swirl chambers and swirl tubes. Hartnett and Eckert [44] provided a contemporary overview of the swirl flow in a tube. They focused on the detailed measurement of the flow field and temperature in a vortex flow that was generated at the nozzle cross-section and proceeded in one direction to the far end of the tube. The published data were discussed with respect to an analytical description considering energy separation phenomena.
Lately, Ligrani et al. [75] investigated flow phenomena in swirl chambers, which models cooling passages located near the leading edge of turbine blades, as shown in Fig. 2.9. This flow is generally characterised by the significant axial and tangential velocity components. They made flow visualisation for different Reynolds number, based on the total mass flow rate through a

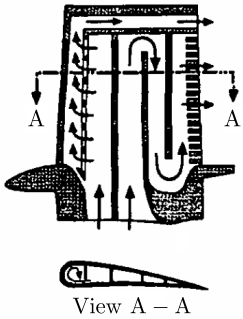

Fig. 2.9: Swirl cooling configuration proposed by Glezer et al. [37]

swirl chamber, surveying the mean velocity components, static pressure and total pressure in order to understand specific mechanisms leading to local enhancement of the surface heat transfer. Thus, they stated that the swirl flow could be very useful in different engineering applications, including, e.g. biomedical applications, heat exchangers, automobile engines. Hedlund et al. [46] followed the work by Ligrani et al. [75] and made an experimental investigation of the flow phenomena and heat transfer in a swirl chamber representing the internal passage for cooling the leading edge of a turbine blade. They analysed the circumferential (tangential) velocity component, the circumferential (tangential) vorticity component, the static and total pressure, in order to obtain characteristics describing the swirl flow in the chamber. Moreover, they measured the surface temperature along the swirl chamber surface in order to resolve the spatial distribution of the temperature. These two measurements gave a link between variations of the surface temperature distribution and swirl flow characteristics. Hedlund and Ligrani [45] analysed local flow behaviour and heat transfer for higher Reynolds numbers on the same model geometry as Ligrani et al. [75] and Hedlund et al. [46]. They again measured and evaluated the swirl characteristics and temperature distribution as in the previous works. Here, they concluded that the axial component of velocity and the surface temperature increased with increasing Reynolds number. They also visualised the flow by smoke injection and showed interacting Görtler vortex pairs. They concluded that an increasing Reynolds number reduced the size of the Görtler vortex pairs and

the phenomenon became to be more unsteady.
Glezer et al. [36] focused on the internal swirling flow and its influence on heat transfer. They used a test rig for simulating the rotating leading edge internal passage of blades with heated walls and screw-shaped cooling swirl resulted from flow generated by tangential slots. The experimental data were obtained for a rotating number, which is directly proportional to the angular velocity and the swirl tube diameter and inversely proportional to the mass-averaged radial velocity in the swirl tube, i.e. $Ro = \Omega D/\overline{u^r}$, ranging from 0 to 0.023 and a Reynolds number of 20,000, which is directly proportional to the mass flow $\dot{m}$ and inversely proportional to the diameter of the swirl tube D and dynamic viscosity μ. They stated that Coriolis forces, appearing during blades rotation, had a positive influence on the internal heat transfer in case of the same direction of the forces with the tangential velocity component. There was an opposite behaviour observed when the direction of the Coriolis forces had an opposing direction to the swirl flow.

The phenomenon of the swirl flow and its influence on the heat transfer was investigated for usage in cooling devices, such as cooling equipment in, e.g. CNC machines, refrigerators, electronic control cabinet, heating processes. In industry, the cooling device utilising swirl flow phenomena called the vortex tube is used for separation of a cold air stream and a hot air stream from compressed air [27]. This device is sometimes referred as the Ranque vortex tube, Hilsch vortex tube or Ranque-Hilsch vortex tube. Ranque [102] focused on the swirling flow in a tube and in 1933 discovered a phenomenon of temperature separation in this flow. Later, Hilsch [48, 49] followed his work and conducted his research related to geometrical and operation parameters of the tube proposed by Ranque. From these reasons, the tube is known as the Ranque-Hilsch vortex tube and is shown in Fig. 2.10. A vortex tube comprises a tube, in which compressed gas is tangentially introduced and which is then separated in a low and high total temperature flow region. Cold gas on the one side leaves the tube through an orifice plate, whereas hot gas leaves the tube on the other side through a peripheral gap, in Fig. 2.10 regulated by a cone valve. This temperature phenomenon is called the Ranque-Hilsch effect. The effect of the temperature separation in a vortex tube is known for many years but it is not fully understood yet.
Gutsol [42] in his work summarised up to date knowledges of the Ranque-Hilsch effect and tried to propose some new ideas for future research. He suggested, for the description of the Ranque-Hilsch effect, developing a theory taking into account kinetics of microvolumes and kinetic energy exchange; the actual distribution of microvolumes in the forward velocity depending on

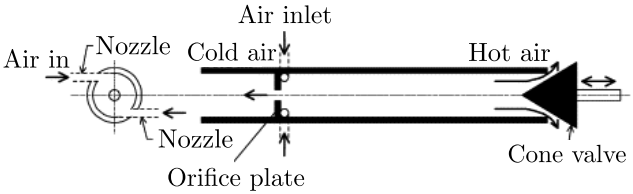

Fig. 2.10: Schematics of a vortex tube [27]

the initial conditions; the arrival of turbulent entities to the central part of the flow from boundary layers; and the radial dependency of the forward velocity of the exhausted gas. He thought that it is possible to obtain a qualitatively dependency of the energy separation efficiency on the tube scale by consideration of the kinetics of the microvolumes motion accounting for the viscosity and heat exchange, which affects separation rate and transformation of the kinetic energy into heat. Leontiev [74] summarised gasdynamic methods of the temperature stratification. Among others, he also mentioned the Ranque-Hilsch vortex tube and used several explanations of the temperature separation.
Eiamsa-ard and Promvonge [27] offered a critical review of experimental and computational research of the vortex tube. They divided experimental work into the two important parameters, i.e. into the geometrical characteristics of the vortex tube, e.g. diameter and length of the hot/cold tube, diameter of the orifice, number of inlet nozzles, etc., and into the thermo-physical parameters of the vortex tube, e.g. inlet gas pressure, moisture of inlet gas, type of gas, etc. The computational work was split into parts concerning quantitative, theoretical, analytical, and numerical aspects of the research. They also provided several explanation of the temperature separation phenomenon based on the mentioned experimental, analytical, and numerical studies. One of the most used explanation of the Ranque-Hilsch phenomenon was also mentioned by the authors. This explanation was stated by Kassner and Knoernschild [58], who used the derived results of the laws of the shear stress in circular flow for case of the vortex tube. They postulated that the initially free vortex (tangential velocity $\propto 1/r$) in the vortex tube is changed by pressure distribution causing temperature distribution that corresponds to an adiabatic expansion leading to a low temperature in the

region of low pressure, i.e. near the axis of the vortex tube. Moreover, the shear stresses cause changes of the flow downstream from a free to a forced vortex (tangential velocity $\propto r$). These changes of the vortex structures begin on the boundaries, at the axis and walls, respectively. Furthermore, these changes cause a radially outward flow of the kinetic energy. Additionally, turbulent transport occurring due to the strong pressure gradient results in a temperature profile almost complying the adiabatic temperature profile that corresponds to the pressure profile of the forced vortex. Transport of energy along this temperature gradient is responsible for even lower temperature in the core [27, 34, 58, 74, 108].
Xue et al. [133] provided a critical summary of the temperature separation phenomenon. Based on literature survey, they stated that the temperature separation in the vortex tube can be followed by two different factors. The first factor was stated as a temperature drop in a vortex tube given by combination of effects of sudden expansion near the entrance, transfer of energy outward due to the internal friction and turbulence, secondary flow structures and static temperature gradient. On the other hand, the author stated the second factor as a temperature rise resulting from compression at the periphery, static temperature gradient, transfer of energy due to the friction between the turbulent layers, friction between air flow and wall, and the secondary circulation.
Yilmaz et al. [135] conducted a review focusing on design parameters. They summarised geometrical parameters (e.g. tube diameter, tube length, tube geometry, type and number of nozzles, control valve on the side of the hot end), mass flow parameters (e.g. cold mass fraction, overall mass flow rate), inlet conditions (e.g. inlet pressure, inlet temperature), gas properties (e.g. content of moisture, isentropic exponent of gas), and other parameters (e.g. tube material, tube roughness, molecular mass of gas). Furthermore, they also provided the influence of the respective parameters on the vortex tube performance.

2.2 Stability of Fluid Flows

Originally, stability of swirl flows was investigated by Taylor in his pioneering work focusing on stability of the flow between two rotating cylinders [119]. He presented huge theoretical analysis of the flow with respect to small disturbances, i.e. perturbation analysis, and showed that the well known Lord

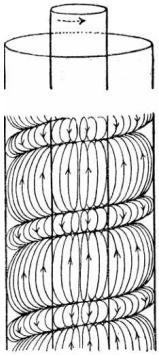

Fig. 2.11: Spiral form of instability observed by Taylor [119]

Rayleigh's condition of stability ($\Omega_2 R_2^2 > \Omega_1 R_1^2$), which was developed for inviscid fluid moving between two cylinders rotating in the same direction [77], can predict the origin of vortex structures, nowadays known as Taylor vortices. In Rayleigh's stability condition, Ω_1 and R_1 represent the angular velocity and radius of the inner cylinder, whereas Ω_2 and R_2 represent the angular velocity and radius of the outer cylinder, respectively. He also observed that the spiral form of the instability appears if the gap between the rotating cylinders compared to the cylinder radius is small. Furthermore, he also noticed that one vortex was wider than the other. The wider vortex had the same component of vorticity in the direction of the axis as that of the steady motion, as shown in Fig. 2.11. On the contrary, for the cylinders rotating in opposite direction, i.e. $\Omega_2/\Omega_1 < -1$, the vortices were so different in their size that one of them nearly disappeared.
Stability analysis made by Taylor [119] was followed by other scientists. Chandrasekhar in his monograph [20] summarised known outcomes, made refinement and extension of the work by Taylor. He also used Rayleigh's inviscid stability condition, which generally states that in absence of viscosity, the necessary and sufficient condition of stability for a distribution of the angular velocity $\Omega(r)$ is [20]

$$\frac{\mathrm{d}}{\mathrm{d}r}\left(r^2\Omega\right)^2 > 0. \tag{2.1}$$

In other words, the term $(r^2\Omega)$ is the angular momentum per unit mass, thus, the condition of stability, Eq. (2.1), can be alternatively interpreted as a stratification of the angular momentum about an axis. So, the stratification of the angular momentum about an axis is stable, if it increases monotonically outward [20]. Chandrasekhar [20] also used the discriminant of stability $\Theta(r)$ that may be written as

$$\Theta(r) = \frac{1}{r^3}\frac{\mathrm{d}}{\mathrm{d}r}\left(r^2\Omega\right)^2 = \frac{2\Omega}{r}\frac{\mathrm{d}}{\mathrm{d}r}\left(r^2\Omega\right) > 0, \tag{2.2}$$

which is an alternative form to the Rayleigh's inviscid stability condition, Eq. (2.1). In addition, Chandrasekhar [20] solved theoretically the problem of a fluid motion in a gap between rotating cylinders with an axial pressure gradient. He analysed the stability of the flow against small perturbations and compared the results with experiments made by Donnelly and Fultz [25]. He found out that the theoretical analysis supported the experimental results, which generally led to an outcome that the axial flow shifted the first appearance of the Taylor vortices. This analysis was made by other scientists as well, e.g. Di Prima and Pridor [23] and references therein.

Ludwieg [79, 81] proposed a stability criterion applicable to a swirling flow in a narrow annulus. His stability criterion, Eq. (2.3), was given by a generalisation of the Rayleigh's stability condition for centrifugal stability and was expressed by

$$(1-h)\left(1-h^2\right) - \left(\frac{5}{3}-h\right)g^2 > 0, \tag{2.3}$$

where

$$h = \frac{r}{u^\phi}\frac{\mathrm{d}u^\phi}{\mathrm{d}r} \text{ and } g = \frac{r}{u^\phi}\frac{\mathrm{d}u^z}{\mathrm{d}r}. \tag{2.4}$$

He applied this condition to helical flows in an annulus and tried to extend his theory to the vortex breakdown phenomena in spite of the simplification made for the specific geometry and applied boundary conditions [73, 80]. Nevertheless, Sarpkaya [112] stated that Ludwieg's criterion predicts instability for many kinds of quasi-cylindrical flows, but this condition was developed for a special case of a narrow annular gap, so its application to other geometries was not recommended.

Howard and Gupta [52] also proposed a stability criterion based on generalisation of the Rayleigh's stability condition, Eq. (2.5). This condition supposed a flow with the axial component of velocity exposed only to axisymmetric

disturbances. They expressed the stability condition in the following form

$$\frac{\mathrm{d}}{\mathrm{d}r}\left(ru^{\phi}\right)^{2} - \frac{1}{4}r^{3}\left(\frac{\mathrm{d}u^{z}}{\mathrm{d}r}\right)^{2} > 0. \tag{2.5}$$

Leibovich and Stewartson [73] developed a more general criterion of stability based on an analysis of an inviscid flow, Eq. (2.6). Hence, they proposed the following stability condition

$$u^{\phi}\frac{\mathrm{d}}{\mathrm{d}r}\left(\frac{u^{\phi}}{r}\right)\left[\frac{\mathrm{d}}{\mathrm{d}r}\left(\frac{u^{\phi}}{r}\right)\frac{\mathrm{d}}{\mathrm{d}r}\left(ru^{\phi}\right) + \left(\frac{\mathrm{d}u^{z}}{\mathrm{d}r}\right)^{2}\right] > 0. \tag{2.6}$$

Althaus et al. [4] discussed this condition with respect to work by Breuer [19], who applied this condition to a stable slender vortex and observed that the condition predicted instability, but the vortex breakdown phenomenon was not observed. So, Althaus et al. [4] explained this discrepancy by the fact that due to the inviscid formulation of the condition the viscous damping effects were not taken into account, which might capture the discrepancy found by Breuer [19].

Wang [124], and Wang and Rusak [125, 126] studied the stability of a flow with respect to small disturbances by the linear and non-linear stability theory used for solving the eigenvalue problems. Their approach revealed the energy separation phenomenon in a swirling flow and the complexity of a swirling flow. They stated that a swirling flow comprising high density of the kinetic energy is sensitive to the change of the flow conditions and tends to lose the stability. Due to these reasons, the problem of a swirling flow must be defined precisely in order to be properly solved by mathematical analysis.

Dou et al. [26] developed the gradient theory method to analyse the stability of a swirl flow. They tested this method on the Taylor-Couette flow between two rotating cylinders and compared the results with the Rayleigh's stability condition, and with experimental results by Taylor [119] and Coles [21]. The gradient theory assumed that the gradient of the total mechanical energy in the transverse direction of the main flow and loss of the total mechanical energy by viscous friction in the streamwise direction are dominant for both the instability phenomena and the flow transition for a given disturbance, respectively [26]. So, the flow instability depends on amplification and damping of the initial disturbance by the energy gradient and viscous friction. They found a very good agreement with experimental data and concluded that the gradient theory method is generally applicable to problems of flow stability.

Biegger [16] used an alternative stability analysis based on the balance of total enthalpy, which was preliminary tested in the work by Ben Hmidene [13]. This stability condition followed work by Marsik [84, 85] and supposed a dominating swirling flow of perfect gas, i.e. the axial and radial velocity components could be neglected, the temperature and pressure depend only on the radial coordinate. Moreover, it was supposed that there are small radial differences in the temperature, i.e. $\rho \neq f(T)$, and that the pressure gradient is given by the balance of momentum for the rotational flow, i.e. $(u^{\phi})^2/r = (1/\rho)(\mathrm{d}p/\mathrm{d}r)$. Thus, the stability condition assuming a steady isentropic flow was determined as

$$\frac{1}{2r^2}\frac{\mathrm{d}}{\mathrm{d}r}\left(ru^{\phi}\right)^2 + c_p\frac{\mathrm{d}T}{\mathrm{d}r} - \frac{\left(u^{\phi}\right)^2}{r} = 0. \tag{2.7}$$

This condition has two parts, the first part corresponds to the mechanical stability representing the Rayleigh's stability condition, Eq. (2.8), and the second part corresponds to the thermal stability condition, Eq. (2.9).

Mechanical stability condition
$$\frac{1}{2r^2}\frac{\mathrm{d}}{\mathrm{d}r}\left(ru^{\phi}\right)^2 \geq 0, \tag{2.8}$$

Thermal stability condition
$$c_p\frac{\mathrm{d}T}{\mathrm{d}r} - \frac{\left(u^{\phi}\right)^2}{r} \geq 0. \tag{2.9}$$

Biegger [16] used this condition in his work and compared it with Eq. (2.3) proposed by Ludwieg [79, 81], with Eq. (2.5) by Howard and Gupta [52], and with Eq. (2.6) by Leibovich and Stewartson [73]. He found out that the stability conditions by Howard and Gupta, and by Leibovich and Stewartson gave very similar results indicating instability in the region near the wall. He also stated that the Ludwieg's stability condition to spiral disturbances indicated instability in regions with the maximum tangential velocity. Moreover, Biegger [16] concluded that the stability condition based on the total enthalpy has an advantage in considering temperature effect, which affects the final radial distribution of the stability condition.
Another alternative approach of the stability analysis, i.e. based on thermodynamics, is the main goal of this work and is developed and analysed in Chapter 3.

2.3 Vortex Breakdown

Vortex breakdown is, in literature, referred as an abrupt change in the structure of the core of a swirling flow, as stated by Sarpkaya [112]. This phenomenon might be observed due to a flow over a delta wing influencing the lift and stability of the wing and in an axisymmetric swirling flow in a tube. Vortex breakdown is usually characterised by a deformation and deceleration of the vortex core, changes of velocity distribution (with flow reversal), and changes of pressure distribution in the swirling flow. Thus, the occurrence of vortex breakdown has a strong influence on the performance of the studied system, such as turbines, trailing vortices behind a wing, cyclone separators, vortex tubes, swirl chambers, etc.
The phenomenon of vortex breakdown was studied by researchers for decades and, as mentioned by Lucca-Negro and O'Doherty in [78], there might be an association of flow instabilities to vortex breakdown. For example, Chandrasekhar [20] interpreted the Rayleigh's stability condition for inviscid flow as a condition that the flow is stable, if the angular momentum increases monotonically outward. On the other hand, the swirl velocity component in tubes approaches zero values at the wall, but an inertial stability is present for high Reynolds numbers. This could lead to the occurrence of Görtler vortices confined to the wall region. Görtler [38, 39] investigated the stability problem of the laminar boundary layer on slightly curved walls, where he supposed vortices whose axes would be parallel to the direction of fluid. He made an analytical stability analysis to small disturbances and determined conditions, at which these structures can appear. Schlichting in his monograph [113] discussed the occurrence of Görtler vortices as a phenomenon appearing in the transition between laminar and turbulent flow at concave walls. Saric [111] summarised and generalised contemporary known outcomes in the field of stability and development of Görtler vortices. His work provides a nice overview of the Görtler vortices phenomena.
Thus, the stability criteria summarised in the previous, Section 2.2, can be associated with vortex breakdown. The vortex breakdown phenomena was studied by many researches from point of view of experimental research, theoretical analysis, and numerical methods. This phenomenon was summarised and reviewed for many times [3, 4, 43, 72, 112, 117]. One of the most recent reviews of the vortex breakdown phenomena summarising the types of vortex breakdown, stability criteria, and prediction of vortex breakdown, was provided by Lucca-Negro and O'Doherty [78]. Some of the elementary outcomes are presented in the following.

Sarpkaya [112] in his study of a swirling flow in a mildly diverging cylindrical tube visualised flow structures with dye. He observed three types of vortex breakdown, i.e. 1) double-helix form, 2) spiral forms, and 3) axisymmetric form. Faler and Leibovich [30] also made visualisations of the vortex breakdown phenomena occurring in a swirling flow and they observed seven types of vortex breakdown, as shown in Fig. 2.12. These seven types of vortex breakdown can be described as follows.

- ***Type 0 - Axisymmetric closed (or bubble) vortex breakdown***
  This type of vortex breakdown is characterised by a stagnation point on the swirl axis, which is followed by an expansion to form an envelope of a bubble recirculating fluid. One or two tails rotating with the flow are generated, Fig. 2.12 a).

- ***Type 1 - Axisymmetric open vortex breakdown***
  This type of vortex breakdown has a non-smooth envelope and opened tail of vortex breakdown, Fig. 2.12 b).

- ***Type 2 - Spiral breakdown***
  The spiral type of vortex breakdown is characterised by deceleration causing a stagnation. This stagnation is followed by sharp kink into corkscrew-shaped twist of the dye [78]. This shape persists for few turns before it breaks up into turbulence, Fig. 2.12 c).

- ***Type 3 - Modification of spiral breakdown***
  The modified spiral breakdown posses characteristics of type 2 and type 4, Fig. 2.12 d). Furthermore, this type of vortex breakdown is accompanied by reverse flow [2].

- ***Type 4 - Flattened bubble breakdown***
  Flattened bubble breakdown originates spontaneously or by increasing swirling flow from type 6. Moreover, this type of vortex breakdown is usually wider than thicker, as shown in Fig. 2.12 e1) and e2) and does not rotate.

- ***Type 5 - Double helix breakdown***
  This type of vortex breakdown also originates from type 6 and is accompanied by deceleration and then expansion into curved triangular sheet. Furthermore, each half of the expanded sheet is wrapped around the other to form a double helix [78]. Evolution of this type show Figs. 2.12 f1) - f4).

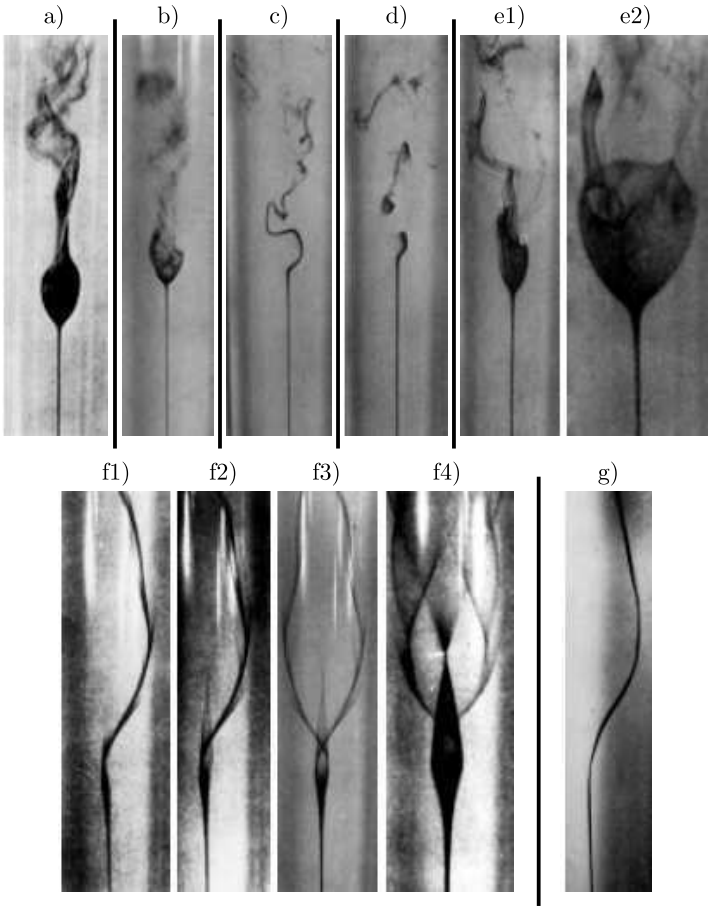

Fig. 2.12: Types of vortex breakdown [2, 30]; a) type 0, b) type 1, c) type 2, d) type 3, e1) type 4 - side view, e2) type 4 - top view, f1) type 5 - at $t = 0$ min, f2) type 5 - at $t = 5$ min, f3) type 5 - at $t = 10$ min, f4) type 5 - at $t = 15$ min, g) type 6

- ***Type 6 - Filament disruption***
  Filament disruption characterises a stable and a fixed state of a filament moving near the axis. If the filament moves away from the axis, the filament will obtain the spiralling sense of the flow, Fig. 2.12 g).

Lucca-Negro and O'Doherty [78] stated that breakdowns of types 3 - 6 are not so often observed and occur at lower Reynolds numbers. At higher Reynolds numbers, observable characteristics are usually the bubble and the spiral breakdowns [72]. Novak and Sarpkaya [97] analysed vortex breakdown at high Reynolds number and observed in very short exposure a conical breakdown that consisted of two or more wrapped helical structures with a conical envelope rotating contrary to the flow, as shown in Fig. 2.13. This type of vortex breakdown is sometimes called type C [2].

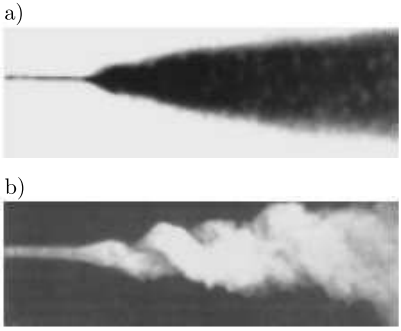

Fig. 2.13: Conical vortex breakdown [97]; a) vortex breakdown at low Reynolds number, b) vortex breakdown at high Reynolds number

Moreover, the here presented types of vortex breakdown assumed a bounded flow. Types of vortex breakdown in an unbounded flow are summarised in monograph of Alekseenko et al. [2].
Regarding the types of vortex breakdown, there have been developed some theories describing and explaining this phenomenon. Thus, there are three basic theories that are associated with the vortex breakdown phenomenon as stated by Escudier [29] or by Hall [43]

- instability, i.e. axisymmetric disturbances, spiral disturbances, non-linear interactions,

- stagnation, i.e. separation analogy, quasi-cylindrical approximation (failure of slender core),
- wave phenomena, i.e. inertia waves, solitary waves, transition between conjugate flow states, shock or hydraulic jump analogy.

The instability criteria, which are used in this sense have been presented in Section 2.2. Here only two other theories are presented.
Vortex breakdown is generally accepted, if there is a flow stagnation at the vortex axis. Hall [43] suggested that vortex breakdown is comparable to a boundary layer separation. This approach assumes an influence of adverse pressure on the flow, which would cause the appearance of an internal domain of flow reversal similar to a wake. Keller [61] stated that this approach seems to be useful to study the flow upstream of vortex breakdown waves, but it is not expected to be useful for studying the internal structures of a vortex breakdown.
Wave phenomena was independently used for analysis of an axisymmetric, inviscid, and steady vortex by Squire [118] and Benjamin [14], as mentioned in [78]. Both of them stated that there is a critical state, which separates flow between the subcritical and supecritical state of the flow. In the subcritical flow, disturbances can propagate upstream and downstream, whereas in the supercritical flow, disturbances can propagate only downstream, as stated in [29, 62, 78]. Moreover, Hall [43] stated that their interpretations were different. Thus, Squire took the breakdown as accumulation of upstream travelling disturbances in place of the critical state, whereas Benjamin understood the breakdown as an abrupt change between two conjugate flow states. Squire's analogy corresponds to a shock wave problem, whereas Benjamin's analogy corresponds to a hydraulic jump in a channel flow.
Keller et al. [63] described the problem of transitions between the flow states. They used the original approach by Benjamin [14] and extended it. The new developed approach was then applied to a hydraulic problem, in which the flow states of a channel flow were analysed. This extended approach agreed well with results obtained by Benjamin, who analysed the flow states with respect to Froude number relating flow velocity, channel height, water depth, and gravitational acceleration, so that $F_1 = u_1/(gh)^{1/2}$, $F_2 = u_2/(gD)^{1/2}$, and $F > F_c$ is the condition for the supercritical flow, and $F < F_c$ for the subcritical flow. They also analysed the flow states of a flow in an annulus, where a condition dividing the flow states to the supercritical, critical, and subcritical states was determined. Moreover, the flow states of a Rankine vortex, i.e. vortex consisting of the vortex core rotating as a solid body surrounded by a potential vortex, were studied in their work. They again

analysed states and states transition, i.e. difference between states, of the flow, which was assumed as inviscid and axisymmetric, see also [9]. By this approach, the vortex breakdown region might be predicted, as also shown in the work by Biegger [16].
Biegger [16] also discussed an analytical estimation of a swirl number limit determined by Kobiela [66]. This swirl number limit can predict the occurrence of an axial backflow, which is supposed to be connected to vortex breakdown in swirl tubes. They both stated that for the occurrence of backflow, the minimum swirl number is $S = 0.928$, assuming a parabolic axial velocity profile.
Spall et al. [117] proposed a criterion in order to predict the onset of vortex breakdown. Their criterion was derived based on previous experimental, numerical, and theoretical studies and followed the works by Squire [118] and Benjamin [14]. The proposed critical condition was expressed by the Rossby number as

$$Ro = \frac{u^{z*}}{r^*\Omega}, \tag{2.10}$$

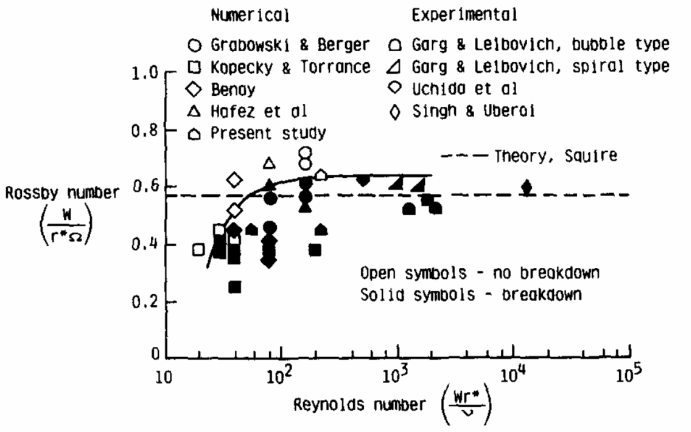

Fig. 2.14: Rossby number dependency of wing-tip vortices [117]; variable W represents the characteristic axial velocity (in the text denoted by u^{z*})

where u^{z*}, r^*, and Ω represent the characteristic axial velocity, a characteristic length scale, and a characteristic rotation rate of the vortex core, respectively. Thus, r^* defines the radial coordinate, where the swirl velocity reaches its maximum. This radial coordinate corresponds to the viscous length scale for swirling flows, as stated by Leibovich [72]. The characteristic axial velocity u^{z*} is the velocity at this radial position r^*. Moreover, this radial coordinate determines a consistent velocity scale for uniform and radially varying axial velocities, and also for swirl velocities given by $r^*\Omega$ with the rotation rate Ω representing an angular velocity of a solid body rotation. To ensure consistency, Spall et al. [117] defined the Reynolds number in terms of the viscous length scale r^* and axial velocity u^{z*} at the radial coordinate r^*. Results of Spall and of other investigations are shown in Fig. 2.14. It is evident from the plot that the critical Rossby number, roughly 0.65, appears for a Reynolds number greater than 100. For a lower Reynolds number, the Rossby number is lowered due to the dominant influence of the viscosity. The plot also shows the result of the theoretical analysis for the existence of axisymmetric standing waves by Squire [118] that resulted in a critical Rossby number of 0.57. Nevertheless, Spall et al. [117] also concluded that their criterion is, due to characteristic scales related to the vortex, applicable to confined and unconfined vortical flows.
For other possibilities how to understand and interpret vortex breakdown, the readers are referred to the review of Lucca-Negro and O'Doherty [78].

CHAPTER 3

Stability Condition

In this chapter, an introduction to the balancing of quantities is given. Moreover, definition of entropy is also included. At the end of this chapter, the derivation of the thermodynamic stability condition with its application to simplified kinds of flow, i.e. steady axial flow, represented by a laminar and turbulent flow, and a steady flow in an annulus, represented by a Couette flow between rotating cylinders and a flow in a rotating tube is provided.

3.1 General Balance Law

In general, the balanced quantity is supposed to be in the following form

$$\Phi(t) = \int\limits_{V_0-\Upsilon} \phi(\mathbf{X},t)\mathrm{d}\overline{V} = \int\limits_{V-v} \phi(\mathbf{x},t)\mathrm{d}\overline{V}, \tag{3.1}$$

where $\phi(\mathbf{X},t)$ and $\phi(\mathbf{x},t)$ are successively a volumetric density of the balanced quantity in the material description and a volumetric density of the balanced

quantity in the actual description, respectively. These densities are given as

$$\phi(\mathbf{X},t) = \lim_{\Delta V_0 \to 0} \frac{\Delta\Phi(t)}{\Delta V_0}, \tag{3.2}$$

$$\phi(\mathbf{x},t) = \lim_{\Delta V \to 0} \frac{\Delta\Phi(t)}{\Delta V}. \tag{3.3}$$

So, the general balance law for an arbitrary material point P at position $\mathbf{X} \in V_0$ is obtained by reduction of a finite volume ΔV_0 containing the material point P, i.e. via the limit $\Delta V_0 \to 0$. Due to this reduction, i.e. deformation or generally thermodynamic process, the position of the material point P is changed to the position $\mathbf{x} = \mathbf{x}(\mathbf{X},t)$. Note that, by a thermodynamic process, the temperature of the material point P is also changed, i.e. $T = T(\mathbf{X},t) = T(\mathbf{X}(\mathbf{x},t),t) = T(\mathbf{x},t)$.
Moreover, the time change of the balanced quantity $\Phi(t)$ in an investigated body, or system, may be caused only in two ways. The first is an inflow, or an outflow, of the balanced quantity $\Phi(t)$ into, or out of, the investigated body through its boundary. The second is a source, or a sink, of the balanced quantity $\Phi(t)$ inside the investigated body, or system. This fact can be formulated by the fundamental balance relation

$$\frac{\mathrm{D}\Phi(t)}{\mathrm{D}t} = \dot{\Phi} = J(\Phi) + P(\Phi), \tag{3.4}$$

i.e. by the so-called general balance law. Here, $J(\Phi)$ expresses a total flux of the quantity Φ through a body boundary, i.e. it can be expressed by a surface integral

$$J(\Phi) = \int_{A_0} J^K(\Phi)\mathrm{d}A_K = \int_A j^k(\Phi)\mathrm{d}a_k, \tag{3.5}$$

and $P(\Phi)$ expresses a production or destruction of the quantity Φ in the entire body per unit time, i.e. it can be expressed by a volumetric integral

$$P(\Phi) = \int_{V_0-\Upsilon} \Sigma(\Phi)\mathrm{d}\overline{V} = \int_{V-v} \sigma(\Phi)\mathrm{d}\overline{V}, \tag{3.6}$$

where $\Sigma(\Phi)$ and $\sigma(\Phi)$ are densities production of quantity in the material and actual description.
Furthermore, the investigated body, or system, can also include discontinuity

surfaces $\Upsilon = \Upsilon(\mathbf{X},t)$ in the material description and $\upsilon = \upsilon(\mathbf{x},t)$ in the actual description, respectively. As an example of a discontinuity surface, a shock wave can be mentioned. So, these discontinuities are, in general, the material surfaces but they are called singular surfaces [28, 85, 110]. Thus, the final form of the general balance law, after using the mean value theorem [28], at point $\mathbf{X}$ is expressed by

$$\dot{\phi} - \frac{\partial J^K(\Phi)}{\partial X^K} - \Sigma(\Phi) = 0, \quad \text{for} \quad \mathbf{X} \in V_0 - \Upsilon, \tag{3.7}$$

$$\left\| \phi(U^K - V^K) - J^K(\Phi) \right\| N_K = 0, \quad \text{for} \quad \mathbf{X} \in \Upsilon. \tag{3.8}$$

Here, $\|\cdot\|$ expresses a jump of the discontinuity, i.e. values difference, on the discontinuity surface Υ. Definition of this jump is $\left\| A^K \right\| = A^K|_{\Upsilon+} - A^K|_{\Upsilon-}$. These equations represent successively the local balance law in a volume V_0 and on the singular surface Υ, where N_K is an outer normal to the surface Υ and V^K is a propagation velocity of the surface Υ.
The same method, i.e. reduction of the volume V, is applied in order to determine a local balance law in the actual description

$$\frac{\partial \phi}{\partial t} + \frac{\partial (\phi u^k)}{\partial x^k} - \frac{\partial j^k(\Phi)}{\partial x^k} - \sigma(\Phi) = 0, \quad \text{for} \quad \mathbf{x} \in V - \upsilon, \tag{3.9}$$

$$\left\| \phi(u^k - v^k) - j^k(\Phi) \right\| n_k = 0, \quad \text{for} \quad \mathbf{x} \in \upsilon. \tag{3.10}$$

The last mentioned equations are successively valid for the actual volume $V - \upsilon$ and for the singular surface υ. The outer normal to this singular surface is n_k and its propagation velocity is v^k.

3.2 Definition of Entropy

Entropy is an extensive quantity, or also an extensive thermodynamic property, and characterises the macroscopic state of systems and running processes inside systems. Furthermore, entropy is defined by an inequality, the so-called Clausius inequality $đQ/T \leq \mathrm{d}S$ or $\dot{Q}/T \leq \dot{S}$ [85]. If a physical quantity is defined via an inequality, a dependency of a physical quantity will not be exactly defined, which results in the possibility to obtain an infinite number of definitions. Due to this, a general definition of the entropy has not been found yet.

A frequently used definition of entropy is the equilibrium entropy

$$\mathrm{d}S = \frac{đQ_{rev}}{T}, \tag{3.11}$$

where Q_{rev} denotes the fact that heat exchange hast to be part of a reversible process. In addition, another possible definition of entropy is expressed via the local equilibrium entropy, also known as the Gibbs definition of entropy

$$T\mathrm{d}s = \mathrm{d}u + \mathrm{d}w, \quad \text{or} \quad T\mathrm{d}\dot{s} = \mathrm{d}\dot{u} + \mathrm{d}\dot{w}. \tag{3.12}$$

The equilibrium entropy complies a condition of equality in the general Clausius inequality, whereas the local equilibrium entropy may also be understood as a definition of the mass density of entropy, or the specific entropy, in systems out of equilibrium [71].
Thus, the total entropy of a system is defined by the general balance law

$$\begin{aligned} S &= \int\limits_{V_0-\Upsilon} \rho_0(\mathbf{X}) s(\mathbf{X},t) \mathrm{d}\overline{V} \\ &= \int\limits_{V-v} \rho(\mathbf{x},t) s(\mathbf{x},t) \mathrm{d}\overline{V}, \end{aligned} \tag{3.13}$$

where s is the specific entropy relative to the mass of a system or body.
It can be assumed that the Clausius inequality is valid for each material point. The material point exchanges a total amount of heat $đQ$ at temperature T with its surroundings. Thus, the total amount of heat $đQ$ may be divided into heat flux density, i.e. Q^K or q^k, and density of the absorbed or emitted energy, i.e. $\tilde{Q}$ or $\tilde{q}$. Then, generalisation of the Clausius inequality for the entire system, or body, has for the material description the form

$$\int\limits_{V_0-\Upsilon} \rho_0 \dot{s} \mathrm{d}\overline{V} \geq -\int\limits_{A_0-\Upsilon} \frac{Q^K}{T} \mathrm{d}A_K + \int\limits_{V_0-\Upsilon} \frac{\tilde{Q}}{T} \mathrm{d}\overline{V}, \tag{3.14}$$

and for the actual description becomes

$$\dot{\int\limits_{V-v}} \rho s \mathrm{d}\overline{V} \geq -\int\limits_{A-v} \frac{q^k}{T} \mathrm{d}a_k + \int\limits_{V-v} \frac{\tilde{q}}{T} \mathrm{d}\overline{V}. \tag{3.15}$$

Moreover, the total production of entropy must be defined in order to comply

with the above mentioned inequalities. Then, the total production of entropy is defined by

$$\begin{aligned} P(S) &= \int\limits_{V_0-\Upsilon} \Sigma(S)\mathrm{d}\overline{V} \geq 0 \\ &= \int\limits_{V-\upsilon} \sigma(S)\mathrm{d}\overline{V} \geq 0, \end{aligned} \tag{3.16}$$

where

$$\Sigma(S) = \rho_0 \dot{s} + \frac{\partial}{\partial X^K}\left(\frac{Q^K}{T}\right) - \frac{\tilde{Q}}{T} \geq 0, \quad \text{for} \quad \mathbf{X} \in V_0 - \Upsilon, \tag{3.17}$$

and

$$\sigma(S) = \rho \dot{s} + \frac{\partial}{\partial x^k}\left(\frac{q^k}{T}\right) - \frac{\tilde{q}}{T} \geq 0, \quad \text{for} \quad \mathbf{x} \in V - \upsilon, \tag{3.18}$$

are densities of the production of entropy in the material and actual description, respectively. Eq. (3.17) and Eq. (3.18) represent a local form of the second law of thermodynamics or a local form of the balance of entropy and are called as the Clausius-Duhem inequalities [71, 85].
In general, the balance law of the total entropy is given by

$$\dot{S} - J(S) = P(S) \geq 0. \tag{3.19}$$

Thus, the balance law of the total entropy has in the material description, i.e. by Eq. (3.14) and Eq. (3.17), following form

$$\int\limits_{V_0-\Upsilon} \rho_0 \dot{s}\mathrm{d}\overline{V} = -\int\limits_{A_0-\Upsilon} \frac{Q^K}{T}\mathrm{d}A_K + \int\limits_{V_0-\Upsilon} \frac{\tilde{Q}}{T}\mathrm{d}\overline{V} + \int\limits_{V_0-\Upsilon} \Sigma(S)\mathrm{d}\overline{V}. \tag{3.20}$$

In the actual description, i.e. by Eq. (3.15) and Eq. (3.18), the balance law of the total entropy can be expressed by

$$\overline{\int\limits_{V-\upsilon} \rho s\mathrm{d}\overline{V}}^{\cdot} = -\int\limits_{A-\upsilon} \frac{q^k}{T}\mathrm{d}a_k + \int\limits_{V-\upsilon} \frac{\tilde{q}}{T}\mathrm{d}\overline{V} + \int\limits_{V-\upsilon} \sigma(S)\mathrm{d}\overline{V}. \tag{3.21}$$

Comparing Eq. (3.19) with Eq. (3.20) and Eq. (3.21), a flux of the entropy

into a body is determined as

$$\begin{aligned} J(S) &= -\int\limits_{A_0-\Upsilon} \frac{Q^K}{T}\mathrm{d}A_K + \int\limits_{V_0-\Upsilon} \frac{\tilde{Q}}{T}\mathrm{d}\overline{V} \\ &= -\int\limits_{A-\upsilon} \frac{q^k}{T}\mathrm{d}a_k + \int\limits_{V-\upsilon} \frac{\tilde{q}}{T}\mathrm{d}\overline{V}. \end{aligned} \tag{3.22}$$

Here, a negative sign expresses the flux against the direction of the outer normal to the body surface.
If an absorption or an emission of the radiation energy is neglected, the density of the entropy flux will be obtained in the following form

$$\begin{aligned} J^K(S) &= -\frac{Q^K}{T}, \\ j^k(S) &= -\frac{q^k}{T}. \end{aligned} \tag{3.23}$$

Moreover, it is also suitable to determine the local balance law for the balance of entropy on the discontinuity surface [28, 85]. The balance of entropy for the discontinuity surface has, according to Eq. (3.7) and Eq. (3.9), the following form

$$\left\|\rho_0 s(U^K - V^K) - J^K(S)\right\| N_K \geq 0, \quad \text{for} \quad \mathbf{X} \in \Upsilon, \tag{3.24}$$

$$\left\|\rho s(u^k - v^k) - j^k(S)\right\| n_k \geq 0, \quad \text{for} \quad \mathbf{x} \in \upsilon. \tag{3.25}$$

If the surface of discontinuity, e.g. a shock wave, passes through an environment, the entropy of that environment will increase or more precisely will not decrease.
Furthermore, the production of entropy may be understood as the most general form of the second law of thermodynamics, which also expresses density of the dissipated energy formulated via the so-called fundamental thermodynamic inequality. Thus, in the material description, the fundamental thermodynamic inequality is given by

$$\begin{aligned} \bar{\Pi} &= T\Sigma(S) \\ &= \rho_0 T\dot{s} + \frac{\partial Q^K}{\partial X^K} - \frac{Q^K}{T}\frac{\partial T}{\partial X^K} - \tilde{Q} \geq 0, \quad \text{for} \quad \mathbf{X} \in V_0 - \Upsilon. \end{aligned} \tag{3.26}$$

Analogously, in the actual description, the fundamental thermodynamic inequality is written as

$$\begin{aligned}\bar{\pi} &= T\sigma(S) \\ &= \rho T\dot{s} + \frac{\partial q^k}{\partial x^k} - \frac{q^k}{T}\frac{\partial T}{\partial x^k} - \tilde{q} \geq 0, \quad \text{for} \quad \mathbf{x} \in V - v.\end{aligned} \tag{3.27}$$

3.3 Thermodynamic Stability Condition (TSC)

In order to analyse a flow stability, it is convenient to use a definition of the fundamental thermodynamic inequality together with the first law of thermodynamics formulated via the total enthalpy. Nevertheless, because flow problems are usually solved in the actual description, derivation of the thermodynamic stability condition (TSC function) based on the fundamental thermodynamic inequality is conducted only for the actual description of the system, i.e. for $\mathbf{x} \in V - v$. Moreover, the production of entropy term in the fundamental thermodynamic inequality depends on the other quantities, as shown by Eq. (3.18). However, the production of entropy can be obtained from the balance of the total enthalpy, which is the thermodynamic potential reaching its minimum in a local thermodynamic equilibrium, i.e. $\mathrm{d}^2 h_t$.
The total enthalpy, or the total specific enthalpy, is expressed by

$$h_t = u + \frac{p}{\rho} + \frac{\mathbf{u}^2}{2} + \phi, \tag{3.28}$$

where u, ρ, $\mathbf{u}$, and ϕ are successively the internal energy, density, velocity vector, and a potential, respectively. Moreover, pressure p is given by the elastic part of the Cauchy stress tensor

$$t^{ik} = -p\,(\rho,T)\,\delta^{ik} + t^{ik}_{dis}\left(\rho,d^{ik},T,\frac{\partial T}{\partial x^i}\right). \tag{3.29}$$

Furthermore, the balance of the total enthalpy is given by

$$\rho\dot{h}_t - \frac{\partial p}{\partial t} + \frac{\partial q^k}{\partial x^k} - t^{ik}_{dis}\frac{\partial u_i}{\partial x^k} - u_i\frac{\partial t^{ik}_{dis}}{\partial x^k} - \tilde{q} = 0. \tag{3.30}$$

Density of the absorbed or emitted energy, $\tilde{q}$, expressed from the balance of

the total enthalpy, Eq. (3.30), is inserted into the fundamental thermodynamic inequality, Eq. (3.27). Then, Eq. (3.27) becomes

$$\bar{\pi} = \rho T\dot{s} + \frac{\partial q^k}{\partial x^k} - \frac{q^k}{T}\frac{\partial T}{\partial x^k} - \rho\dot{h}_t + \frac{\partial p}{\partial t} - \frac{\partial q^k}{\partial x^k} + t^{ik}_{dis}\frac{\partial u_i}{\partial x^k} + u_i\frac{\partial t^{ik}_{dis}}{\partial x^k} \geq 0, \quad (3.31)$$

$$\bar{\pi} = \rho T\dot{s} - \rho\dot{h}_t + \frac{\partial p}{\partial t} - \frac{q^k}{T}\frac{\partial T}{\partial x^k} + t^{ik}_{dis}\frac{\partial u_i}{\partial x^k} + u_i\frac{\partial t^{ik}_{dis}}{\partial x^k} \geq 0, \quad (3.32)$$

$$\bar{\pi} = \rho\left(T\dot{s} + \frac{1}{\rho}\frac{\partial p}{\partial t} - \dot{h}_t\right) - \frac{q^k}{T}\frac{\partial T}{\partial x^k} + t^{ik}_{dis}\frac{\partial u_i}{\partial x^k} + u_i\frac{\partial t^{ik}_{dis}}{\partial x^k} \geq 0. \quad (3.33)$$

It is noticeable that the total enthalpy depends only on the entropy and the pressure. For steady isentropic processes, i.e. $\partial p/\partial t$, $\dot{s}$, and $t^{ik}_{dis} = 0$, the total enthalpy is expressed by

$$h_t = u + \frac{p}{\rho} + \frac{\mathbf{u}^2}{2} + \phi = \text{constant}, \quad (3.34)$$

meaning that the total energy of the material point during its movement along a trajectory $x^k = x^k(X^k,t)$ is constant. Furthermore, according to the above noted conditions and expressions, the TSC function, Eq. (3.33), can be rewritten as

$$\bar{\pi} = \rho\left[T - \left(\frac{\partial h_t}{\partial s}\right)_p\right]\dot{s} + \rho\left[\frac{1}{\rho} - \left(\frac{\partial h_t}{\partial p}\right)_s\right]\frac{\partial p}{\partial t} - \frac{q^k}{T}\frac{\partial T}{\partial x^k} + t^{ik}_{dis}\frac{\partial u_i}{\partial x^k} + u_i\frac{\partial t^{ik}_{dis}}{\partial x^k} \geq 0. \quad (3.35)$$

This inequality shows a dependency of the temperature and density on the total enthalpy, so that

$$T = \left(\frac{\partial h_t}{\partial s}\right)_p \text{ and } \frac{1}{\rho} = \left(\frac{\partial h_t}{\partial p}\right)_s. \quad (3.36)$$

Assuming a flow problem being in a thermodynamic equilibrium, then, Eq. (3.33) becomes

$$\bar{\pi} = \bar{\pi}_0 = \rho_0\left(T_0\dot{s}_0 + \frac{1}{\rho_0}\frac{\partial p_0}{\partial t} - \dot{h}_{t0}\right) = 0. \quad (3.37)$$

Nevertheless, a thermodynamic equilibrium deviates by an influence of fluctuations of the specific entropy and pressure out of equilibrium, which results in the following occurrence of dissipative and destabilising processes

$$\bar{\pi} = \rho \left(T\dot{s} + \frac{1}{\rho}\frac{\partial p}{\partial t} - \dot{h}_t \right) + \pi \geq 0, \tag{3.38}$$

where

$$\pi = -\frac{q^k}{T}\frac{\partial T}{\partial x^k} + t^{ik}_{dis}\frac{\partial u_i}{\partial x^k} + u_i\frac{\partial t^{ik}_{dis}}{\partial x^k}. \tag{3.39}$$

As the entropy is a function of variables h_t, p and has extremes, i.e. maxima and minima, fluctuations of the total enthalpy and pressure around their reference states are introduced

$$s = s_0 + \delta s,\ p = p_0 + \delta p. \tag{3.40}$$

It is also convenient to expand the total enthalpy into a Taylor series

$$h_t(s,p) = h_{t0}(s_0,p_0) + \mathrm{d}h_t(\delta s, \delta p) + \frac{1}{2}\mathrm{d}^2 h_t(\delta s, \delta p) + \ldots \tag{3.41}$$

Then, the TSC function, Eq. (3.33), becomes

$$\begin{aligned}\bar{\pi} = \rho \Bigg[T\left(\dot{s_0} + \dot{\overline{\delta s}}\right) + \frac{1}{\rho_0}\frac{\partial}{\partial t}\left(p_0 + \delta p\right) - \dot{h}_{t0} - \dot{\overline{\mathrm{d}h_t}} - \frac{\dot{\overline{\mathrm{d}^2 h_t}}}{2} \Bigg] \\ - \frac{q^k}{T}\frac{\partial T}{\partial x^k} + t^{ik}_{dis}\frac{\partial u_i}{\partial x^k} + u_i\frac{\partial t^{ik}_{dis}}{\partial x^k} \geq 0,\end{aligned} \tag{3.42}$$

where entropy, i.e. a thermodynamic equilibrium and a local thermodynamic equilibrium, can be defined by the following relations

$$\dot{h}_{t0} = T\dot{s_0} + \frac{1}{\rho}\frac{\partial p_0}{\partial t},\ \dot{\overline{\mathrm{d}h_t}} = T\dot{\overline{\delta s}} + \frac{1}{\rho}\frac{\partial \delta p}{\partial t}. \tag{3.43}$$

Thus, the reference state, i.e. equilibrium, may be defined by

$$T\left(\dot{s_0} + \dot{\overline{\delta s}}\right) + \frac{1}{\rho_0}\frac{\partial}{\partial t}\left(p_0 + \delta p\right) - \dot{h}_t - \dot{\overline{\mathrm{d}h_t}} = 0. \tag{3.44}$$

Then, the remaining term in the square brackets of Eq. (3.42) represents the energy of fluctuations that should be attenuated by proceeding processes

in a system, i.e. by dissipative and destabilising processes in a fluid. These processes act against induced fluctuations in order to keep a system in an equilibrium and must satisfy

$$-\frac{\rho}{2}\dot{\overline{\mathrm{d}^2 h_t}} + \pi \geq 0. \tag{3.45}$$

Hence, the TSC function may be expressed as

$$\bar{\pi} = -\frac{\rho}{2}\dot{\overline{\mathrm{d}^2 h_t}} - \frac{q^k}{T}\frac{\partial T}{\partial x^k} + t_{dis}^{ik}\frac{\partial u_i}{\partial x^k} + u_i\frac{\partial t_{dis}^{ik}}{\partial x^k} \geq 0. \tag{3.46}$$

Thus, the equality assigns a balance between the energy of fluctuations and dissipative and destabilising processes, i.e. $\pi = (\rho_0/2)\dot{\overline{\mathrm{d}^2 h_t}}$. If the inequality is satisfied, dissipative and destabilising processes will attenuate fluctuations and a system is stable in sense of the TSC function. Furthermore, a general condition for a system with dominant convection processes states that a system is stable, if $\mathrm{d}^2 h_t \geq 0$ and $\dot{\overline{\mathrm{d}^2 h_t}} \leq 0$ [85]. Then, it may be stated that the total enthalpy serves as the Lyapunov function of stability for a system with dominant convection. So, if the TSC function, Eq. (3.33), is not satisfied, a convective instability may occur.
Hence, with respect to the above mentioned generalisation, the final expression for the TSC function is

$$\pi = -\frac{q^k}{T}\frac{\partial T}{\partial x^k} + t_{dis}^{ik}\frac{\partial u_i}{\partial x^k} + u_i\frac{\partial t_{dis}^{ik}}{\partial x^k} \geq 0 \text{ for } \mathbf{x} \in V, \tag{3.47}$$

and represents dissipative processes, given by gradients of temperature and velocity, and also destabilising processes, given by divergence of dissipative part of the stress tensor.
In order to complete Eq. (3.47), the dissipative part of the stress tensor needs to be expressed. Assuming low Mach numbers of the flow, the dissipative part of the stress tensor is given via the Cauchy stress tensor for a Newtonian incompressible fluids using the strain rate tensor d^{ik} by [50]

$$t_{dis}^{ik} = 2\mu d^{ik} = \mu\left(\frac{\partial u^i}{\partial x^k} + \frac{\partial u^k}{\partial x^i}\right), \tag{3.48}$$

$$d^{ik} = \frac{1}{2}\left(\frac{\partial u^i}{\partial x^k} + \frac{\partial u^k}{\partial x^i}\right). \tag{3.49}$$

So, the inequality, Eq. (3.47) or Eq. (A.1), represents the so-called local TSC function. Moreover, the so-called global, or integral, TSC function,

estimating whether an entire investigated system satisfies the TSC function, is given by a volume integral of the local TSC function. Thus, the general form of the global TSC function becomes

$$\Pi = \int_{V} \pi \mathrm{d}\overline{V}. \tag{3.50}$$

3.4 Application of the Thermodynamic Stability Condition

The previous sections showed the derivation of the local TSC function via the balance of entropy and balance of total enthalpy. This section focuses on the application of the local TSC function to simplified general flow, i.e. axial flow in a straight rigid tube, Couette flow between rotating cylinders, and flow in a rotating tube.

3.4.1 Steady Axial Flow

An isothermal incompressible fluid with constant viscosity and a steady 1D flow along the z-axis in a rigid tube, i.e. the velocity vector has the following form $\mathbf{u} = (u^r, u^\phi, u^z) = (0, 0, u^z(r))$, is considered, as schematically shown in Fig. 3.1.

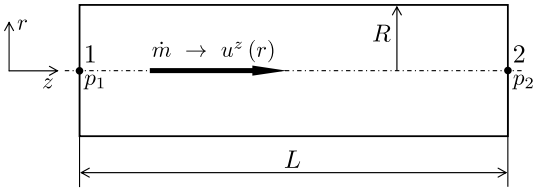

Fig. 3.1: Schematics of 1D flow in the rigid tube

The local TSC function has for this type of flow and for the cylindrical coordinates the following form

$$\begin{aligned}\pi &= \mu u^z \left(\frac{\partial^2 u^z}{\partial r^2} + \frac{1}{r}\frac{\partial u^z}{\partial r} \right) + \mu \left(\frac{\partial u^z}{\partial r} \right)^2 \\ &= \frac{\mu}{r}\frac{\partial}{\partial r}\left(r u^z \frac{\partial u^z}{\partial r} \right) \geq 0.\end{aligned} \tag{3.51}$$

Derivation of Eq. (3.51) is shown in Appendix A.

3.4.1.1 Laminar Flow

A laminar fluid flow in channels or tubes is characterised by a parabolic velocity profile, i.e. the so-called Poiseuille flow [50]. In cylindrical coordinates, this velocity profile can be expressed by

$$u^z = u(r) = K\left[1 - \left(\frac{r}{R} \right)^2 \right] = Kf(r), \tag{3.52}$$

where K is a constant characterising a maximum value of the velocity. This expression, Eq. (3.52), is inserted into the local TSC function, Eq. (3.51). After simple algebra, see Appendix B, the first interesting result is obtained

$$\pi = 4K^2\mu \left(2\frac{r^2}{R^4} - \frac{1}{R^2} \right) \geq 0. \tag{3.53}$$

Thus, as shown in Fig. 3.2, the local TSC function, Eq. (3.51), is for the velocity profile, Eq. (3.52), satisfied in the region, where $r > \pm R/\sqrt{2}$, see Appendix B. This means that the laminar flow in a tube is stable in this region. On the other hand, in the region where the radial coordinate is $r < \pm R/\sqrt{2}$, the laminar flow in a tube is in an unstable region. The radial coordinate $r = \pm R/\sqrt{2}$ represents a margin of the local stability.
In addition, in order to obtain the so-called global TSC function, Eq. (3.50), the volume integration of the local TSC function is necessary, see Appendix B. If the positive values of the local TSC function prevails, the global TSC

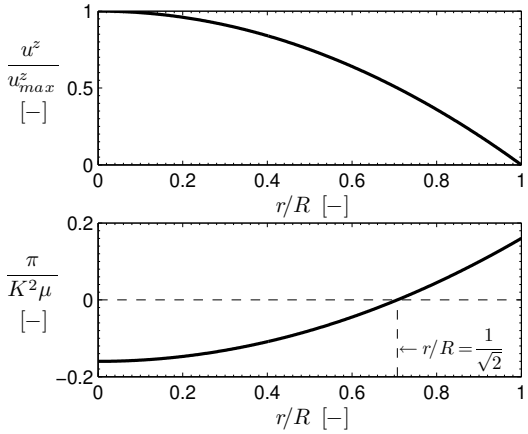

Fig. 3.2: Velocity profile of a laminar flow in a tube and corresponding shape of the local TSC function

function will be positive as well. Hence, the global TSC function of the laminar flow in the rigid tube is

$$\Pi = \int_V 4K^2\mu \left(2\frac{r^2}{R^4} - \frac{1}{R^2}\right) \mathrm{d}\overline{V} = 0. \tag{3.54}$$

So, the laminar flow in a tube is according to the global TSC function at the margin of stability, i.e. a small disturbance may destabilise the flow.

3.4.1.2 Turbulent Flow

A turbulent fluid flow, in case of the flow in the boundary layer, can be approximated via the 1/7 power law [113]. Unfortunately, this approximation leads to the inaccurate shear stress at the channel or tube wall. Nevertheless, due to this approximation, it is possible to express this flow, e.g. a boundary

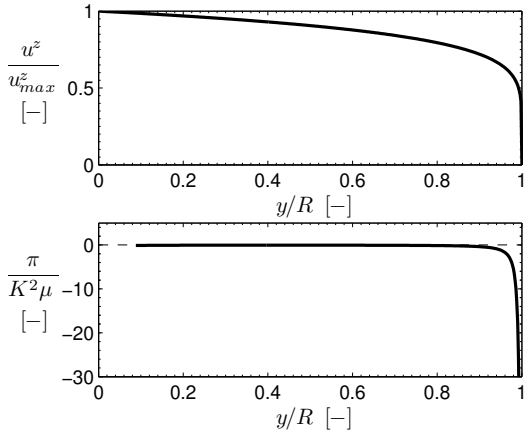

Fig. 3.3: Velocity profile of a turbulent flow given by the power law in a tube and corresponding shape of the local TSC function

layer near a tube wall, by

$$u^z = u(r) = K(R-r)^{1/7} = Kf(r), \tag{3.55}$$

where K is a constant characterising a maximum value of the velocity. Unfortunately, this approximation of a turbulent flow in a tube leads to a discontinuity near the tube axis, but it still provides a qualitative flow characteristic. Hence, the approximated velocity, Eq. (3.55), is inserted into the local TSC function, Eq. (3.51). After simple algebra, see Appendix C, the following result is obtained

$$\pi = K^2\mu\left[-\frac{1}{7r(R-r)^{5/7}} - \frac{5}{49(R-r)^{12/7}}\right] \leq 0. \tag{3.56}$$

Thus, the local TSC function for the turbulent flow reaches for $r \in (0; R)$ always negative values,as shown in Fig. 3.3. Here, the local TSC function is shown without region near the tube axis, where a discontinuity of the used power law velocity profile for a turbulent flow in a tube, which results in more negative values of the local TSC function, causes a results distortion.

Furthermore, the global TSC function is again given by the volume integral, Eq. (3.50), by

$$\Pi = \int_V K^2 \mu \left[-\frac{1}{7r\,(R-r)^{5/7}} - \frac{5}{49\,(R-r)^{12/7}} \right] \mathrm{d}\overline{V} \leq 0. \tag{3.57}$$

Hence, the turbulent flow in the boundary layer is according to the global TSC function unstable, i.e. a small disturbance shall not attenuate.

3.4.2 Steady Flow in an Annulus

This subsection focuses on the Couette flow between two rotating cylinders and the flow in rotating tubes. So, an isothermal incompressible fluid with a constant viscosity and a steady velocity in axial and tangential direction is assumed. Components of the velocity vector are a function of the radial coordinate r, i.e. the velocity vector has the following form $\mathbf{u} = (u^r, u^\phi, u^z) = (0, u^\phi(r), u^z(r))$.
The local TSC function is for the tangential and the axial components of the velocity, see Appendix A and Eq. (A.1), given by

$$\begin{aligned} \pi = \mu \Bigg[& u^\phi \left(\frac{\partial^2 u^\phi}{\partial r^2} + \frac{\partial u^\phi}{r \partial r} - \frac{u^\phi}{r^2} \right) + \left(\frac{\partial u^\phi}{\partial r} - \frac{u^\phi}{r} \right) \left(\frac{\partial u^\phi}{\partial r} \right) \\ & + \left(\frac{\partial u^\phi}{\partial r} - \frac{u^\phi}{r} \right) \left(-\frac{u^\phi}{r} \right) + \left(\frac{\partial u^z}{\partial r} \right)^2 \\ & + u^z \left(\frac{\partial^2 u^z}{\partial r^2} + \frac{1}{r} \frac{\partial u^z}{\partial r} \right) \Bigg] \geq 0. \end{aligned} \tag{3.58}$$

Determination of a shape of the local TSC function is the main task. Moreover, in case of the Couette flow between rotating cylinders, the obtained results are compared with results of the Rayleigh's stability condition.

3.4.2.1 Couette Flow between Two Rotating Cylinders

The local TSC function has for the Couette flow between two rotating cylinders, characterised by the tangential component of the velocity vector $u^\phi = u^\phi(r)$, the following form

$$\pi = \mu \left[u^\phi \left(\frac{\partial^2 u^\phi}{\partial r^2} + \frac{\partial u^\phi}{r \partial r} \right) + \left(\frac{\partial u^\phi}{\partial r} \right)^2 - 2 \frac{u^\phi}{r} \frac{\partial u^\phi}{\partial r} \right] \geq 0. \tag{3.59}$$

The tangential component of the velocity is assumed by $u^\phi = u^\phi(r) = r\Omega(r)$, i.e. a fluid rotates as a solid body with the angular velocity depending on the position r. Thus, this expression of the tangential velocity is inserted into Eq. (3.59), which results in

$$\pi = \mu \left\{ r^2 \Omega(r) \frac{\partial^2 \Omega(r)}{\partial r^2} + 3r\Omega(r) \frac{\partial \Omega(r)}{\partial r} + r^2 \left[\frac{\partial \Omega(r)}{\partial r} \right]^2 \right\} \geq 0. \tag{3.60}$$

For comparison, the results of the inviscid Rayleigh's theory for the same velocity profile, i.e. $u^\phi = u^\phi(r) = r\Omega(r)$, based on the discriminant of stability, published by Chandrasekhar [20], are also given here

$$\begin{aligned} \Theta(r) &= \frac{1}{r^3} \frac{\mathrm{d}}{\mathrm{d}r} \left(r u^\phi \right)^2 \\ &= \frac{1}{r^3} \frac{\mathrm{d}}{\mathrm{d}r} \left\{ r^4 \left[\Omega(r) \right]^2 \right\} \\ &= 4 \left[\Omega(r) \right]^2 + 2r\Omega(r) \frac{\mathrm{d}\Omega(r)}{\mathrm{d}r} > 0. \end{aligned} \tag{3.61}$$

Derivation of inequalities, Eq. (3.60) and Eq. (3.61), and further calculations are given in Appendix D.
On the first view, the Rayleigh's inviscid theory contradicts the local TSC function in the following simplified case of the solid body vortex formulated as $u^\phi = r\Omega$, i.e. for $\Omega(r) = \Omega = \text{constant}$. For this case, the local TSC function complies the inequality (3.60) only partly, i.e. $\pi = 0$, but the Rayleigh's condition (3.61) is satisfied, i.e. $\Theta(r) > 0$. This discrepancy can be caused by the fact that in evaluation of the local TSC function are, moreover, reflected mutual relations between the velocity gradients and the dissipative stress tensor of fluid motion in contrast to the inviscid Rayleigh's condition.

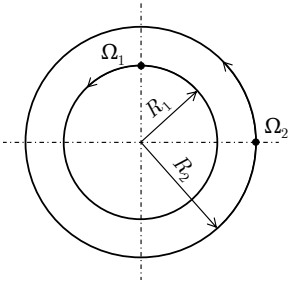

Fig. 3.4: Flow between two rotating cylinders

Furthermore, the general Couette flow between two rotating cylinders, Fig. 3.4, is given by the expression [20]

$$\Omega(r) = A + \frac{B}{r^2}, \tag{3.62}$$

where

$$\begin{aligned} A &= -\Omega_1 \eta_C^2 \frac{1 - \dfrac{\mu_C}{\eta_C^2}}{1 - \eta_C^2}, \\ B &= \Omega_1 \frac{R_1^2 (1 - \mu_C)}{1 - \eta_C^2}, \\ \mu_C &= \frac{\Omega_2}{\Omega_1},\ \eta_C = \frac{R_1}{R_2}. \end{aligned} \tag{3.63}$$

For the angular velocity Eq. (3.62), the discriminant of stability, Eq. (3.61), or eventually Eq. (D.4), becomes

$$\begin{aligned} \Theta(r) &= 4\left[\Omega(r)\right]^2 + 2r\Omega(r)\frac{\mathrm{d}\Omega(r)}{\mathrm{d}r} \\ &= 4\left(A + \frac{B}{r^2}\right)^2 + 2r\left(A + \frac{B}{r^2}\right)\left(-\frac{2B}{r^3}\right) \\ &= 4A\left(A + \frac{B}{r^2}\right) > 0, \end{aligned} \tag{3.64}$$

which is, then, by use of Eq. (3.63) rewritten as

$$\Theta(r) = -4\Omega_1^2\eta_C^2 \frac{\left(1-\frac{\mu_C}{\eta_C^2}\right)(1-\mu_C)}{\left(1-\eta_C^2\right)^2}\left(\frac{R_1^2}{r^2}-\frac{\eta_C^2-\mu_C}{1-\mu_C}\right) > 0. \tag{3.65}$$

From the inequality Eq. (3.65) it follows that the Rayleigh's condition will be satisfied only, if the discriminant of stability is larger than zero, i.e. $\Theta(r) > 0$. Because of $\eta_C < 1$, $1-\eta_C^2 > 0$ and, moreover, assuming $\mu_C > 1$, $1-\mu_C < 0$ meaning that the parentheses showing a dependency on the radial coordinate is less than zero, the relation between η_C and μ_C must comply the following inequality

$$1-\frac{\mu_C}{\eta_C^2} < 0 \;\rightarrow\; \eta_C^2-\mu_C < 0 \;\rightarrow\; \mu_C > \eta_C^2 \;\rightarrow\; \Omega_2 > \Omega_1\eta_C^2, \tag{3.66}$$

which is a well known result for the Couette flow between two rotating cylinders underlined by Chandrasekhar [20].
Also, the local TSC function Eq. (3.60) is solved for the angular velocity given by Eq. (3.62). So, the local TSC function Eq. (3.60) will be satisfied, if the following relation is valid

$$r^2\Omega(r)\frac{\partial^2\Omega(r)}{\partial r^2} + 3r\Omega(r)\frac{\partial\Omega(r)}{\partial r} + r^2\left[\frac{\partial\Omega(r)}{\partial r}\right]^2 \geq 0. \tag{3.67}$$

Thus, one obtains

$$\begin{aligned} r^2\left(A+\frac{B}{r^2}\right)\frac{\partial^2}{\partial r^2}\left(A+\frac{B}{r^2}\right) + 3r\left(A+\frac{B}{r^2}\right)\frac{\partial}{\partial r}\left(A+\frac{B}{r^2}\right) \\ +r^2\left[\frac{\partial}{\partial r}\left(A+\frac{B}{r^2}\right)\right]^2 \geq 0, \\ \frac{4B^2}{r^4} \geq 0. \end{aligned} \tag{3.68}$$

Then, relations in Eq. (3.63) are inserted into the inequality Eq. (3.68), see Appendix D, and the following conclusions are found

$$\frac{\pi}{\mu} = \frac{4\Omega_1^2R_1^4\left(1-\mu_C\right)^2}{r^4\left(1-\eta_C^2\right)^2} \geq 0 \text{ or } \frac{\pi}{\mu} = \frac{4\Omega_1^2\eta_C^4\left(1-\mu_C\right)^2}{\tilde{r}^4\left(1-\eta_C^2\right)^2} \geq 0, \tag{3.69}$$

where $\tilde{r} = r/R_2$. This inequality, Eq. (3.69), is valid, if $1-\eta_C^2 \neq 0 \rightarrow \eta_C \neq$

± 1, which is always satisfied, because of the definition of η_C by Eq. (3.63). Nevertheless, there is one condition, for which the local TSC function reaches zero values meaning that the Couette flow between two rotating cylinders is at the margin of stability, i.e. $\pi = 0$ for $\mu_C = 0$ or $\Omega_2 = \Omega_1$. The same condition, i.e. $\mu_C = 0$ or $\Omega_2 = \Omega_1$, is valid for the global TSC function, as shown in the following analysis, see Appendix D,

$$\frac{\Pi}{\mu} = \int_V \left[\frac{4\Omega_1^2 R_1^4 \left(1-\mu_C\right)^2}{r^4 \left(1-\eta_C^2\right)^2} \right] \mathrm{d}\overline{V} \geq 0, \tag{3.70}$$

$$\frac{\Pi}{\mu} = -\frac{4\pi L \Omega_1^2 \eta_C^2 \left(1-\mu_C\right)^2 \left(R_1^2 - R_2^2\right)}{\left(1-\eta_C^2\right)^2} \geq 0, \tag{3.71}$$

$$\frac{\Pi}{\mu} = -\frac{4\pi L \Omega_1^2 R_2^2 \eta_C^2 \left(1-\mu_C\right)^2 \left(\eta_C^2 - 1\right)}{\left(1-\eta_C^2\right)^2} \geq 0. \tag{3.72}$$

Hence, the global TSC function is always positive because $\eta_C < 1$, Eq. (3.72). Nevertheless, there is again only one condition, for which the inequality is zero, i.e. for $\mu_C = 0$ or $\Omega_2 = \Omega_1$, as already mentioned above.
Comparison of the obtained theoretical results with well known experiments made by Taylor shows an qualitative agreement between experimental and theoretical results, Fig. 3.5; experimental data and radii of cylinders, i.e.

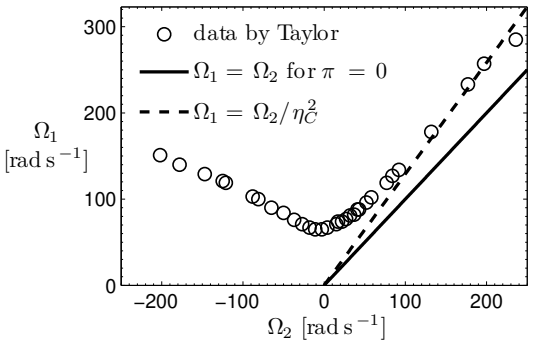

Fig. 3.5: Onset of coherent structures, i.e. instability, for flow between two rotating cylinders

$R_1 = 0.03550$ m, $R_2 = 0.04035$ m, $\eta_C = 0.8798$, are taken from [26, 119]. Moreover, the line $\Omega_1 = \Omega_2/\eta_C^2$ follows the results from the Rayleigh's inviscid theory and predicts the onset of coherent structures for the Couette flow between two rotating cylinders.

3.4.2.2 Axial Flow in an Annulus between Rotating Tubes

Now, the TSC function, Eq. (3.58), is applied to the flow in rotating tubes, which represents an example of the axial and Couette flow between two rotating cylinders. In order to show an influence of rotation on the stability of the axial flow in the gap bounded by the cylinders, i.e. flow in the rotating tube, the works by Pfitzer [99] and Rothe [109] are utilised. Furthermore, the rotation of the inner and outer cylinder (tube) is characterised by the so-called rotation numbers N_1 and N_2 as follows

$$N_1 = u_1^{\phi}/\overline{U^z},\ N_2 = u_2^{\phi}/\overline{U^z}. \tag{3.73}$$

Pfitzer [99] focused on the problem of an axial turbulent flow with inner and/or outer rotating cylinder, or tube, whose geometrical parameters were $R_1 = 0.0770$ m, $R_2 = 0.0898$ m, $\eta_C = 0.8575$, and length 1.56 m. He generally studied an influence of rotation on the heat transfer and found out that the inner rotating cylinder has more pronounced positive influence.
Thus, the data obtained by Pfitzer are taken as a test case for the use of the local TSC function. In order to obtain dimensionless values, the local TSC function is, in the following analysis, normalised by the dynamic viscosity μ, the hydraulic diameter of the rotating tube $D_h = 2(R_2 - R_1)$, and the axial bulk velocity $\overline{U^z}$, i.e. the plotted values are given as $\hat{\pi} = \pi D_h^2/(\overline{U^z}^2\mu)$.
Firstly, the case with an outer rotating cylinder, which is represented by the data plotted in Fig. 3.6, is investigated. Thus, an influence of the outer rotating cylinder on the local TSC function shows Fig. 3.7, which is due to the strong influence of the tube walls on the stability plotted without wall regions. In the wall regions, there is a high energy dissipation due to the velocity gradient that causes high positive values of the local TSC function leading to unclearness and distortion of results.
Hence, the local TSC function concerning only the tangential velocity components, Eq. (3.59), is drawn in the left graph of Fig. 3.7 and is characterised by positive values of the local TSC function in the centre of the gap. On the other hand, the local TSC function concerning the axial and tangential

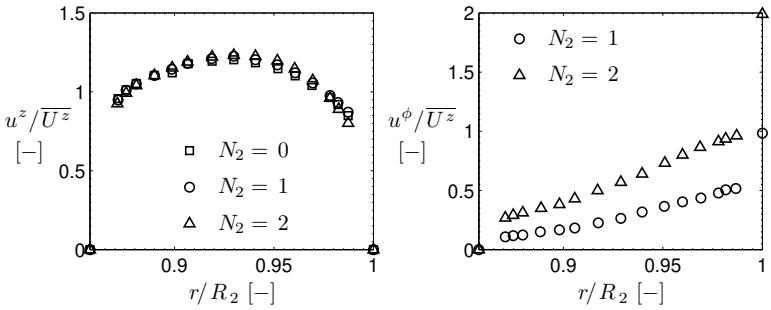

Fig. 3.6: Axial and tangential velocities by Pfitzer [99]; $Re = 10{,}000$, $\eta_C = 0.8575$, outer rotating cylinder

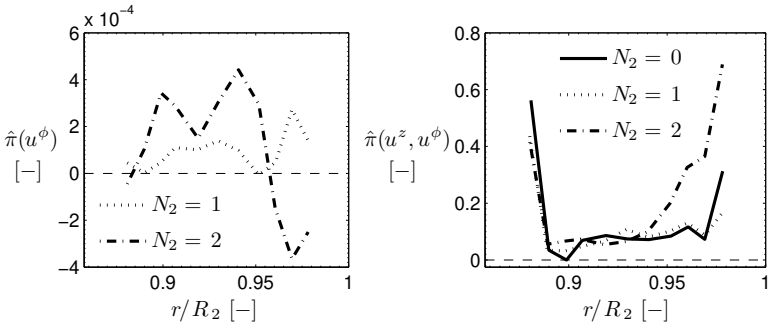

Fig. 3.7: Local TSC function determined from data by Pfitzer [99]; $Re = 10{,}000$, $\eta_C = 0.8575$, $\hat{\pi} = \pi D_h^2/(\overline{U^z}^2\mu)$, outer rotating cylinder

velocity components, Eq. (3.58), the right graph of Fig. 3.7, is characterised by positive values across the entire gap.
Secondly, the case, when the inner cylinder rotates, represented by the data shown in Fig. 3.8, is looked at. Thus, an influence of the inner rotating cylinder on the local TSC function shows Fig. 3.9, which is again due to the strong influence of the tube walls on the stability also plotted without wall regions.
The local TSC function concerning only the tangential velocity, Eq. (3.59),

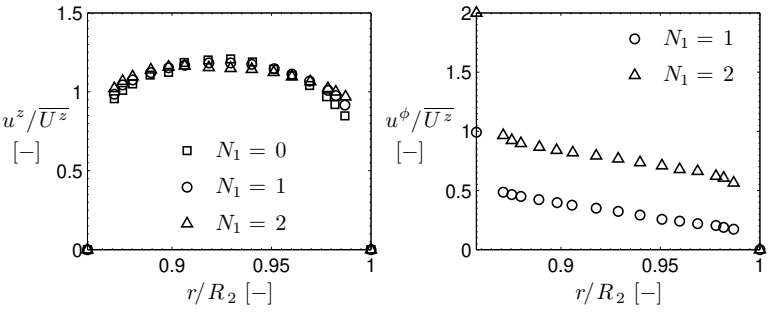

Fig. 3.8: Axial and tangential velocities by Pfitzer [99]; $Re = 10{,}000$, $\eta_C = 0.8575$, inner rotating cylinder

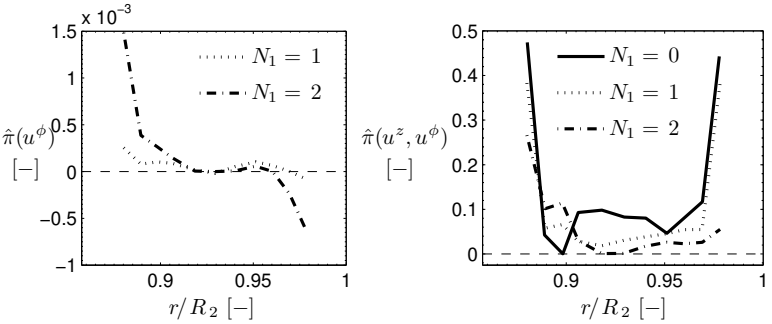

Fig. 3.9: Local TSC function determined from data by Pfitzer [99]; $Re = 10{,}000$, $\eta_C = 0.8575$, $\hat{\pi} = \pi D_h^2/(\overline{U^z}^2 \mu)$, inner rotating cylinder

is shown in the left graph of Fig. 3.9 and is again characterised by positive values of the local TSC function in the centre of the gap. Moreover, near the rotating tube the local TSC function approaches more positive values, which is a consequence of the here increasing dissipative processes. It is also evident that near the non-rotating tube the local TSC function reaches negative values, which may indicate destabilising effects in this region. On the other hand, the local TSC function concerning the axial and tangential velocity components, Eq. (3.58), shown in the right graph of Fig. 3.9, is

characterised again by positive values across the entire gap like in the case shown in Fig. 3.7.
Similar work dealing with an influence of rotation on the turbulent axial flow was also done by Rothe [109]. His work follows and confirms the general outcomes of the work by Pfitzer and also provides more detailed measured flow field for the use of the local TSC function. Moreover, Rothe investigated the flow phenomena in a rotating tube on the same apparatus as Pfitzer, i.e. the same geometrical and flow parameters can be utilised.
So, as in the case of the data by Pfitzer, the interest is firstly taken on the case, when the outer cylinder rotates, which is represented by the data plotted in Fig. 3.10. Thus, an influence of the outer rotating cylinder on the local TSC function with omitted wall region shows Fig. 3.11.
The left graph of Fig. 3.11 concerns only the tangential velocity, Eq. (3.59), and is characterised by positive values of the TSC function in the centre of the gap and near to the outer rotating tube. There is also a small region with negative values of the local TSC function indicating destabilising effects near to the inner non-rotating tube. This result is in contradiction to results of the data of Pfitzer shown in Fig. 3.7. This contradiction may be caused by Pfitzer due to not smoothly measured trend of the tangential velocity in case of an outer rotating tube. Assuming both components of the velocity, i.e. the axial and tangential velocity components, the local TSC function, Eq. (3.58), is characterised by the positive values over the entire gap reaching higher values near the walls, which is mainly given by the strong dissipation

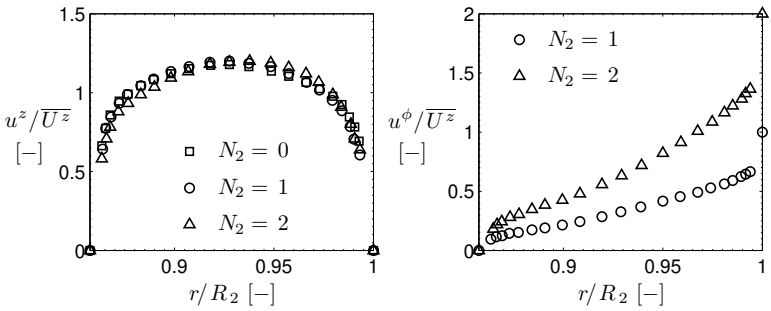

Fig. 3.10: Axial and tangential velocities by Rothe [109]; $Re = 10{,}000$, $\eta_C = 0.8575$, outer rotating cylinder

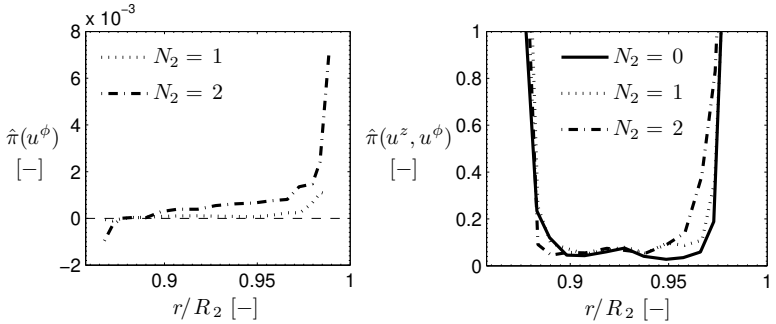

Fig. 3.11: Local TSC function determined from data by Rothe [109]; $Re = 10{,}000$, $\eta_C = 0.8575$, $\hat{\pi} = \pi D_h^2/(\overline{U^z}^2 \mu)$, outer rotating cylinder

due to the axial velocity gradient near the wall region, shown in the right graph of Fig. 3.11.
Now, the focus is set on the case of an inner rotating cylinder, represented by the data shown in Fig. 3.12. Hence, an influence of the inner rotating cylinder on the local TSC function, again with omitted wall region, shows Fig. 3.13.
The left graph of Fig. 3.13 covering only an influence of the tangential veloc-

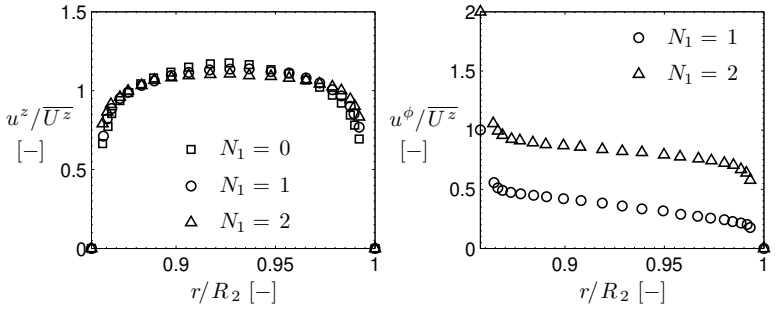

Fig. 3.12: Axial and tangential velocities by Rothe [109]; $Re = 10{,}000$, $\eta_C = 0.8575$, inner rotating cylinder

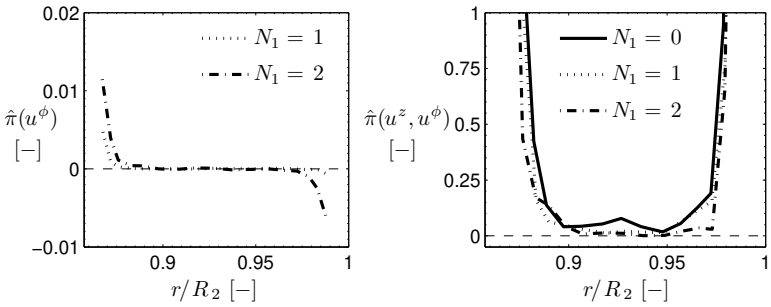

Fig. 3.13: Local TSC function determined from data by Rothe [109]; $Re = 10{,}000$, $\eta_C = 0.8575$, $\hat{\pi} = \pi D_h^2/(\overline{U^z}^2\mu)$, inner rotating cylinder

ity, Eq. (3.59), is characterised by positive values of the local TSC function in the centre of the gap and near to the inner rotating tube. There is also a small region with negative values of the local TSC function indicating destabilising effects near to the outer non-rotating tube. So, the general trend of the local TSC function for the data by Rothe qualitatively agrees with the trend of the local TSC function for the data by Pfitzer, see Fig. 3.9. Moreover, for both components of the velocity, i.e. the axial and tangential velocity, the local TSC function, Eq. (3.58), is characterised by positive values over the entire gap and reaches higher values near the walls that is caused mainly by the strong dissipation due to the axial velocity gradient in the wall region, which is visible in the right graph of Fig. 3.13.
Furthermore, the elementary stability analysis of the data by Pfitzer and by Rothe may also be interpreted as the influence of rotation on laminarisation of a turbulent axial flow. Nishibori et al. [96] related the laminarisation to the tube rotation and found out that the laminarisation is dominant near the rotating tube wall due to strong dissipative processes. This outcome confirms the elementary stability analysis of the tangential velocity, i.e. the dissipative processes are dominant near the rotating tube, or wall, see left graphs of Fig. 3.9, Fig. 3.11 and Fig 3.13.

CHAPTER 4

Experimental Methods

This chapter summarises the experimental methods that are mandatory to adjust and visualise the flow field. Control of the mass flow is obtained by a laminar flow element. The velocity field is measured via Particle Image Velocimetry. At the end of this chapter, the possible measurement uncertainties are mentioned and discussed.

4.1 Experimental Apparatus

The experiments to obtain the flow field, i.e. the axial and tangential velocity profiles, are carried out on the model swirl tube at the ITLR, as shown in a CAD plot in Fig. 4.1. The test rig consists of an open loop and is driven by a central vacuum pump, which is not shown in the figure. The laminar flow element (1) is the place, where the air enters and the mass flow rate is determined. The inlet plenum (2) is followed by the plenum (3), where the air is tranquillized and seeded with tracers for the Particle Image Velocimetry (PIV) measurement, and by the swirl generator (4) consisting of two tangential ducts, by which the air enters the swirl tube (5). The air

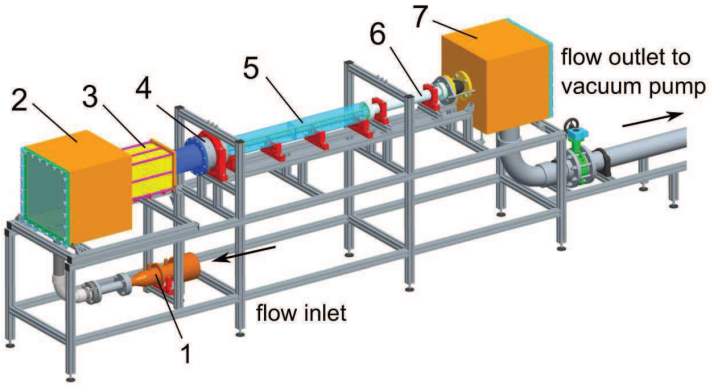

Fig. 4.1: Experimental apparatus (CAD) [16]; 1 - laminar flow element, 2 - inlet plenum, 3 - seeding chamber, 4 - swirl generator, 5 - swirl tube, 6 - outlet tube (changeable section), 7 - outlet plenum

leaves the swirl tube (5) through an outlet tube (6) into an outlet plenum (7), which is connected to the vacuum pump.

4.2 Mass Flow Measurement

In order to determine the mass flow rate, a laminar flow element LFE 50MC02-02-F by TetraTec Instruments located in the measuring section is used. This element includes a segment with some long thin tubes, in which the Reynolds number is small enough to suppose laminar flow. Thus, dependency of the mass flow rate on the pressure drop over the thin tubes is linear. Moreover, the temperature, humidity, and ambient pressure are also monitored to specify the viscosity that is necessary for determination of the mass flow rate and volume flow rate. The maximum uncertainty of the laminar flow element for the volume flow rate measurement was guaranteed as 1 % by the manufacturer.

4.3 Particle Image Velocimetry

Basic principles of the Particle Image Velocimetry (PIV), shown in Fig. 4.2, are discussed in a practical guide written by Raffel et al. [101] and also in works by Biegger [16] and Kobiela [66]. PIV is an optical technique used for flow measurement and visualisation to get instantaneous velocity fields. This technique uses light scattering particles, or so-called tracer particles, which are illuminated by a laser light sheet with two pulses in a short time interval Δt. The scattered light is recorded on a sequence of frames by a CCD camera.

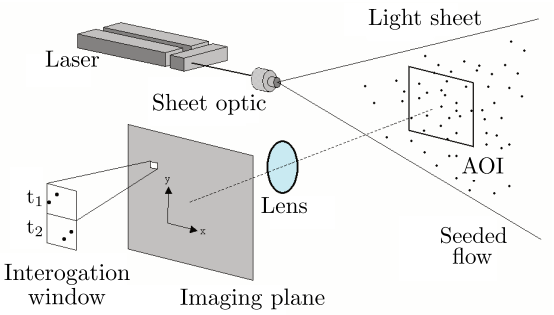

Fig. 4.2: Schematics of PIV principle [70]

The displacement of the particle images between the individual light pulses is given by evaluation of the PIV recordings. For evaluation, the PIV recordings are divided in small interrogation windows. For each window, the local displacement vector can be calculated from the shift of the particle between two frames in a sequence by using the cross-correlation method. Moreover, it is assumed a homogeneous movement of all particles between the two illuminations. So, the velocity vector projected into the plane of the light sheet, i.e. two component velocity vector, is given by the time period between two pulses, i.e. illumination, Δt and the magnification at imaging [101].
For the conducted measurements, a PIV system from LaVision with the software DaVis 6.2 is utilised. As light scattering particles, the oil diethylhexyl sebacate transformed to oil droplets via the Atomizer Aerosol Generator ATM 210 from Topas is used. The generated droplets comply the elemen-

tary demands given by Raffel et al. [101], i.e. to be large enough to ensure sufficient light scattering and on the other hand, to be small enough for a proper tracking. The laser light sheet was generated by a double pulse Nd:YAG laser with a wavelength of 532 nm. The laser frequency was kept at the fixed value of 8 Hz. As in the work by Kobiela [66], it is assumed 5 pixels as the optimal displacement of the oil droplets between framed images. Thus, the time interval between the frames is set to $\Delta t = 20 - 100$ μs respecting the investigated Reynolds number, i.e. mass flow rate or flow velocity, respectively. Moreover, to ensure a sufficient number of oil droplets in the laser light sheet, the thickness of the laser light sheet is kept at values of 2 to 3 mm. So, the values of the measured velocities result from the spatial averaging over the thickness of the laser light sheet. The used CCD camera is a Flowmaster 3S by LaVision (double frame rate 4 Hz, resolution 1280 x 1024).
The axial velocity is obtained via a configuration, where the laser light sheet intersected the glass tube in the tube axis. The CCD camera takes the double frames from the side of the glass tube. On the other hand, for the tangential velocity, the laser light sheet intersects the glass tube from the side at the desired position. The CCD camera took the double frames through a plexiglass wall in the outlet plenum. For each measured point 200 double frames are obtained.

4.4 Measurement Uncertainty

Measurement of the individual velocity component by using the PIV method causes uncertainties of instantaneous measured values, as summarised e.g. in [114, 115]. In the study of Sciacchitano and Wieneke [115], an uncertainty propagation related to the PIV method is discussed. The authors stated that the uncertainty of the instantaneous velocity components propagates into derived quantities of interests. So, quantification of the uncertainty of derived quantities depends on these considerations

- uncertainties of the velocity components propagate to uncertainties of the derived quantities;
- correlations of the velocity components, e.g. in time, in space or inter-component correlations, have an influence on uncertainties of the derived quantities;

- influence of the statistical quantities on statistical convergence due to additional uncertainty caused by the finite number of samples.

The following description of the measurement uncertainties respects these considerations and, moreover, refers to the work by Moffat [91], which takes into account the root-sum-square method and a confidence level of 95 %. Moffat [91] assumed that a measured value $\hat{y}$ is a general function of measured variables, i.e.

$$\hat{y} = f\left(x_1, x_2, ..., x_M\right). \tag{4.1}$$

A variation, δx_i, in quantity x_i would lead to a variation $\delta \hat{y}_i$ in a measured value $\hat{y}$. This fact is expressed as

$$\delta \hat{y}_i = \frac{\partial f}{\partial x_i} \delta x_i. \tag{4.2}$$

Then, the relative variation can be formulated by

$$\frac{\delta \hat{y}_i}{\hat{y}} = \frac{1}{\hat{y}} \frac{\partial f}{\partial x_i} \delta x_i = \frac{x_i}{\hat{y}} \frac{\partial f}{\partial x_i} \frac{\delta x_i}{x_i}. \tag{4.3}$$

The relative uncertainty relating to all variables is then obtained by

$$\frac{\delta \hat{y}}{\hat{y}} = \pm \sqrt{\sum_{i=1}^{M} \left(\frac{x_i}{\hat{y}} \frac{\partial f}{\partial x_i} \frac{\delta x_i}{x_i} \right)^2}. \tag{4.4}$$

The production variance of the tube diameter is $\pm$ 1.0 %. The mass flow rate measurement by the calibrated laminar flow element LFE 50MC02-02-F has an uncertainty $\pm$ 1.0 %, which is guaranteed by manufacturer. According to Eq. (4.4), these uncertainties result in an uncertainty on of the Reynolds numbers of $\pm$ 1.4 %. Moreover, according to the rules of the uncertainty propagation, mentioned by many authors in literature, e.g. [91, 114, 115], and by Eq. (4.4), the mean velocity corresponding to the Reynolds number has an uncertainty $\pm$ 2.2 %.
According to the confidence level of 95 %, the uncertainties of the measured mean axial velocity by PIV are determined as $\pm$ 8.0 $-$ 11.0 %, assuming that true values of the velocity are based on the mass flow rate. So, this uncertainty is determined via a formula taking into account the abso-

lute error of a measured value, or value of interest, from a true value using

$$\sigma = \sqrt{\frac{1}{M-1}\sum_{i=1}^{M}\left(\overline{u^z} - \overline{U^z}\right)^2}. \tag{4.5}$$

Here, M represents the number of samples, i.e. set of observations, $\overline{U^z}$ is taken as a true value of the axial mean velocity determined from the measured mass flow rate, and $\overline{u^z}$ is the mean axial velocity determined via the PIV method. Moreover, in order to ensure the chosen confidence level, it is convenient to report 2σ values. Moffat [91] also stated that for multiple sample analysis, this values have to be related to the deviation of the mean of the sample by

$$\hat{\epsilon} = \hat{t}\frac{\sigma}{\sqrt{M}}. \tag{4.6}$$

Here, $\hat{\epsilon}$ represents the uncertainty of the mean axial velocity obtained via PIV method and $\hat{t}$ is the Student's multiplier for M samples. For the data published in this work, the Student's multiplier is $\hat{t} = 2.086$, which is taken for a set of observations, i.e. measured positions, $M = 20$ [132]. The final uncertainty value is then determined as the calculated value of $\hat{\epsilon}$ relative to the true value of $\overline{U^z}$.
Typical values and measurement uncertainties for relevant parameters are summarised in Tab. 4.1.

Tab. 4.1: Values of experimental parameters and the measurement uncertainties

parameter	unit	typical value	measurement uncertainty
D	[m]	0.05	± 1.0 %
$\dot{m}$	[kg s^{-1}]	0.0007 – 0.0035	± 1.0 %
Re	[-]	1,000 – 5,000	± 1.4 %
$\overline{U^z}$	[m s^{-1}]	0.3 – 1.5	± 2.2 %
$\overline{u^z}$	[m s^{-1}]	0.3 – 1.5	± 8.0 – 11.0 %

CHAPTER 5

Numerical Methods

Recently, technical and scientific problems are more often investigated numerically via the solution of the related Partial Differential Equations (PDE) with computational methods. Usage of the PDE to a specific technical problem, i.e. structural or fluid mechanics, determines their numerical solution, i.e. Finite Element Method (FEM) or Finite Volume Method (FVM), respectively. In order to solve problems in fluid mechanics, turbulence and heat transfer, the Computational Fluid Dynamics (CFD) based on the FVM is usually employed. CFD may be used to study complex technical and scientific problems in order to assist the experimental research or to substitute the experimental research in cases, where experiments are too difficult or too expensive. At this time, CFD is commonly used in industrial and as well as scientific applications.
So, this chapter introduces the numerical methods used in this work. Firstly, the governing equations are briefly shown. The following section offers a description of the Reynold-Averaged Navier-Stokes (RANS) equations together with turbulence models available in the commercial code ANSYS CFX, which is for its acceptable accuracy, rate of converge, and computational cost commonly used in industry in order to solve complex fluid flow problems. At the

end of this chapter, the numerical methods in the commercial code ANSYS CFX including the setup of the numerical solution and possible numerical errors are described.

5.1 Governing Equations

This section deals with the transport equations used for numerical modeling in order to obtain flow structures of the swirl flow in the tube. The transport equations are derived for a control volume and describe the temporal change of mass and momentum in a Cartesian coordinate system, i.e. $i = (x,y,z)$ [17]. Thus, in the following subsections, the equations describing the balance of mass and balance of momentum for compressible and incompressible fluid in one of the usual form are shown [50]. Furthermore, the Navier-Stokes equations for an incompressible Newtonian flow are also introduced.

5.1.1 Balance of Mass

In general, the balance of mass of a compressible fluid, describing material derivative of the fluid density, can be expressed by

$$\frac{\partial \rho}{\partial t} + \frac{\partial (\rho u_i)}{\partial x_i} = 0, \tag{5.1}$$

which for the steady case changes into

$$\frac{\partial (\rho u_i)}{\partial x_i} = 0. \tag{5.2}$$

Assuming steady flow and an incompressible fluid, i.e. substantial change of the density is negligible, the balance of mass becomes

$$\frac{\partial u_i}{\partial x_i} = 0. \tag{5.3}$$

5.1.2 Balance of Momentum

The balance of momentum of an compressible Newtonian fluid can be written in the following form

$$\rho\left(\frac{\partial u_i}{\partial t}+u_j\frac{\partial u_i}{\partial x_j}\right)=\rho f_i-\frac{\partial p}{\partial x_i}+\frac{\partial}{\partial x_j}\left[\mu\left(\frac{\partial u_i}{\partial x_j}+\frac{\partial u_j}{\partial x_i}\right)\right] - \frac{\partial}{\partial x_i}\left[\frac{2}{3}\mu\left(\frac{\partial u_k}{\partial x_k}\right)\right]. \tag{5.4}$$

Assuming an incompressible Newtonian fluid, the balance of momentum becomes

$$\rho\left(\frac{\partial u_i}{\partial t}+u_j\frac{\partial u_i}{\partial x_j}\right)=\rho f_i-\frac{\partial p}{\partial x_i}+\mu\frac{\partial^2 u_i}{\partial x_j^2}. \tag{5.5}$$

In case of an incompressible turbulent flow of a Newtonian fluid, the continuity and the Navier-Stokes equations, i.e. the balance of mass, Eq. (5.3), and the balance of momentum, Eq. (5.5), need to be averaged in order to capture random fluctuations of fluid properties [131]. Averaging of the equations is usually performed by the Reynolds averaging taking into account instantaneous values of fluid properties consisting of a mean value and a fluctuating part, i.e. u_i+u_i', $p+p'$. After the averaging procedure, the following equations for the incompressible Newtonian fluid are obtained [131]

$$\frac{\partial u_i}{\partial x_i}=0, \tag{5.6}$$

$$\rho\left(\frac{\partial u_i}{\partial t}+u_j\frac{\partial u_i}{\partial x_j}\right)=\rho f_i-\frac{\partial p}{\partial x_i} + \frac{\partial}{\partial x_j}\left[\mu\left(\frac{\partial u_i}{\partial x_j}+\frac{\partial u_j}{\partial x_i}\right)-\rho\overline{u_i'u_j'}\right]. \tag{5.7}$$

Here, Eq. (5.7) is usually referred as Reynolds-Averaged Navier-Stokes equations (RANS) [131], where the term

$$\tau_{ij}=-\rho\overline{u_i'u_j'} \tag{5.8}$$

is the Reynolds stress tensor. The Reynolds stress tensor is symmetric and has six independent variables. Thus, the Reynolds averaging results in six new unknown quantities, which must be determined.

5.2 Turbulence Modeling

In order to properly model the velocity fields, a suitable turbulence model approximating the turbulent character of a flow is needed. In industry, the most often used turbulence models are two equation models, like e.g. the $k-\epsilon$ model. In this work, as a turbulence model in order to capture the complex flow structure, the Baseline Explicit Algebraic Reynolds Stress Model is used. This model represents an acceptable compromise between accuracy, rate of converge and computational costs. Nevertheless, Vogler [121] compared the RANS turbulence models, used by Kobiela [66], and a Detached Eddy Simulation (DES), used by Biegger [16], with experimental results and discussed the accuracy of the used models in predicting the complex flow structures of swirl flow. Thus, Vogler results may be interpreted as that the DES approach is more accurate. However, turbulence models still provide a very good compromise between accuracy and computational costs.
Moreover, in case of the low Reynolds number, application of the Gamma Transition Model (GTM), dealing with the modeling of transition to turbulence by solving an equation for the intermittency, is suitable, therefore this model is also presented.

5.2.1 Baseline Explicit Algebraic Reynolds Stress Model

This subsection focuses on the turbulence model, which is used in the entire work in order to obtain the Reynolds stresses. Thus, the turbulence stresses are approximated by the Baseline Explicit Algebraic Reynolds Stress Model (BSLEARSM), already available in ANSYS CFX.
Firstly, equations for the Baseline turbulence model (BSL) are shown. This turbulence model utilises two of the most common used two equations turbulence models, i.e. the $k-\epsilon$ turbulence model by Menter [89] and the $k-\omega$ turbulence model by Wilcox [131]. In the BSL turbulence model, the $k-\epsilon$ turbulence model and the $k-\omega$ turbulence model are both reformulated via a specific dissipation rate, i.e. ω-formulation, proposed by Menter in [89]. This formulation reflects the sensitivity of the Wilcox model to free-stream conditions, which Menter stated in his earlier work [88].
Thus, in the original $k-\omega$ model proposed by Wilcox [131], the transport

equation for the turbulent kinetic energy has the following form

$$\frac{\partial(\rho k)}{\partial t} + \frac{\partial(u_j \rho k)}{\partial x_j} = P_k - \beta' \rho k \omega + \frac{\partial}{\partial x_j}\left[\left(\mu + \frac{\mu_t}{\sigma_{k1}}\right)\frac{\partial \omega}{\partial x_j}\right], \tag{5.9}$$

whereas the transport equation for the turbulent frequency, i.e. the specific dissipation rate, is given by

$$\frac{\partial(\rho \omega)}{\partial t} + \frac{\partial(u_j \rho \omega)}{\partial x_j} = \alpha_1 \frac{\omega}{k} P_k - \beta_1 \rho \omega^2 + \frac{\partial}{\partial x_j}\left[\left(\mu + \frac{\mu_t}{\sigma_{\omega 1}}\right)\frac{\partial \omega}{\partial x_j}\right]. \tag{5.10}$$

In addition, in the transformed $k-\epsilon$ turbulence model proposed by Menter [89], the transport equation of the turbulent kinetic energy remains the same, but the constant σ_k is adapted. Thus, the equation may be written as

$$\frac{\partial(\rho k)}{\partial t} + \frac{\partial(u_j \rho k)}{\partial x_j} = P_k - \beta' \rho k \omega + \frac{\partial}{\partial x_j}\left[\left(\mu + \frac{\mu_t}{\sigma_{k2}}\right)\frac{\partial \omega}{\partial x_j}\right], \tag{5.11}$$

whereas the transport equation for the turbulent frequency is formulated by

$$\begin{aligned}\frac{\partial(\rho \omega)}{\partial t} + \frac{\partial(u_j \rho \omega)}{\partial x_j} = {} & \alpha_2 \frac{\omega}{k} P_k - \beta_2 \rho \omega^2 + \frac{2\rho}{\sigma_{\omega 2}\omega}\frac{\partial k}{\partial x_j}\frac{\partial \omega}{\partial x_j} \\ & + \frac{\partial}{\partial x_j}\left[\left(\mu + \frac{\mu_t}{\sigma_{\omega 2}}\right)\frac{\partial \omega}{\partial x_j}\right].\end{aligned} \tag{5.12}$$

Finally, the BSL turbulence model, i.e. the transport equations for the turbulent kinetic energy and specific dissipation rate, is introduced by

$$\frac{\partial(\rho k)}{\partial t} + \frac{\partial(u_j \rho k)}{\partial x_j} = P_k - \beta' \rho k \omega + \frac{\partial}{\partial x_j}\left[\left(\mu + \frac{\mu_t}{\sigma_{kBSL}}\right)\frac{\partial \omega}{\partial x_j}\right], \tag{5.13}$$

$$\begin{aligned}\frac{\partial(\rho \omega)}{\partial t} + \frac{\partial(u_j \rho \omega)}{\partial x_j} = {} & \alpha_{BSL} \frac{\omega}{k} P_k - \beta_{BSL} \rho \omega^2 \\ & + \frac{\partial}{\partial x_j}\left[\left(\mu + \frac{\mu_t}{\sigma_{\omega BSL}}\right)\frac{\partial \omega}{\partial x_j}\right] \\ & + (1 - F_1)\frac{2\rho}{\sigma_{\omega 2}\omega}\frac{\partial k}{\partial x_j}\frac{\partial \omega}{\partial x_j}.\end{aligned} \tag{5.14}$$

The coefficients used in the BSL turbulence model (c_{BSL}) are a linear com-

bination of the corresponding coefficients of the original models, i.e. the Wilcox model (c_1) and the transformed $k-\epsilon$ model (c_2), and are given by

$$c_{BSL} = F_1 c_1 + (1 - F_1)\, c_2. \tag{5.15}$$

Here, the coefficients of the Wilcox model are as follows

$$\beta' = 0.09,\ \alpha_1 = \frac{5}{9},\ \beta_1 = 0.075,\ \sigma_{k1} = 2,\ \sigma_{\omega 1} = 2, \tag{5.16}$$

whereas the coefficients of the transformed $k-\epsilon$ model have the following values

$$\beta' = 0.09,\ \alpha_2 = 0.44,\ \beta_2 = 0.0828,\ \sigma_{k2} = 1,\ \sigma_{\omega 2} = \frac{1}{0.856}. \tag{5.17}$$

So, both models utilise the same coefficient β'. Finally, the weighting function F_1 in Eq. (5.15) is given by

$$F_1 = \tanh\left(\arg^4\right) \tag{5.18}$$

for

$$\arg = \min\left[\max\left(\frac{\sqrt{k}}{\beta'\omega y^2}, \frac{500\nu}{y^2\omega}\right), \frac{4\rho k}{CD_{k\omega}\sigma_{\omega 2} y^2}\right], \tag{5.19}$$

where y and ν represent a distance to the nearest wall and the kinematic viscosity, respectively. The parameter $CD_{k\omega}$ is given as

$$CD_{k\omega} = \max\left(\frac{2\rho}{\sigma_{\omega 2}\omega}\frac{\partial k}{\partial x_j}\frac{\partial \omega}{\partial x_j}, 1 \cdot 10^{-10}\right). \tag{5.20}$$

Moreover, the following limiting condition of the turbulence production term assures that the turbulent kinetic energy reaches only physical values

$$P_k = \min\left(P_k, C_{lim}\rho\epsilon\right), \tag{5.21}$$

where $C_{lim} = 10$ for ω-based models.
In order to capture flows with streamline curvature, system rotation, or secondary flows, the above described turbulence model is extended by the Explicit Algebraic Reynolds Stress Model (EARSM) to formulate the Baseline Explicit Algebraic Reynolds Stress Model (BSLEARSM). For this case, i.e. coupling of the BSL and EARSM models, Hellsten in [47] proposed the recalibrated coefficients of the BSL model and the mixing function F_1. So, the

new coefficients of the Wilcox model used in the BSL model are as follows

$$\beta' = 0.09,\ \alpha_1 = 0.518,\ \beta_1 = 0.0747,\ \sigma_{k1} = \frac{1}{1.1},\ \sigma_{\omega 1} = \frac{1}{0.53}, \tag{5.22}$$

whereas the new coefficients of the transformed $k-\epsilon$ model used in the BSL model are recalibrated only slightly

$$\beta' = 0.09,\ \alpha_2 = 0.4404,\ \beta_2 = 0.0828,\ \sigma_{k2} = 1,\ \sigma_{\omega 2} = \frac{1}{0.856}. \tag{5.23}$$

Thus, these coefficients have been used for the BSL model coupled with the EARSM model in ANSYS CFX [6]. The BSLEARSM turbulence model provides a nonlinear relation between the Reynolds stresses, the mean strain rate and the rotation rate tensors. A lot of flow phenomena are included in this model with no need to solve transport equations, because of higher order terms in the Reynolds stresses.
The implementation used in ANSYS CFX is based on the EARSM model of Wallin and Johansson [122]. Nevertheless, the implementation respects the formulation given by Hellsten [47]. Hence, the Reynolds stresses are modeled by the anisotropy tensor as

$$\tau_{ij} = -\rho\overline{u_i' u_j'} = -\rho k \left(a_{ij} + \frac{2}{3}\delta_{ij} \right), \tag{5.24}$$

where the anisotropy tensor a_{ij} is expressed by the following relation

$$\begin{aligned} a_{ij} = {} & \beta_1 S_{ij}^* + \beta_3 \left(\Omega_{ik}^* \Omega_{kj}^* - \frac{1}{3} II_{\Omega^*} \delta_{ij} \right) + \beta_4 \left(S_{ik}^* \Omega_{kj}^* - \Omega_{ik}^* S_{kj}^* \right) \\ & + \beta_6 \left(S_{ik}^* \Omega_{kl}^* \Omega_{lj}^* + \Omega_{ik}^* \Omega_{kl}^* S_{lj}^* - \frac{2}{3} IV \delta_{ij} \right) \\ & + \beta_9 \left(\Omega_{ik}^* S_{kl}^* \Omega_{lm}^* \Omega_{mj}^* - \Omega_{ik}^* \Omega_{kl}^* S_{lm}^* \Omega_{mj}^* \right). \end{aligned} \tag{5.25}$$

In the anisotropy tensor, S_{ij}^* and Ω_{ij}^* represent the dimensionless strain rate and rotation rate tensors and are given by

$$S_{ij}^* = \frac{1}{2}\tau \left(\frac{\partial u_i}{\partial x_j} + \frac{\partial u_j}{\partial x_i} \right), \tag{5.26}$$

$$\Omega_{ij}^* = \frac{1}{2}\tau \left(\frac{\partial u_i}{\partial x_j} - \frac{\partial u_j}{\partial x_i} \right). \tag{5.27}$$

Here, τ represents a time scale that is given by

$$\tau = \max\left(\frac{1}{\beta^*\omega}, C_\tau\sqrt{\frac{\nu}{\beta^* k\omega}}\right), \text{ where } C_\tau = 6.0 \text{ and } \beta^* = 0.09. \quad (5.28)$$

Moreover, the β - coefficients and the parameter Q are defined by

$$\beta_1 = -\frac{N\left(2N^2 - 7II_\Omega\right)}{Q},\ \beta_3 = -\frac{12IV}{NQ},\ \beta_4 = -\frac{N\left(2N^2 - 2II_\Omega\right)}{Q},$$
$$\beta_6 = -\frac{6N}{Q},\ \beta_9 = \frac{6}{Q},\ Q = \frac{5}{6}\left(N^2 - 2II_\Omega\right)\left(2N^2 - II_\Omega\right). \quad (5.29)$$

The other terms and coefficients appearing in the anisotropy tensor are defined as

$$II_S = S^*_{kl}S^*_{lk},\ II_{\Omega^*} = \Omega^*_{kl}\Omega^*_{lk},\ IV = S^*_{kl}\Omega^*_{lm}\Omega^*_{mk}. \quad (5.30)$$

In a 3D case, an equation solving the function N is of the sixth order, so there is no explicit solution. On the other hand, in 2D case, the function N can be solved from a cubic equation and has the following solutions

$$N = \begin{cases} \frac{A'_3}{3} + \left(P_1 + \sqrt{P_2}\right)^{1/3} \\ \qquad + \operatorname{sign}\left(P_1 - \sqrt{P_2}\right)\left|P_1 - \sqrt{P_2}\right|^{1/3} \text{ for } P_2 \geq 0, \\ \frac{A'_3}{3} + 2\left(P_1^2 - P_2\right)^{1/6} \\ \qquad \times \cos\left[\frac{1}{3}\arccos\left(\frac{P_1}{\sqrt{P_1^2 - P_2}}\right)\right] \text{ for } P_2 < 0. \end{cases} \quad (5.31)$$

Here, the parameters are given as follows

$$P_1 = \left(\frac{A'^2_3}{27} + \frac{9}{20}II_S - \frac{2}{3}II_\Omega\right)A'_3, \quad (5.32)$$

$$P_2 = P_1^2 - \left(\frac{A'^2_3}{9} + \frac{9}{10}II_S + \frac{2}{3}II_\Omega\right)^3, \quad (5.33)$$

$$A'_3 = \frac{9}{5} + \frac{9}{4}C_{Diff}\max\left(1 + \beta_1^{(eq)}II_S, 0\right), \quad (5.34)$$

$$\beta_1^{(eq)} = -\frac{6}{5}\frac{N^{(eq)}}{\left(N^{(eq)}\right)^2 - 2II_\Omega},\ N^{(eq)} = \frac{81}{20},\ C_{Diff} = 2.2, \quad (5.35)$$

where A_3' represents the term, which models the ignored diffusion of the anisotropy [47]. Furthermore, Hellsten [47] modeled the eddy viscosity in the original model by

$$\nu_t = C_\mu k\tau,\; C_\mu = -\frac{1}{2}\left(\beta_1 + II_\Omega \beta_6\right). \tag{5.36}$$

In addition, Hellsten also proposed that the parameter N for the 2D case may be used also in the 3D case, which is utilised for the implementation in ANSYS CFX [6, 47]. Nevertheless, due to problems with the simulation stability in ANSYS CFX, the turbulent viscosity in the model is computed by the standard formulation, i.e. $\nu_t = k/\omega$, where $\nu_t = \mu_t/\rho$ [6].
In order to include the influence of streamline curvature effects, the dimensionless rotation rate tensor, Eq. (5.27), is extended to capture curvature effects according to the work by Hellsten [47], Spalart and Shur [116] and Wallin and Johansson [123]. Thus, the BSLEARSM turbulence model is modified by the following expression

$$\Omega_{ij}^* = \frac{1}{2}\tau\left(\frac{\partial u_i}{\partial x_j} - \frac{\partial u_j}{\partial x_i}\right) - C_{scale}\frac{\tau}{A_0}\left(-\epsilon_{ijk}\frac{S_{pl}^* S_{lq}' \epsilon_{pqk}}{2II_S}\right), \tag{5.37}$$

where

$$S_{ij}' = \frac{\mathrm{D}S_{ij}^*}{\mathrm{D}t} + \left(\epsilon_{imn}S_{jn}^* + \epsilon_{jmn}S_{in}^*\right)\Omega_m^{rot}. \tag{5.38}$$

Here, ϵ_{ijk} is the Levi-Civita symbol that can reach the value 0 if two or more indices in $\{ijk\}$ are equal, value 1 if the indices $\{ijk\}$ form an even permutation, and value -1 if the indices $\{ijk\}$ form an odd permutation. Moreover, the coefficient A_0 is -0.4 and Ω_m^{rot} represents components of the rotation vector of the coordinate system [6]. Finally, the coefficient C_{scale} is a free parameter to change and has a default value 1.0 [6].
In order to avoid numerical noise produced by the second velocity derivatives, i.e. given by the term $\mathrm{D}S_{ij}^*/\mathrm{D}t$, two sets of Reynolds stresses with the EARSM turbulence model are computed [6]. Firstly, the Reynolds stresses without curvature correction are used to solve the momentum equations. Secondly, the Reynolds stresses with curvature correction are used to solve the equations for k and ω. Thus, the influence of curvature on the turbulence production is captured, but this influence is not directly affecting the momentum equations. This fact may cause some loss in accuracy.

5.2.2 Gamma Transition Model

The Gamma Transition Model (GTM) deals with the modeling of the transition from laminar to turbulent flow by solving the equation for the intermittency γ. This model includes an empirical correlation, which covers a standard bypass transition and flows in low free-stream turbulence [69, 90]. This transition model can be used together with the BSL turbulence models and is utilised in this work for modeling the flow structures of the swirl flow in case of the lowest Reynolds number.
The transport equation for the intermittency, based on the work by Langtry and Menter [69] and Menter et al. [90], is already available in ANSYS CFX [6] and has the following form

$$\frac{\partial \rho\gamma}{\partial t} + \frac{\partial (\rho u_j \gamma)}{\partial x_j} = P_{\gamma 1} - E_{\gamma 1} + P_{\gamma 2} - E_{\gamma 2} + \frac{\partial}{\partial x_j}\left[\frac{\partial \gamma}{\partial x_j}\left(\mu + \frac{\mu_t}{\sigma_\gamma}\right)\right]. \quad (5.39)$$

The sources of the transition are defined by

$$P_{\gamma 1} = 2F_{length}\rho S\left(\gamma F_{onset}\right)^{c_{\gamma 3}}, \quad E_{\gamma 1} = P_{\gamma 1}\gamma, \quad (5.40)$$

where S is the magnitude of the strain rate tensor S_{ij}, so that

$$S = \sqrt{2S_{ij}S_{ij}}, \; S_{ij} = \frac{1}{2}\left(\frac{\partial u_i}{\partial x_j} + \frac{\partial u_j}{\partial x_i}\right). \quad (5.41)$$

The length of the transition region is controlled by an empirical correlation F_{length}. Moreover, the source of destruction, i.e. relaminarisation, is governed by the following source terms

$$P_{\gamma 2} = 2c_{\gamma 1}\rho\Omega\gamma F_{turb}, \quad E_{\gamma 2} = c_{\gamma 2}P_{\gamma 2}\gamma, \quad (5.42)$$

where analogically Ω is the magnitude of the rotation rate tensor Ω_{ij}, so that

$$\Omega = \sqrt{2\Omega_{ij}\Omega_{ij}}, \quad \Omega_{ij} = \frac{1}{2}\left(\frac{\partial u_i}{\partial x_j} - \frac{\partial u_j}{\partial x_i}\right). \quad (5.43)$$

The onset of the transition is then controlled by the onset functions as follows

$$F_{onset\ 1} = \frac{Re_\nu}{2.193 Re_{\theta c}}, \quad (5.44)$$

$$F_{onset\ 2} = \min\left[\max\left(F_{onset\ 1}, F^4_{onset\ 1}\right), 2.0\right], \quad (5.45)$$

$$F_{onset\ 3} = \max\left[1 - \left(\frac{R_T}{2.5}\right)^3, 0\right], \tag{5.46}$$

$$F_{onset} = \max\left(F_{onset\ 2} - F_{onset\ 3}, 0\right), \tag{5.47}$$

$$F_{turb} = \exp\left[-\left(\frac{R_T}{4}\right)^4\right], \tag{5.48}$$

$$Re_\nu = \frac{\rho y^2 S}{\mu}, \quad R_T = \frac{k\rho}{\omega\mu}. \tag{5.49}$$

Here, $Re_{\theta c}$ is the critical Reynolds number characterising the Reynolds number, where the intermittency increases in the boundary layer. This occurs upstream of the transition Reynolds number $Re_{\theta t}$. The difference between both Reynolds numbers must be gained from an empirical correlation [69, 90]. Moreover, both correlations, i.e. F_{length} and $Re_{\theta c}$, depend on $\tilde{Re}_{\theta t}$, thus

$$F_{length} = f\left(\tilde{Re}_{\theta t}\right), \quad Re_{\theta c} = f\left(\tilde{Re}_{\theta t}\right). \tag{5.50}$$

Furthermore, the coefficients used in Eq. (5.39) are

$$c_{\gamma 1} = 0.03, \quad c_{\gamma 2} = 50, \quad c_{\gamma 3} = 0.5, \quad \sigma_\gamma = 1.0. \tag{5.51}$$

For the sake of completeness, also a modification for separation-induced transition should be mentioned. The leading edge of thin airfoils and gas turbine blades are examples, where this transition might occur and might have a negative impact on the flow [55, 68]. Thus, this modification is described by

$$\gamma_{sep} = \min\left\{2\max\left[\left(\frac{Re_\nu}{3.235 Re_{\theta c}}\right) - 1, 0\right] F_{reattach}, 2\right\} F_{\theta t}, \tag{5.52}$$

$$F_{reattach} = \exp\left[-\left(\frac{R_T}{20}\right)^4\right], \tag{5.53}$$

$$\gamma_{eff} = \max\left(\gamma, \gamma_{sep}\right). \tag{5.54}$$

The main difference caused by this modification is a constant controlling the relation between Re_ν and $Re_{\theta c}$, i.e. in Eq. (5.44). The constant is changed

from 2.193 to 3.235. Moreover, the boundary condition for γ is zero normal flux at the wall, but the boundary condition for an inlet γ is equal to 1 [69]. In addition, the yet unknown parameter $F_{\theta t}$ in Eq. (5.52) is a blending function defined as follows

$$F_{\theta t} = \min \left\{ \max \left[F_{wake} \exp \left(- \left(\frac{y}{\delta} \right)^4 \right), 1 - \left(\frac{\gamma - \frac{1}{c_{e2}}}{1 - \frac{1}{c_{e2}}} \right)^2 \right], 1 \right\}, \quad (5.55)$$

for $c_{e2} = 50$. The other parameters in Eq. (5.55) are

$$\delta = \frac{50 \Omega y}{U} \delta_{BL}, \; \delta_{BL} = \frac{15}{2} \theta_{BL}, \theta_{BL} = \frac{\tilde{R} e_{\theta t} \mu}{\rho U}, \quad (5.56)$$

$$F_{wake} = \exp \left[- \left(\frac{Re_\omega}{1 \cdot 10^5} \right)^2 \right], \; Re_\omega = \frac{\rho \omega y^2}{\mu}, \quad (5.57)$$

where U is the magnitude of the velocity, i.e. $U = \sqrt{u_x^2 + u_y^2 + u_z^2} = \sqrt{u^2 + v^2 + w^2}$ in the Cartesian coordinate system.

5.3 Numerical Setup

Here, the numerical solution methods used in the commercial code ANSYS CFX, which is commonly used in industrial CFD simulations, are presented. Time and spatial discretisations are introduced. Also, the possible discretisation and numerical errors are discussed.

5.3.1 Numerical Solution

Numerical solution of the PDEs describing flow problems is done via an approximation of the PDEs by a system of algebraic equations. Fluid dynamics generally uses the finite volume method (FVM) as a discretisation method utilising the integral form of the governing equations [17]. Then, a computational domain will be subdivided into a finite number of small control volumes (CV), over which the governing equations are integrated. The computational node is in the CV centre, so variables at the node surface are interpolated between values in the CV centres. This results in an algebraic equation for the each CV. Hence, solution of all discrete points forms the

overall solution. Moreover, FVM ensures, by its construction, the conservation of mass and momentum in each CV as well as in the entire computation domain.
The geometrical domain is discretely represented by the numerical grid where variables are computed. Accuracy of the FVM is strongly affected by the mesh resolution [17]. Thus, the mesh should sufficiently resolve the geometric domain in order to avoid discretisation errors. The grid quality may be determined in terms of aspect ratio, determinant, and skewness that are implemented in ANSYS ICEM CFD [7]. The aspect ratio is defined by the size of the minimum element edge divided by the size of the maximum element edge, where the obtained values are scaled indicating value 0 for an element with zero volume and a value 1 for the perfectly regular element. The determinant or more precisely the relative determinant is the ratio of the smallest determinant of the Jacobian matrix divided by the largest determinant of the Jacobian matrix characterising a perfectly regular element by a value of 1 and strongly degenerate elements by a value of 0. Construction of the Jacobian matrix of the element, or cell, is described in Bathe's monograph [10]. The skewness is computed as the normalised maximum deviation from an ideal angle at the face corners for surface elements, or the normalised maximum deviation from an ideal angle between the face normals for volume elements, defining the regular element by a value of 0 and degenerate element by a value of 1.
For transient numerical simulations of the investigated problem, ANSYS CFX Release 12.1 is utilised. ANSYS CFX uses a coupled solver that solves the equations for velocity and pressure, i.e. the hydrodynamic equations, as a single system. In this approach, a fully implicit discretisation of the equations at any time step is used. In the steady state case, a time step serves as acceleration parameter in order to approach a steady state solution. Due to this, the number of iterations for a convergence to steady state is reduced, and in case of a time dependent problem, a solution for each time step is calculated. Generally, the solution itself consists of two operations [6]. Firstly, the non-linear equations are linearised and assembled into a solution matrix. Secondly, the obtained linear equations are solved via an algebraic multigrid method. The solution method used in ANSYS CFX is a multigrid accelerated Incomplete Lower Upper (ILU) factorisation, which is an iterative solver enabling to obtain an exact solution of the equations during several iterations [17]. However, the performance of the ILU decreases with increasing number of computational elements and also with the occurrence of elements with a high aspect ratio. Nevertheless, multigrid methods are a powerful acceleration technique enabling a solution of the linearised

equations on a series of virtual coarser meshes [17]. An algebraic multigrid applies a virtual coarse mesh and sums equations of the fine mesh to form the equations of the applied virtual coarse mesh. A reduced system representing a coarse level is then solved in order to obtain a correction to approach an accurate solution at the fine level [6, 17].
In ANSYS CFX, the chosen time discretisation is expressed by a second order backward Euler scheme using three time levels of variable φ, thus

$$\frac{\partial(\rho\varphi)}{\partial t} \approx \frac{(\rho\varphi)^{n+1/2} - (\rho\varphi)^{n-1/2}}{\Delta t}, \tag{5.58}$$

where

$$\begin{aligned}(\rho\varphi)^{n-1/2} &= (\rho\varphi)^{t} + \frac{1}{2}\left[(\rho\varphi)^{t} - (\rho\varphi)^{t-\Delta t}\right], \\ (\rho\varphi)^{n+1/2} &= (\rho\varphi)^{t+\Delta t} + \frac{1}{2}\left[(\rho\varphi)^{t+\Delta t} - (\rho\varphi)^{t}\right].\end{aligned} \tag{5.59}$$

After substitution of these values into Eq. (5.58) the resulting discretisation is obtained

$$\frac{\partial(\rho\varphi)}{\partial t} \approx \frac{1}{\Delta t}\left[\frac{3}{2}(\rho\varphi)^{t+\Delta t} - 2(\rho\varphi)^{t} + \frac{1}{2}(\rho\varphi)^{t-\Delta t}\right]. \tag{5.60}$$

This scheme represents a robust, implicit and time conservative discretisation. Furthermore, the stability of convection dominated problems is ensured by the Courant-Friedrichs-Lewy (CFL) number meaning that the time step Δt should be equal or smaller than the time, which is required to transport information by velocity u across the spatial discretisation Δx, e.g. grid cell [17]. Thus, the CFL number is expressed as

$$\mathrm{CFL} = \frac{u\Delta t}{\Delta x} < 1. \tag{5.61}$$

Convective and viscous fluxes are approximated with high accuracy meaning that the software uses the second order upwind differencing scheme with a blending function to the first order upwind differencing scheme, if it is necessary for the flux in order to converge. So, the scheme implemented in ANSYS CFX handles integration point values in terms of nodal values and can be written as follows

$$\varphi_{ip} = \varphi_{up} + \beta\nabla\varphi \cdot \Delta\mathbf{r}, \tag{5.62}$$

where the used variables are values at the integration point φ_{ip} located at the centre of each segment surface within an element, a value at the upwind node φ_{up}, and a vector from the upwind node to the integration point $\mathbf{r}$, respectively. The high resolution schemes follow the work by Barth and Jespersen [8]. Thus, the scheme utilises a nonlinear prescription for a blend parameter β at each node that is computed to be close to the value of 1. The flux is then determined by the values of β and $\nabla\varphi$ from the upwind node. Barth and Jespersen [8] proposed a methodology based on the first computing φ_{min} and φ_{max} at each node using a pattern involving all adjacent nodes including the node itself. Then, Eq. (5.62) is solved at each integration point for β in order to be sure that values φ_{min} and φ_{max} are not undershot and overshot, respectively. The nodal value of β is taken as a minimum value of values for all integration points surrounding the node and has to be, furthermore, less than 1 [6].

5.3.2 Numerical Errors

Numerical techniques of discretised equations compute, in general, only an approximate solution that may differ from an exact solution. Thus, numerical technique introduces errors into the solution [32]. A nice summary of numerical errors can also be found in the work by Biegger [16], which can be rewritten as follows.
Numerical errors can be caused by the used physical/mathematical model, represented by the governing/transport equations, and its exact solution describing the real flow problem. These errors can be introduced by the simplified geometrical domain representing the real flow problem, used boundary conditions, and also by the choice of the turbulence model. In order to determine them, comparison of the obtained solution with an exact solution, and/or with accurate experimental data, and/or with results of a more accurate model should be carried out. In this work, the conducted numerical simulations of the swirl tube are compared with own experimental results.
The other errors can be introduced by a discretisation of the used model meaning a difference between a solution of the algebraic system of discretised equations and an exact solution of the conservation/governing equations. These error can be reduced by mesh refinement and/or by the time step refinement. Furthermore, the accuracy is a function of the order of the discretisation method. In this work, the swirl tube simulations are performed on the mesh that followed the results made by Kobiela in [66]. The obtained results are compared with experiments in order to conclude that the mesh is

fine enough to capture the velocity field with sufficient accuracy. Moreover, the chosen discretisation schemes are second order accurate in time and space ensuring a good accuracy.
The next error can be represented by the difference between an exact solution of the algebraic system of discretised solution and its exact solution. This error is controlled by the measure of convergence. This measure determines the local imbalance of a conserved variable in the each CV, thus, each CV will have a residual value for each solved equation [6]. Generally, the lower residual value means a more numerically accurate solution.
The numerical details related to the simulations carried out in this work are introduced and summarised in Section 6.2.

CHAPTER 6

Results

This chapter shows the obtained results of the investigated flow in the swirl tube with two tangential inlet jets at the upstream end of the tube. Thus, the investigated flow is characterised by the following parameters, i.e. by the investigated Reynolds numbers covering laminar, intermediate and turbulent flow regimes, i.e. Re = 1,000, Re = 2,000, and Re = 5,000, and by the constant geometrical swirl number $S_{IG} = 5.3$.
Firstly, a detailed description of the experimental and numerical setup are provided. Secondly, results of the flow field are discussed. Thirdly, analysis of flow in terms of the swirl number and vortex breakdown are introduced. Finally, the application of the local and global TSC function on the flow field is shown and discussed.
In the entire work, the numerically obtained velocity profiles are extended by the profile near the tangential inlet jets, position z/D = -1 in the figures, where the measurement is impossible. These profiles are presented for a better understanding of the redistribution of the velocity field from the tube inlets to the tube outlet.

6.1 Experimental Details

The coordinate system and schematics of the geometry is shown in Fig. 6.1. The swirl tube is on the side of the inlets closed. Thus, the fluid enters the tube by two tangential rectangular inlets. The inner diameter of the tube is $D = 50$ mm, the dimensionless length of the tube is $L/D = 20$. The tangential inlets have a dimensionless width $w/D = 0.67$ and a dimensionless height $h/D = 0.1$. So, the geometrical swirl number is $S_{IG} = 5.3$. The axial velocity profiles are measured in the tube axis over the entire length. On the other hand, the tangential velocity profiles are measured at the positions $z/D = 0 - 19$, which are $1D$ apart from each other.

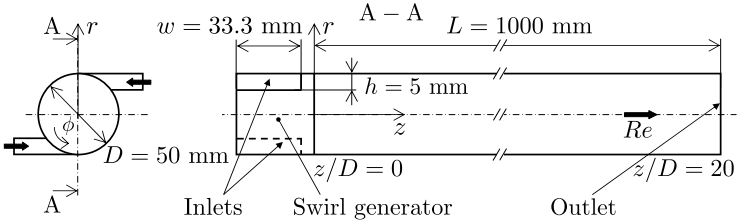

Fig. 6.1: Schematics of the swirl tube geometry

The range of the examined Reynolds numbers with the corresponding axial bulk velocities are shown in Tab. 6.1. Moreover, the angular velocity taken from the experimentally obtained tangential velocity profile near the tangential inlets, where the tangential velocity profile corresponds to a solid body rotation, is also given in Tab. 6.1. The axial bulk velocity and angular velocity will be used as parameters to plot the results in dimensionless form.

Tab. 6.1: Examined Reynolds numbers and corresponding axial bulk velocity, mass flow rate and angular velocity of solid body rotation

Re [-]	$\overline{U^z}$ [m s^{-1}]	$\dot{m}$ [kg s^{-1}]	Ω [s^{-1}]
1,000	0.3	0.0007	100
2,000	0.6	0.0014	200
5,000	1.5	0.0035	500

6.2 Numerical Details

The domain for the numerical simulations approximates close as possible the swirl tube depicted in Fig. 6.1. The tube diameter and dimensionless length are $D = 50$ mm and $L/D = 20$. The swirl generator consists of two inlet sections with the height of $h/D = 0.1$ and the width of $w/D = 0.67$. In order to correctly model the swirl generator, the total width of the swirl generator is enlarged by $0.8D$. So, the total length of the domain is $21.47D$.
The performed simulations correspond to the conducted measurements. So that, three cases, characterised by the constant geometrical swirl number $S_{IG} = 5.3$ and three Reynolds numbers $Re = 1{,}000$, $2{,}000$, and $5{,}000$, are simulated. The wall boundary condition is set to a no-slip condition. Other details of these simulations respecting the different Reynolds numbers are listed in Tab. 6.2.

Tab. 6.2: Numerically simulated Reynolds numbers, inlet velocities and outlet boundary condition for $S_{IG} = 5.3$

Re [-]	U_{inlet} [m s^{-1}]	$\dot{m}$ [kg s^{-1}]
1,000	1.74	0.0007
2,000	3.48	0.0014
5,000	8.69	0.0035

The swirl tube geometry is meshed for the three Reynolds numbers, respecting the mesh description by Kobiela [66], via hexahedral O-grids with a total mesh size of 1.1 million cells. The mesh of the swirl tube is schematically shown in Fig. 6.2, where a cross-section of the swirl tube mesh with a detail view of the wall resolution is seen. The wall mesh is chosen in order to provide a dimensionless wall distance of $y_1^+ \leq 1$ for the first cell near the wall. The time step is adjusted in order to comply a limit of the Courant-Friedrichs-Lewy (CFL) number of CFL ≤ 1, which may ensure stability of the solution. CFL number is a function of the local flow velocity u, the iteration time step Δt and a grid size Δx, and is given by Eq. (5.61). The numerical simulations are run for $3\Delta t_{domain}$ in order to ensure that the entire domain has been calculated and that the simulations have already converged. Here, the time domain is $\Delta t_{domain} = L/\overline{U^z}$.
The numerical simulations are conducted for a turbulent flow, i.e. the Baseline Explicit Algebraic Reynolds Stress Model (BSLEARSM) is employed.

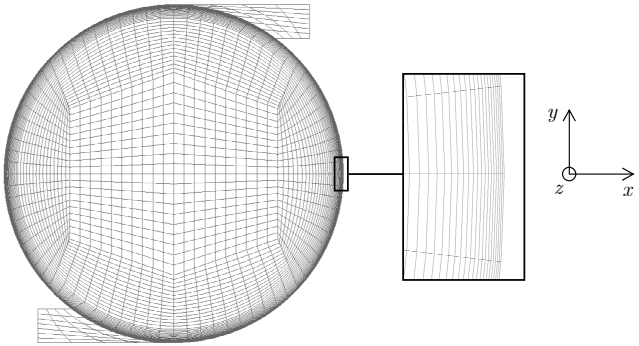

Fig. 6.2: Hexahedral mesh of the tube with a detail view of the wall resolution

In case of the lowest Reynolds number Re = 1,000, the Gamma Transition Model (GTM) is used in order to model the transition to turbulence with a default value of the transition Reynolds number $\tilde{Re}_{\theta t}$ = 260, Eq. (5.56), and with the low turbulence intensity, i.e. a value of 1 %, and eddy viscosity ratio, i.e. a value of 1. The usage of the GTM in case of the Reynolds number Re = 2,000 was also tested, but no positive feedback was observed, so the GTM model is not utilised in this case. Hence, in cases of the Reynolds numbers Re = 2,000 and Re = 5,000, the turbulence is set to a medium turbulence intensity and eddy viscosity ratio, i.e. values of 5 % and 10, and to a high turbulence intensity and eddy viscosity ratio, i.e. values of 10 % and 100, respectively.

6.3 Approximation of the Results

The velocity field given by the measurements and the numerical simulations are analysed with respect to the thermodynamic stability condition, i.e. the local and global TSC function, swirl number, and vortex breakdown. According to this analysis, smooth functions evenly distributed along the radial coordinate are desired. Thus, the obtained flow field is approximated, i.e fitted, in order to get smooth curves. A suitable model, which is able to be used for the swirl flow in the tube, is developed for an axisymmetrical helical vortex

[2, 3]. In this work, the published model is modified in order to capture the wall region of the swirl tube, so that the final form of the model used for the data interpretation is

$$u^{\phi} = \frac{\Gamma}{2\pi r}\left[1 - \exp\left(-\frac{r^2}{r_c^2}\right)\right]\left\{1 - \frac{1}{\exp\left[k\,(R-r)\right]}\right\}, \tag{6.1}$$

$$u^{z} = u^{0} - \frac{\Gamma}{2\pi l}\left[1 - \exp\left(-\frac{r^2}{r_c^2}\right)\right]\left\{1 - \frac{1}{\exp\left[k\,(R-r)\right]}\right\}. \tag{6.2}$$

In these approximations, Γ is the circulation, r_c is the vortex core size, l is the pitch of the helical symmetry, and u^0 is the velocity at the vortex axis. These parameters are obtained via the Toolbox EzyFit in Matlab [92]. The accuracy of the approximation is determined by the correlation coefficient, i.e. R_{fit}, as follows

$$R_{fit} = \sqrt{\frac{\sum\limits_{i}\left(u^{vc}_{fit,\,i} - \overline{u^{vc}}\right)^2}{\sum\limits_{i}\left(u^{vc}_{i} - \overline{u^{vc}}\right)^2}}, \tag{6.3}$$

where the numerator and denominator represent the regression sum of squares and the total sum of squares, respectively. Furthermore, the superscript vc represents the superscripts z and ϕ; u^{vc}_{fit} and u^{vc} are values obtained by fitting, and by experimental and/or numerical method at the position r; and $\overline{u^{vc}}$ is the mean value of the data obtained experimentally and/or numerically.
Thus, R_{fit} for the experimentally evaluated axial and tangential velocity components, i.e. $R_{fit}(u^z)$ and $R_{fit}(u^{\phi})$, obtains values that are given in Tab. 6.3.

Tab. 6.3: R_{fit} values for approximated velocities obtained experimentally

Re [-]	$R_{fit}(u^z)$	$R_{fit}(u^{\phi})$
1,000	0.714 – 0.997	0.855 – 0.992
2,000	0.882 – 0.995	0.964 – 0.994
5,000	0.880 – 0.993	0.965 – 0.994

Analogously, R_{fit} values for the numerically obtained axial and tangential velocity components, i.e. $R_{fit}(u^z)$ and $R_{fit}(u^{\phi})$, are summarised in Tab. 6.4.

Tab. 6.4: R_{fit} values for approximated velocities obtained numerically

Re [-]	$R_{fit}(u^z)$	$R_{fit}(u^\phi)$
1,000	0.976 – 0.999	0.964 – 0.998
2,000	0.982 – 0.999	0.981 – 0.998
5,000	0.949 – 0.996	0.963 – 0.996

The lowest R_{fit} values, given in Tab. 6.3 and Tab. 6.4, take place near the tangential inlets, where the fluid rotates as a solid body. Furthermore, according to the R_{fit} values, it can be assumed that the obtained data are interpreted correctly and that the fitted smooth functions may be used in the stability and vortex breakdown analysis.

6.4 Velocity Field

This section deals with the velocity field obtained experimentally and numerically. Here, for the investigated Reynolds numbers, the axial and tangential velocity profiles normalised by the axial bulk velocity $\overline{U^z}$ are shown. Moreover, redistributions in the dimensionless axial and tangential velocity profiles are also presented.

6.4.1 Axial Velocity Distribution

The dimensionless axial velocity distribution in the swirl tube with the constant geometrical swirl number and for the investigated Reynolds numbers are shown in Figs. 6.3 - 6.5, in which solid lines represent the experimental data (experiment) and dashed lines represent the numerically obtained velocity profiles (numerics). The dimensionless axial velocity profiles are shown at 20 axial positions z/D, as already mentioned in Section 6.1 and depicted in Fig. 6.1. Moreover, contour plots of the dimensionless axial velocity fields are given in Appendix E.1. From the contour plots of the velocity, it can be stated that the flow is symmetric over the tube axis.
The axial velocity reaches its maximum near the wall region and has an axial backflow in the tube centre, which has a connection to a vortex breakdown. The redistribution of the axial velocities in the outer regions shows

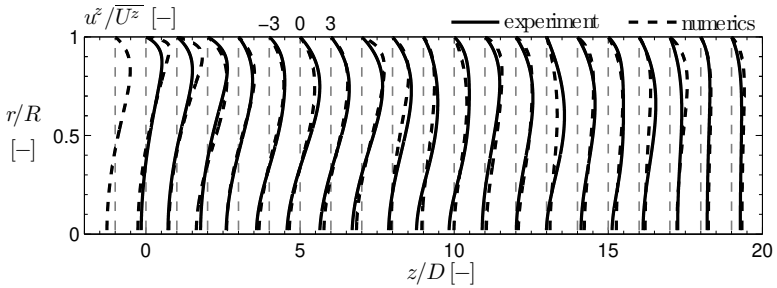

Fig. 6.3: Comparison of experimental (experiment) and numerical (numerics) dimensionless axial velocity profiles; $Re = 1{,}000$, $S_{IG} = 5.3$

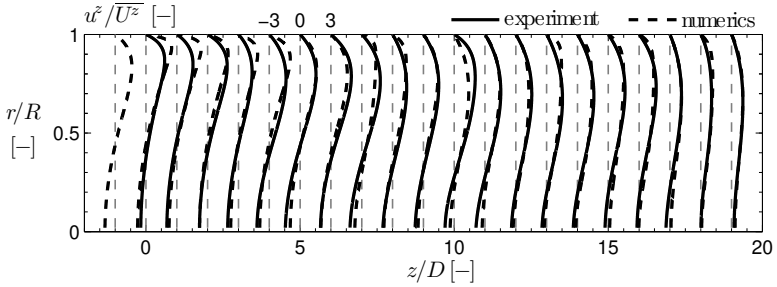

Fig. 6.4: Comparison of experimental (experiment) and numerical (numerics) dimensionless axial velocity profiles; $Re = 2{,}000$, $S_{IG} = 5.3$

a decrease of the magnitude due to wall friction. The case of $Re = 1{,}000$ is characterised by a decrease of the axial backflow towards the tube outlet due the lack of swirl strength in the second half of the tube length. A similar behaviour is observed for $Re = 2{,}000$ as well, but the swirl flow is strong enough to keep the axial backflow almost over the entire tube length. Only in case of $Re = 5{,}000$, an axial backflow is observable over the entire tube length. Thus, the dimensionless axial velocities as well as the axial backflow slightly increase with increasing Reynolds numbers.
Furthermore, the numerical data show a good agreement with the experimental data, but there are differences occurring in the tube centre. This slight

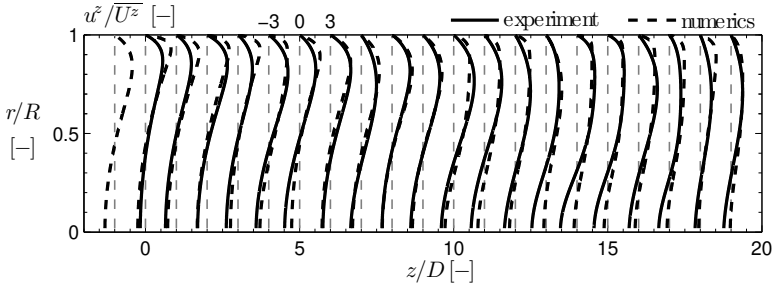

Fig. 6.5: Comparison of experimental (experiment) and numerical (numerics) dimensionless axial velocity profiles; $Re = 5{,}000$, $S_{IG} = 5.3$

deviation might be caused by the use of the turbulence model, especially the BSLEARSM, see also in Section 5.2.

6.4.2 Tangential Velocity Distribution

The dimensionless tangential velocity distribution in the swirl tube with the constant geometrical swirl number and for the investigated Reynolds numbers are plotted in Figs. 6.6 - 6.8. Here, again solid lines represent the experimental data (experiment) and dashed lines represent the numerically obtained velocity profiles (numerics). Moreover, contour plots of the dimensionless tangential velocity fields at the positions $z/D = 1$, 4, 7, 10, 13, 16 are given in Appendix E.1.
The tangential velocity component is the largest velocity component and is approximately twice as large as the axial velocity for the investigated swirl number. The magnitude of the tangential velocities, so the angular momentum, decreases considerably towards the tube outlet. This decrease is mainly caused by the viscous and turbulent dissipation and, furthermore, the maximum of the tangential velocity shifts to the tube centre. Moreover, the shape of the tangential velocity profiles can be approximate by a Rankine vortex consisting of a solid body vortex ($u^\phi = \Omega r$) and a potential vortex ($u^\phi = \Gamma / r$) as stated in [86]. Thus, the tangential velocities are described by the angular velocity Ω, the circulation Γ and the vortex radius r. Furthermore, there is a threshold in the vortex radius ($r = r_c$) that splits the Rankine vortex into a

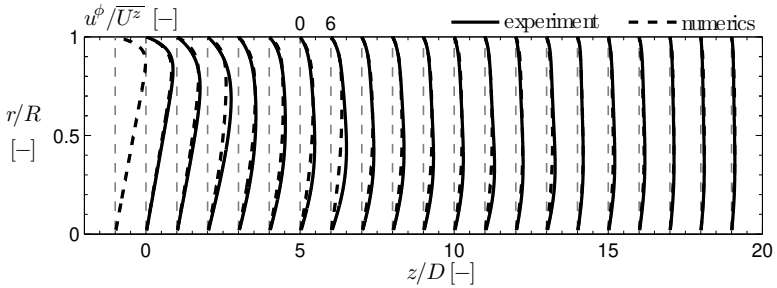

Fig. 6.6: Comparison of experimental (experiment) and numerical (numerics) dimensionless tangential velocity profiles; $Re = 1{,}000$, $S_{IG} = 5.3$

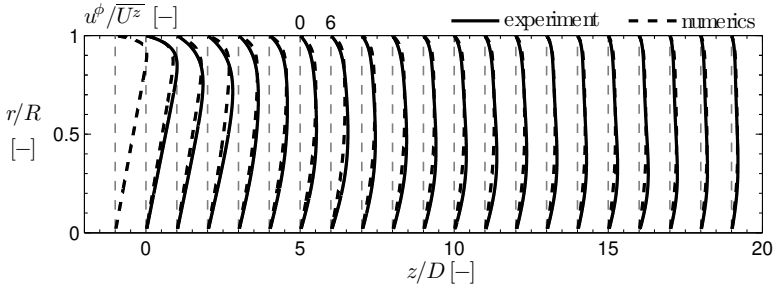

Fig. 6.7: Comparison of experimental (experiment) and numerical (numerics) dimensionless tangential velocity profiles; $Re = 2{,}000$, $S_{IG} = 5.3$

solid body vortex in the tube centre region ($r < r_c$), and a potential vortex in the outer region and partly in the near wall region ($r > r_c$). Near the tangential inlets, up to $z/D \approx 2-3$, the solid body vortex is dominant. As the flow approaches the tube outlet, the solid body vortex shrinks in size and the magnitude of the tangential velocity decreases, but the angular velocity Ω increases with the higher velocity gradient near the tube centre. Moreover, near the tube outlet, the redistribution of the tangential velocity results in a confined Rankine-like vortex, where the potential vortex may dominate.

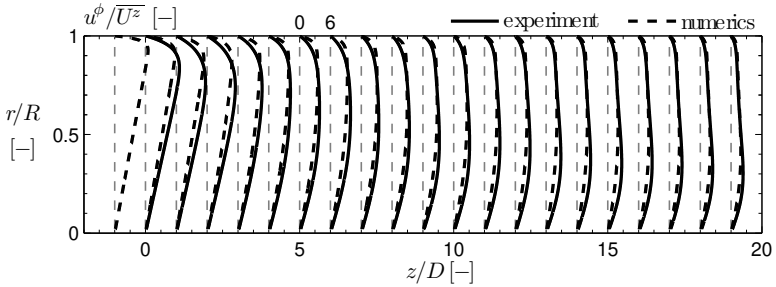

Fig. 6.8: Comparison of experimental (experiment) and numerical (numerics) dimensionless tangential velocity profiles; $Re = 5{,}000$, $S_{IG} = 5.3$

In case of $Re = 1{,}000$, the redistribution of the tangential velocity causes a significant decrease in its values, as shown in Fig. 6.6, and the flow is dominated by the axial velocity component. The similar behaviour is observed for $Re = 2{,}000$, where near the tube outlet, the tangential and axial velocities reach similar values and it is difficult to determine which component of the velocity is dominant. On the contrary, for $Re = 5{,}000$, the flow is dominated by the tangential velocity.
Also for the tangential velocity, the numerical data show a good agreement with the experimental data. Nevertheless, the tangential velocity is predicted by the numerical simulations more precisely compared to the axial velocity. From this point of view, the usage of the turbulence model can be understood as a good compromise between accuracy and computational cost.

6.5 Vortex Structure

Vortex structures in a swirl flow may be spatially represented via an isosurface of the Q - criterion [16, 53, 57, 66, 120]. The Q - criterion depends generally on rotation. Furthermore, in order to spatially visualise vortex structures, the shear stress, i.e. the shear strain rate, also affected by rotation, needs to be removed. Thus, the square of the symmetric part of the velocity

gradient (S_{ij}) is subtracted from the square of the antisymmetric part of the velocity gradient (Ω_{ij}), i.e.

$$Q = \frac{1}{2}\left(\Omega_{ij}^2 - S_{ij}^2\right), \tag{6.4}$$

where

$$S_{ij} = \frac{1}{2}\left(\frac{\partial u_i}{\partial x_j} + \frac{\partial u_j}{\partial x_i}\right), \quad \Omega_{ij} = \frac{1}{2}\left(\frac{\partial u_i}{\partial x_j} - \frac{\partial u_j}{\partial x_i}\right). \tag{6.5}$$

The antisymmetric part of the velocity gradient consists of the elements lying in the orthogonal planes to the axial direction. Hence, in order to properly visualise the vortex structures, the dominant rotation of the fluid around the tube axis is neglected, i.e. $\Omega_{r\phi} = \Omega_{\phi r} = 0$.
The Q - criterion is applied and solved only for the numerically solved cases in order to show its connection to the velocity field. Hence, the vortex structures in the swirl tube consist of a double-helix vortex, whose highest intensity takes place near the tangential inlets, i.e. in the region with the highest velocities as shown in Fig. 6.9. Thus, the intensity of the double-helix decreases towards the tube outlet. Furthermore, in case of the Reynolds number $Re = 1{,}000$, Fig. 6.9 a), the double-helix breaks inside the tube and does not reach the tube outlet as in the cases of $Re = 2{,}000$ and $Re = 5{,}000$ shown in Fig. 6.9 b), c). These outcomes also correspond to the redistribution of the velocity fields discussed in Section 6.4.

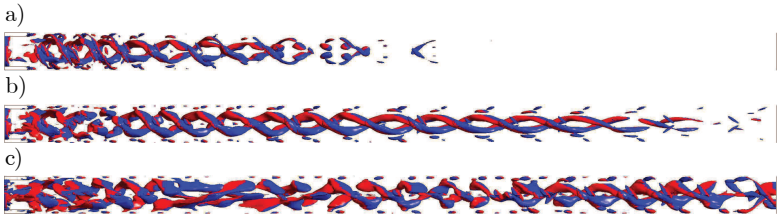

Fig. 6.9: Vortex structures in the swirl tube; a) $Re = 1{,}000$, b) $Re = 2{,}000$, and c) $Re = 5{,}000$; $S_{IG} = 5.3$; red and blue colours represent positive and negative radial velocities

6.6 Flow Analysis

The following flow analysis shows the decay of the swirl number over the tube length. In fact, the swirl number represents the swirl strength of the fluid, and influences the axial backflow in the tube centre and vortex structures in the tube. An analytical derivation of the limiting swirl number $S_{limit} = 0.928$, for which axial backflow may occur, has been given by Kobiela in [66] and later by Biegger in [16]. However, both assume that the axial velocity is characterised by a parabolic profile, which is not the case of the swirl flow in the tube. Nevertheless, their obtained value is taken as an informative parameter analysing the swirl number. Furthermore, Biegger, in his work [16], numerically analysed cases with swirl numbers $S = 5.3$, $S = 1$, and $S = 0.5$. He showed that for lower swirl numbers, changes of the local swirl number towards the tube outlet are not so significant as in the case of the highest swirl number, where the flow is swirl dominated by the tangential velocity.
The character of the flow domination, i.e. the swirl strength, is also related to the vortex breakdown phenomenon and the occurrence of axial backflow. Moreover, the main types of the vortex breakdown phenomena and common theories are mentioned in Section 2.3. Nevertheless, the presented study is characterised by an axisymmetric vortex breakdown with the occurrence of axial backflow for the flow of a sufficient swirl strength. This type of breakdown consists of a transition from a supercritical to a subcritical flow state, which is accompanied by spreading the flow upstream, where the flow transfers information about downstream conditions. Moreover, in order to predict vortex breakdown, a condition based on the Rossby number proposed by Spall et al. [117] and a decrease of the local tangential Reynolds numbers over the tube length are examined.

6.6.1 Swirl Number

Local values of the swirl number for the investigated Reynolds numbers and the constant geometrical swirl number are plotted in Fig. 6.10 and Fig. 6.11. The swirl number is defined as the ratio of the axial flux of the angular momentum divided by the tube radius to the axial flux of the axial momentum, as already mentioned in Section 1.4.
The local swirl numbers slightly oscillate for both, the experimentally and

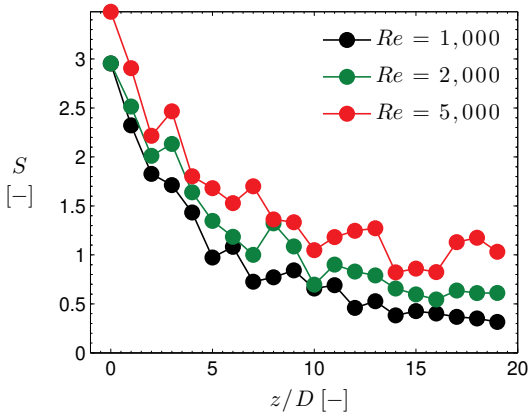

Fig. 6.10: Local swirl numbers determined from the experimental results; $S_{IG} = 5.3$

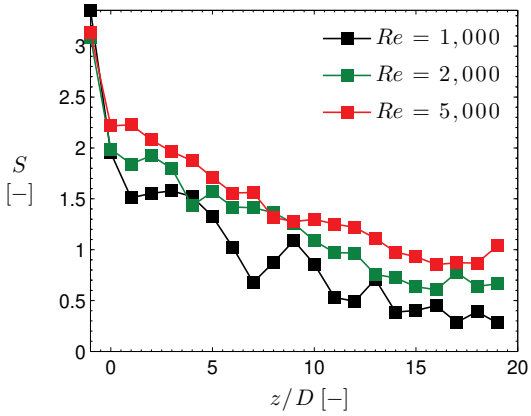

Fig. 6.11: Local swirl numbers determined from the numerical results; $S_{IG} = 5.3$

numerically obtained values, respectively. Nevertheless, the decreasing character of the swirl number over the tube length is obvious. For all investigated Reynolds numbers, the geometrical swirl number (S_{IG}) near the tangential inlets is higher than the local swirl number (S). This difference is caused by the assumption that for the idealised geometrical swirl number, the tangential velocity transforms completely into the axial velocity. Hence, the highest losses of the swirl number occur near the tangential inlets, where part of the tangential inflow is converted to the axial velocity.
Thus, the local swirl numbers decrease towards the tube outlet. In case of $Re = 1{,}000$, the swirl strength of the flow decreases under the limiting swirl number, i.e. $S < 0.928$, and the axial flow becomes dominant in the second half of the tube length. For $Re = 2{,}000$, values of the swirl strength approaches the limiting value of the swirl number, i.e. $S \leq 0.928$, near the tube outlet. So, the flow is tangential, or swirl, dominated over half of the tube length, where $S \geq 0.928$, and the axial backflow occurs. The axial backflow also occurs in case of $Re = 5{,}000$, in which the local values are greater or very close to the limiting swirl number and the axial backflow may be observable over the entire tube length.

6.6.2 Vortex Breakdown

Spall et al. [117] proposed a criterion based on the Rossby number that may be used in order to predict the onset of vortex breakdown. Local values of the Rossby number are computed by the ratio of the axial velocity to the tangential velocity $Ro = u^{z*}/(r^*\Omega)$. Spall et al. defined r^* as the radial position where the swirl velocity reaches its maximum, $r^*\Omega$ as the swirl velocity where Ω is the angular velocity of the solid body rotation, and u^{z*} is the axial velocity at the position r^*. These scales, i.e. u^{z*} and r^*, are also used for determination of the Reynolds numbers Re_z^*. Furthermore, the work by Spall et al. [117] also provides the determination of the critical Rossby number for vortex breakdown of 0.65, as already mentioned in Section 2.3 and shown in Fig. 2.14. If the Rossby number is lower than this value, the tangential velocity is dominant and vortex breakdown may occur.
The local Rossby numbers over the modified axial Reynolds numbers for the investigated Reynolds number are plotted in Fig. 6.12 representing values determined from the experimental data and in Fig. 6.13 representing values determined from the numerical data. Moreover, the black straight line in the figures depicts the limiting value of the Rossby number of 0.65. Hence, all points lying above the limiting Rossby number indicate no vortex breakdown.

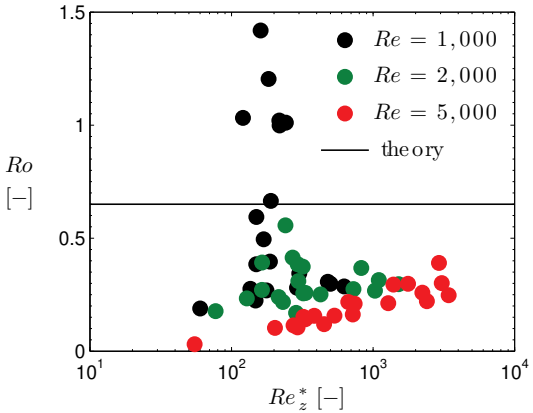

Fig. 6.12: Local Rossby numbers over modified axial Reynolds number determined from experimental results; $S_{IG} = 5.3$

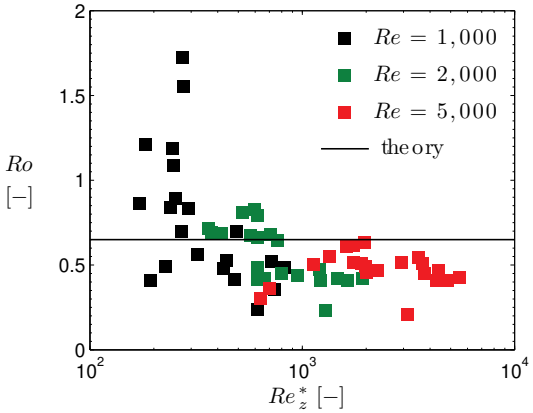

Fig. 6.13: Local Rossby numbers over modified axial Reynolds number determined from numerical results; $S_{IG} = 5.3$

On the other hand, all points below the limiting Rossby number indicate possible vortex breakdown.
From Fig. 6.12 and Fig. 6.13, it is obvious that for the highest Reynolds number, i.e. Re = 5,000, vortex breakdown occurs over the entire tube length. In case of Re = 2,000, analysis of vortex breakdown obtained from the numerical results slightly differs from the analysis obtained from the experimental results. Whereas the analysis of the experimental results shows an occurrence of vortex breakdown over the entire tube length, the analysis of the numerical results predicts no vortex breakdown for some points. Thus, it can be concluded that the disagreement between analysis of the experimental and numerical results can be assigned to slight inaccuracy of the numerical method for simulating the axial velocity, as mentioned in Section 6.4.1. Hence, as the axial backflow is reduced, i.e. the flow loses its swirl strength, the Rossby number increases and flow approaches the onset of vortex breakdown, i.e. the limiting Rossby number. This fact is also observable in Fig. 6.4 (Section 6.4.1), where the axial backflow decreases towards tube outlet. The similar behaviour is observed in case of Re = 1,000, where according to the local Rossby number, vortex breakdown may occur in the first half of the tube length where the swirl flow is strong enough.
Nevertheless, vortex breakdown can also be predicted by change of the mean axial velocity $\overline{u^z}$ and the mean tangential velocity $\overline{u^\phi}$ over the tube length [98]. In order to study changes of the mean velocities, two different Reynolds numbers are considered, the local axial Reynolds number Re_z and the local tangential Reynolds number Re_ϕ, respectively. In contrast to the Rossby number, these Reynolds numbers are used in order to study the effect of the mean velocities. The decreasing trends of the calculated local tangential Reynolds numbers and almost constant trend of the local axial Reynolds numbers at the different axial positions z/D are obvious from Fig. 6.14 to Fig. 6.19. Here, solid lines represent the local axial Reynolds number and dotted lines represent the local tangential Reynolds number. Furthermore, bullets and squares represent the experimental results and the numerical results, respectively. The local axial and tangential Reynolds numbers are determined for all investigated Reynolds numbers.
The case of Re = 1,000 is shown in Fig. 6.14 and Fig. 6.15, where the local tangential Reynolds number, Re_ϕ, is higher than the local axial Reynolds number, Re_z, in the region near the tangential inlets. This indicates that in this region, vortex breakdown may occur, which corresponds to the prediction based on the Rossby number shown in Fig. 6.12 and Fig. 6.13. As the fluid approaches the tube outlet, the flow becomes axial dominated without the axial backflow indicating no vortex breakdown. This fact is represented

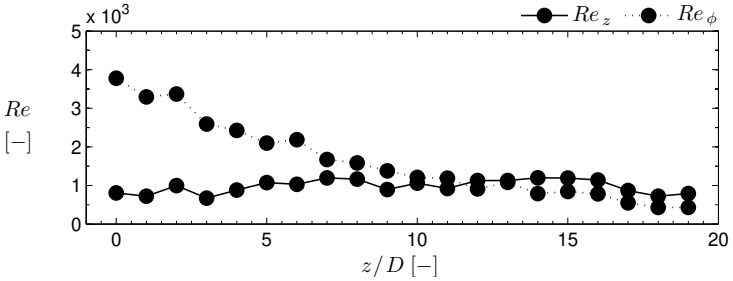

Fig. 6.14: Local axial Reynolds number and local tangential Reynolds number determined from experimental results; $Re = 1{,}000$, $S_{IG} = 5.3$

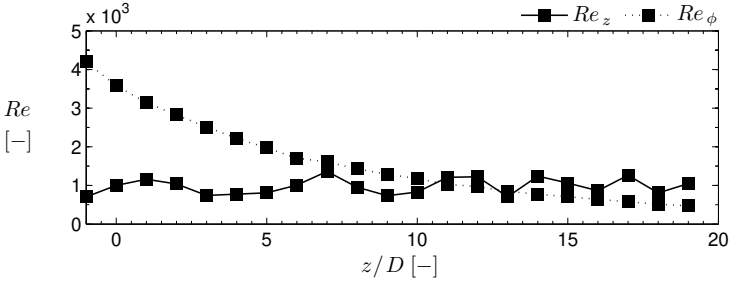

Fig. 6.15: Local axial Reynolds number and local tangential Reynolds number determined from numerical results; $Re = 1{,}000$, $S_{IG} = 5.3$

by an intersection of the local tangential and the local axial Reynolds numbers followed by a drop of the local tangential Reynolds number below the local axial Reynolds number.

With an increase in Reynolds number to $Re = 2{,}000$, the flow state near the inlet regions remains unchanged. The local tangential Reynolds number, Re_ϕ, is higher than the local axial Reynolds number, Re_z, indicating occurrence of vortex breakdown. Towards the tube outlet, the local tangential Reynolds number, Re_ϕ, approaches, but it does not intersect, the local axial Reynolds number, Re_z. This means that near the tube outlet, the flow state approaches the onset of vortex breakdown as indicated by the Rossby num-

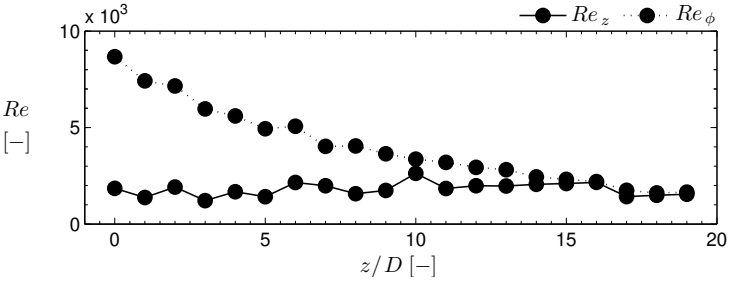

Fig. 6.16: Local axial Reynolds number and local tangential Reynolds number determined from experimental results; $Re = 2{,}000$, $S_{IG} = 5.3$

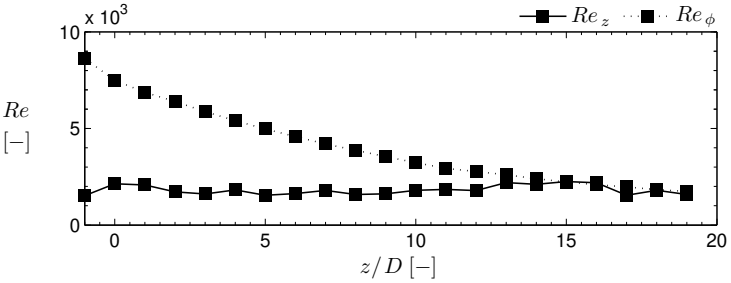

Fig. 6.17: Local axial Reynolds number and local tangential Reynolds number determined from numerical results; $Re = 2{,}000$, $S_{IG} = 5.3$

ber in Fig. 6.12 and Fig. 6.13.
For the highest Reynolds number, $Re = 5{,}000$, the widest gap between the local tangential Reynolds number, Re_ϕ, and the local axial Reynolds number, Re_z, near the tangential inlets is obvious. Vortex breakdown in this case takes place over the entire tube length, because the local tangential and local axial Reynolds numbers do not intersect. This also agrees with the analysis based on the Rossby number in Fig. 6.12 and Fig. 6.13.
Thus, this analysis shows that the case of $Re = 2{,}000$ is close to the onset of vortex breakdown in the region near the tube outlet. Whereas in the case $Re = 1{,}000$, in the second half of the tube, no vortex breakdown is predicted.

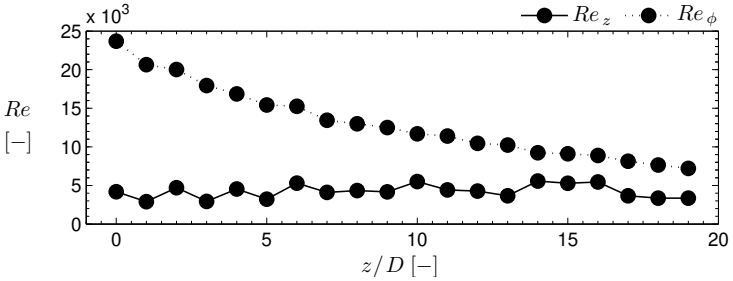

Fig. 6.18: Local axial Reynolds number and local tangential Reynolds number determined from experimental results; $Re = 5{,}000$, $S_{IG} = 5.3$

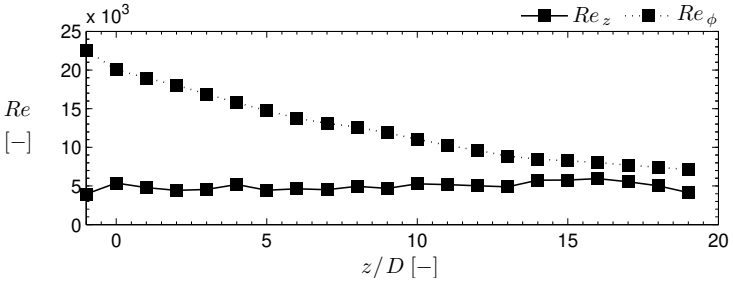

Fig. 6.19: Local axial Reynolds number and local tangential Reynolds number determined from numerical results; $Re = 5{,}000$, $S_{IG} = 5.3$

Vortex breakdown occurs in the entire tube only for $Re = 5{,}000$. These results are in accordance with the estimation proposed by Squire [118], who stated that the flow is subcritical, if the maximum swirl velocity is higher than the axial velocity. Hence, the vortex breakdown phenomena may be predicted by usage of the following flow characteristics: by the Rossby number based on the maximum velocity values and by the local tangential and local axial Reynolds number using the mean velocity values.

6.7 Stability

Stability of the vortex flow has been studied by many authors including Lord Rayleigh [77], Chandrasekhar [20], Howard and Gupta [52], Ludwieg [80, 81], Leibovich and Stewartson [73], as already mentioned in Section 2.2. Outcomes of these works, i.e. the derived stability criteria, are summarised and applied to the swirl flow in a tube by Ben Hmidene [13] and Biegger [16]. Furthermore, Ben Hmidene and Biegger introduced, in their works, the stability concept based on the minimum of the total enthalpy, which is a consequence of the stability concept arising from thermodynamics.
The stability concept based on thermodynamics was introduced in Sections 3.1 - 3.3 and follows the work of Marsik [84, 85]. Furthermore, the preliminary outcomes of this thermodynamic concept can be found in works by Marsik et al. [86, 87]. Hence, the derived stability concept based on thermodynamics, in Appendix A transformed into cylindrical coordinates, is used in the following section in order to analyse stability of the swirl flow in tubes.

6.7.1 Local Values of the Thermodynamic Stability Condition

The thermodynamic stability condition, i.e. the local TSC function Eq. (3.47), respectively Eq. (A.1), assuming only axial and tangential velocity components has the form

$$\begin{aligned}\pi = \mu \Bigg[& u^{\phi} \left(\frac{\partial^2 u^{\phi}}{\partial r^2} + \frac{\partial u^{\phi}}{r \partial r} - \frac{u^{\phi}}{r^2} \right) + \left(\frac{\partial u^{\phi}}{\partial r} - \frac{u^{\phi}}{r} \right) \left(\frac{\partial u^{\phi}}{\partial r} \right) \\ & + \left(\frac{\partial u^{\phi}}{\partial r} - \frac{u^{\phi}}{r} \right) \left(-\frac{u^{\phi}}{r} \right) + \left(\frac{\partial u^{z}}{\partial r} \right)^2 \\ & + u^{z} \left(\frac{\partial^2 u^{z}}{\partial r^2} + \frac{1}{r} \frac{\partial u^{z}}{\partial r} \right) \Bigg] \geq 0. \end{aligned} \tag{6.6}$$

This expression can be rearranged to

$$\begin{aligned}\pi = \mu \Bigg[& u^{\phi} \frac{\partial^2 u^{\phi}}{\partial r^2} + \left(\frac{\partial u^{\phi}}{\partial r} \right)^2 - \frac{u^{\phi}}{r} \frac{\partial u^{\phi}}{\partial r} + \left(\frac{\partial u^{z}}{\partial r} \right)^2 \\ & + u^{z} \left(\frac{\partial^2 u^{z}}{\partial r^2} + \frac{1}{r} \frac{\partial u^{z}}{\partial r} \right) \Bigg] \geq 0. \end{aligned} \tag{6.7}$$

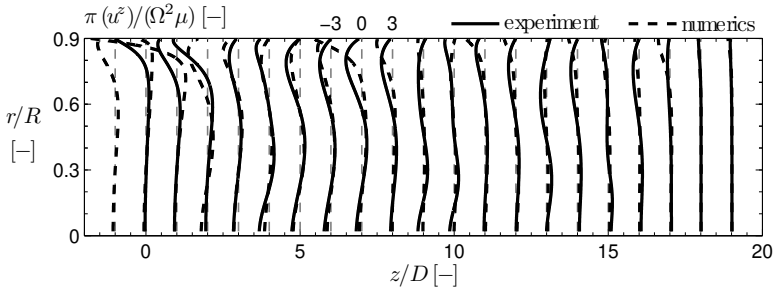

Fig. 6.20: Comparison of experimental (experiment) and numerical (numerics) dimensionless values of the local TSC function with omitted influence of the wall for the axial velocity; $Re = 1{,}000$, $S_{IG} = 5.3$

The obtained results are presented in dimensionless form, so that the local TSC function is expressed in the plots as $\pi/(\Omega^2\mu)$, where the angular velocity Ω is taken from Tab. 6.1 in Section 6.1.
In this section, the shape of the local TSC function is shown without the influence of the tube wall in order to show more clearly changes of the function along the radial coordinate at a given axial position z/D. The results including the influence of the tube wall can be found in Appendix E.2.

6.7.1.1 Axial Velocity

Values of the local TSC function computed for the axial velocity component are plotted in Figs. 6.20 - 6.22. Thus, the TSC function is, respecting the second part of Eq. (6.7), expressed by

$$\pi = \mu \left[u^z \frac{\partial^2 u^z}{\partial r^2} + \left(\frac{\partial u^z}{\partial r} \right)^2 + \frac{u^z}{r} \frac{\partial u^z}{\partial r} \right] \geq 0. \tag{6.8}$$

The shape of the local TSC function shows slightly negative values in the tube centre corresponding to the axial backflow in this region. In cases of $Re = 1{,}000$ and $Re = 2{,}000$, these negative values near the tube outlet change to positive and zero values, respectively. This behaviour respects the redistribution of the axial velocity in the tube, where in case of $Re = 1{,}000$,

the flow becomes axial dominated in this region and in the case of $Re = 2{,}000$, the flow is neither axial nor swirl dominated.

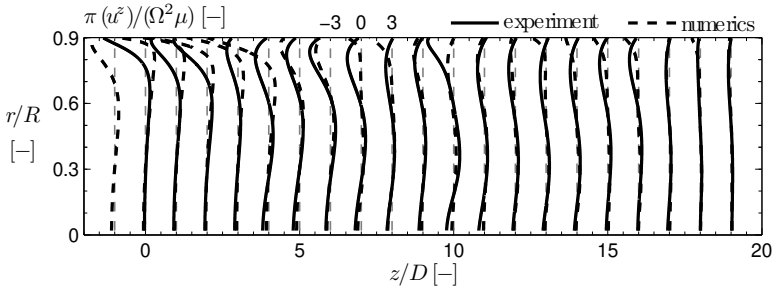

Fig. 6.21: Comparison of experimental (experiment) and numerical (numerics) dimensionless values of the local TSC function with omitted influence of the wall for the axial velocity; $Re = 2{,}000$, $S_{IG} = 5.3$

As the fluid approaches the wall, the local TSC function takes negative values due the destabilisation term in the TSC function, i.e. the second derivative of the velocity. This negative values region shifts towards the tube centre downstream to the tube outlet. Consequently, positive values of the local TSC function also appear. Moreover, near the tube wall, the viscous damping becomes to be dominant and the local TSC function gains positive values as shown in Appendix E.2.1. Hence, there are some regions, in which the flow in the axial direction may be locally unstable due to local effects of the velocity field redistribution. These locally unstable regions are then attenuated and redistributed due to the stabilising and destabilising processes along the radial coordinate.
In all cases, there is a region in the tube, where the determined values of the local TSC function from the experimental and numerical results differ. This may be induced by the discrepancies in shapes of the axial velocities obtained experimentally and numerically, as shown in Section 6.4.1. So, these discrepancies are observable at the following positions $z/D \approx 4 - 8$ for $Re = 1{,}000$, $z/D \approx 10 - 11$ for $Re = 2{,}000$, and $z/D \approx 13 - 17$ for $Re = 5{,}000$.

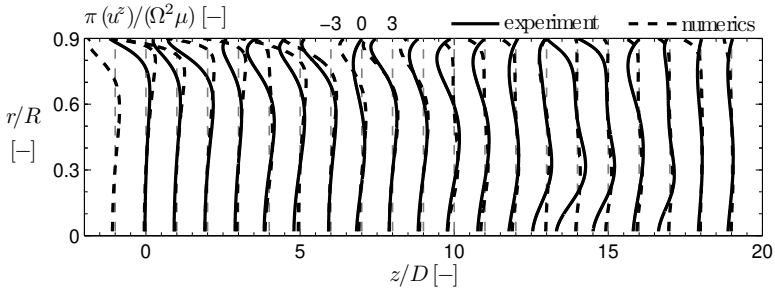

Fig. 6.22: Comparison of experimental (experiment) and numerical (numerics) dimensionless values of the local TSC function with omitted influence of the wall for the axial velocity; $Re = 5{,}000$, $S_{IG} = 5.3$

6.7.1.2 Tangential Velocity

The values of the local TSC function computed for the tangential velocity component are depicted in Figs. 6.23 - 6.25. In this case, the local TSC function is given by the first part of Eq. (6.7)

$$\pi = \mu \left[u^{\phi} \frac{\partial^2 u^{\phi}}{\partial r^2} + \left(\frac{\partial u^{\phi}}{\partial r} \right)^2 - \frac{u^{\phi}}{r} \frac{\partial u^{\phi}}{\partial r} \right] \geq 0. \tag{6.9}$$

As already mentioned in Section 6.4.2, the tangential velocity profiles can be approximated by a Rankine vortex consisting of a solid body vortex ($u^{\phi} = \Omega r$) and a potential vortex ($u^{\phi} = \Gamma / r$). If a fluid rotates as a solid body, the TSC function takes zero value, i.e. $\pi(u^{\phi}) = 0$. So, the fluid flow is at the margin of stability and a disturbance may not be attenuated by dissipative processes. Whereas, if a fluid rotates as a potential vortex, the TSC function takes a positive value, i.e. $\pi(u^{\phi}) = \mu(4\Gamma^2/r^4)$. Thus, the fluid flow is stable and dissipative processes may damp out a disturbance. Nevertheless, this short analysis is valid for an ideal case of an unbounded flow.
For the tangential velocity, the shape of the local TSC function reaches zero values in the tube centre. The size of the region with zero values decreases towards the tube outlet due the velocity field redistribution, which corresponds to a suppression of the solid body rotation of the flow. As the solid body rotation decreases the destabilising effects become dominant, which is

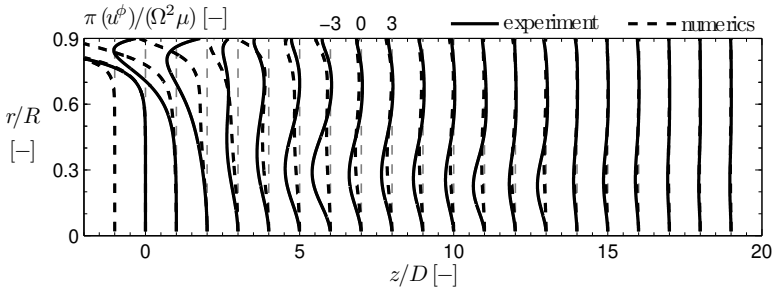

Fig. 6.23: Comparison of experimental (experiment) and numerical (numerics) dimensionless values of the local TSC function with omitted influence of the wall for the tangential velocity; $Re = 1{,}000$, $S_{IG} = 5.3$

characterised by the negative values of the local TSC function. The negative values region decreases towards the tube outlet in cases of $Re = 1{,}000$ and $Re = 2{,}000$, where the flow becomes axial dominated and neither axial nor swirl dominated, respectively. In case of $Re = 5{,}000$, i.e. swirl dominated flow, the negative values region increases its magnitude towards the tube outlet. Near the tube wall, the dissipative effects, i.e. viscous damping, play a crucial role and the local TSC function gains positive values as shown in Appendix E.2.2.

It is also obvious that towards the tube outlet, there is another region with positive values of the TSC function. This region is weakest for $Re = 1{,}000$ and is noticeable from the position $z/D = 5$. Near the tube outlet, where the axial flow is dominant, this region almost diminishes. In case of $Re = 2{,}000$, where the flow is neither axial nor swirl dominated, this region becomes more noticeable. It starts at the position $z/D = 7$, but also near the tube outlet this region is very small. For the swirl dominated flow, i.e. $Re = 5{,}000$, this region begins at the position $z/D = 8$ and is clearly observable. Thus, its evolution may be detectable.

According to theses observations and analogy to the Rankine vortex, it can be concluded that for the swirl flow in a tube, regions with potential-like vortex, characterised by the positive values of the local TSC function, are observable. Due to this fact, it is assumed that the flow is being stabilised.

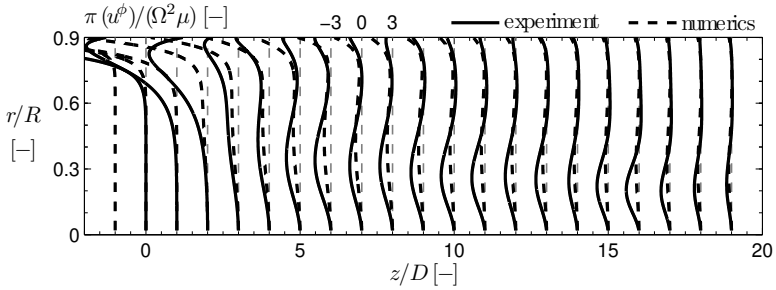

Fig. 6.24: Comparison of experimental (experiment) and numerical (numerics) dimensionless values of the local TSC function with omitted influence of the wall for the tangential velocity; $Re = 2{,}000$, $S_{IG} = 5.3$

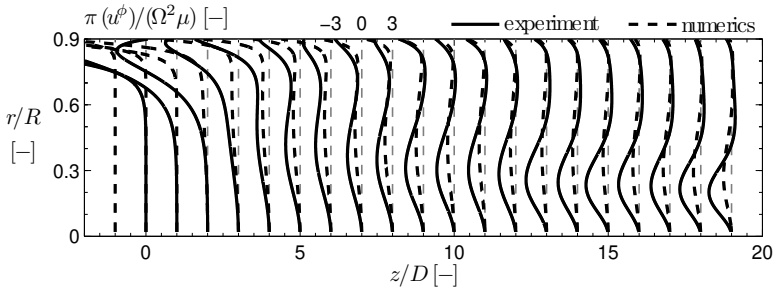

Fig. 6.25: Comparison of experimental (experiment) and numerical (numerics) dimensionless values of the local TSC function with omitted influence of the wall for the tangential velocity; $Re = 5{,}000$, $S_{IG} = 5.3$

6.7.1.3 Axial and Tangential Velocities

The values of the local TSC function for both assumed velocities, i.e. the axial and tangential velocity components, are computed by Eq. (6.7) and are shown in Figs. 6.26 - 6.28.

In case of $Re = 1{,}000$, the local TSC function reflects the domination of the solid body like velocity profile and the axial backflow near the tangential inlets, i.e. it takes nearly zero values that change to negative values as the fluid approaches the tube wall. For the positions $z/D = 2 - 12$, the local TSC function starts from negative values in the region of the tube centre and then, due to the velocity redistribution representing destabilising and dissipative processes, reaches zero or slightly positive values followed again by a decrease to negative values as the fluid approaches the tube wall. For the remaining tube length, the local TSC function oscillates around zero values. Furthermore, regions of negative values due to the velocity redistribution near the tube centre and in the region of $r/R \approx 0.5 - 0.8$ are also observable. For the cases of $Re = 2{,}000$ and $Re = 5{,}000$, the local TSC functions also respect the solid body like velocity profile near the tangential inlets, the axial backflow over almost the entire tube length for $Re = 2{,}000$ and the axial backflow over the entire tube length for $Re = 5{,}000$, respectively. Moreover, the local TSC function reaches approximately zero values changing to negative values as the fluid departs from the tube centre to the tube wall. From the positions $z/D = 2$ in case of $Re = 2{,}000$ and $z/D = 3$ in case of $Re = 5{,}000$ to the tube outlet, the local TSC function begins with negative values in the tube centre region and then due to the velocity redistribution, i.e. destabilising and dissipative processes, obtains more negative values followed by an increase to less negative or slightly positive values.

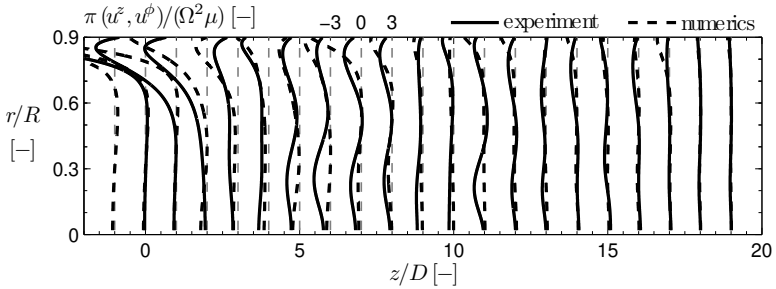

Fig. 6.26: Comparison of experimental (experiment) and numerical (numerics) dimensionless values of the local TSC function with omitted influence of the wall for the axial and tangential velocities; $Re = 1{,}000$, $S_{IG} = 5.3$

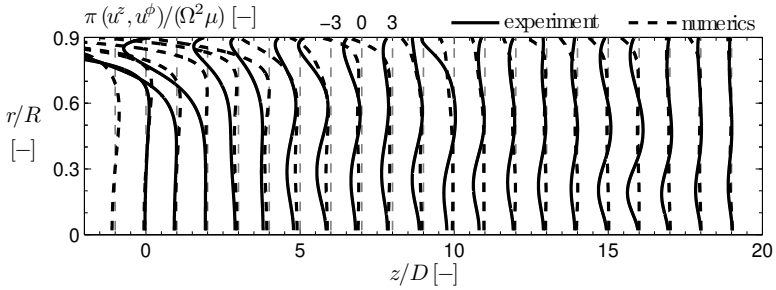

Fig. 6.27: Comparison of experimental (experiment) and numerical (numerics) dimensionless values of the local TSC function with omitted influence of the wall for the axial and tangential velocities; $Re = 2{,}000$, $S_{IG} = 5.3$

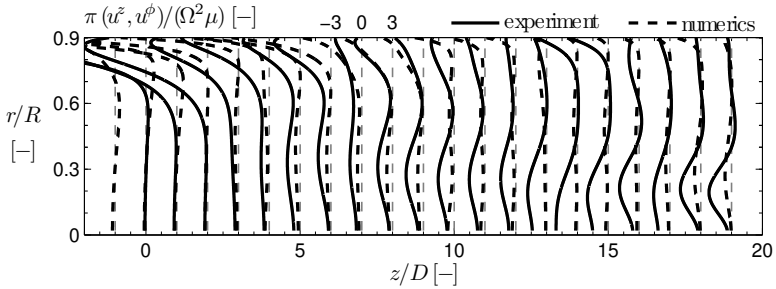

Fig. 6.28: Comparison of experimental (experiment) and numerical (numerics) dimensionless values of the local TSC function with omitted influence of the wall for the axial and tangential velocities; $Re = 5{,}000$, $S_{IG} = 5.3$

Furthermore, in all cases, as the fluid approaches the tube wall, the local TSC function again decreases up to a point, where dissipative processes become to be dominant and the local TSC function reaches positive values. This conclusion is supported by supplementary results that include the influence of the wall region and that are summarised in Appendix E.2.3.

6.7.2 Global Values of the Thermodynamic Stability Condition

The values of the global thermodynamic stability condition, i.e. the global TSC function, are given by the volume integral Eq. (3.50) introduced in Section 3.3. In order to obtain the values of the global TSC function in dimensionless form, the volume integral is normalised by the inner volume of the tube V_t and is expressed as

$$\frac{\Pi}{V_t \Omega^2 \mu} = \frac{1}{V_t} \int_V \frac{\pi}{\Omega^2 \mu} \mathrm{d}\overline{V}, \text{ for } \mathrm{d}\overline{V} = \overline{r}\mathrm{d}\overline{\phi}\mathrm{d}\overline{r}\mathrm{d}\overline{z}. \tag{6.10}$$

In the volume integral, the angular velocity Ω is taken from Tab. 6.1 in Section 6.1. Moreover, the expression for the global TSC function can be simplified, after some algebra, to

$$\frac{\Pi}{V_t \Omega^2 \mu} = \int_r 2 \frac{\pi}{\Omega^2 \mu} \frac{\mathrm{d}\overline{z}}{L} \frac{\overline{r}}{R} \frac{\mathrm{d}\overline{r}}{R}. \tag{6.11}$$

Here, moreover, the axial coordinate in the integral $\mathrm{d}\overline{z}$ varies between 0 to 1 mm and represents the thickness of the slice with a radius r changing from 0 to R, for which a value of the global TSC function at a position z/D is calculated.
In this section, the values of the global TSC function are shown without the influence of the tube wall. The results including the influence of the tube wall are given in Appendix E.3. The influence of the tube wall, i.e. integration over the radial coordinate from 0 to R, results in positive values of the global TSC function, which imply a stable character of the flow from the thermodynamic point of view. On the other hand, due to the velocity redistribution in the tube, there are processes in the flow that the global TSC function should cover and clarify. Due to this hypothesis, the values of the global TSC function are computed by Eq. (6.11) at a position z/D without an influence of the tube wall in order to show their development towards the tube outlet. Thus, these values are integrated over the radial coordinate from 0 to $0.9R$.

6.7.2.1 Axial Velocity

The values of the global TSC function computed for the axial velocity component are plotted in Figs. 6.29 - 6.31. Thus, the global TSC function is

obtained by Eq. (6.11), where π is given by Eq. (6.8).
The trend of the global TSC function values are not smooth and oscillate for all investigated Reynolds numbers. Moreover, in case of the axial velocity analysis, there are discrepancies in the values determined from the experimental and numerical data near the tangential inlets, where the axial backflow takes place. From the position $z/D \approx 4$ in cases of $Re = 1{,}000$ and $Re = 2{,}000$, the global TSC function shows an increasing trend from more negative values to less negative values towards the tube outlet that implies stabilisation of the axial flow. In these cases, the flow near the tube outlet, for $Re = 1{,}000$, is axial dominated and, for $Re = 2{,}000$, is neither axial nor swirl dominated.
In case of $Re = 5{,}000$, a trend of the global TSC function is difficult to determinate. However, from the position $z/D \approx 10$, the global TSC function shows also an increasing trend to less negative values as the fluid approaches the tube outlet indicating a stabilisation of the axial flow.
Hence, this analysis shows that as the axial flow becomes stronger towards the tube outlet, i.e. the axial backflow decreases, the global TSC function is approaching less negative values. On the other hand, the global values of the TSC function with influence of the tube wall are characterised by positive values that decrease towards the tube outlet as shown in Appendix E.3.1. In case of $Re = 5{,}000$, furthermore, the global TSC function is accompanied with oscillations in the computed values.

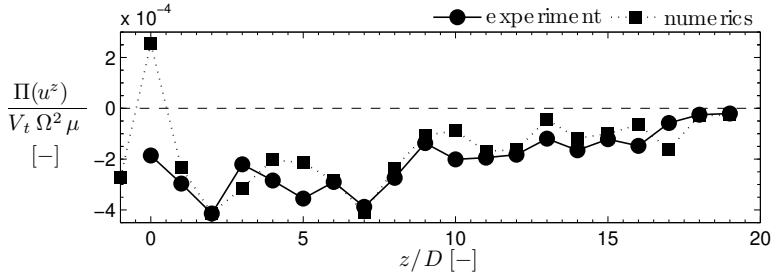

Fig. 6.29: Comparison of experimental (experiment) and numerical (numerics) dimensionless values of the global TSC function with omitted influence of the wall for the axial velocity; $Re = 1{,}000$, $S_{IG} = 5.3$

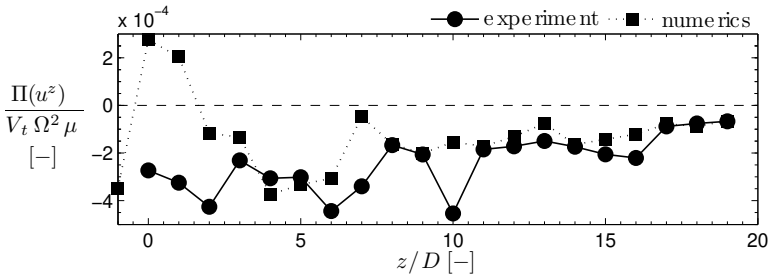

Fig. 6.30: Comparison of experimental (experiment) and numerical (numerics) dimensionless values of the global TSC function with omitted influence of the wall for the axial velocity; $Re = 2{,}000$, $S_{IG} = 5.3$

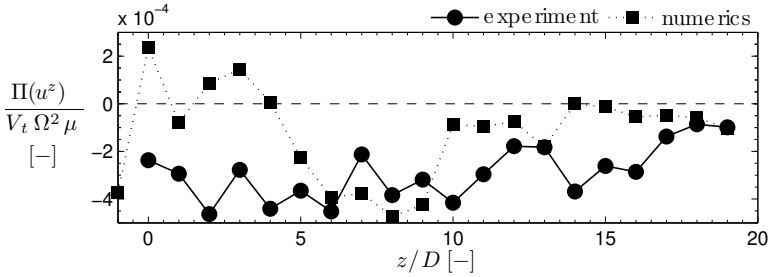

Fig. 6.31: Comparison of experimental (experiment) and numerical (numerics) dimensionless values of the global TSC function with omitted influence of the wall for the axial velocity; $Re = 5{,}000$, $S_{IG} = 5.3$

6.7.2.2 Tangential Velocity

In Figs. 6.32 - 6.34, the values of the global TSC function determined for the tangential velocity component are presented. Thus, the global TSC function is obtained by Eq. (6.11), where π is given by Eq. (6.9).
The trend of the global TSC function values is relatively smooth for all investigated Reynolds numbers. Near the tangential inlets, the values of the global TSC function, determined from the experimental and numerical data,

differ for $Re = 2{,}000$ and $Re = 5{,}000$. On the other hand, the global TSC function for $Re = 1{,}000$ is characterised by a good agreement between values computed from experimental and numerical data. Moreover, an increase in the global TSC function from more negative values to less negative values towards the tube outlet is obvious. A similar trend is also observed for $Re = 2{,}000$ and $Re = 5{,}000$, where the global TSC function determined from the experimental and numerical data matches at the positions $z/D \approx 3$ and $z/D \approx 7$, respectively.
From this analysis, it can be summarised that as the tangential velocity near the tangential inlets, where fluid rotates as a solid body, moves to the tube outlet, the solid body shape of the tangential velocity changes to a more stable shape. In case of $Re = 1{,}000$, it is evident that the values of the global TSC function near the tube outlet are almost constant with no observable trend. This is due to the fact that near the tube outlet, the flow becomes axial dominated.
Moreover, the values of the global TSC function with the influence of the tube wall are characterised by positive values near the tangential inlets that then decrease and reach the trend with no significant changes towards the tube outlet, as shown in Appendix E.3.2.

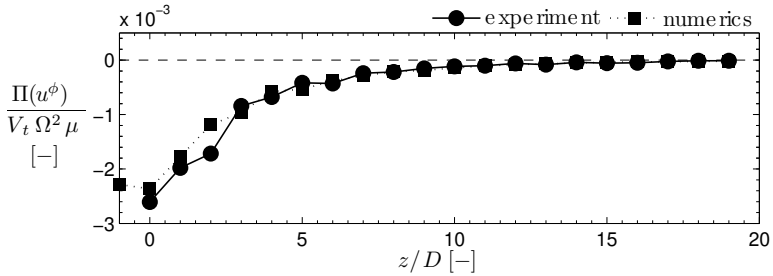

Fig. 6.32: Comparison of experimental (experiment) and numerical (numerics) dimensionless values of the global TSC function with omitted influence of the wall for the tangential velocity; $Re = 1{,}000$, $S_{IG} = 5.3$

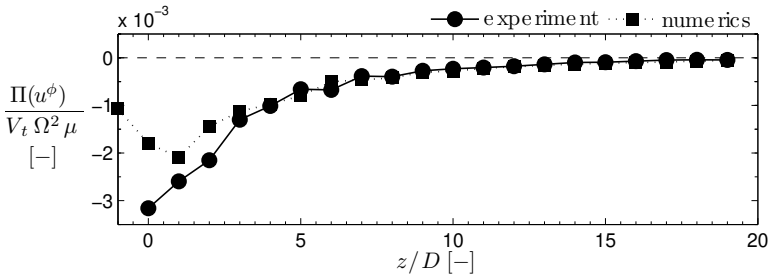

Fig. 6.33: Comparison of experimental (experiment) and numerical (numerics) dimensionless values of the global TSC function with omitted influence of the wall for the tangential velocity; $Re = 2{,}000$, $S_{IG} = 5.3$

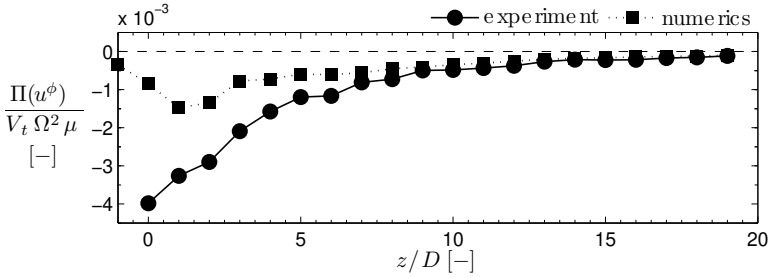

Fig. 6.34: Comparison of experimental (experiment) and numerical (numerics) dimensionless values of the global TSC function with omitted influence of the wall for the tangential velocity; $Re = 5{,}000$, $S_{IG} = 5.3$

6.7.2.3 Axial and Tangential Velocities

The values of the global TSC function computed for the axial and tangential velocity components are depicted in Figs. 6.35 - 6.37. In this case, the global TSC function is obtained by Eq. (6.11), where π is given by Eq. (6.7).
The trend of the global TSC function relates the trend of the global TSC

function determined for the tangential velocity. This is given by the one order higher values of the global TSC function for the tangential velocity than for the axial velocity.
The values of the global TSC function show a good agreement between experimentally and numerically obtained data, but near the tangential inlets, the values of the global TSC function differ. The global TSC functions determined from the numerical and experimental data match at the position $z/D \approx 3$ for $Re = 1{,}000$ and $Re = 2{,}000$, and $z/D \approx 7$ for $Re = 5{,}000$, respectively.
The global TSC function shows an increasing trend towards larger values for growing z/D indicating that an initial form of the velocity field redistributes, from a thermodynamic point of view, to a more stable form. It is also observable that a redistribution, due to dissipative and destabilising processes, of the velocity field is more dominant in the first third of the tube length, i.e. at the positions $z/D \approx 0 - 6$. At these positions, the flow loses approximately one half of its swirl strength, as shown in Fig. 6.10 and Fig. 6.11. Moreover, this loss of the swirl strength may result in a strong fluid mixing in this region, which may also affect the heat transfer to its local maximum performance, as also deduced in the work by Biegger [16] and Kobiela [66].
Nevertheless, the global values of the TSC function with influence of the tube wall show the positive values decreasing towards the tube outlet. The global TSC functions for all investigated Reynolds numbers are accompanied by an oscillation. This is due to the fact that contrary to the cases with omit-

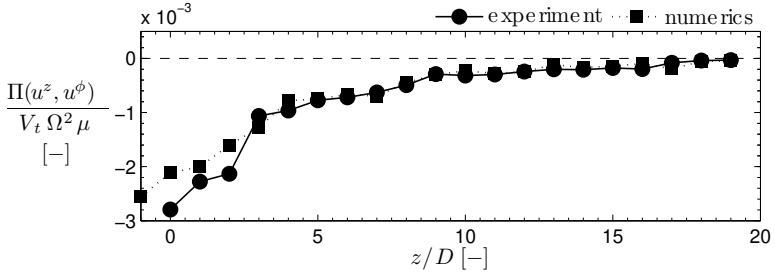

Fig. 6.35: Comparison of experimental (experiment) and numerical (numerics) dimensionless values of the global TSC function with omitted influence of the wall for the axial and tangential velocities; $Re = 1{,}000$, $S_{IG} = 5.3$

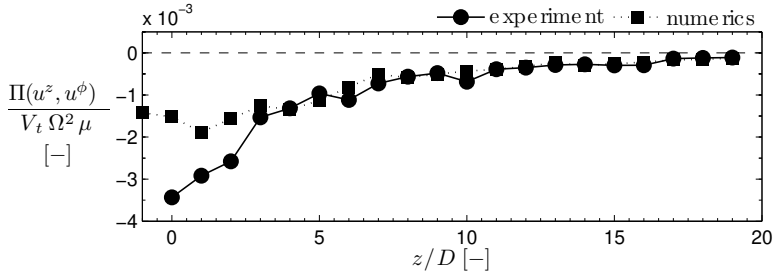

Fig. 6.36: Comparison of experimental (experiment) and numerical (numerics) dimensionless values of the global TSC function with omitted influence of the wall for the axial and tangential velocities; $Re = 2{,}000$, $S_{IG} = 5.3$

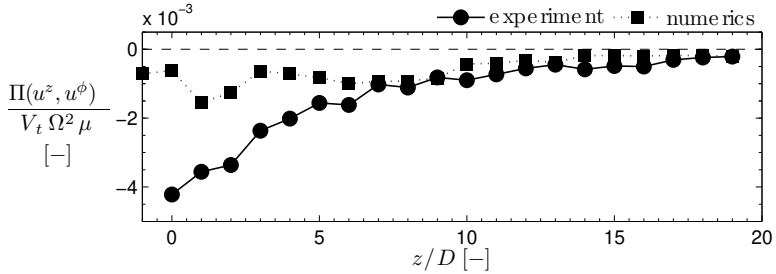

Fig. 6.37: Comparison of experimental (experiment) and numerical (numerics) dimensionless values of the global TSC function with omitted influence of the wall for the axial and tangential velocities; $Re = 5{,}000$, $S_{IG} = 5.3$

ted walls, the global TSC function for the tangential velocity is smaller by five orders of magnitude for $Re = 1{,}000$ and four orders of magnitude for $Re = 2{,}000$ and $Re = 5{,}000$. Thus, the global TSC function for the axial and tangential velocity components reflects the global TSC function determined for the axial velocity, as shown in Appendix E.3.3.

6.7.3 Stability and Vortex Breakdown

Vortex breakdown can be predicted by using the condition based on the Rossby number proposed by Spall et al. [117], which is already shown in Section 6.6.2. Thus, the Rossby number is computed by the ratio of the axial velocity to the tangential velocity $Ro = u^{z*}/(r^*\Omega)$. Here, r^* is the radial position where the swirl velocity reaches its maximum, $r^*\Omega$ is the swirl velocity, where Ω is taken as the angular velocity of the solid body rotation, and u^{z*} is the axial velocity at the position r^*. The onset of vortex breakdown is proposed to be given by the critical Rossby number value of 0.65, below which vortex breakdown may occur and above which there is no vortex breakdown, as mentioned in Section 2.3.
So, the values of the global TSC function with omitted influence of the tube wall determined for the axial and tangential velocity components, Eq. (6.7) and Eq. (6.11), are plotted over the local values of the Rossby number. These plots are shown in Fig. 6.38 representing values determined from the experimental data and in Fig. 6.39 representing values determined from the numerical data. Furthermore, the black straight line in the figures depicts

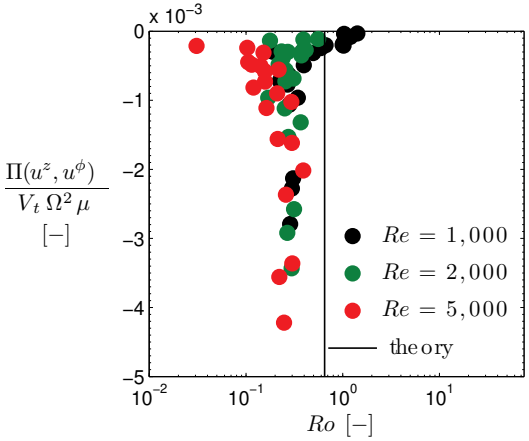

Fig. 6.38: Global TSC function with omitted influence of the wall for the axial and tangential velocity component over the local Rossby number determined from experimental results; $S_{IG} = 5.3$

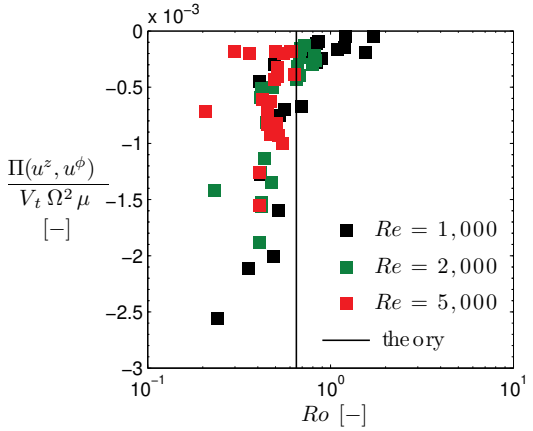

Fig. 6.39: Global TSC function with omitted influence of the wall for the axial and tangential velocity component over the local Rossby number determined from numerical results; $S_{IG} = 5.3$

the limiting value of the Rossby number of 0.65.
The results given in Section 6.6.2 are supported by Fig. 6.38 and Fig. 6.39, so vortex breakdown occurs over the entire tube length for $Re = 5{,}000$. For $Re = 2{,}000$, there are different values determined from the experimental and numerical data. The analysis of the experimentally obtained data shows the occurrence of vortex breakdown over the entire tube length, whereas the analysis of the numerically obtained data predicts no vortex breakdown in the region near tube outlet. This disagreement may be assigned to a slight inaccuracy of the numerically computed axial velocity and due to the difference in the values of the global TSC function near the tangential inlets, as mentioned in Section 6.4.1 and Section 6.7.2, respectively. In case of $Re = 1{,}000$, vortex breakdown is predicted in the tube region where the flow is swirl dominated and the axial backflow is assumed. Near the tube outlet, no vortex breakdown is assumed.
The values of the global TSC function determined for the axial and tangential velocity components decrease towards the tube outlet. Thus, for all investigated Reynolds numbers, as the fluid moves to the tube outlet, the global TSC function approaches less negative values and the flow is stabilised

from a thermodynamic point of view. The local Rossby number increases in the region near the tube outlet for $Re = 1{,}000$, where the flow is axial dominated. In case of $Re = 2{,}000$, the local Rossby number also increases in the region near the tube outlet, but this increase is not so significant as in the case of $Re = 1{,}000$. This is due to the fact that in this case the flow is neither axial nor swirl dominated, so that the Rossby numbers are very close to the limiting value in this region. For swirl dominated flow, $Re = 5{,}000$, the local Rossby number decreases in the region near the tube outlet. This decrease might correspond to a decrease in swirl strength as the fluid moves towards the tube outlet.
Thus, the global TSC function together with the Rossby number provide information about the vortex breakdown prediction in connection to the redistribution of the velocity field inside the tube. This connection shows that vortex breakdown is accompanied by processes causing a stabilisation of the flow from a thermodynamic point of view.

CHAPTER 7

Conclusions and Outlook

The present work investigated the flow phenomena and flow stability of a swirl flow in a tube. A swirl flow in a tube, or a swirl tube, is characterised by one or more tangential inlet jets, or nozzles, due to which a complex swirling flow is generated. Typical for swirling flows are large velocities near the tube wall and high turbulence in the tube affecting mixing, heat transfer, and stability. Thus, a swirl tube can be used as a cooling technique for gas turbine blades. Nevertheless, this work is focused mainly on the development of a suitable stability criterion, based on thermodynamics, being applicable to general flow problems in order to capture and quantify processes taking place in the swirl flow in a tube.

Firstly, a theoretical background in order to derive a stability criterion based on thermodynamics is provided. Thus, general rules for balancing of quantities, the thermodynamic property entropy, balance of the total enthalpy, general thermodynamic inequality, and finally, thermodynamic stability condition, i.e. the TSC function, are introduced. Then, the application of the TSC function to simplified flow problems, i.e. to axial flow in a tube, to a Couette flow between rotating cylinders, and to the flow problem in rotating tubes, is also included. The analysis of these simplified flow problems shows

that the derived stability criterion is applicable in order to investigate a flow stability from a thermodynamic point of view.
Then, a swirl tube with two tangential inlets at the upstream end of the tube is investigated. In an extensive examination, the flow field for a constant swirl number ($S_{IG} = 5.3$) and several mass flow rates, i.e. the Reynolds numbers, covering laminar-like ($Re = 1{,}000$), intermediate ($Re = 2{,}000$), and turbulent ($Re = 5{,}000$) flow regimes, is studied experimentally and also numerically. Hence, the flow field is experimentally obtained via Particle Image Velocimetry (PIV). Then, numerical simulations are conducted for an isothermal turbulent flow via the commercial code ANSYS CFX. In order to model the turbulence, the Baseline Explicit Algebraic Reynolds Stress Model (BSLEARSM) model is employed, which is extended for the laminar case by the Gamma Transition Model (GTM) in order to capture the transition to turbulence. The obtained results are utilised in order to analyse swirling flow in terms of the vortex breakdown phenomenon and stability from a thermodynamic point of view. Moreover, the swirl flow is assumed to be dominated by the tangential velocity, which may be approximated by a Rankine vortex with a solid body vortex in the tube centre and a potential vortex in the outer region. The preliminary stability analysis of the unbounded Rankine vortex indicates that the solid body vortex being at the margin of stability is redistributed to the more stable potential vortex. This result supports the assumption that the flow is being stabilised.
Thus, the followed analysis of the velocity field shows that the swirl flow in the tube is dominated by the tangential velocity. However, in the laminar-like flow regime, $Re = 1{,}000$, the flow is, in the second half of the tube length, dominated by the axial velocity. Similarly, in case of the intermediate flow regime, $Re = 2{,}000$, the flow is, near the tube outlet, neither axial nor swirl dominated. In the turbulent flow regime, $Re = 5{,}000$, the swirl flow is dominated by the tangential velocity over the entire tube length. However, the domination of the tangential velocity, generally, decreases downstream from the tangential inlets, as confirmed by the investigation via the swirl number. The decrease of the swirl number confirms an analytical result by Biegger [16] and by Kobiela [66], who have estimated the limiting swirl number $S = 0.928$ as the limit, for which a backflow near the tube centre might appear. The axial backflow is, thus, represented by the axial velocity flowing upstream. Moreover, it is shown that for swirl flows, a vortex breakdown is observable for the Rossby number lower than the limiting Rossby number 0.65, as proposed by Spall et al. [117], which is given as the ratio of the axial velocity at the radial position of the maximum tangential velocity and the maximum tangential velocity. For comparison, the change of the local

axial and local tangential Reynolds numbers, based on the mean values of the axial and tangential velocity components, shows that vortex breakdown is expected when the flow is swirl dominated, and if an axial backflow occurs. Hence, in case of an axial dominated flow, no vortex breakdown is expected. The further analysis of the investigated swirl flow is related to the stability criterion based on thermodynamics. In general, the results confirm an assumption that the swirl flow rotates dominantly as a solid body near the tangential inlets and is, then, redistributed downstream to a potential-like vortex, which is energetically more suitable. According to the stability criterion based on thermodynamics, a solid body vortex is at the margin of stability, whereas a potential vortex is stable. Thus, the swirl flow is being stabilised. Furthermore, local values of the stability criterion show stabilising and destabilising processes in the swirl flow affecting its redistribution and stability. In order to cover stabilising, i.e. dissipative, and destabilising processes, the stability criterion is, individually, determined for a case with omitted influence of the tube wall and for a case with included influence of the tube wall, where dissipative processes are dominant. Thus, in case with omitted influence of the tube wall, the redistribution of the swirl flow reflects changes of the velocity field and also implicitly covers vortex breakdown that might be followed by destabilising processes resulting in a local non-compliance of the stability criterion. These destabilising processes are found for all investigated flow regimes. For the laminar-like flow regime, $Re = 1{,}000$, these destabilising processes are attenuated downstream to the tube outlet, where the flow becomes to be axial dominated. In case of the intermediate flow regime, $Re = 2{,}000$, destabilising processes are slightly attenuated but are still observable, because this flow regime is neither axial nor swirl dominated. The turbulent flow regime, $Re = 5{,}000$, is characterised by an occurrence of destabilising processes over the entire tube length. This fact confirms that the turbulent flow regime is swirl dominated and vortex breakdown is detectable over the entire tube length.

In order to characterise the swirl flow, integral values of the stability criterion are also determined. The first results, including also an influence of the tube wall, show a stable character of the swirl flow over the entire tube length. This is due to the fact that there is a huge dissipation in the tube wall region resulting in positive integral values. On the other hand, the analysis of the swirl flow with omitted influence of the wall region, reflects more precisely the redistribution of the velocity field accompanied by stabilising and destabilising processes. For all flow regimes, integral values of the stability criterion reaches negative values that change downstream towards the tube outlet to less negative values. This also confirms the outcome that the

swirl flow is being stabilised. Moreover, in regions of the tube where these changes prevail, i.e. approximately the first fifth of the tube length, stabilising and destabilising processes are dominant resulting in fluid mixing and, thus, energy transformation. It could be expected that in this region the heat transfer influenced by the swirl flow would reach its maximum performance, which is supported by results of Biegger [16] and Kobiela [66]. Thus, the swirl tube with several tangential inlets along the tube length would lead to a more homogeneous heat transfer, as also investigated by Biegger [16] and by Rao et al. [103].

A connection between the derived stability criterion and vortex breakdown with regard to the Rossby number and integral values of the derived stability criterion is also investigated. The performed analysis results in the confirmation of the vortex breakdown analysis. Furthermore, for all investigated flow regimes, the integral values of the derived stability criterion approach less negative values downstream to the tube outlet. The local Rossby number increases in the region near the tube outlet for the laminar-like flow regime, $Re = 1{,}000$, where the flow is axial dominated. The intermediate flow regime, $Re = 2{,}000$, is also characterised by the increased local Rossby number near the tube outlet. This increase is not so significant as for the laminar-like flow regime, mainly due to the fact that in this case the flow is neither axial nor swirl dominated. Hence, the local Rossby numbers are very close to the limiting value of 0.65 in this region. For the turbulent flow regime, $Re = 5{,}000$, the local Rossby number decreases near the tube outlet, which might be connected to a decrease of the swirl strength downstream to the tube outlet. Thus, this analysis confirms that vortex breakdown is accompanied by processes causing a stabilisation of the flow from a thermodynamic point of view.

Thus, this work presented an application of a thermodynamic stability concept to a swirl flow in a tube. However, the presented stability concept is applicable to any kind of flows satisfying the condition of incompressibility, i.e. flow at low Mach numbers, of a Newtonian fluid, e.g. a flow in a tube, a flow over a wing or blade including also heat transfer. In the future, this approach to investigate flow stability, based on a thermodynamic approach, could also be extended to compressible flows and to flows of non-Newtonian fluids. This requires a modification of the TSC function for these kind of applications. The final aim of all these studies could be to show if and where the here investigated concept can be used and where it gives similar results to classical stability concepts and also where the TSC concept could provide a broader scope than classical stability concepts.

Bibliography

[1] Akonur, A. and Lueptow, R. M. (2003). Three-Dimensional Velocity Field for Wavy Taylor-Couette Flow. *Physics of Fluids* **15**(4), pp. 947–960. DOI: 10.1063/1.1556615.

[2] Alekseenko, S. V., Kuibin, P. A., and Okulov, V. L. (2007). Theory of Concentrated Vortices. Heidelberg: Springer. ISBN: 3-540-73375-2.

[3] Alekseenko, S. V., Kuibin, P. A., Okulov, V. L., and Shtork, S. I. (1999). Helical Vortices in Swirl Flow. *Journal of Fluid Mechanics* **382**, pp. 195–243. DOI: 10.1017/S0022112098003772.

[4] Althaus, W., Brücker, C., and Weimer, M. (1995). Breakdown of Slender Vortices. In: *Fluid Mechanics and Its Applications, Volume 30. Fluid Vortices*. Ed. by Green, S. I. Dordrecht: Springer. Chap. 9, pp. 373–426. DOI: 10.1007/978-94-011-0249-0_9.

[5] Andereck, C. D., Liu, S. S., and Swinney, H. L. (1986). Flow Regimes in a Circular Couette System with Independently Rotating Cylinders. *Journal of Fluid Mechanics* **164**, pp. 155–183. DOI: 10.1017/S0022112086002513.

[6] ANSYS (2009a). ANSYS CFX - Solver Theory Guide. Release 12.0. ANSYS, Inc. Southpointe, 275 Technology Drive, PA 15317 Canonsburg, USA.

[7] ANSYS (2009b). ANSYS ICEM CFD - Help Manual. Release 12.1. ANSYS, Inc. Southpointe, 275 Technology Drive, PA 15317 Canonsburg, USA.

[8] Barth, T. J. and Jespersen, D. C. (1989). The Design and Application of Upwind Schemes on Unstructured Meshes. In: *27th Aerospace Sciences Meeting. Reno, Nevada, January 9-12, 1989. AIAA Paper 89-0366*. DOI: 10.2514/6.1989-366.

[9] Batchelor, G. K. (2002). An Introduction to Fluid Dynamics. New York: Cambridge University Press. ISBN: 0-521-66396-2.

[10] Bathe, K. J. (1996). Finite Element Procedures. New Jersey: Prentice-Hall, Inc. ISBN: 0-13-301458-4.

[11] Becker, K. M. and Kaye, J. (1962). Measurements of Diabatic Flow in an Annulus With an Inner Rotating Cylinder. *Journal of Heat Transfer* **84**(2), pp. 97–104. DOI: 10.1115/1.3684335.

[12] Belisle, M. J. (2007). Experiments on Mode Competition in Temporally-Modulated Taylor-Couette Flow. MA thesis. Arizona State University: Faculty of Aerospace Engineering.

[13] Ben Hmidene, M. (2015). Stabilitätsanalyse der Strömungsphänomene in einem Wirbelrohr. BA thesis. Universität Stuttgart: Institut für Thermodynamik der Luft- und Raumfahrt (ITLR).

[14] Benjamin, T. B. (1965). Significance of the Vortex Breakdown Phenomenon. *Journal of Basic Engineering* **87**(2), pp. 518–522. DOI: 10.1115/1.3650590.

[15] Betz, A. (1950). Wie entsteht ein Wirbel in einer wenig zähen Flüssigkeit? *Die Naturwissenschaften* **37**(9), pp. 193–196. DOI: 10.1007/BF00622314.

[16] Biegger, C. (2017). Flow and Heat Transfer Investigations in Swirl Tubes for Gas Turbine Blade Cooling. PhD thesis. Universität Stuttgart: Institut für Thermodynamik der Luft- und Raumfahrt (ITLR).

[17] Blazek, J. (2001). Computational Fluid Dynamics: Principles and Applications. First Edition. Oxford: Elsevier. ISBN: 0-08-043009-0.

[18] Borisenko, A. I. and Tarapov, I. E. (1979). Vector and Tensor Analysis with Applications. Trans. by Silverman, R. A. New York: Dover Publications. ISBN: 978-0-486-63833-2.

[19] Breuer, M. (1991). Numerische Lösung der Navier-Stokes Gleichungen für dreidimensionale inkompressible instationäre Strömungen zur Simulation des Wirbelaufplatzens. PhD thesis. RWTH Aachen: Aerodynamisches Institut.

[20] Chandrasekhar, S. (1961). Hydrodynamic and Hydromagnetic Stability. Oxford: Clarendon Press. ISBN: 0-486-64071-X.

[21] Coles, D. (1965). Transition in Circular Couette Flow. *Journal of Fluid Mechanics* **21**(3), pp. 385–425. DOI: 10.1017/S0022112065000241.

[22] Davis, M. W. and Weber, E. J. (1960). Liquid-Liquid Extraction between Rotating Concentric Cylinders. *Industrial and Engineering Chemistry* **52**(11), pp. 929–934. DOI: 10.1021/ie50611a027.

[23] Di Prima, R. C. and Pridor, A. (1979). The Stability of Viscous Flow between Rotating Concentric Cylinders with an Axial Flow. *Proceedings of the Royal Society of London. Series A, Mathematical and Physical Sciences* **366**(1727), pp. 555–573. URL: http://www.jstor.org/stable/79820.

[24] Donnelly, R. J. (1991). Taylor-Couette flow: The Early Days. *Physics Today* **44**(11), pp. 32–39. DOI: 10.1063/1.881296.

[25] Donnelly, R. J. and Fultz, D. (1960). Experiments on the Stability of Spiral Flow between Rotating Cylinders. *Proceedings of the National Academy of Sciences of the United States of America* **46**(8), pp. 1150–1154. URL: http://www.jstor.org/stable/70841.

[26] Dou, H.-S., Khoo, B. C., and Yeo, K. S. (2008). Instability of Taylor-Couette Flow between Concentric Rotating Cylinders. *International Journal of Thermal Science* **47**(11), pp. 1422–1435. DOI: 10.1016/j.ijthermalsci.2007.12.012.

[27] Eiamsa-ard, S. and Promvonge, P. (2008). Review of Ranque-Hilsch Effects in Vortex Tubes. *Renewable and Sustainable Energy Reviews* **12**(7), pp. 1822–1842. DOI: 10.1016/j.rser.2007.03.006.

[28] Erringen, A. C. (1999). Microcontinuum Field Theories: I. Foundations and Solids. New York: Springer. ISBN: 0-387-98620-0.

[29] Escudier, M. (1988). Vortex Breakdown: Observations and Explanations. *Progress in Aerospace Sciences* **25**(2), pp. 189–229. DOI: 10.1016/0376-0421(88)90007-3.

[30] Faler, J. H. and Leibovich, S. (1977). Disrupted States of Vortex Flow and Vortex Breakdown. *Physics of Fluids* **20**(9), pp. 1385–1400. DOI: 10.1063/1.862033.

[31] Fénot, M., Bertin, Y., Dorignac, E., and Lalizel, G. (2011). A Review of Heat Transfer between Concentric Rotating Cylinders with or without Axial Flow. *International Journal of Thermal Sciences* **50**(7), pp. 1138–1155. DOI: 10.1016/j.ijthermalsci.2011.02.013.

[32] Fletcher, C. A. J. (1991). Computational Techniques for Fluid Dynamics 1: Fundamental and General Techniques. Second Edition. Berlin, Heidelberg: Springer. ISBN: 3-540-53058-4.

[33] Fujita, T. T. (1973). Tornadoes around the World. *Weatherwise* **26**(2), pp. 56–83. DOI: 10.1080/00431672.1973.9931633.

[34] Fulton, C. D. (1950). Ranque's Tube. *Journal of the ASRE: Refrigerating Engineering* **58**(5), pp. 473–479.

[35] Gellert, M. and Rüdiger, G. (2009). Stratorotational Instability in Taylor-Couette Flow Heated from Above. *Journal of Fluid mechanics* **623**, pp. 375–385. DOI: 10.1017/S002211200800551X.

[36] Glezer, B., Moon, H.-K., Kerrebrock, J., Bons, J., and Guenette, G. (1998). Heat Transfer in a Rotating Radial Channel With Swirling Internal Flow. In: *ASME International Gas Turbine and Aeroengine Congress and Exhibition. Volume 4: Heat Transfer; Electric Power; Industrial and Cogeneration. Stockholm, Sweden, June 2-5, 1998. Paper No. 98-GT-214.* ISBN: 978-0-7918-7865-1. DOI: 10.1115/98-GT-214.

[37] Glezer, B., Moon, H.-K., and O'Connell, T. (1996). A Novel Technique for the Internal Blade Cooling. In: *ASME International Gas Turbine and Aeroengine Congress and Exhibition. Volume 4: Heat Transfer; Electric Power; Industrial and Cogeneration. Birmingham, UK, June 10-13, 1996. Paper No. 96-GT-181.* ISBN: 978-0-7918-7875-0. DOI: 10.1115/96-GT-181.

[38] Görtler, H. (1941). Instabilität laminarer Grenzschichten an konkaven Wänden gegenüber gewissen dreidimensionalen Störungen. *Journal of Applied Mathematics and Mechanics (ZAMM)* **21**(4), pp. 250–252. DOI: 10.1002/zamm.19410210408.

[39] Görtler, H. (1954). On the Three-Dimensional Instability of Laminar Boundary Layers on Concave Walls. Tech. rep. NACA TM 1375. Washington, D. C., USA: National Advisory Committee for Aeronautics (NACA).

[40] Guillerm, R., Kang, C., Savaro, C., Lepiller, V., Prigent, A., Yang, K.-S., and Mutabazi, I. (2015). Flow Regimes in a Vertical Taylor-Couette System with a Radial Thermal Gradient. *Physics of Fluids* **27**(9), pages. DOI: 10.1063/1.4930588.

[41] Gupta, A. K., Lilley, D. G., and Syred, N. (1984). Swirl Flows. Energy and Engineering Science Series. Tunbridge Wells: Abacus Press. ISBN: 0-856-26175-0.

[42] Gutsol, A. F. (1997). The Ranque Effect. *Physics-Uspekhi* **40**(6), pp. 639–658. DOI: 10.1070/PU1997v040n06ABEH000248.

[43] Hall, M. G. (1972). Vortex Breakdown. *Annual Review of Fluid Mechanics* **4**, pp. 195–218. DOI: 10.1146/annurev.fl.04.010172.001211.

[44] Hartnett, J. P. and Eckert, E. R. G. (1957). Experimental Study of the Velocity and Temperature Distribution in a High-Velocity Vortex-Type Flow. *Transactions of the ASME* **79**, pp. 751–758.

[45] Hedlund, C. R. and Ligrani, P. M. (2000). Local Swirl Chamber Heat Transfer and Flow Structure at Different Reynolds Numbers. *Journal of Turbomachinery* **122**(2), pp. 375–385. DOI: 10.1115/1.555458.

[46] Hedlund, C. R., Ligrani, P. M., Moon, H.-K., and Glezer, B. (1999). Heat Transfer and Flow Phenomena in a Swirl Chamber Simulating Turbine Blade Internal Cooling. *Journal of Turbomachinery* **121**(4), pp. 804–813. DOI: 10.1115/1.2836734.

[47] Hellsten, A. (2005). New Advanced $k-\omega$ Turbulence Model for High-Lift Aerodynamics. *AIAA Journal* **43**(9), pp. 1857–1869. DOI: 10.2514/1.13754.

[48] Hilsch, R. (1946). Die Expansion von Gasen im Zentrifugalfeld als Kälteprozeß. *Zeitschrift für Naturforschung A* **1**(4), pp. 208–214. DOI: 10.1515/zna-1946-0406.

[49] Hilsch, R. (1947). The Use of the Expansion of Gases in a Centrifugal Field as Cooling Process. *Review of Scientific Instruments* **18**(2), pp. 108–113. DOI: 10.1063/1.1740893.

[50] Hoffmann, K. A., Chiang, S. T., Siddiqui, S., and Papadakis, M. (1996). Fundamental Equations of Fluid Mechanics. Wichita: Engineering Education System. ISBN: 0-9623731-9-2.

[51] Holeschovsky, U. B. and Cooney, C. L. (1991). Quantitative Description of Ultrafiltration in a Rotating Filtration Device. *AIChE Journal* **37**(8), pp. 1219–1226. DOI: 10.1002/aic.690370811.

[52] Howard, L. N. and Gupta, A. S. (1962). On the Hydrodynamic and Hydromagnetic Stability of Swirling Flows. *Journal of Fluid Mechanics* **14**(3), pp. 463–476. DOI: 10.1017/S0022112062001366.

[53] Hunt, J. C. R., Wray, A. A., and Moin, P. (1988). Eddies, Streams, and Convergence Zones in Turbulent Flows. Tech. rep. CTR-S88. Stanford, USA: Center for Turbulence Research Report (CTR), pp. 193–208.

[54] Itskov, M. (2007). Tensor Algebra and Tensor Analysis for Engineers. Berlin, Heidelberg: Springer. ISBN: 978-3-540-36046-9.

[55] Jahanmiri, M. (2011). Laminar Separation Bubble: Its Structure, Dynamics and Control. Tech. rep. 2011:06. Göteborg, Sweden: Chalmers University of Technology.

[56] Janes, D. A., Thomas, N. H., and Callow, J. A. (1987). Demonstration of a Bubble-Free Annular-Vortex Membrane Bioreactor for Batch Culture of Red Beet Cells. *Biotechnology Techniques* **1**(4), pp. 257–262. DOI: 10.1007/BF00155465.

[57] Jeong, J. and Hussain, F. (1995). On the Identification of a Vortex. *Journal of Fluid Mechanics* **285**, pp. 69–94. DOI: 10.1017/S0022112095000462.

[58] Kassner, R. and Knoernschild, E. (1948). Friction Laws and Energy Transfer in Circular Flow. Tech. rep. F-TR-2198ND. Dayton, Ohio, USA: Wright-Patterson Air Force Base.

[59] Kaye, J. and Elgar, E. C. (1958). Modes of Adiabatic and Diabatic Fluid Flow in an Annulus with an Inner Rotating Cylinder. *Transactions of the ASME* **80**, pp. 753–765.

[60] Keller, J. J. (1994). On Tornado-Like Vortex Flows. *Physics of Fluids* **6**(4), pp. 1524–1534. DOI: 10.1063/1.868266.

[61] Keller, J. J. (1995). On the Interpretation of Vortex Breakdown. *Physics of Fluids* **7**(7), pp. 1695–1702. DOI: 10.1063/1.868757.

[62] Keller, J. J., Egli, W., and Althaus, R. (1988). Vortex Breakdown as a Fundamental Element of Vortex Dynamics. *Journal of Applied Mathematics and Physics (ZAMP)* **39**(3), pp. 404–440. DOI: 10.1007/BF00945061.

[63] Keller, J. J., Egli, W., and Exley, J. (1985). Force-and Loss-Free Transitions between Flow States. *Journal of Applied Mathematics and Physics (ZAMP)* **36**(6), pp. 854–889. DOI: 10.1007/BF00944899.

[64] Kieu, C. Q. and Zhang, D.-L. (2009). An Analytical Model for the Rapid Intensification of Tropical Cyclones. *Quarterly Journal of the Royal Meteorological Society* **135**(642), pp. 1336–1349. DOI: 10.1002/qj.433.

[65] Klein, F. (1910). Über die Bildung von Wirbeln in reibungslosen Flüssigkeiten. *Zeitschrift für Mathematik und Physik* **58**, pp. 259–262.

[66] Kobiela, B. (2013). Wärmeübertragung in einer Zyklonkühlkammer einer Gasturbinenschaufel. PhD thesis. Universität Stuttgart: Institut für Thermodynamik der Luft- und Raumfahrt (ITLR).

[67] Kossin, J. P., McNoldy, B. D., and Schubert, W. H. (2002). Vortical Swirls in Hurricane Eye Clouds. *Monthly Weather Review* **130**(12), pp. 3144–3149. DOI: 10.1175/1520-0493(2002)130<3144:VSIHEC>2.0.CO;2.

[68] Langtry, R. B. (2006). A Correlation-Based Transition Model using Local Variables for Unstructured Parallelized CFD Codes. PhD thesis. Universität Stuttgart: Institut für Thermische Strömungsmaschinen und Maschinenlaboratorium (ITSM).

[69] Langtry, R. B. and Menter, F. R. (2005). Transition Modeling for General CFD Applications in Aeronautics. In: *43rd AIAA Aerospace Sciences Meeting and Exhibit. Reno, Nevada, January 10-13, 2005. AIAA paper 2005-522.* DOI: 10.2514/6.2005-522.

[70] LaVision (2002). FlowMaster Manual for DaVis 6.2. LaVision GmbH, Anna-Vandenhoeck-Ring 19, D-37081 Göttingen, Germany.

[71] Lebon, G., Jou, D., and Casas-Vázquez, J. (2008). Understanding Non-euilibrium Thermodynamics. Berlin, Heidelberg: Springer. ISBN: 978-3-540-74251-7.

[72] Leibovich, S. (1984). Vortex Stability and Breakdown-Survey and Extension. *AIAA Journal* **22**(9), pp. 1192–1206. DOI: 10.2514/3.8761.

[73] Leibovich, S. and Stewartson, K. (1983). A Sufficient Condition for the Instability of Columnar Vortices. *Journal of Fluid Mechanics* **126**, pp. 335–356. DOI: 10.1017/S0022112083000191.

[74] Leontiev, A. I. (2002). Gas-Dynamic Methods of Temperature Stratification. *Fluid Dynamics* **37**(4), pp. 512–529. DOI: 10.1023/A:1020629000437.

[75] Ligrani, P. M., Hedlund, C. R., Babinchak, B. T., Thambu, R., Moon, H.-K., and Glezer, B. (1998). Flow Phenomena in Swirl Chambers. *Experiments in Fluids* **24**(3), pp. 254–264. DOI: 10.1007/s003480050172.

[76] Lim, T. T., Chew, Y. T., and Xiao, Q. (1998). A New Flow Regime in a Taylor-Couette Flow. *Physics of Fluids* **10**(12), pp. 3233–3235. DOI: 10.1063/1.869851.

[77] Lord Rayleigh (1917). On the Dynamics of Revolving Fluids. *Proceedings of the Royal Society of London. Series A, Containing Papers of a Mathematical and Physical Character* **93**(648), pp. 148–154. DOI: 10.1098/rspa.1917.0010.

[78] Lucca-Negro, O. and O'Doherty, T. (2001). Vortex Breakdown: A Review. *Progress in Energy and Combustion Science* **27**(4), pp. 431–481. DOI: 10.1016/S0360-1285(00)00022-8.

[79] Ludwieg, H. (1962). Zur Erklärung der Instabilität der über angestellten Deltaflügeln auftretenden freien Wirbelkerne. *Zeitschrift für Flugwissenschaften* **10**(6), pp. 242–249.

[80] Ludwieg, H. (1966). Experimentelle Nachprüfung der Stabilitätstheorien für reibungsfreie Strömungen mit schraubenlinienförmigen Stromlinien. In: *Applied Mechanics*. Ed. by Görtler, H. Berlin, Heidelberg: Springer, pp. 1045–1051. ISBN: 978-3-662-29364-5.

[81] Ludwieg, H. (1980). An Explanation of the Instability of the Free Vortex Cores Occurring over Delta Winds with Raised Edges. Tech. rep. NASA-TM-75861. Washington, D. C., USA: National Aeronautics and Space Administration (NASA).

[82] Lueptow, R. M. (2000). Stability and Experimental Velocity Field in Taylor-Couette Flow with Axial and Radial Flow. In: *Physics of Rotating Fluids*. Ed. by Egbers, C. and Pfister, G. Heidelberg: Springer, pp. 137–155. ISBN: 3-540-67514-0.

[83] Markowski, P. and Richardson, Y. (2014). What we know and don't know about Tornado Formation. *Physics Today* **67**(9), pp. 26–31. DOI: 10.1063/PT.3.2514.

[84] Marsik, F. (1989). Consequences of Thermodynamical Conditions of Stability for Thermoviscous Fluids and Thermoviscoelastic Solids. *Acta Physica Hungarica* **66**, pp. 195–202. DOI: 10.1007/BF03155792.

[85] Marsik, F. (1999). Termodynamika Kontinua. Praha: Academia. ISBN: 80-200-0758-X.

[86] Marsik, F., Kobiela, B., Novotny, P., and Weigand, B. (2010a). Thermodynamic Analysis and Experimental Investigation of Swirl Tube Flow. In: *Proceedings of the 21st International Symposium on Transport Phenomena. Kaohsiung, Taiwan, November 2-5, 2010*, pp. 416–422. ISBN: 978-986-6184-25-3.

[87] Marsik, F., Travnicek, Z., Novotny, P., and Werner, E. (2010b). Stability of a Swirling Annular Flow. *Journal of Flow Visualization and Image Processing* **17**(3), pp. 267–279. DOI: 10.1615/JFlowVisImageProc.v17.i3.70.

[88] Menter, F. R. (1993). Zonal Two Equation $k-\omega$ Turbulence Models for Aerodynamic Flows. In: *24th Fluid Dynamics Conference. Orlando, Florida, July 6-9, 1993. AIAA Paper 93-2906*. DOI: 10.2514/6.1993-2906.

[89] Menter, F. R. (1994). Two-Equation Eddy-Viscosity Turbulence Models for Engineering Applications. *AIAA Journal* **32**(8), pp. 1598–1605. DOI: 10.2514/3.12149.

[90] Menter, F. R., Langtry, R., and Völker, S. (2006). Transition Modelling for General Purpose CFD Codes. *Flow, Turbulence and Combustion* **77**, pp. 277–303. DOI: 10.1007/s10494-006-9047-1.

[91] Moffat, R. J. (1988). Describing the Uncertainties in Experimental Results. *Experimental Thermal and Fluid Science* **1**(1), pp. 3–17. DOI: 10.1016/0894-1777(88)90043-X.

[92] Moisy, F. (2012). Ezyfit: A free curve fitting toolbox for Matlab, v 2.41. http://www.fast.u-psud.fr/ezyfit/.

[93] Moore, C. M. V. and Cooney, C. L. (1995). Axial Dispersion in Taylor-Couette Flow. *AIChE Journal* **41**(3), pp. 723–727. DOI: 10.1002/aic.690410329.

[94] Moser, K. W., Raguin, L. G., Harris, A., Morris, H. D., Georgiadis, J., Shannon, M., and Philpott, M. (2000). Visualization of Taylor–Couette and Spiral Poiseuille flows using a Snapshot FLASH Spatial Tagging Sequence. *Magnetic Resonance Imaging* **18**(2), pp. 199–207. DOI: 10.1016/S0730-725X(99)00121-6.

[95] Nechayev, A. (2011). Physics of the Atmospheric Vortex: Hurricane, Polar low, Tornado. Moscow: Logata. ISBN: 978-5-900858-43-2.

[96] Nishibori, K., Kikuyama, K., and Murakami, M. (1987). Laminarization of Turbulent Flow in the Inlet Region of an Axially Rotating Pipe. *JSME International Journal* **30**(260), pp. 255–262. DOI: 10.1299/jsme1987.30.255.

[97] Novak, F. and Sarpkaya, T. (2000). Turbulent Vortex Breakdown at High Reynolds Numbers. *AIAA Journal* **38**(5), pp. 825–834. DOI: 10.2514/2.1036.

[98] Novotny, P., Weigand, B., Marsik, F., Biegger, C., and Tomas, M. (2018). Flow Structures in a Swirl Flow - Vortex Breakdown Condition. *Journal of Physics: Conference Series* **1045**, pages. DOI: 10.1088/1742-6596/1045/1/012031.

[99] Pfitzer, H. (1992). Konvektiver Wärmetransport im axial durchströmten Ringspalt zwischen rotierenden Hohlwehlen. PhD thesis. Technische Hochschule Darmstadt: Institut für Technische Thermodynamik.

[100] Pfitzer, H. and Beer, H. (1992). Heat Transfer in an Annulus between Independently Rotating Tubes with Turbulent Axial Flow. *International Journal of Heat and Mass Transfer* **35**(3), pp. 623–633. DOI: 10.1016/0017-9310(92)90121-8.

[101] Raffel, M., Willert, C. E., Wereley, S. T., and Kompenhans, J. (2007). Particle Image Velocimetry: A Practical Guide. Second Edition. Berlin, Heidelberg: Springer. ISBN: 978-3-540-72307-3.

[102] Ranque, G. J. (1933). Expériences sur la Détente Giratoire avec Productions Simultanées d'un Echappement d'air Chaud et d'un Echappement d'air Froid. *Journal de Physique et le Radium* **4**(7), pp. 112–114.

[103] Rao, Y., Biegger, C., and Weigand, B. (2017). Heat Transfer and Pressure Loss in Swirl Tubes with One and Multiple Tangential Jets Pertinent to Gas Turbine Internal Cooling. *International Journal of Heat and Mass Transfer* **106**, pp. 1356–1367. DOI: 10.1016/j.ijheatmasstransfer.2016.10.119.

[104] Refan, M. and Hangan, H. (2016). Characterization of Tornado-Like Flow Fields in a New Model Scale Wind Testing Chamber. *Journal of Wind Engineering and Industrial Aerodynamics* **151**, pp. 107–121. DOI: 10.1016/j.jweia.2016.02.002.

[105] Refan, M., Hangan, H., and Wurman, J. (2014). Reproducing Tornadoes in Laboratory using Proper Scaling. *Journal of Wind Engineering and Industrial Aerodynamics* **135**, pp. 136–148. DOI: 10.1016/j.jweia.2014.10.008.

[106] Reich, G. and Beer, H. (1989). Fluid Flow and Heat Transfer in an Axially Rotating Pipe - I. Effect of Rotation on Turbulent Pipe Flow. *International Journal of Heat and Mass Transfer* **32**(3), pp. 551–562. DOI: 10.1016/0017-9310(89)90143-9.

[107] Reich, G., Weigand, B., and Beer, H. (1989). Fluid Flow and Heat Transfer in an Axially Rotating Pipe - II. Effect of Rotation on Laminar Pipe Flow. *International Journal of Heat and Mass Transfer* **32**(3), pp. 563–574. DOI: 10.1016/0017-9310(89)90144-0.

[108] Reynolds, A. J. (1961). Energy Flows in a Vortex Tube. *Journal of Applied Mathematics and Physics (ZAMP)* **12**(4), pp. 343–357. DOI: 10.1007/BF01591284.

[109] Rothe, T. (1994). Der Einfluß der Rotation af die Strömung und den Wärmetransport im turbulent durchströmten Ringspalt zwischen zwei rotierenden Wellen. PhD thesis. Technische Hochschule Darmstadt: Institut für Technische Thermodynamik.

[110] Saffman, P. G. (1992). Vortex Dynamics. New York: Cambridge University Press. ISBN: 978-0-521477-39-0.

[111] Saric, W. S. (1994). Görtler Vortices. *Annual Review of Fluid Mechanics* **26**, pp. 379–409. DOI: 10.1146/annurev.fl.26.010194.002115.

[112] Sarpkaya, T. (1971). Vortex Breakdown in Swirling Conical Flows. *AIAA Journal* **9**(9), pp. 1792–1799. DOI: 10.2514/3.49981.

[113] Schlichting, H. (1979). Boundary-Layer Theory. Trans. by Kestin, J. Seventh Edition. New York: McGraw-Hill. ISBN: 0-07-055334-3.

[114] Sciacchitano, A. (2014). Uncertainty Quantification in Particle Image Velocimetry and Advances in Time-Resolved Image and Data Analysis. PhD thesis. Delft University of Technology: Faculty of Aerospace Engineering.

[115] Sciacchitano, A. and Wieneke, B. (2016). PIV Uncertainty Propagation. *Measurement Science and Technology* **27**(8), pages. DOI: 10.1088/0957-0233/27/8/084006.

[116] Spalart, P. R. and Shur, M. (1997). On the Sensitization of Turbulence Models to Rotation and Curvature. *Aerospace Science and Technology* **1**(5), pp. 297–302. DOI: 10.1016/S1270-9638(97)90051-1.

[117] Spall, R. E., Gatski, T. B., and Grosch, C. E. (1987). A Criterion for Vortex Breakdown. *Physics of Fluids* **30**(11), pp. 3434–3440. DOI: 10.1063/1.866475.

[118] Squire, H. B. (1960). Analysis of the "Vortex Breakdown" Phenomenon, Part I. Tech. rep. Department Report No. 102. London, UK: Imperial College London, Department of Aeronautics.

[119] Taylor, G. I. (1923). Stability of a Viscous Liquid Contained between Two Rotating Cylinders. *Philosophical Transactions of the Royal Society of London* **223**(605-615), pp. 289–343. DOI: 10.1098/rsta.1923.0008.

[120] Uddin, N. (2008). Turbulence Modeling of Complex Flow in CFD. PhD thesis. Universität Stuttgart: Institut für Thermodynamik der Luft- und Raumfahrt (ITLR).

[121] Vogler, P. (2015). Numerische Simulation einer Wirbelrohrströmung mit Explizit Algebraischen Reynolds-Spannungs-modellen (EARSM)

in OpenFOAM. MA thesis. Universität Stuttgart: Institut für Thermodynamik der Luft- und Raumfahrt (ITLR).

[122] Wallin, S. and Johansson, A. V. (2000). An Explicit Algebraic Reynolds Stress Model for Incompressible and Compressible Turbulent Flows. *Journal of Fluid Mechanics* **403**, pp. 89–132. DOI: 10.1017/S0022112099007004.

[123] Wallin, S. and Johansson, A. V. (2002). Modelling Streamline Curvature Effects in Explicit Algebraic Reynolds Stress Turbulence Models. *International Journal of Heat and Fluid Flow* **23**(5), pp. 721–730. DOI: 10.1016/S0142-727X(02)00168-6.

[124] Wang, S. (2007). On the Stability of Swirling Flows in a Finite Pipe. Tech. rep. Research Reports-558. Auckland, New Zealand: The University of Auckland.

[125] Wang, S. and Rusak, Z. (1996a). On the Stability of an Axisymmetric Rotating Flow in a Pipe. *Physics of Fluids* **8**(4), pp. 1007–1016. DOI: 10.1063/1.868882.

[126] Wang, S. and Rusak, Z. (1996b). On the Stability of Non-Columnar Swirling Flows. *Physics of Fluids* **8**(4), pp. 1017–1023. DOI: 10.1063/1.868878.

[127] Weigand, B. and Beer, H. (1992). Fluid Flow and Heat Transfer in an Axially Rotating Pipe Subjected to External Convection. *International Journal of Heat and Mass Transfer* **35**(7), pp. 1803–1809. DOI: 10.1016/0017-9310(92)90151-H.

[128] Weigand, B. and Beer, H. (1994). On the Universality of the Velocity Profiles of a Turbulent Flow in an Axially Rotating Pipe. *Applied Scientific Research* **52**(2), pp. 115–132. DOI: 10.1007/BF00868054.

[129] Wereley, S. T. and Lueptow, R. M. (1998). Spatio-Temporal Character of Non-Wavy and Wavy Taylor-Couette Flow. *Journal of Fluid Mechanics* **364**, pp. 59–80. DOI: 10.1017/S0022112098008969.

[130] Wereley, S. T. and Lueptow, R. M. (1999). Velocity Field for Taylor-Couette Flow with an Axial Flow. *Physics of Fluids* **11**(12), pp. 3637–3649. DOI: 10.1063/1.870228.

[131] Wilcox, D. C. (1993). Turbulence Modeling for CFD. First Edition. La Cañada: DCW Industries, Inc. ISBN: 0-9636051-0-0.

[132] Wooldridge, J. M. (2013). Introductory Econometrics: A Modern Approach. Fifth Edition. Mason: South-Western, Cengage Learning. ISBN: 1-111-53104-8.

[133] Xue, Y., Arjomandi, M., and Kelso, R. (2010). A Critical Review of Temperature Separation in a Vortex Tube. *Experimental Thermal and Fluid Science* **34**(8), pp. 1367–1374. DOI: 10.1016/j.expthermflusci.2010.06.010.

[134] Yih, C.-S. (2007). Tornado-Like Flows. *Physics of Fluids* **19**(7), pages. DOI: 10.1063/1.2742728.

[135] Yilmaz, M., Kaya, M., Karagoz, S., and Erdogan, S. (2009). A Review on Design Criteria for Vortex Tubes. *Heat and Mass Transfer* **45**(5), pp. 613–632. DOI: 10.1007/s00231-008-0447-8.

APPENDIX A

Thermodynamic Stability Condition in Cylindrical Coordinates

In this Appendix, the transformation of the thermodynamic inequality, i.e. the local TSC function, from a Cartesian coordinate system, Eq. (3.47), into a cylindrical coordinate system is presented. Moreover, the presented transformation follows the monograph of Borisenko and Tarapov in translation by Silverman [18] and the monograph of Itskov [54].
Thus, relation between the Cartesian ($x^1 = x$, $x^2 = y$, $x^3 = z$) and cylindrical ($\xi^1 = r$, $\xi^2 = \phi$, $\xi^3 = z$) coordinate system, Fig. A.1, is given by

$$x = r\cos\phi,\ y = r\sin\phi,\ z = z.$$

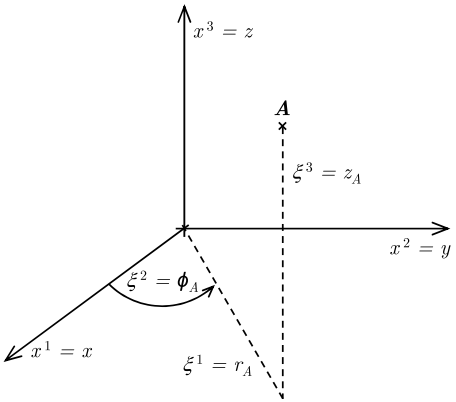

Fig. A.1: Relations between the Cartesian and cylindrical coordinate system

A.1 Covariant and Contravariant Basis

The covariant basis can be basically described as

$$\mathbf{g}_r = \frac{\partial x_j}{\partial r}\mathbf{e}_j = \begin{bmatrix} \cos\phi \\ \sin\phi \\ 0 \end{bmatrix}, \; |\mathbf{g}_r| = \sqrt{(\cos\phi)^2 + (\sin\phi)^2} = 1,$$

$$\mathbf{g}_\phi = \frac{\partial x_j}{\partial \phi}\mathbf{e}_j = \begin{bmatrix} -r\sin\phi \\ r\cos\phi \\ 0 \end{bmatrix}, \; |\mathbf{g}_\phi| = \sqrt{-(r\sin\phi)^2 + (r\cos\phi)^2} = r,$$

$$\mathbf{g}_z = \frac{\partial x_j}{\partial z}\mathbf{e}_j = \begin{bmatrix} 0 \\ 0 \\ 1 \end{bmatrix}, \; |\mathbf{g}_z| = \sqrt{1^2} = 1.$$

The normalised covariant basis is given from the non-normalised covariant basis by the following simple recalculations

$$\mathbf{g}_{\bar{r}} = \frac{\mathbf{g}_r}{|\mathbf{g}_r|} = \begin{bmatrix} \cos\phi \\ \sin\phi \\ 0 \end{bmatrix},$$

$$\mathbf{g}_{\bar{\phi}} = \frac{\mathbf{g}_\phi}{|\mathbf{g}_\phi|} = \begin{bmatrix} -\sin\phi \\ \cos\phi \\ 0 \end{bmatrix},$$

$$\mathbf{g}_{\bar{z}} = \frac{\mathbf{g}_z}{|\mathbf{g}_z|} = \begin{bmatrix} 0 \\ 0 \\ 1 \end{bmatrix}.$$

On the other hand, the contravariant basis can be basically prescribed by

$$\mathbf{g}^i = g^{ij}\mathbf{g}_j,$$

where g^{ij} is the metric tensor for the contravariant basis and is given by the following expression

$$g^{ij} = \frac{\mathrm{cof}\,(g_{ij})}{\det|g_{ij}|}.$$

Here, $\mathrm{cof}\,(g_{ij})$ denotes a sub-determinant to an element g_{ij}. Moreover, it is possible to calculate the metric tensor for the covariant basis and its determinant by

$$g_{ij} = \mathbf{g}_i \cdot \mathbf{g}_j = \begin{bmatrix} 1 & 0 & 0 \\ 0 & r^2 & 0 \\ 0 & 0 & 1 \end{bmatrix}, \ \det|g_{ij}| = r^2.$$

Thus, components of the metric tensor for the contravariant basis can be determined as follows

$$g^{rr} = \frac{r^2 \times 1}{r^2} = 1,\ g^{r\phi} = g^{rz} = 0,$$
$$g^{\phi\phi} = \frac{1 \times 1}{r^2} = \frac{1}{r^2},\ g^{\phi r} = g^{\phi z} = 0,$$
$$g^{zz} = \frac{1 \times r^2}{r^2} = 1,\ g^{zr} = g^{z\phi} = 0,$$

$$g^{ij} = \begin{bmatrix} 1 & 0 & 0 \\ 0 & r^{-2} & 0 \\ 0 & 0 & 1 \end{bmatrix}, \ \det|g^{ij}| = \frac{1}{r^2}.$$

The contravariant basis is then given by

$$\mathbf{g}^r = g^{rr}\mathbf{g}_r = \begin{bmatrix} \cos\phi \\ \sin\phi \\ 0 \end{bmatrix}, \; |\mathbf{g}^r| = \sqrt{(\cos\phi)^2 + (\sin\phi)^2} = 1$$

$$\mathbf{g}^\phi = g^{\phi\phi}\mathbf{g}_\phi = r^{-2}\begin{bmatrix} -r\sin\phi \\ r\cos\phi \\ 0 \end{bmatrix} = \begin{bmatrix} -r^{-1}\sin\phi \\ r^{-1}\cos\phi \\ 0 \end{bmatrix},$$

$$|\mathbf{g}^\phi| = \sqrt{(-r^{-1}\sin\phi)^2 + (r^{-1}\cos\phi)^2} = r^{-1}$$

$$\mathbf{g}^z = g^{zz}\mathbf{g}_z = \begin{bmatrix} 0 \\ 0 \\ 1 \end{bmatrix}, \; |\mathbf{g}^z| = \sqrt{1^2} = 1.$$

The normalised contravariant basis is obtained as well as the normalised covariant basis by the following simple recalculations

$$\mathbf{g}^{\bar{r}} = \frac{\mathbf{g}^r}{|\mathbf{g}^r|} = \begin{bmatrix} \cos\phi \\ \sin\phi \\ 0 \end{bmatrix},$$

$$\mathbf{g}^{\bar{\phi}} = \frac{\mathbf{g}^\phi}{|\mathbf{g}^\phi|} = \begin{bmatrix} -\sin\phi \\ \cos\phi \\ 0 \end{bmatrix},$$

$$\mathbf{g}^{\bar{z}} = \frac{\mathbf{g}^z}{|\mathbf{g}^z|} = \begin{bmatrix} 0 \\ 0 \\ 1 \end{bmatrix}.$$

A.2 Relations between Coordinates

According to the covariant and contravariant basis, it is possible to express the components of the velocity vector $\mathbf{u}$ by

$$\mathbf{u} = u^i\mathbf{g}_i = u^i\frac{\mathbf{g}_i}{|\mathbf{g}_i|} = u^{\bar{i}}\mathbf{g}_{\bar{i}},$$

$$\mathbf{u} = u_i\mathbf{g}^i = u_i\frac{\mathbf{g}^i}{|\mathbf{g}^i|} = u_{\bar{i}}\mathbf{g}^{\bar{i}}.$$

The components of the velocity vector with overlined indices represent the so-called physical components and correspond to the normalised basis. Furthermore, due to their correct dimensions (units), these components of the velocity vector are used for further calculations. Thus, the following expressions are, then, obvious

$$
\begin{aligned}
&u^{\bar{r}} = u^{r}, && u^{\bar{r}} = u_{\bar{r}}, && u_{\bar{r}} = u_{r},\\
&u^{\bar{\phi}} = r u^{\phi}, && u^{\bar{\phi}} = u_{\bar{\phi}}, && u_{\bar{\phi}} = r^{-1} u_{\phi},\\
&u^{\bar{z}} = u^{z}, && u^{\bar{z}} = u_{\bar{z}}, && u_{\bar{z}} = u_{z}.
\end{aligned}
$$

A.3 Covariant Derivative

The covariant derivatives of the covariant and contravariant components of vectors and the second order tensors in the cylindrical coordinates can be expressed as follows

- covariant derivative of the contravariant vector components

$$u^{i}\big|_{j} = \frac{\partial u^{i}}{\partial \xi^{j}} + u^{j}\Gamma^{i}_{kj},$$

- covariant derivative of the contravariant second order tensor components

$$A^{ij}\big|_{k} = \frac{\partial A^{ij}}{\partial \xi^{k}} + A^{lj}\Gamma^{i}_{lk} + A^{il}\Gamma^{j}_{lk},$$

- covariant derivative of the covariant vector components

$$u_{i}\big|_{j} = \frac{\partial u_{i}}{\partial \xi^{j}} - u_{k}\Gamma^{k}_{ij},$$

- covariant derivative of the covariant second order tensor components

$$A_{ij}|_{k} = \frac{\partial A_{ij}}{\partial \xi^{k}} - A_{lj}\Gamma^{l}_{ik} - A_{il}\Gamma^{l}_{jk}.$$

In these relations Γ^{k}_{ij}, and analogous, represent the Christoffel's symbol of the second kind, [54].

A.4 Christoffel Symbols

A.4.1 Christoffel Symbol of the First Kind

The Christoffel symbol of the first kind is given by

$$[ij,k] = \frac{1}{2}\left(\frac{\partial g_{ki}}{\partial \xi^j} + \frac{\partial g_{kj}}{\partial \xi^i} - \frac{\partial g_{ij}}{\partial \xi^k}\right).$$

So, in the cylindrical coordinates, it can be expressed as

$$\begin{aligned}
[\phi\phi,r] &= \frac{1}{2}\left(\frac{\partial g_{r\phi}}{\partial \phi} + \frac{\partial g_{r\phi}}{\partial \phi} - \frac{\partial g_{\phi\phi}}{\partial r}\right) = \frac{1}{2}\left(0 + 0 - \frac{\partial r^2}{\partial r}\right) \\
&= \frac{1}{2}\left(-2 \times r\right) = -r, \\
[r\phi,\phi] &= \frac{1}{2}\left(\frac{\partial g_{\phi r}}{\partial \phi} + \frac{\partial g_{\phi\phi}}{\partial r} - \frac{\partial g_{r\phi}}{\partial \phi}\right) = \frac{1}{2}\left(0 + \frac{\partial r^2}{\partial r} - 0\right) \\
&= \frac{1}{2}\left(2 \times r\right) = r, \\
[\phi r,\phi] &= \frac{1}{2}\left(\frac{\partial g_{\phi\phi}}{\partial r} + \frac{\partial g_{\phi r}}{\partial \phi} - \frac{\partial g_{\phi r}}{\partial \phi}\right) = \frac{1}{2}\left(\frac{\partial r^2}{\partial r} + 0 - 0\right) \\
&= \frac{1}{2}\left(2 \times r\right) = r, \\
[rr,\phi] &= \frac{1}{2}\left(\frac{\partial g_{\phi r}}{\partial r} + \frac{\partial g_{\phi r}}{\partial r} - \frac{\partial g_{rr}}{\partial \phi}\right) = 0.
\end{aligned}$$

Moreover, the cylindrical coordinates are orthogonal coordinates, thus, symmetry $[r\phi,\phi] = [\phi r,\phi]$ can be applied. For all other combinations of indices i, j, k, which are not shown here, the Christoffel's symbols of the first kind are zero.

A.4.2 Christoffel Symbol of the Second Kind

The Christoffel symbol of the second kind is given by

$$\Gamma^m_{il} = \frac{1}{2} g^{km}\left(\frac{\partial g_{lk}}{\partial \xi^i} + \frac{\partial g_{ik}}{\partial \xi^l} - \frac{\partial g_{li}}{\partial \xi^k}\right) = [il,k]\, g^{km}.$$

So, in the cylindrical coordinates, it can be expressed as

$$\Gamma^{\phi}_{r\phi} = [r\phi,\phi]\, g^{\phi\phi} = r\frac{1}{r^2} = \frac{1}{r},$$
$$\Gamma^{\phi}_{\phi r} = [\phi r,\phi]\, g^{\phi\phi} = r\frac{1}{r^2} = \frac{1}{r},$$
$$\Gamma^{r}_{\phi\phi} = [\phi\phi,r]\, g^{rr} = -r.$$

For the Christoffel symbol of the second kind, symmetry can be applied as well, i.e. $\Gamma^{\phi}_{\phi r} = \Gamma^{\phi}_{r\phi}$. Here, also for all other combinations of indices i, j, k, the Christoffel symbols of the second kind are zero.

A.5 Covariant and Contravariant Components of the Velocity Vector

The derivatives of the velocity components in the cylindrical coordinates are determined via the Christofell's symbols, [54], as introduced in Section A.4. For the contravariant velocity components in the non-normalised basis, the covariant derivatives are given by

$$u^r\big|_r = \frac{\partial u^r}{\partial r} + u^r\Gamma^r_{rr} + u^\phi\Gamma^r_{\phi r} + u^z\Gamma^r_{zr} = \frac{\partial u^r}{\partial r},$$
$$u^r\big|_\phi = \frac{\partial u^r}{\partial \phi} + u^r\Gamma^r_{r\phi} + u^\phi\Gamma^r_{\phi\phi} + u^z\Gamma^r_{z\phi} = \frac{\partial u^r}{\partial \phi} - ru^\phi,$$
$$u^r\big|_z = \frac{\partial u^r}{\partial z} + u^r\Gamma^r_{rz} + u^\phi\Gamma^r_{\phi z} + u^z\Gamma^r_{zz} = \frac{\partial u^r}{\partial z},$$
$$u^\phi\big|_r = \frac{\partial u^\phi}{\partial r} + u^r\Gamma^\phi_{rr} + u^\phi\Gamma^\phi_{\phi r} + u^z\Gamma^\phi_{zr} = \frac{\partial u^\phi}{\partial r} + \frac{u^\phi}{r},$$
$$u^\phi\big|_\phi = \frac{\partial u^\phi}{\partial \phi} + u^r\Gamma^\phi_{r\phi} + u^\phi\Gamma^\phi_{\phi\phi} + u^z\Gamma^\phi_{z\phi} = \frac{\partial u^\phi}{\partial \phi} + \frac{u^r}{r},$$
$$u^\phi\big|_z = \frac{\partial u^\phi}{\partial z} + u^r\Gamma^\phi_{rz} + u^\phi\Gamma^\phi_{\phi z} + u^z\Gamma^\phi_{zz} = \frac{\partial u^\phi}{\partial z},$$
$$u^z\big|_r = \frac{\partial u^z}{\partial r} + u^r\Gamma^z_{rr} + u^\phi\Gamma^z_{\phi r} + u^z\Gamma^z_{zr} = \frac{\partial u^z}{\partial r},$$
$$u^z\big|_\phi = \frac{\partial u^z}{\partial \phi} + u^r\Gamma^z_{r\phi} + u^\phi\Gamma^z_{\phi\phi} + u^z\Gamma^z_{z\phi} = \frac{\partial u^z}{\partial \phi},$$

$$u^z|_z = \frac{\partial u^z}{\partial z} + u^r\Gamma^z_{rz} + u^\phi\Gamma^z_{\phi z} + u^z\Gamma^z_{zz} = \frac{\partial u^z}{\partial z}.$$

Whereas for the covariant velocity components in the non-normalised basis, the covariant derivatives are expressed as

$$\begin{aligned}
u_r|_r &= \frac{\partial u_r}{\partial r} - u_r\Gamma^r_{rr} - u_\phi\Gamma^\phi_{rr} - u_z\Gamma^z_{rr} = \frac{\partial u_r}{\partial r},\\
u_r|_\phi &= \frac{\partial u_r}{\partial \phi} - u_r\Gamma^r_{r\phi} - u_\phi\Gamma^\phi_{r\phi} - u_z\Gamma^z_{r\phi} = \frac{\partial u_r}{\partial \phi} - \frac{u_\phi}{r},\\
u_r|_z &= \frac{\partial u_r}{\partial z} - u_r\Gamma^r_{rz} - u_\phi\Gamma^\phi_{rz} - u_z\Gamma^z_{rz} = \frac{\partial u_r}{\partial z},\\
u_\phi|_r &= \frac{\partial u_\phi}{\partial r} - u_r\Gamma^r_{\phi r} - u_\phi\Gamma^\phi_{\phi r} - u_z\Gamma^z_{\phi r} = \frac{\partial u_\phi}{\partial r} - \frac{u_\phi}{r},\\
u_\phi|_\phi &= \frac{\partial u_\phi}{\partial \phi} - u_r\Gamma^r_{\phi\phi} - u_\phi\Gamma^\phi_{\phi\phi} - u_z\Gamma^z_{\phi\phi} = \frac{\partial u_\phi}{\partial \phi} + ru_r,\\
u_\phi|_z &= \frac{\partial u_\phi}{\partial z} - u_r\Gamma^r_{\phi z} - u_\phi\Gamma^\phi_{\phi z} - u_z\Gamma^z_{\phi z} = \frac{\partial u_\phi}{\partial z},\\
u_z|_r &= \frac{\partial u_z}{\partial r} - u_r\Gamma^r_{zr} - u_\phi\Gamma^\phi_{zr} - u_z\Gamma^z_{zr} = \frac{\partial u_z}{\partial r},\\
u_z|_\phi &= \frac{\partial u_z}{\partial \phi} - u_r\Gamma^r_{z\phi} - u_\phi\Gamma^\phi_{z\phi} - u_z\Gamma^z_{z\phi} = \frac{\partial u_z}{\partial \phi},\\
u_z|_z &= \frac{\partial u_z}{\partial z} - u_r\Gamma^r_{zz} - u_\phi\Gamma^\phi_{zz} - u_z\Gamma^z_{zz} = \frac{\partial u_z}{\partial z}.
\end{aligned}$$

The derivatives of the contravariant velocity components with respect to the normalised basis are given by

$$u^{\bar{i}}\Big|_j = u^i|_j|\mathbf{g}_i||\mathbf{g}^j|\mathbf{g}_{\bar{i}} \otimes \mathbf{g}^{\bar{j}} = u^{\bar{i}}|_{\bar{j}}\mathbf{g}_{\bar{i}} \otimes \mathbf{g}^{\bar{j}},$$

and, on the other hand, the derivatives of the covariant velocity components with respect to the normalised basis are formulated by

$$u_{\bar{i}}|_j = u_i|_j|\mathbf{g}^i||\mathbf{g}^j|\mathbf{g}^{\bar{i}} \otimes \mathbf{g}^{\bar{j}} = u_{\bar{i}}|_{\bar{j}}\mathbf{g}^{\bar{i}} \otimes \mathbf{g}^{\bar{j}}.$$

Then, the covariant derivatives of the contravariant velocity components are

expressed as follows

$$
\begin{aligned}
u^{\bar{r}}\big|_{\bar{r}} &= \frac{\partial u^r}{\partial r}|\mathbf{g}_r||\mathbf{g}^r| = \frac{\partial u^{\bar{r}}}{\partial r},\\
u^{\bar{r}}\big|_{\bar{\phi}} &= \left(\frac{\partial u^r}{\partial \phi} - r u^{\phi}\right)|\mathbf{g}_r||\mathbf{g}^{\phi}| = \left(\frac{\partial u^{\bar{r}}}{\partial \phi} - u^{\bar{\phi}}\right)\frac{1}{r} = \frac{1}{r}\frac{\partial u^{\bar{r}}}{\partial \phi} - \frac{u^{\bar{\phi}}}{r},\\
u^{\bar{r}}\big|_{\bar{z}} &= \frac{\partial u^r}{\partial z}|\mathbf{g}_r||\mathbf{g}^z| = \frac{\partial u^{\bar{r}}}{\partial z},\\
u^{\bar{\phi}}\big|_{\bar{r}} &= \left(\frac{\partial u^{\phi}}{\partial r} + \frac{u^{\phi}}{r}\right)|\mathbf{g}_{\phi}||\mathbf{g}^r| = \left[\frac{\partial}{\partial r}\left(\frac{u^{\bar{\phi}}}{r}\right) + \frac{u^{\bar{\phi}}}{r^2}\right] r\\
&= \left(\frac{1}{r}\frac{\partial u^{\bar{\phi}}}{\partial r} - \frac{u^{\bar{\phi}}}{r^2} + \frac{u^{\bar{\phi}}}{r^2}\right) r = \frac{\partial u^{\bar{\phi}}}{\partial r},\\
u^{\bar{\phi}}\big|_{\bar{\phi}} &= \left(\frac{\partial u^{\phi}}{\partial \phi} + \frac{u^r}{r}\right)|\mathbf{g}_{\phi}||\mathbf{g}^{\phi}| = \left[\frac{\partial}{\partial \phi}\left(\frac{u^{\bar{\phi}}}{r}\right) + \frac{u^{\bar{r}}}{r}\right] r\frac{1}{r}\\
&= \frac{1}{r}\frac{\partial u^{\bar{\phi}}}{\partial \phi} + \frac{u^{\bar{r}}}{r},\\
u^{\bar{\phi}}\big|_{\bar{z}} &= \frac{\partial u^{\phi}}{\partial z}|\mathbf{g}_{\phi}||\mathbf{g}^z| = \left[\frac{\partial}{\partial z}\left(\frac{u^{\bar{\phi}}}{r}\right)\right] r = \left(\frac{1}{r}\frac{\partial u^{\bar{\phi}}}{\partial z}\right) r = \frac{\partial u^{\bar{\phi}}}{\partial z},\\
u^{\bar{z}}\big|_{\bar{r}} &= \frac{\partial u^z}{\partial r}|\mathbf{g}_z||\mathbf{g}^r| = \frac{\partial u^{\bar{z}}}{\partial r},\\
u^{\bar{z}}\big|_{\bar{\phi}} &= \frac{\partial u^z}{\partial \phi}|\mathbf{g}_z||\mathbf{g}^{\phi}| = \frac{1}{r}\frac{\partial u^{\bar{z}}}{\partial \phi},\\
u^{\bar{z}}\big|_{\bar{z}} &= \frac{\partial u^z}{\partial z}|\mathbf{g}_z||\mathbf{g}^z| = \frac{\partial u^{\bar{z}}}{\partial z}.
\end{aligned}
$$

In addition, the covariant derivatives of the covariant velocity components are written as follows

$$
\begin{aligned}
u_{\bar{r}}|_{\bar{r}} &= \frac{\partial u_r}{\partial r}|\mathbf{g}^r||\mathbf{g}^r| = \frac{\partial u_{\bar{r}}}{\partial r},\\
u_{\bar{r}}|_{\bar{\phi}} &= \left(\frac{\partial u_r}{\partial \phi} - \frac{u_{\phi}}{r}\right)|\mathbf{g}^r||\mathbf{g}^{\phi}| = \left(\frac{\partial u_{\bar{r}}}{\partial \phi} - u_{\bar{\phi}}\right)\frac{1}{r} = \frac{1}{r}\frac{\partial u_{\bar{r}}}{\partial \phi} - \frac{u_{\bar{\phi}}}{r},\\
u_{\bar{r}}|_{\bar{z}} &= \frac{\partial u_r}{\partial z}|\mathbf{g}^r||\mathbf{g}^z| = \frac{\partial u_{\bar{r}}}{\partial z},
\end{aligned}
$$

$$
\begin{aligned}
u_{\bar{\phi}}\big|_{\bar{r}} &= \left(\frac{\partial u_\phi}{\partial r} - \frac{u_\phi}{r}\right)|\mathbf{g}^\phi||\mathbf{g}^r| = \left[\frac{\partial}{\partial r}\left(r u_{\bar{\phi}}\right) - u_{\bar{\phi}}\right]\frac{1}{r} \\
&= \left(r\frac{\partial u_{\bar{\phi}}}{\partial r} + u_{\bar{\phi}} - u_{\bar{\phi}}\right)\frac{1}{r} = \frac{\partial u_{\bar{\phi}}}{\partial r}, \\
u_{\bar{\phi}}\big|_{\bar{\phi}} &= \left(\frac{\partial u_\phi}{\partial \phi} + r u_r\right)|\mathbf{g}^\phi||\mathbf{g}^\phi| = \left[\frac{\partial}{\partial \phi}\left(r u_{\bar{\phi}}\right) + r u_{\bar{r}}\right]\frac{1}{r^2} \\
&= \frac{1}{r}\frac{\partial u_{\bar{\phi}}}{\partial \phi} + \frac{u_{\bar{r}}}{r}, \\
u_{\bar{\phi}}\big|_{\bar{z}} &= \frac{\partial u_\phi}{\partial z}|\mathbf{g}^\phi||\mathbf{g}^z| = \left[\frac{\partial}{\partial z}\left(r u_{\bar{\phi}}\right)\right]\frac{1}{r} = \left(r\frac{\partial u_{\bar{\phi}}}{\partial z}\right)\frac{1}{r} = \frac{\partial u_{\bar{\phi}}}{\partial z}, \\
u_{\bar{z}}\big|_{\bar{r}} &= \frac{\partial u_z}{\partial r}|\mathbf{g}^z||\mathbf{g}^r| = \frac{\partial u_{\bar{z}}}{\partial r}, \\
u_{\bar{z}}\big|_{\bar{\phi}} &= \frac{\partial u_z}{\partial \phi}|\mathbf{g}^z||\mathbf{g}^\phi| = \frac{1}{r}\frac{\partial u_{\bar{z}}}{\partial \phi}, \\
u_{\bar{z}}\big|_{\bar{z}} &= \frac{\partial u_z}{\partial z}|\mathbf{g}^z||\mathbf{g}^z| = \frac{\partial u_{\bar{z}}}{\partial z}.
\end{aligned}
$$

Thus, the covariant derivatives of the covariant and contravariant velocity components confirm the relation between the velocity components in the non-normalised and normalised basis introduced in Section A.2.

A.6 Divergence of the Second Order Tensor

In this work, only low Mach number flows are considered, hence, as a constitutive, i.e. material, model of the fluid the Cauchy stress tensor for the Newtonian incompressible fluid [50] is chosen. The Cauchy stress tensor for the incompressible fluid and for the physical components is defined by

$$t^{\bar{i}\bar{j}} = -p\delta^{\bar{i}\bar{j}} + t^{\bar{i}\bar{j}}_{dis}.$$

In order to determine the local TSC function, only the dissipative part of the Cauchy stress tensor is utilised. Thus, the dissipative part of the Cauchy stress tensor in the normalised basis, i.e. in the physical components, is for-

mulated as

$$t_{dis}^{\bar{i}\bar{j}} = \frac{1}{2}\mu\left(u^{\bar{i}}\Big|_{\bar{j}} + u^{\bar{j}}\Big|_{\bar{i}}\right) = \mu d^{\bar{i}\bar{j}}\left(= \mu d_{\bar{i}\bar{j}}\right),$$

where $d^{\bar{i}\bar{j}}$ is the strain rate tensor, which is the symmetric second order tensor, as well as the Cauchy stress tensor, for the incompressible fluid. The strain rate tensor, in the cylindrical coordinates, may be written as follows

$$\begin{aligned}
d^{\bar{r}\bar{r}} &= \frac{1}{2}\left(u^{\bar{r}}\Big|_{\bar{r}} + u^{\bar{r}}\Big|_{\bar{r}}\right) = \frac{\partial u^{\bar{r}}}{\partial r},\\
d^{\bar{r}\bar{\phi}} &= \frac{1}{2}\left(u^{\bar{r}}\Big|_{\bar{\phi}} + u^{\bar{\phi}}\Big|_{\bar{r}}\right) = \frac{1}{2}\left(\frac{1}{r}\frac{\partial u^{\bar{r}}}{\partial \phi} + \frac{\partial u^{\bar{\phi}}}{\partial r} - \frac{u^{\bar{\phi}}}{r}\right),\\
d^{\bar{r}\bar{z}} &= \frac{1}{2}\left(u^{\bar{r}}\Big|_{\bar{z}} + u^{\bar{z}}\Big|_{\bar{r}}\right) = \frac{1}{2}\left(\frac{\partial u^{\bar{r}}}{\partial z} + \frac{\partial u^{\bar{z}}}{\partial r}\right),\\
d^{\bar{\phi}\bar{r}} &= \frac{1}{2}\left(u^{\bar{\phi}}\Big|_{\bar{r}} + u^{\bar{r}}\Big|_{\bar{\phi}}\right) = \frac{1}{2}\left(\frac{1}{r}\frac{\partial u^{\bar{r}}}{\partial \phi} + \frac{\partial u^{\bar{\phi}}}{\partial r} - \frac{u^{\bar{\phi}}}{r}\right),\\
d^{\bar{\phi}\bar{\phi}} &= \frac{1}{2}\left(u^{\bar{\phi}}\Big|_{\bar{\phi}} + u^{\bar{\phi}}\Big|_{\bar{\phi}}\right) = \frac{1}{r}\frac{\partial u^{\bar{\phi}}}{\partial \phi} + \frac{u^{\bar{r}}}{r},\\
d^{\bar{\phi}\bar{z}} &= \frac{1}{2}\left(u^{\bar{\phi}}\Big|_{\bar{z}} + u^{\bar{z}}\Big|_{\bar{\phi}}\right) = \frac{1}{2}\left(\frac{\partial u^{\bar{\phi}}}{\partial z} + \frac{1}{r}\frac{\partial u^{\bar{z}}}{\partial \phi}\right),\\
d^{\bar{z}\bar{r}} &= \frac{1}{2}\left(u^{\bar{z}}\Big|_{\bar{r}} + u^{\bar{r}}\Big|_{\bar{z}}\right) = \frac{1}{2}\left(\frac{\partial u^{\bar{z}}}{\partial r} + \frac{\partial u^{\bar{r}}}{\partial z}\right),\\
d^{\bar{z}\bar{\phi}} &= \frac{1}{2}\left(u^{\bar{z}}\Big|_{\bar{\phi}} + u^{\bar{\phi}}\Big|_{\bar{z}}\right) = \frac{1}{2}\left(\frac{1}{r}\frac{\partial u^{\bar{z}}}{\partial \phi} + \frac{\partial u^{\bar{\phi}}}{\partial z}\right),\\
d^{\bar{z}\bar{z}} &= \frac{1}{2}\left(u^{\bar{z}}\Big|_{\bar{z}} + u^{\bar{z}}\Big|_{\bar{z}}\right) = \frac{\partial u^{\bar{z}}}{\partial z}.
\end{aligned}$$

Then, the strain rate tensor is simple rewritten into the matrix form as follows

$$d^{\bar{i}\bar{j}} = \begin{bmatrix} d^{\bar{r}\bar{r}} & d^{\bar{r}\bar{\phi}} & d^{\bar{r}\bar{z}} \\ d^{\bar{\phi}\bar{r}} & d^{\bar{\phi}\bar{\phi}} & d^{\bar{\phi}\bar{z}} \\ d^{\bar{z}\bar{r}} & d^{\bar{z}\bar{\phi}} & d^{\bar{z}\bar{z}} \end{bmatrix}.$$

For the local TSC function in cylindrical coordinates, it is important to express the divergence of the strain rate tensor [54]. The divergence of the strain rate tensor in the non-normalised basis is expressed by the relation for the covariant derivative of the second order tensor, as shown in Section A.3. In the case of the divergence of the second order tensor, the indices j and k are equal, i.e. $j = k$, thus

$$\nabla \cdot \mathbf{A} = A^{ij}\big|_j = \frac{\partial A^{ij}}{\partial \xi^j} + A^{lj}\Gamma^i_{lj} + A^{il}\Gamma^j_{lj}.$$

Also, the divergence of the second order tensor with respect to the normalised basis can be formulated by

$$A^{\bar{i}\bar{j}}\Big|_j = A^{\bar{i}\bar{j}}\Big|_{\bar{j}} |\mathbf{g}_i|\mathbf{g}_{\bar{i}}.$$

Moreover, the physical components of the second order tensor follow the expression

$$A^{\bar{i}\bar{j}} = A^{ij}\sqrt{g_{ii}g_{jj}}\ \mathbf{g}_{\bar{i}} \otimes \mathbf{g}_{\bar{j}},\ A_{\bar{i}\bar{j}} = A_{ij}\sqrt{g^{ii}g^{jj}}\ \mathbf{g}^{\bar{i}} \otimes \mathbf{g}^{\bar{j}}.$$

In addition, in cylindrical coordinates, i.e. orthogonal curvilinear coordinates, the components of the strain rate tensor in the physical components are given by

$$\begin{aligned}
&d^{\bar{r}\bar{r}} = d^{rr}, && d^{\bar{r}\bar{r}} = d_{\bar{r}\bar{r}}, && d_{\bar{r}\bar{r}} = d_{rr},\\
&d^{\bar{r}\bar{\phi}} = rd^{r\phi}, && d^{\bar{r}\bar{\phi}} = d_{\bar{r}\bar{\phi}}, && d_{\bar{r}\bar{\phi}} = r^{-1}d_{r\phi},\\
&d^{\bar{r}\bar{z}} = d^{rz}, && d^{\bar{r}\bar{z}} = d_{\bar{r}\bar{z}}, && d_{\bar{r}\bar{z}} = d_{rz},\\
&d^{\bar{\phi}\bar{r}} = rd^{\phi r}, && d^{\bar{\phi}\bar{r}} = d_{\bar{\phi}\bar{r}}, && d_{\bar{\phi}\bar{r}} = r^{-1}d_{\phi r},\\
&d^{\bar{\phi}\bar{\phi}} = r^2d^{\phi\phi}, && d^{\bar{\phi}\bar{\phi}} = d_{\bar{\phi}\bar{\phi}}, && d_{\bar{\phi}\bar{\phi}} = r^{-2}d_{\phi\phi},\\
&d^{\bar{\phi}\bar{z}} = rd^{\phi z}, && d^{\bar{\phi}\bar{z}} = d_{\bar{\phi}\bar{z}}, && d_{\bar{\phi}\bar{z}} = d_{\phi z},\\
&d^{\bar{z}\bar{r}} = d^{zr}, && d^{\bar{z}\bar{r}} = d_{\bar{z}\bar{r}}, && d_{\bar{z}\bar{r}} = d_{zr},\\
&d^{\bar{z}\bar{\phi}} = rd^{z\phi}, && d^{\bar{z}\bar{\phi}} = d_{\bar{z}\bar{\phi}}, && d_{\bar{z}\bar{\phi}} = r^{-1}d_{z\phi},\\
&d^{\bar{z}\bar{z}} = d^{zz}, && d^{\bar{z}\bar{z}} = d_{\bar{z}\bar{z}}, && d_{\bar{z}\bar{z}} = d_{zz}.
\end{aligned}$$

Hence, the divergence of the strain rate tensor in the non-normalised base is expresses as

$$
\begin{aligned}
d^{rr}\big|_r &= \frac{\partial d^{rr}}{\partial r} + d^{rr}\Gamma^r_{rr} + d^{\phi r}\Gamma^r_{\phi r} + d^{zr}\Gamma^r_{zr} + d^{rr}\Gamma^r_{rr} + d^{r\phi}\Gamma^r_{\phi r} + d^{rz}\Gamma^r_{zr} \\
&= \frac{\partial d^{rr}}{\partial r}, \\
d^{r\phi}\Big|_\phi &= \frac{\partial d^{r\phi}}{\partial \phi} + d^{r\phi}\Gamma^r_{r\phi} + d^{\phi\phi}\Gamma^r_{\phi\phi} + d^{z\phi}\Gamma^r_{z\phi} + d^{rr}\Gamma^\phi_{r\phi} + d^{r\phi}\Gamma^\phi_{\phi\phi} + d^{rz}\Gamma^\phi_{z\phi} \\
&= \frac{\partial d^{r\phi}}{\partial \phi} - r d^{\phi\phi} + \frac{d^{rr}}{r}, \\
d^{rz}\big|_z &= \frac{\partial d^{rz}}{\partial z} + d^{rz}\Gamma^r_{rz} + d^{\phi z}\Gamma^r_{\phi z} + d^{zz}\Gamma^r_{zz} + d^{rr}\Gamma^z_{rz} + d^{r\phi}\Gamma^z_{\phi z} + d^{rz}\Gamma^z_{zz} \\
&= \frac{\partial d^{rz}}{\partial z}, \\
d^{\phi r}\Big|_r &= \frac{\partial d^{\phi r}}{\partial r} + d^{rr}\Gamma^\phi_{rr} + d^{\phi r}\Gamma^\phi_{\phi r} + d^{zr}\Gamma^\phi_{zr} + d^{\phi r}\Gamma^r_{rr} + d^{\phi\phi}\Gamma^r_{\phi r} + d^{\phi z}\Gamma^r_{zr} \\
&= \frac{\partial d^{\phi r}}{\partial r} + \frac{d^{\phi r}}{r}, \\
d^{\phi\phi}\Big|_\phi &= \frac{\partial d^{\phi\phi}}{\partial \phi} + d^{r\phi}\Gamma^\phi_{r\phi} + d^{\phi\phi}\Gamma^\phi_{\phi\phi} + d^{z\phi}\Gamma^\phi_{z\phi} + d^{\phi r}\Gamma^\phi_{r\phi} + d^{\phi\phi}\Gamma^\phi_{\phi\phi} + d^{\phi z}\Gamma^\phi_{z\phi} \\
&= \frac{\partial d^{\phi\phi}}{\partial \phi} + \frac{d^{r\phi}}{r} + \frac{d^{\phi r}}{r}, \\
d^{\phi z}\Big|_z &= \frac{\partial d^{\phi z}}{\partial z} + d^{rz}\Gamma^\phi_{rz} + d^{\phi z}\Gamma^\phi_{\phi z} + d^{zz}\Gamma^\phi_{zz} + d^{\phi r}\Gamma^z_{rz} + d^{\phi\phi}\Gamma^z_{\phi z} + d^{\phi z}\Gamma^z_{zz} \\
&= \frac{\partial d^{\phi z}}{\partial z}, \\
d^{zr}\big|_r &= \frac{\partial d^{zr}}{\partial r} + d^{rr}\Gamma^z_{rr} + d^{\phi r}\Gamma^z_{\phi r} + d^{zr}\Gamma^z_{zr} + d^{zr}\Gamma^r_{rr} + d^{z\phi}\Gamma^r_{\phi r} + d^{zz}\Gamma^r_{zr} \\
&= \frac{\partial d^{zr}}{\partial r}, \\
d^{z\phi}\Big|_\phi &= \frac{\partial d^{z\phi}}{\partial \phi} + d^{r\phi}\Gamma^z_{r\phi} + d^{\phi\phi}\Gamma^z_{\phi\phi} + d^{zz}\Gamma^z_{z\phi} + d^{zr}\Gamma^\phi_{r\phi} + d^{z\phi}\Gamma^\phi_{\phi\phi} + d^{zz}\Gamma^\phi_{z\phi} \\
&= \frac{\partial d^{z\phi}}{\partial \phi} + \frac{d^{zr}}{r},
\end{aligned}
$$

$$d^{zz}\big|_z = \frac{\partial d^{zz}}{\partial z} + d^{rz}\Gamma^z_{rz} + d^{\phi z}\Gamma^z_{\phi z} + d^{zz}\Gamma^z_{zz} + d^{zr}\Gamma^z_{rz} + d^{z\phi}\Gamma^z_{\phi z} + d^{zz}\Gamma^z_{zz}$$
$$= \frac{\partial d^{zz}}{\partial z}.$$

According to the expressions of the strain rate tensor for the physical components, the divergence of the second-order tensor, i.e. the divergence of the strain rate tensor in the normalised basis, is given by

$$d^{\bar{r}\bar{r}}\Big|_r = d^{\bar{r}\bar{r}}\Big|_r |\mathbf{g}_r| = \frac{\partial d^{\bar{r}\bar{r}}}{\partial r},$$
$$d^{\bar{r}\bar{\phi}}\Big|_\phi = d^{\bar{r}\bar{\phi}}\Big|_\phi |\mathbf{g}_r| = \frac{\partial}{\partial \phi}\left(\frac{d^{\bar{r}\bar{\phi}}}{r}\right) - r\frac{d^{\bar{\phi}\bar{\phi}}}{r^2} + \frac{d^{\bar{r}\bar{r}}}{r}$$
$$= \frac{\partial d^{\bar{r}\bar{\phi}}}{r\partial\phi} - \frac{d^{\bar{\phi}\bar{\phi}}}{r} + \frac{d^{\bar{r}\bar{r}}}{r},$$
$$d^{\bar{r}\bar{z}}\Big|_z = d^{\bar{r}\bar{z}}\Big|_z |\mathbf{g}_r| = \frac{\partial d^{\bar{r}\bar{z}}}{\partial z},$$
$$d^{\bar{\phi}\bar{r}}\Big|_r = d^{\bar{\phi}\bar{r}}\Big|_r |\mathbf{g}_\phi| = \left[\frac{\partial}{\partial r}\left(\frac{d^{\bar{\phi}\bar{r}}}{r}\right) + \frac{1}{r}\frac{d^{\bar{\phi}\bar{r}}}{r}\right] r$$
$$= \left(-\frac{d^{\bar{\phi}\bar{r}}}{r^2} + \frac{\partial d^{\bar{\phi}\bar{r}}}{r\partial r} + \frac{d^{\bar{\phi}\bar{r}}}{r^2}\right) r = \frac{\partial d^{\bar{\phi}\bar{r}}}{\partial r},$$
$$d^{\bar{\phi}\bar{\phi}}\Big|_\phi = d^{\bar{\phi}\bar{\phi}}\Big|_\phi |\mathbf{g}_\phi| = \left[\frac{\partial}{\partial \phi}\left(\frac{d^{\bar{\phi}\bar{\phi}}}{r^2}\right) + \frac{1}{r}\frac{d^{\bar{r}\bar{\phi}}}{r} + \frac{1}{r}\frac{d^{\bar{\phi}\bar{r}}}{r}\right] r$$
$$= \left(\frac{\partial d^{\bar{\phi}\bar{\phi}}}{r^2\partial\phi} + \frac{d^{\bar{r}\bar{\phi}}}{r^2} + \frac{d^{\bar{\phi}\bar{r}}}{r^2}\right) r = \frac{\partial d^{\bar{\phi}\bar{\phi}}}{r\partial\phi} + \frac{d^{\bar{r}\bar{\phi}}}{r} + \frac{d^{\bar{\phi}\bar{r}}}{r},$$
$$d^{\bar{\phi}\bar{z}}\Big|_z = d^{\bar{\phi}\bar{z}}\Big|_z |\mathbf{g}_\phi| = \left[\frac{\partial}{\partial z}\left(\frac{\partial d^{\bar{\phi}\bar{z}}}{r}\right)\right] r = \frac{\partial d^{\bar{\phi}\bar{z}}}{\partial z},$$
$$d^{\bar{z}\bar{r}}\Big|_r = d^{\bar{z}\bar{r}}\Big|_r |\mathbf{g}_z| = \frac{\partial d^{\bar{z}\bar{r}}}{\partial r},$$
$$d^{\bar{z}\bar{\phi}}\Big|_\phi = d^{\bar{z}\bar{\phi}}\Big|_\phi |\mathbf{g}_z| = \frac{\partial}{\partial \phi}\left(\frac{d^{\bar{z}\bar{\phi}}}{r}\right) + \frac{d^{\bar{z}\bar{r}}}{r} = \frac{\partial d^{\bar{z}\bar{\phi}}}{r\partial\phi} + \frac{d^{\bar{z}\bar{r}}}{r},$$
$$d^{\bar{z}\bar{z}}\Big|_z = d^{\bar{z}\bar{z}}\Big|_z |\mathbf{g}_z| = \frac{\partial d^{\bar{z}\bar{z}}}{\partial z}.$$

Then, with respect to the symmetry of the strain rate tensor, i.e. $d^{\bar{i}\bar{j}} = d^{\bar{j}\bar{i}}$, $i \neq j = r,\, \phi,\, z$, the divergence of the strain rate tensor is rewritten into the following matrix form

$$d^{\bar{i}\bar{j}}\Big|_{\bar{j}} = \begin{bmatrix} \frac{1}{r}\frac{\partial\left(r d^{\bar{r}\bar{r}}\right)}{\partial r} + \frac{1}{r}\frac{\partial d^{\bar{r}\bar{\phi}}}{\partial \phi} + \frac{\partial d^{\bar{r}\bar{z}}}{\partial z} - \frac{d^{\bar{\phi}\bar{\phi}}}{r} \\ \frac{1}{r}\frac{\partial\left(r d^{\bar{\phi}\bar{r}}\right)}{\partial r} + \frac{1}{r}\frac{\partial d^{\bar{\phi}\bar{\phi}}}{\partial \phi} + \frac{\partial d^{\bar{\phi}\bar{z}}}{\partial z} + \frac{d^{\bar{r}\bar{\phi}}}{r} \\ \frac{1}{r}\frac{\partial\left(r d^{\bar{z}\bar{r}}\right)}{\partial r} + \frac{1}{r}\frac{\partial d^{\bar{z}\bar{\phi}}}{\partial \phi} + \frac{\partial d^{\bar{z}\bar{z}}}{\partial z} \end{bmatrix}.$$

Assuming an incompressible fluid, i.e. $\nabla \cdot \mathbf{u} = 0$, the divergence of the strain rate tensor becomes

$$d^{\bar{i}\bar{j}}\Big|_{\bar{j}} = \begin{bmatrix} \frac{1}{2}\left(\frac{\partial^2 u^{\bar{r}}}{\partial r^2} + \frac{1}{r}\frac{\partial u^{\bar{r}}}{\partial r} + \frac{1}{r^2}\frac{\partial^2 u^{\bar{r}}}{\partial \phi^2} + \frac{\partial^2 u^{\bar{r}}}{\partial z^2} - \frac{2}{r^2}\frac{\partial u^{\bar{\phi}}}{\partial \phi} - \frac{u^{\bar{r}}}{r^2}\right) \\ \frac{1}{2}\left(\frac{\partial^2 u^{\bar{\phi}}}{\partial r^2} + \frac{1}{r}\frac{\partial u^{\bar{\phi}}}{\partial r} + \frac{1}{r^2}\frac{\partial^2 u^{\bar{\phi}}}{\partial \phi^2} + \frac{\partial^2 u^{\bar{\phi}}}{\partial z^2} + \frac{2}{r^2}\frac{\partial u^{\bar{r}}}{\partial \phi} - \frac{u^{\bar{\phi}}}{r^2}\right) \\ \frac{1}{2}\left(\frac{\partial^2 u^{\bar{z}}}{\partial r^2} + \frac{1}{r}\frac{\partial u^{\bar{z}}}{\partial r} + \frac{1}{r^2}\frac{\partial^2 u^{\bar{z}}}{\partial \phi^2} + \frac{\partial^2 u^{\bar{z}}}{\partial z^2}\right) \end{bmatrix}.$$

A.7 Covariant Derivative of a Constant

In the local TSC function, Eq. (3.47), expression for the gradient of a scalar in cylindrical coordinates is also necessary to introduce. Thus, the gradient of a scalar is for cylindrical coordinates, generally for curvilinear orthogonal coordinates, expressed as

$$\nabla c = \frac{\partial c}{\partial \xi^j} |\mathbf{g}^j| \mathbf{g}^{\bar{j}}.$$

Now, it is possible to transform the dissipative term containing the heat flux from Cartesian coordinates into cylindrical coordinates [54]. Hence, the

dissipative term containing the heat flux in Cartesian coordinates is given by [50]

$$-\frac{q^j}{T}\frac{\partial T}{\partial x^j}, \text{ where the heat flux is } q^j = -\lambda\frac{\partial T}{\partial x^j}.$$

Firstly, the physical components of the gradient of temperature in cylindrical coordinates are introduced as follows

$$\begin{aligned}
T|_{\bar{r}} &= \frac{\partial T}{\partial r}|\mathbf{g}^r|\mathbf{g}^{\bar{r}} = \frac{\partial T}{\partial r},\\
T|_{\bar{\phi}} &= \frac{\partial T}{\partial \phi}|\mathbf{g}^{\phi}|\mathbf{g}^{\bar{\phi}} = \frac{\partial T}{\partial \phi}\frac{1}{r} = \frac{\partial T}{r\partial \phi},\\
T|_{\bar{z}} &= \frac{\partial T}{\partial z}|\mathbf{g}^z|\mathbf{g}^{\bar{z}} = \frac{\partial T}{\partial z},
\end{aligned}$$

and rewritten into vector form

$$\nabla T = \left(\frac{\partial T}{\partial r}, \frac{\partial T}{r\partial \phi}, \frac{\partial T}{\partial z}\right).$$

Then, the heat flux becomes

$$q^{\bar{r}} = -\lambda\frac{\partial T}{\partial r},\ q^{\bar{\phi}} = -\lambda\frac{1}{r}\frac{\partial T}{\partial \phi},\ q^{\bar{z}} = -\lambda\frac{\partial T}{\partial z}.$$

Hence, the dissipative term related to the gradient of temperature is thereafter given by [50]

$$\begin{aligned}
-\frac{q^{\bar{j}}}{T}\frac{\partial T}{\partial x^{\bar{j}}} &= -\frac{q^{\bar{r}}}{T}\frac{\partial T}{\partial r} - \frac{q^{\bar{\phi}}}{T}\frac{1}{r}\frac{\partial T}{\partial \phi} - \frac{q^{\bar{z}}}{T}\frac{\partial T}{\partial z}\\
&= -\frac{\lambda}{T}\left(\frac{\partial T}{\partial r}\right)\left(\frac{\partial T}{\partial r}\right) - \frac{\lambda}{T}\left(\frac{1}{r}\frac{\partial T}{\partial \phi}\right)\left(\frac{1}{r}\frac{\partial T}{\partial \phi}\right)\\
&\quad - \frac{\lambda}{T}\left(\frac{\partial T}{\partial z}\right)\left(\frac{\partial T}{\partial z}\right)\\
&= -\frac{\lambda}{T}\left[\left(\frac{\partial T}{\partial r}\right)^2 + \left(\frac{1}{r}\frac{\partial T}{\partial \phi}\right)^2 + \left(\frac{\partial T}{\partial z}\right)^2\right].
\end{aligned}$$

A.8 Thermodynamic Stability Condition in the Cylindrical Coordinates

Finally, the local TSC function, i.e. the thermodynamic stability condition, in Cartesian coordinates, Eq. (3.47), may be written as follows

$$\pi = -\frac{q^j}{T} T|_j + u_i t^{ji}_{dis}|_j + t^{ji}_{dis} u_i|_j \geq 0.$$

For curvilinear orthogonal physical coordinates, i.e. cylindrical coordinates, the local TSC function becomes

$$\pi = -\frac{q^{\bar{j}}}{T}\, T|_{\bar{j}} + u^{\bar{i}} \left(2\mu d^{\bar{j}\bar{i}}\right)\Big|_{\bar{j}} + \left(2\mu d^{\bar{j}\bar{i}}\right)\, u^{\bar{i}}\Big|_{\bar{j}} \geq 0.$$

Here, the Cauchy stress tensor for an incompressible fluid and the equality between the physical components in the covariant and contravariant bases are utilised, i.e. $u^{\bar{i}} = u_{\bar{i}}$, as discussed in Section A.2. Moreover, in the main text of the presented work, all subscripts and superscripts representing physical components are, for simplicity and lucidity, written without overline.
Thus, according to the expressions for the covariant derivatives, divergence, and gradient in cylindrical coordinates, the local TSC function, has for the physical components the following form

$$\begin{aligned}
\pi = &-\frac{\lambda}{T}\left[\left(\frac{\partial T}{\partial r}\right)^2 + \left(\frac{1}{r}\frac{\partial T}{\partial \phi}\right)^2 + \left(\frac{\partial T}{\partial z}\right)^2\right] + 2u^{\bar{r}}\frac{\partial u^{\bar{r}}}{\partial r}\frac{\partial \mu}{\partial r} \\
&+ u^{\bar{r}}\left(\frac{1}{r}\frac{\partial u^{\bar{r}}}{\partial \phi} + \frac{\partial u^{\bar{\phi}}}{\partial r} - \frac{u^{\bar{\phi}}}{r}\right)\frac{1}{r}\frac{\partial \mu}{\partial \phi} + u^{\bar{r}}\left(\frac{\partial u^{\bar{z}}}{\partial r} + \frac{\partial u^{\bar{r}}}{\partial z}\right)\frac{\partial \mu}{\partial z} \\
&+ u^{\bar{\phi}}\left(\frac{1}{r}\frac{\partial u^{\bar{r}}}{\partial \phi} + \frac{\partial u^{\bar{\phi}}}{\partial r} - \frac{u^{\bar{\phi}}}{r}\right)\frac{\partial \mu}{\partial r} + 2u^{\bar{\phi}}\left(\frac{1}{r}\frac{\partial u^{\bar{\phi}}}{\partial \phi} + \frac{u^{\bar{r}}}{r}\right)\frac{1}{r}\frac{\partial \mu}{\partial \phi} \\
&+ u^{\bar{\phi}}\left(\frac{\partial u^{\bar{\phi}}}{\partial z} + \frac{1}{r}\frac{\partial u^{\bar{z}}}{\partial \phi}\right)\frac{\partial \mu}{\partial z} + u^{\bar{z}}\left(\frac{\partial u^{\bar{z}}}{\partial r} + \frac{\partial u^{\bar{r}}}{\partial z}\right)\frac{\partial \mu}{\partial r} \\
&+ u^{\bar{z}}\left(\frac{1}{r}\frac{\partial u^{\bar{z}}}{\partial \phi} + \frac{\partial u^{\bar{\phi}}}{\partial z}\right)\frac{1}{r}\frac{\partial \mu}{\partial \phi} + 2u^{\bar{z}}\frac{\partial u^{\bar{z}}}{\partial z}\frac{\partial \mu}{\partial z} \\
&+ \mu u^{\bar{r}}\left(\frac{\partial^2 u^{\bar{r}}}{\partial r^2} + \frac{1}{r}\frac{\partial u^{\bar{r}}}{\partial r} + \frac{1}{r^2}\frac{\partial^2 u^{\bar{r}}}{\partial \phi^2} + \frac{\partial^2 u^{\bar{r}}}{\partial z^2} - \frac{2}{r^2}\frac{\partial u^{\bar{\phi}}}{\partial \phi} - \frac{u^{\bar{r}}}{r^2}\right)
\end{aligned}$$

$$
\begin{aligned}
&+ \mu u^{\bar{\phi}} \left(\frac{\partial^2 u^{\bar{\phi}}}{\partial r^2} + \frac{1}{r}\frac{\partial u^{\bar{\phi}}}{\partial r} + \frac{1}{r^2}\frac{\partial^2 u^{\bar{\phi}}}{\partial \phi^2} + \frac{\partial^2 u^{\bar{\phi}}}{\partial z^2} + \frac{2}{r^2}\frac{\partial u^{\bar{r}}}{\partial \phi} - \frac{u^{\bar{\phi}}}{r^2} \right) \\
&+ \mu u^{\bar{z}} \left(\frac{\partial^2 u^{\bar{z}}}{\partial r^2} + \frac{1}{r}\frac{\partial u^{\bar{z}}}{\partial r} + \frac{1}{r^2}\frac{\partial^2 u^{\bar{z}}}{\partial \phi^2} + \frac{\partial^2 u^{\bar{z}}}{\partial z^2} \right) + 2\mu \left(\frac{\partial u^{\bar{r}}}{\partial r} \right)^2 \\
&+ \mu \left(\frac{1}{r}\frac{\partial u^{\bar{r}}}{\partial \phi} + \frac{\partial u^{\bar{\phi}}}{\partial r} - \frac{u^{\bar{\phi}}}{r} \right) \left(\frac{1}{r}\frac{\partial u^{\bar{r}}}{\partial \phi} - \frac{u^{\bar{\phi}}}{r} \right) \\
&+ \mu \left(\frac{\partial u^{\bar{z}}}{\partial r} + \frac{\partial u^{\bar{r}}}{\partial z} \right) \frac{\partial u^{\bar{r}}}{\partial z} + \mu \left(\frac{1}{r}\frac{\partial u^{\bar{r}}}{\partial \phi} + \frac{\partial u^{\bar{\phi}}}{\partial r} - \frac{u^{\bar{\phi}}}{r} \right) \frac{\partial u^{\bar{\phi}}}{\partial r} \\
&+ 2\mu \left(\frac{1}{r}\frac{\partial u^{\bar{\phi}}}{\partial \phi} + \frac{u^{\bar{r}}}{r} \right)^2 + \mu \left(\frac{\partial u^{\bar{\phi}}}{\partial z} + \frac{1}{r}\frac{\partial u^{\bar{z}}}{\partial \phi} \right) \frac{\partial u^{\bar{\phi}}}{\partial z} \\
&+ \mu \left(\frac{\partial u^{\bar{z}}}{\partial r} + \frac{\partial u^{\bar{r}}}{\partial z} \right) \frac{\partial u^{\bar{z}}}{\partial r} + \mu \left(\frac{\partial u^{\bar{\phi}}}{\partial z} + \frac{1}{r}\frac{\partial u^{\bar{z}}}{\partial \phi} \right) \frac{1}{r}\frac{\partial u^{\bar{z}}}{\partial \phi} \\
&+ 2\mu \left(\frac{\partial u^{\bar{z}}}{\partial z} \right)^2 \geq 0. \qquad \text{(A.1)}
\end{aligned}
$$

APPENDIX B

Thermodynamic Stability Condition for Laminar Flow

In this Appendix, the calculation of the local and global TSC functions for a steady laminar flow in a circular rigid tube is shown.
Thus, into the local TSC function, Eq. (3.51), Eq. (3.52) is inserted for the axial velocity characterising a 1D simplified model of the steady laminar flow in a tube. Then, the local TSC function becomes

$$\begin{aligned}
\pi &= \frac{\mu}{r}\frac{\partial}{\partial r}\left(ru^z\frac{\partial u^z}{\partial r}\right) \\
&= K^2\frac{\mu}{r}\frac{\partial}{\partial r}\left\{r\left[1-\left(\frac{r}{R}\right)^2\right]\frac{\partial\left[1-\left(\frac{r}{R}\right)^2\right]}{\partial r}\right\} \\
&= K^2\frac{\mu}{r}\frac{\partial}{\partial r}\left[\left(r-\frac{r^3}{R^2}\right)\left(-2\frac{r}{R^2}\right)\right] \\
&= K^2\frac{\mu}{r}\frac{\partial}{\partial r}\left(-2\frac{r^2}{R^2}+2\frac{r^4}{R^4}\right) \geq 0,
\end{aligned}$$

$$\begin{aligned}\pi &= K^2 \frac{\mu}{r}\left(-4\frac{r}{R^2} + 8\frac{r^3}{R^4}\right) \\ &= 4K^2\mu\left(2\frac{r^2}{R^4} - \frac{1}{R^2}\right) \geq 0. \end{aligned} \tag{B.1}$$

The laminar flow in a tube is stable from a thermodynamic point of view, if the following conditions are satisfied

$$\begin{aligned}\pi \geq 0 \;&\rightarrow\; 4K^2\mu\left(2\frac{r^2}{R^4} - \frac{1}{R^2}\right) \geq 0 \;\rightarrow\; 2\frac{r^2}{R^4} - \frac{1}{R^2} \geq 0 \\ &\rightarrow\; r \geq \pm\sqrt{\frac{R^2}{2}} = \pm R\frac{\sqrt{2}}{2}.\end{aligned}$$

Moreover, in order to obtain an integral information characterising the flow, the global value of the TSC function for the laminar flow in a tube needs to be determined. Thus, the global TSC function is given by

$$\begin{aligned}\Pi &= \int_V 4K^2\mu\left(2\frac{r^2}{R^4} - \frac{1}{R^2}\right)\mathrm{d}\overline{V} \\ &= 2L\pi\int_0^R 4K^2\mu\left(2\frac{r^2}{R^4} - \frac{1}{R^2}\right)r\mathrm{d}r \\ &= LK^2\pi\mu\int_0^R\left(16\frac{r^3}{R^4} - 8\frac{r}{R^2}\right)\mathrm{d}r \\ &= \frac{16}{4}LK^2\pi\mu\,\frac{r^4}{R^4}\bigg|_0^R - \frac{8}{2}LK^2\pi\mu\,\frac{r^2}{R^2}\bigg|_0^R \\ &= 4LK^2\pi\mu\left(\frac{R^4}{R^4} - 0\right) - 4LK^2\pi\mu\left(\frac{R^2}{R^2} - 0\right) \\ &= 0. \end{aligned} \tag{B.2}$$

Here, $\mathrm{d}\overline{V} = r\mathrm{d}\phi\mathrm{d}r\mathrm{d}z$, $\mathrm{d}r \in (0;R)$, $\mathrm{d}\phi \in (0;2\pi)$, $\mathrm{d}z \in (0;L)$.
From the global TSC function, it follows that the steady laminar flow in a tube with radius R and length L is from a thermodynamic point of view at

the margin of stability, i.e. a possible disturbance or fluctuation may initiate an unstable character of the flow.

APPENDIX C

Thermodynamic Stability Condition for Turbulent Flow

In this Appendix, the calculation of the local and global TSC functions for a turbulent flow in a circular rigid tube is presented.
Thus, into the local TSC function, Eq. (3.51), Eq. (3.55) is inserted for the axial velocity characterising a 1D simplified model of the turbulent flow in a tube. Then, the local TSC function becomes

$$\begin{aligned}
\pi &= \frac{\mu}{r}\frac{\partial}{\partial r}\left(r u^z \frac{\partial u^z}{\partial r}\right) \\
&= K^2 \frac{\mu}{r}\frac{\partial}{\partial r}\left[r\left(R-r\right)^{1/7}\frac{\partial (R-r)^{1/7}}{\partial r}\right] \\
&= K^2 \frac{\mu}{r}\frac{\partial}{\partial r}\left[r\left(R-r\right)^{1/7}\frac{1}{7}\frac{-1}{(R-r)^{6/7}}\right] \\
&= K^2 \frac{\mu}{r}\frac{\partial}{\partial r}\left[-\frac{r}{7\left(R-r\right)^{5/7}}\right] \\
&= K^2 \frac{\mu}{r}\left[-\frac{1}{7\left(R-r\right)^{5/7}} + \frac{-5r}{49\left(R-r\right)^{12/7}}\right],
\end{aligned}$$

$$\pi = K^2 \mu \left[-\frac{1}{7r\,(R-r)^{5/7}} - \frac{5}{49\,(R-r)^{12/7}} \right] \leq 0. \tag{C.1}$$

The turbulent flow in a tube is from a thermodynamic point of view unstable in the entire region given by the coordinate r.
Moreover, in order to obtain an integral information characterising the flow, the global value of the TSC function for the turbulent flow in a tube should be calculated. Thus, the global TSC function is given by

$$\Pi = \int\limits_V K^2 \mu \left[-\frac{1}{7r\,(R-r)^{5/7}} - \frac{5}{49\,(R-r)^{12/7}} \right] \mathrm{d}\overline{V} \leq 0. \tag{C.2}$$

Here, $\mathrm{d}\overline{V} = r\mathrm{d}\phi\mathrm{d}r\mathrm{d}z$, $\mathrm{d}r \in (0; R)$, $\mathrm{d}\phi \in (0; 2\pi)$, $\mathrm{d}z \in (0; L)$.
So, from the global TSC function, it follows that the turbulent flow in a tube with radius R and length L is from a thermodynamic point of view unstable, i.e. a possible disturbance or fluctuation is not supposed to be attenuated.

APPENDIX D

Thermodynamic Stability Condition for Couette Flow between Rotating Cylinders

In this Appendix, the calculation of the local and global TSC functions of a Couette flow between two rotating cylinders is shown.
Thus, for the tangential velocity, the following general expression $u^{\phi}(r) = r\Omega(r)$, which characterises a Couette flow between two rotating cylinders, is inserted into the local TSC function, Eq. (3.59). Then, the local TSC function becomes

$$\begin{aligned}
\pi &= \mu \left[u^{\phi} \left(\frac{\partial^2 u^{\phi}}{\partial r^2} + \frac{\partial u\phi}{r \partial r} \right) + \left(\frac{\partial u^{\phi}}{\partial r} \right)^2 - 2 \frac{u^{\phi}}{r} \frac{\partial u^{\phi}}{\partial r} \right] \\
&= \mu \left[u^{\phi} \frac{\partial^2 u^{\phi}}{\partial r^2} + \left(\frac{\partial u^{\phi}}{\partial r} \right)^2 - \frac{u^{\phi}}{r} \frac{\partial u^{\phi}}{\partial r} \right] \\
&= \mu \left\{ r\Omega(r) \frac{\partial^2 [r\Omega(r)]}{\partial r^2} + \left\{ \frac{\partial [r\Omega(r)]}{\partial r} \right\}^2 - \frac{r\Omega(r)}{r} \frac{\partial [r\Omega(r)]}{\partial r} \right\},
\end{aligned}$$

$$
\begin{aligned}
\pi &= \mu \left\{ r\Omega(r) \frac{\partial}{\partial r} \left[\Omega(r) + r \frac{\partial \Omega(r)}{\partial r} \right] + \left[\Omega(r) + r \frac{\partial \Omega(r)}{\partial r} \right]^2 \right. \\
&\qquad \left. - \Omega(r) \left[\Omega(r) + r \frac{\partial \Omega(r)}{\partial r} \right] \right\} \\
&= \mu \left\{ r\Omega(r) \left[r \frac{\partial^2 \Omega(r)}{\partial r^2} + 2 \frac{\partial \Omega(r)}{\partial r} \right] + [\Omega(r)]^2 + 2r\Omega(r) \frac{\partial \Omega(r)}{\partial r} \right. \\
&\qquad \left. + r^2 \left[\frac{\partial \Omega(r)}{\partial r} \right]^2 - \left[[\Omega(r)]^2 + r\Omega(r) \frac{\partial \Omega(r)}{\partial r} \right] \right\} \\
&= \mu \left\{ r^2 \Omega(r) \frac{\partial^2 \Omega(r)}{\partial r^2} + 2r\Omega(r) \frac{\partial \Omega(r)}{\partial r} + [\Omega(r)]^2 + 2r\Omega(r) \frac{\partial \Omega(r)}{\partial r} \right. \\
&\qquad \left. + r^2 \left[\frac{\partial \Omega(r)}{\partial r} \right]^2 - \left[[\Omega(r)]^2 + r\Omega(r) \frac{\partial \Omega(r)}{\partial r} \right] \right\} \geq 0 \\
&= \mu \left\{ r^2 \Omega(r) \frac{\partial^2 \Omega(r)}{\partial r^2} + 3r\Omega(r) \frac{\partial \Omega(r)}{\partial r} + r^2 \left[\frac{\partial \Omega(r)}{\partial r} \right]^2 \right\} \geq 0. \qquad \text{(D.1)}
\end{aligned}
$$

By insertion of the relations given by Eq. (3.62) and Eq. (3.63) into this inequality, Eq. (D.1), the following expression is obtained

$$
\begin{aligned}
\pi &= \mu \left\{ r^2 \left(A + \frac{B}{r^2} \right) \frac{\partial^2}{\partial r^2} \left(A + \frac{B}{r^2} \right) + 3r \left(A + \frac{B}{r^2} \right) \frac{\partial}{\partial r} \left(A + \frac{B}{r^2} \right) \right. \\
&\qquad \left. + r^2 \left[\frac{\partial}{\partial r} \left(A + \frac{B}{r^2} \right) \right]^2 \right\} \\
&= \mu \left[\left(Ar^2 + B \right) \left(\frac{6B}{r^4} \right) + \left(3Ar + \frac{3B}{r} \right) \left(-\frac{2B}{r^3} \right) + r^2 \left(-\frac{2B}{r^3} \right)^2 \right] \\
&= \mu \left(\frac{6AB}{r^2} + \frac{6B^2}{r^4} - \frac{6AB}{r^2} - \frac{6B^2}{r^4} + \frac{4B^2}{r^4} \right) \\
&= \mu \frac{4B^2}{r^4} \\
&= \mu \frac{4\Omega_1^2 R_1^4 \left(1 - \mu_C\right)^2}{r^4 \left(1 - \eta_C^2\right)^2} \geq 0. \qquad \text{(D.2)}
\end{aligned}
$$

Moreover, in order to obtain an integral information characterising the Couette flow between rotating cylinders, the global value of the TSC function shall be calculated. Thus, the global TSC function is given by

$$\begin{aligned}
\frac{\Pi}{\mu} &= \int_V \left[\frac{4\Omega_1^2 R_1^4 \left(1-\mu_C\right)^2}{r^4\left(1-\eta_C^2\right)^2}\right] \mathrm{d}\overline{V} \\
&= \int_0^L \int_{R_1}^{R_2} \int_0^{2\pi} \left[\frac{4\Omega_1^2 R_1^4 \left(1-\mu_C\right)^2}{r^4\left(1-\eta_C^2\right)^2}\right] r \mathrm{d}\phi \mathrm{d}r \mathrm{d}z \\
&= 2\pi L \int_{R_1}^{R_2} \left[\frac{4\Omega_1^2 R_1^4 \left(1-\mu_C\right)^2}{r^4\left(1-\eta_C^2\right)^2}\right] r \mathrm{d}r \\
&= 2\pi L \int_{R_1}^{R_2} \left[\frac{4\Omega_1^2 R_1^4 \left(1-\mu_C\right)^2}{r^3\left(1-\eta_C^2\right)^2}\right] \mathrm{d}r \\
&= 2\pi L \left[-\frac{4\Omega_1^2 R_1^4 \left(1-\mu_C\right)^2}{2r^2\left(1-\eta_C^2\right)^2}\right]\Bigg|_{R_1}^{R_2} \\
&= 2\pi L \left[-\frac{4\Omega_1^2 R_1^4 \left(1-\mu_C\right)^2}{2\left(1-\eta_C^2\right)^2}\right] \left(\frac{1}{R_2^2}-\frac{1}{R_1^2}\right) \\
&= -\frac{4\pi L \Omega_1^2 R_1^4 \left(1-\mu_C\right)^2}{\left(1-\eta_C^2\right)^2} \left(\frac{1}{R_2^2}-\frac{1}{R_1^2}\right) \\
&= -\frac{4\pi L \Omega_1^2 R_1^4 \left(1-\mu_C\right)^2 \left(R_1^2-R_2^2\right)}{R_1^2 R_2^2 \left(1-\eta_C^2\right)^2} \\
&= -\frac{4\pi L \Omega_1^2 \eta_C^2 \left(1-\mu_C\right)^2 \left(R_1^2-R_2^2\right)}{\left(1-\eta_C^2\right)^2} \\
&= -\frac{4\pi L \Omega_1^2 R_2^2 \eta_C^2 \left(1-\mu_C\right)^2 \left(\eta_C^2-1\right)}{\left(1-\eta_C^2\right)^2} \geq 0.
\end{aligned} \tag{D.3}$$

Here, $\mathrm{d}\overline{V} = r\mathrm{d}\phi\mathrm{d}r\mathrm{d}z$, $\mathrm{d}r \in (R_1; R_2)$, $\mathrm{d}\phi \in (0; 2\pi)$ and $\mathrm{d}z \in (0; L)$.
In addition, for comparison, the focus is also taken on the Rayleigh's inviscid theory and its application to the investigated problem. The Rayleigh's

stability condition is given by the discriminant of stability, Eq. (3.61), which is, hence, given by

$$\Theta(r) = \frac{1}{r^3}\frac{\mathrm{d}}{\mathrm{d}r}\left(ru^{\phi}\right)^2 > 0.$$

Then, the general expression for the tangential velocity $u^{\phi}(r) = r\Omega(r)$ is inserted into the discriminant of stability and the following expression is obtained

$$\begin{aligned}\Theta(r) &= \frac{1}{r^3}\frac{\mathrm{d}}{\mathrm{d}r}\left\{r^4\left[\Omega(r)\right]^2\right\} \\ &= \frac{1}{r^3}\left\{4r^3\left[\Omega(r)\right]^2 + 2r^4\Omega(r)\frac{\mathrm{d}\Omega(r)}{\mathrm{d}r}\right\},\end{aligned}$$

$$\Theta(r) = 4\left[\Omega(r)\right]^2 + 2r\Omega(r)\frac{\mathrm{d}\Omega(r)}{\mathrm{d}r} > 0. \tag{D.4}$$

Moreover, assuming the relations given by Eq. (3.62) and Eq. (3.63), then Eq. (D.4) becomes

$$\begin{aligned}\Theta(r) &= 4\left(A + \frac{B}{r^2}\right)^2 + 2r\left(A + \frac{B}{r^2}\right)\left(-\frac{2B}{r^3}\right) \\ &= 4A^2 + \frac{8AB}{r^2} + \frac{4B^2}{r^4} - \frac{4AB}{r^2} - \frac{4B^2}{r^4} \\ &= 4A\left(A + \frac{B}{r^2}\right) \\ &= -4\Omega_1\eta_C^2\frac{1-\dfrac{\mu_C}{\eta_C^2}}{1-\eta_C^2}\left[-\Omega_1\eta_C^2\frac{1-\dfrac{\mu_C}{\eta_C^2}}{1-\eta_C^2} + \Omega_1\frac{R_1^2\left(1-\mu_C\right)}{r^2\left(1-\eta_C^2\right)}\right] \\ &= -4\Omega_1^2\eta_C^2\frac{\left(1-\dfrac{\mu_C}{\eta_C^2}\right)\left(1-\mu_C\right)}{\left(1-\eta_C^2\right)^2}\left(\frac{R_1^2}{r^2} - \frac{\eta_C^2-\mu_C}{1-\mu_C}\right).\end{aligned} \tag{D.5}$$

APPENDIX E

Supplementary Results

For the sake of completeness, the dimensionless experimental and numerical results represented by the contour plots of the obtained velocities are presented. In addition, the dimensionless values of the local and global TSC functions with included influence of the tube wall determined from the experimental and numerical results are also given.

E.1 Contour Plots of the Velocity Field

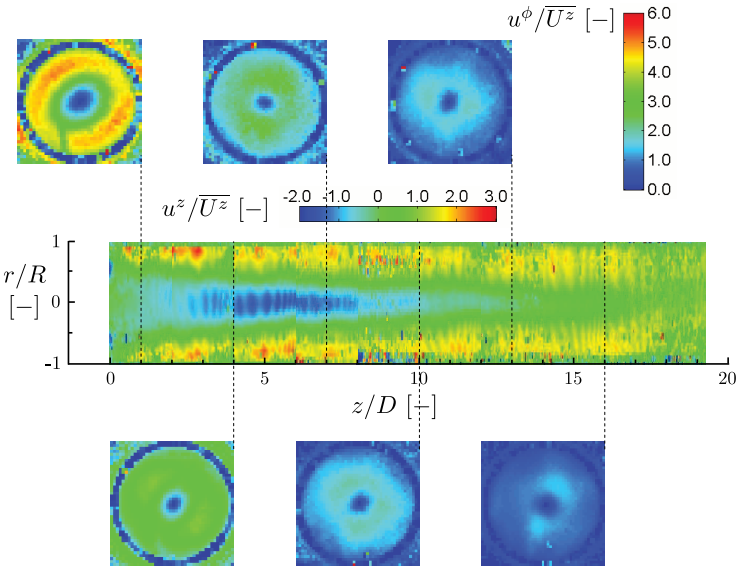

Fig. E.1: Axial and tangential velocities at the selected position determined from experimental results; $Re = 1{,}000$, $S_{IG} = 5.3$

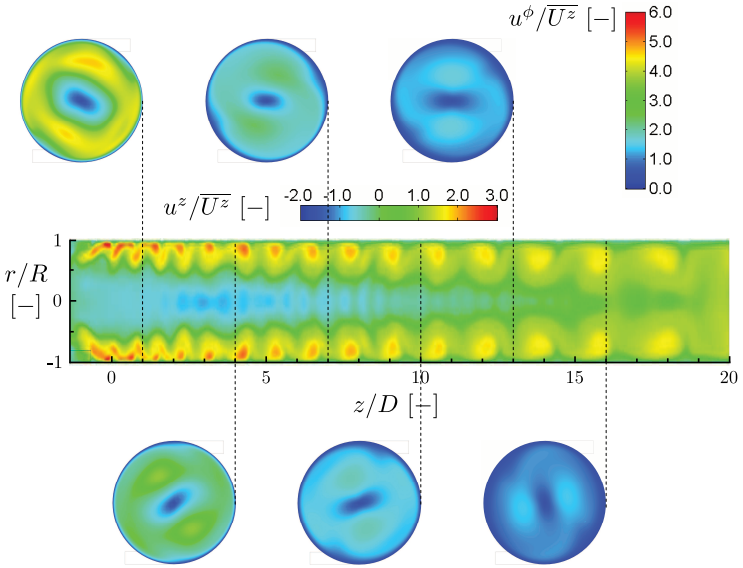

Fig. E.2: Axial and tangential velocities at the selected position determined from numerical results; $Re = 1{,}000$, $S_{IG} = 5.3$

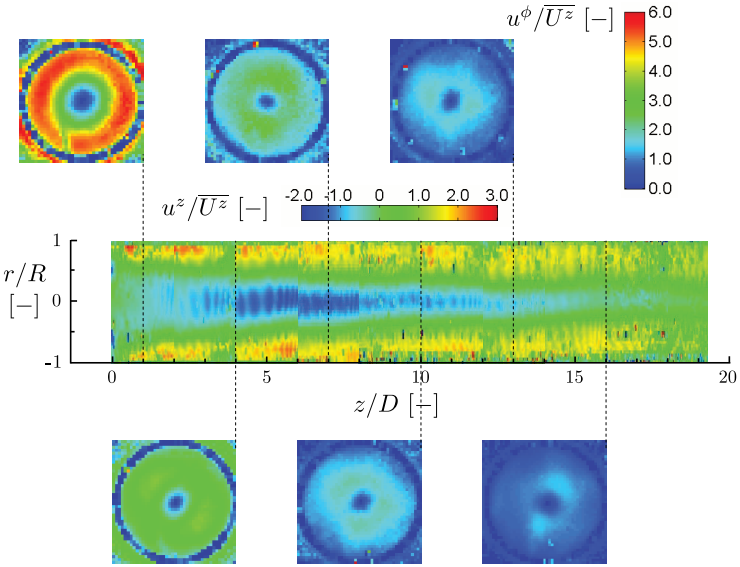

Fig. E.3: Axial and tangential velocities at the selected position determined from experimental results; $Re = 2{,}000$, $S_{IG} = 5.3$

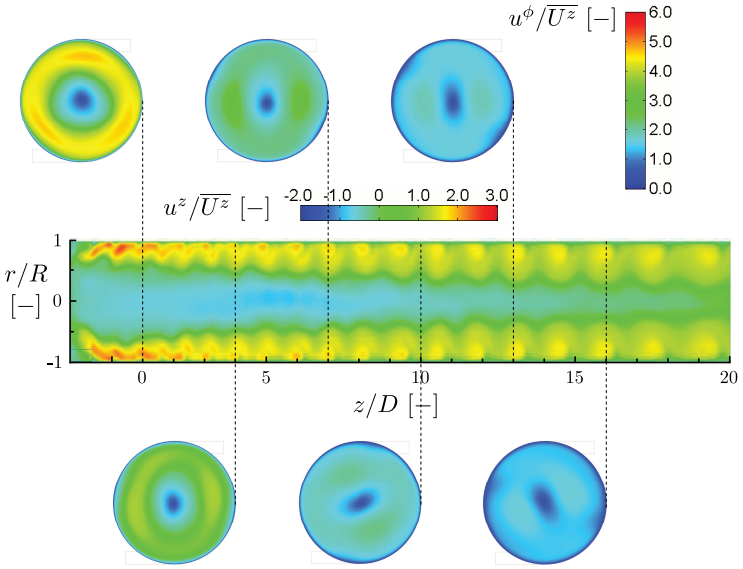

Fig. E.4: Axial and tangential velocities at the selected position determined from numerical results; $Re = 2{,}000$, $S_{IG} = 5.3$

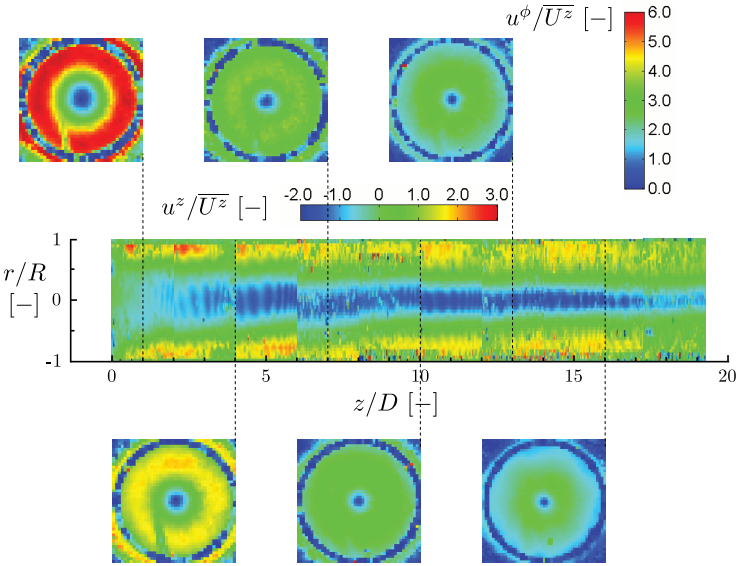

Fig. E.5: Axial and tangential velocities at the selected position determined from experimental results; $Re = 5{,}000$, $S_{IG} = 5.3$

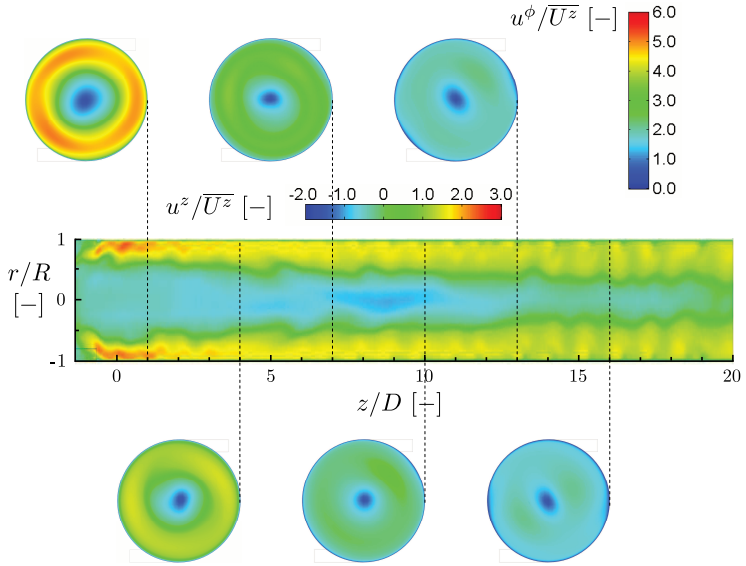

Fig. E.6: Axial and tangential velocities at the selected position determined from numerical results; $Re = 5{,}000$, $S_{IG} = 5.3$

E.2 Local Values of the Thermodynamic Stability Condition

E.2.1 Axial Velocity

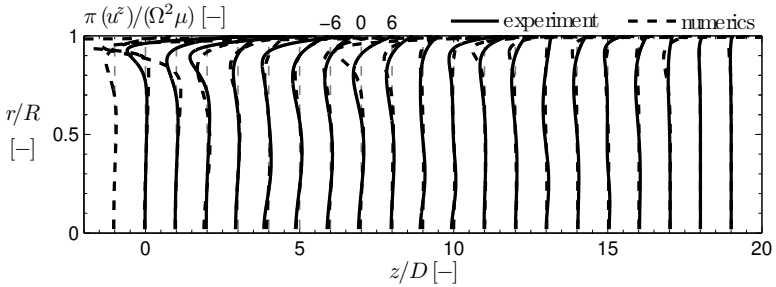

Fig. E.7: Comparison of experimental (experiment) and numerical (numerics) dimensionless values of the local TSC function with included influence of the wall for the axial velocity; $Re = 1{,}000$, $S_{IG} = 5.3$

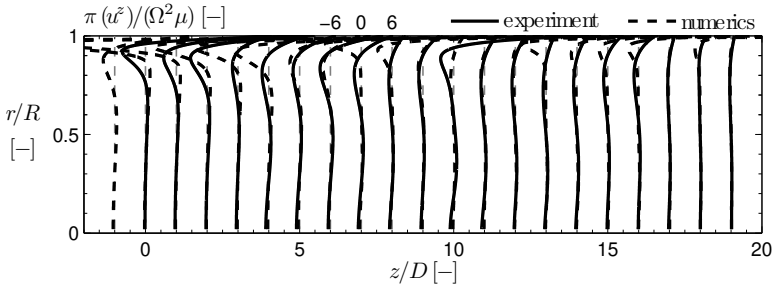

Fig. E.8: Comparison of experimental (experiment) and numerical (numerics) dimensionless values of the local TSC function with included influence of the wall for the axial velocity; $Re = 2{,}000$, $S_{IG} = 5.3$

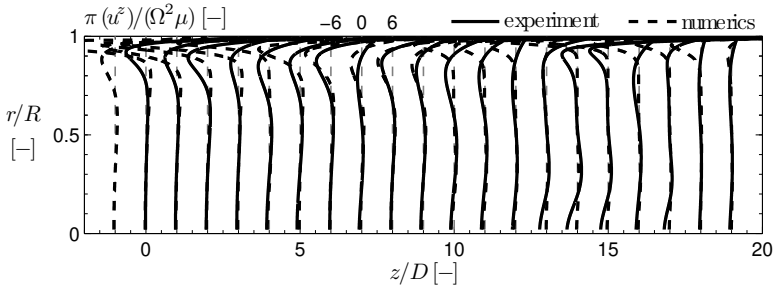

Fig. E.9: Comparison of experimental (experiment) and numerical (numerics) dimensionless values of the local TSC function with included influence of the wall for the axial velocity; $Re = 5{,}000$, $S_{IG} = 5.3$

E.2.2 Tangential Velocity

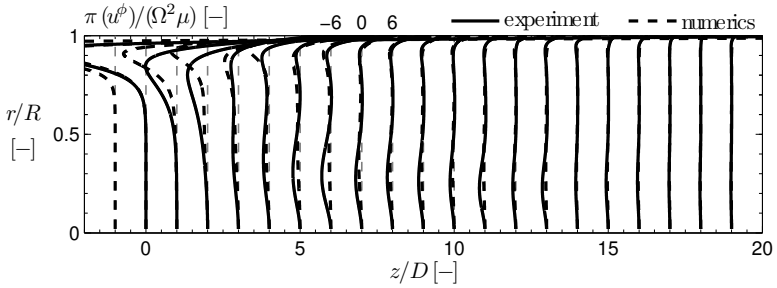

Fig. E.10: Comparison of experimental (experiment) and numerical (numerics) dimensionless values of the local TSC function with included influence of the wall for the tangential velocity; $Re = 1{,}000$, $S_{IG} = 5.3$

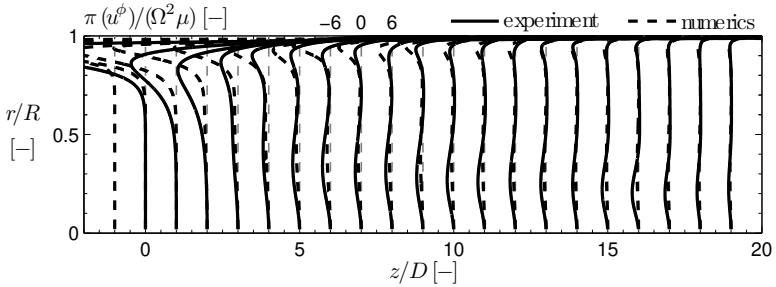

Fig. E.11: Comparison of experimental (experiment) and numerical (numerics) dimensionless values of the local TSC function with included influence of the wall for the tangential velocity; Re = 2,000, $S_{IG} = 5.3$

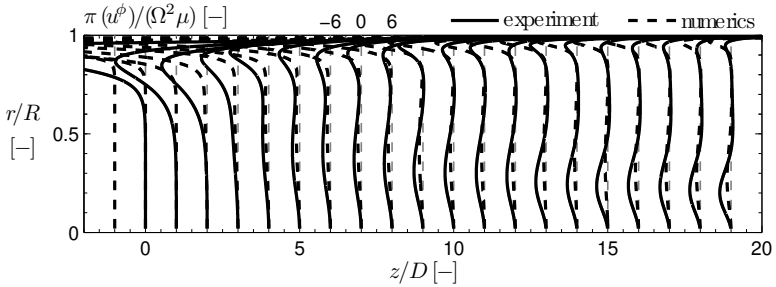

Fig. E.12: Comparison of experimental (experiment) and numerical (numerics) dimensionless values of the local TSC function with included influence of the wall for the tangential velocity; Re = 5,000, $S_{IG} = 5.3$

E.2.3 Axial and Tangential Velocities

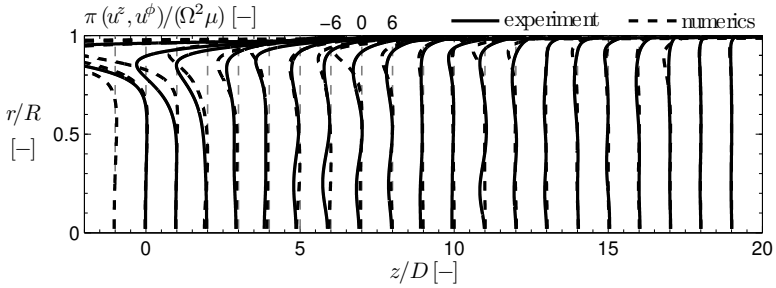

Fig. E.13: Comparison of experimental (experiment) and numerical (numerics) dimensionless values of the local TSC function with included influence of the wall for the axial and tangential velocities; $Re = 1{,}000$, $S_{IG} = 5.3$

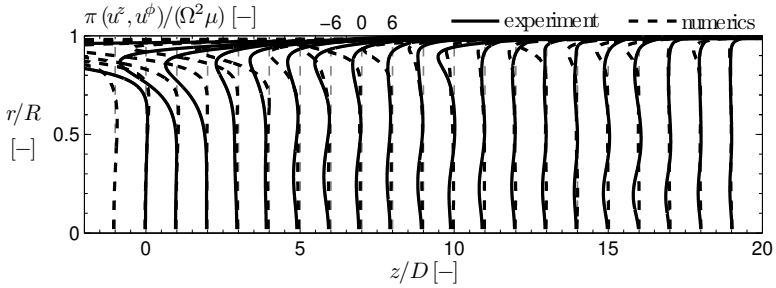

Fig. E.14: Comparison of experimental (experiment) and numerical (numerics) dimensionless values of the local TSC function with included influence of the wall for the axial and tangential velocities; $Re = 2{,}000$, $S_{IG} = 5.3$

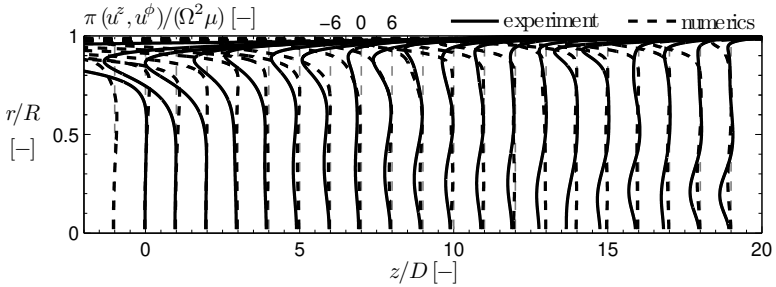

Fig. E.15: Comparison of experimental (experiment) and numerical (numerics) dimensionless values of the local TSC function with included influence of the wall for the axial and tangential velocities; $Re = 5{,}000$, $S_{IG} = 5.3$

E.3 Global Values of the Thermodynamic Stability Condition

E.3.1 Axial Velocity

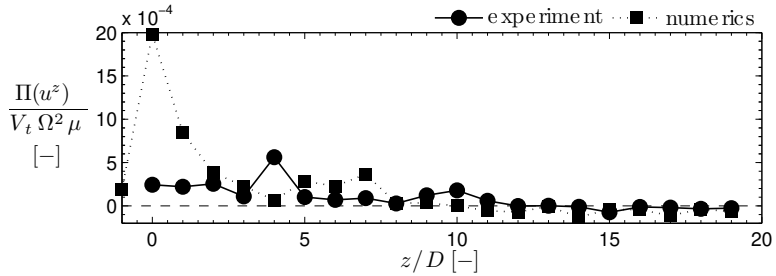

Fig. E.16: Comparison of experimental (experiment) and numerical (numerics) dimensionless values of the global TSC function with included influence of the wall for the axial velocity; $Re = 1{,}000$, $S_{IG} = 5.3$

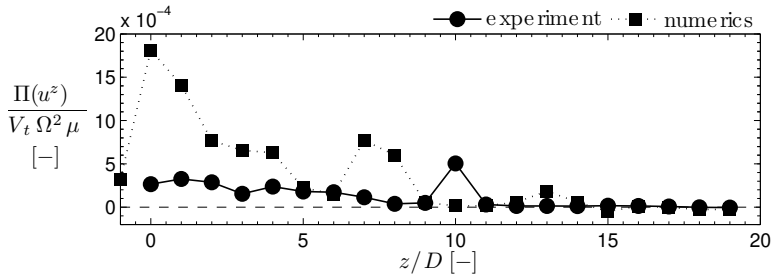

Fig. E.17: Comparison of experimental (experiment) and numerical (numerics) dimensionless values of the global TSC function with included influence of the wall for the axial velocity; $Re = 2{,}000$, $S_{IG} = 5.3$

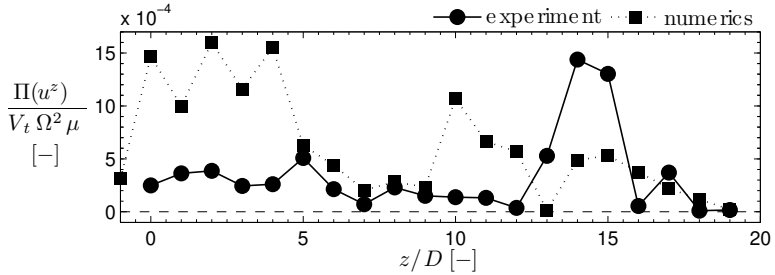

Fig. E.18: Comparison of experimental (experiment) and numerical (numerics) dimensionless values of the global TSC function with included influence of the wall for the axial velocity; $Re = 5{,}000$, $S_{IG} = 5.3$

E.3.2 Tangential Velocity

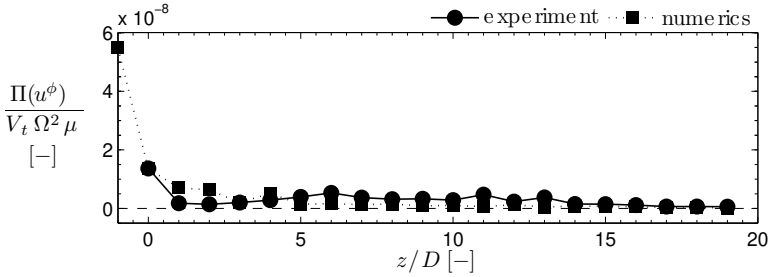

Fig. E.19: Comparison of experimental (experiment) and numerical (numerics) dimensionless values of the global TSC function with included influence of the wall for the tangential velocity; $Re = 1{,}000$, $S_{IG} = 5.3$

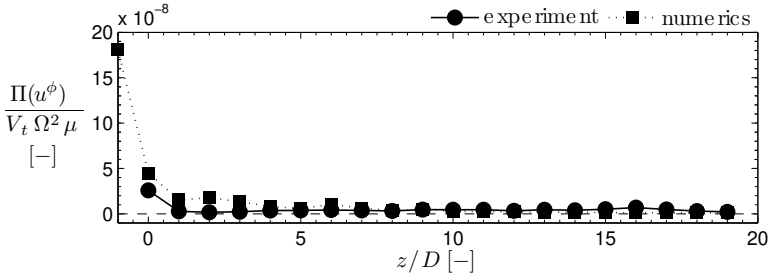

Fig. E.20: Comparison of experimental (experiment) and numerical (numerics) dimensionless values of the global TSC function with included influence of the wall for the tangential velocity; $Re = 2{,}000$, $S_{IG} = 5.3$

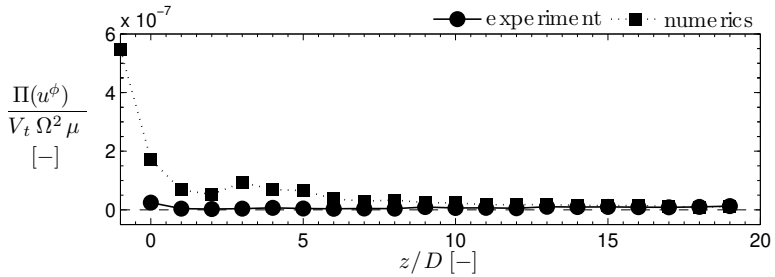

Fig. E.21: Comparison of experimental (experiment) and numerical (numerics) dimensionless values of the global TSC function with included influence of the wall for the tangential velocity; $Re = 5{,}000$, $S_{IG} = 5.3$

E.3.3 Axial and Tangential Velocities

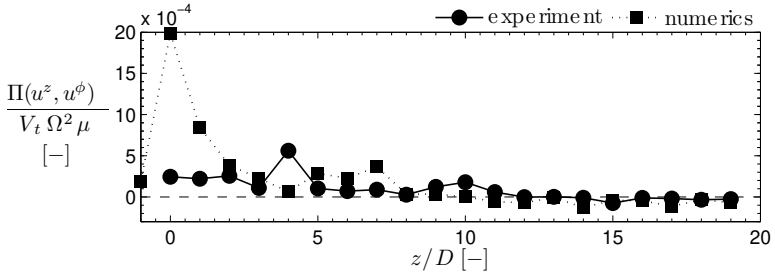

Fig. E.22: Comparison of experimental (experiment) and numerical (numerics) dimensionless values of the global TSC function with included influence of the wall for the axial and tangential velocities; $Re = 1{,}000$, $S_{IG} = 5.3$

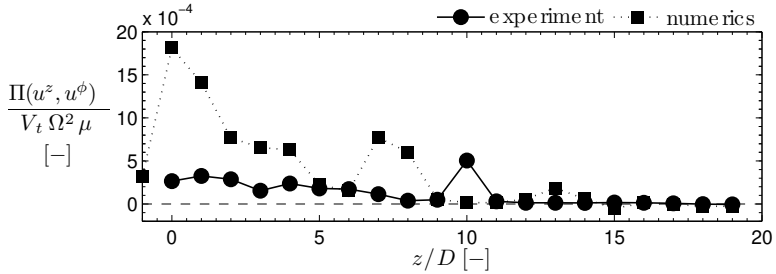

Fig. E.23: Comparison of experimental (experiment) and numerical (numerics) dimensionless values of the global TSC function with included influence of the wall for the axial and tangential velocities; $Re = 2{,}000$, $S_{IG} = 5.3$

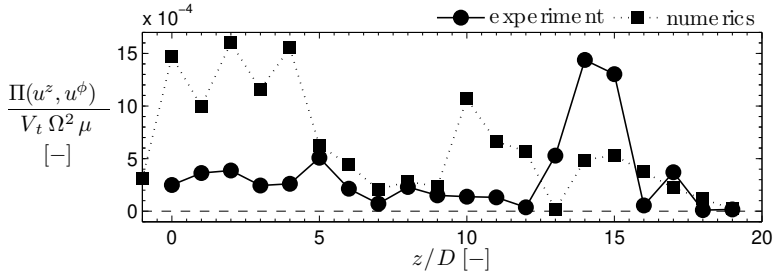

Fig. E.24: Comparison of experimental (experiment) and numerical (numerics) dimensionless values of the global TSC function with included influence of the wall for the axial and tangential velocities; $Re = 5{,}000$, $S_{IG} = 5.3$

Curriculum Vitae

Personal Data

Name:	Pavel Novotný
Date of birth:	26.08.1981
Place of birth:	Vimperk, Czech Republic
Nationality:	Czech

Experiences

since 07/2018	Development engineer at Bosch, České Budějovice, Czech Republic
07/2011-12/2017	Research assistant, New Technologies-Research Centre, University of West Bohemia, Plzeň, Czech Republic
01/2008-12/2011	Research assistant, Institute of Thermomechanics, The Czech Academy of Sciences, Prague, Czech Republic
01/2009-01/2010	Engineer in R&D, Czech Technical University in Prague, Faculty of Mechanical Engineering, Czech Republic
10/2007-12/2008	CAE engineer, TechSoft Engineering, Department of strength analysis, Prague, Czech Republic
05/2007-12/2007	Research assistant, Czech Technical University in Prague, Faculty of Mechanical Engineering, Czech Republic

Education

2001-2007	Czech Technical University in Prague, Faculty of Mechanical Engineering, Biomedical and Rehabilitation Engineering, Czech Republic
1997-2001	Secondary Technical School Volyně, Engineering Equipment of Buildings, Czech Republic